The Effect of Turboprop Propulsion on the Aerodynamic Benefits of Formation Flight

Cameron Cedric McKenzie

Supervisor: Prof. C. Redelinghuys

A dissertation submitted to the Department of Mechanical Engineering at the University of Cape Town, in partial fulfilment of the requirements for the degree of Master of Science in Mechanical Engineering.

February 2017

Declaration

1. I know the meaning of plagiarism and declare that all the work in the document, save for that which is properly acknowledged, is my own. This thesis/dissertation has been submitted to the Turnitin module (or equivalent similarity and originality checking software) and I confirm that my supervisor has seen my report and any concerns revealed by such have been resolved with my supervisor.

2. I have used the IEEE convention for citation and referencing. Each significant contribution to, and quotation in, this dissertation from the work(s) of other people has been attributed, and has been cited and referenced.

Signature: Signed by candidate

Signature removed

Abstract

In order to determine the effect of turboprop propulsion on the aerodynamic benefits of formation flight, a 3D Vortex Filament Method (VFM) programme, which made use of a Burnham-Hallock viscous core model, was formulated and employed to model the progression and interaction of the wing and turboprop trailing wakes. Within this programme, an initial prescribed wake for the turboprop engines was discretised by shed helicoidal vortex filaments generated by the use of an amalgamation of the propeller theory of Goldstein and Theodorsen. The downwash velocity field of a B747 during cruise, obtained via the use of the VFM Burnham-Hallock (VFM B-H) model programme, was verified against both the simulation conducted by Ehret and Oertel, in which an integrated Biot-Savart law VFM was utilised, as well as against experimental results obtained by Burnham et al. in their ground-based measurements of the wake vortex characteristics of a B747 aircraft. The VFM B-H model produced peak upwash and downwash velocities which matched those obtained by Ehret and Oertel to within 95% accuracy. Furthermore, a distance of 47.48 m between the rolled up vortex centres was achieved utilising the programmed VFM B-H model, which differed from the Ehret and Oertel model by only 0.48 m. Qualitatively, the 3D VFM B-H plot displayed similar degrees of roll-up and descent when compared to their Biot-Savart VFM plot. As a result of this positive validation process, the programmed VFM B-H model was utilised to simulate turboprop aircraft wakes of a higher complexity. In order to compare the effects of the number of turboprop engines on the aerodynamic benefits of formation flight, the three-bladed single turboprop engine Lancair Propjet, the six-bladed twin turboprop engine ATR 72 and the four-bladed four engine Lockheed Martin P-3 Orion were selected for comparative simulations. As extended formation flight makes use of aircraft downstream separation distances of more than ten wingspans, a wake length of 330 m (which equates to 10.9 span lengths for the P-3 Orion, 12.4 span lengths for the ATR 72 and 36.3 span lengths for the Lancair Propjet) was selected. All aircraft were simulated via the use of the VFM B-H model programme for a range of flight states from cruise conditions to zero g wing loading with full propeller thrust, such as in vertical ascents. From said simulations a novel viscous core radius to simulation convergence relationship equation was developed. The induced velocity fields at 330 m downstream in the wake were then generated in order to investigate the effects of the inclusion of turboprop engines on the aerodynamic benefits of formation flight. From said downwash plots, it was found that the helicoidal vortices affected that region of the wake within an average value of 35% of the wingspan, measured from the fuselage symmetry plane, for all simulated aircraft. In aircraft design, wing mounted engines are placed in a more inboard position in order to reduce rudder strength requirements as well as to minimize the yawing moment due to asymmetric thrust in the event of an engine failure. These helicoidal vortices' areas of influence are a result of said aircraft design convention as well as the helicoidal vortex sheets having a much lower vortex strength and filament density than the wing wake. The regions of the wing wake dominated by upwash induced velocities are outboard of an average value of 40% of the wingspan, measured from the fuselage symmetry plane. It is this region in which the drag reduction, fuel saving benefits of extended formation flight are harnessed. Therefore, as a result of aircraft engine mounting convention and marginal outboard drift of the helicoidal vortices, the turboprops' helicoidal vortices have minimal to negligible effect on the 10% wing overlap outboard-most region that sees positive fuel savings of 10% to 16% for previous extended formation flight investigations.

Acknowledgements

First and foremost, I would like to thank my supervisor, Prof. C. Redelinghuys, for his continued support and guidance throughout this project. Your knowledge of the field of aeronautics is truly awe-inspiring.

To Airbus and the National Aerospace Centre, the funding you have provided me as well as your continued contributions to the field of aeronautical engineering is greatly appreciated.

Lastly, I would also like to thank my parents, Cedric and Jenny, for their unwavering support and encouragement throughout the duration of my studies.

Luceo Non Uro

Table of Contents

List of Figures

List of Tables

Nomenclature

Symbols:

Wing Reference Frame

A_n	Fourier Series Coefficients
AR	Aspect Ratio
b	Wingspan
$\vec{b}$	Right-Hand Side of the Lifting Line Fourier Series Expansion Equation
c	Wing Chord Length
C_{Di}	Coefficient of Induced Drag
C_l	2-D Lift Coefficient
$C_{l\alpha}$	Lift Slope Coefficient
D	Nonformation Flight Drag Vector
D'	Rotated Formation Flight Drag Vector
ΔD	Drag Force Reduction
D_F	Resultant Formation Flight Drag Force
D_i	Induced Drag
$d\vec{l}$	Differential Directed Vortex Filament Segment
L	Nonformation Flight Lift Vector
L'	Rotated Formation Flight Lift Vector
$L'_{(y)}$	Differential Lift Element (Lift per Unit Span)
ΔL	Lift Force Increase
L_F	Resultant Formation Flight Lift Force
n	Number of LLM Node Stations along Wing Span
n_f	Number of Vortex Filaments on each Semi-Span
n_{poly}	Degree of Polyfit Polynomial
$\vec{r}$	Radius Vector
r_c	Vortex Filament Core Radius

s	Wing Semi-span $\left(s = \frac{b}{2}\right)$
ts	Number of Time Steps
V_∞	Free Stream Velocity (Aircraft Cruising Velocity)
W	Upwash Force of Leading Aircraft
w_i	Induced Downwash Velocity
α	Effective Angle of Attack
$\Delta\alpha$	Change in Wing's Effective Angle of Attack
α_e	Effective Angle of Attack
α_i	Change in Angle of Attack due to Downwash
α_t	Local Change in Angle of Attack due to Geometric Twist of the Wing
α_∞	Free Stream Angle of Attack for the Three-Dimensional Wing
α_0	Zero-Lift Angle of Attack
Γ	Circulation
$\frac{d\Gamma_{(y)}}{dy}$	Circulation Gradient along Wingspan
ρ	Density of Fluid
θ	Polar coordinates of Vortex Filament starting positions

Symbols:

Propeller Reference Frame

B	Number of Blades
D	Propeller Diameter
$G(r, \lambda_2)$	Goldstein Circulation Function $\frac{\Gamma(r)}{hw} = \frac{B\Gamma\Omega}{2\pi w(V+w)}$
h	Axial distance between adjacent turns of the vortex sheets, $\frac{2\pi(V+w)}{\Omega B}$
$K(r_1)$	Tribery and Wrench Tabulated Circulation Function
n	Propeller Revolutions per Second
P	Linear Pitch of Helicoidal Vortex Sheet
R	Propeller Radius

R_1	Helicoidal Vortex Sheet Radius
r	Universal Radial Coordinate
r_0	Propeller Radial Coordinate
r_1	Trailing Helicoidal Vortex Sheet Radial Coordinate
S	Control Surface and Area of Axial Projection of Helicoid, πR_1^2
T	Thrust
U_0	Resultant Velocity at a Blade Element
u_θ	Tangential Velocity
u_z	Axial Velocity
V_∞	Free Stream Velocity/Aircraft Advance Velocity
w	Axial Displacement Velocity of Helicoidal Vortex Sheets in Far Field Propeller Wake
$\overline{w}$	$\frac{w}{V}$
x	$\frac{r}{R}$, Propeller Dimensionless Radial Coordinate
x_1	$\frac{r}{R_1}$, Trailing Helicoidal Vortex Sheet Dimensionless Radial Coordinate
x_h	Dimensionless Radial Coordinate of the Propeller Hub
z	Trailing Wake Axial Coordinate with Origin Located at Propeller Plane
Γ	Circulation
θ	Angular Coordinate in the Polar Coordinate System r, θ, z
λ	Advance Ratio $\frac{V}{\Omega R}$
λ_1	Advance Ratio $\frac{V}{\Omega R_1}$
λ_2	Advance Ratio $\frac{(V+w)}{\Omega R_1} = (1 + \overline{w})\,\lambda_1$
ρ	Density
ϕ	Pitch Angle of Vortex Sheet, $\tan^{-1}\left(\frac{\lambda_2}{x}\right)$
φ	Velocity Potential
Ω	Angular Velocity
κ	Mass Transport Factor

ε	Axial Energy Tip Loss Factor

Subscripts:

c	Core
e	Effective
F	Formation Flight
i	Induced
t	Geometric Twist
∞	Free Stream
0	Propeller Reference Frame
1	Helicoidal Trailing Vortex System Reference Frame
h	At the Propeller Hub
Tip	At the Helicoidal Vortex Sheet Edge/Tip
$Centre$	Centre Line of Helicoidal Trailing Vortex System

Abbreviations:

LLM	Lifting Line Method
VFM	Vortex Filament Method
B-H	Burnham-Hallock viscous core model

Chapter 1

1. Introduction

With the development of aerodynamic theory, it was shown that formation flight could be used to increase an aircraft's range. Only until the last few decades, however, advances in precision navigation and control have made attaining these benefits a feasible possibility [1]. There has thus been an awakening of renewed attention to formation flight.

To date, extensive research has been conducted into quantifying formation flight benefits and how to implement the control required. Most notably, the Autonomous Formation Flight project at NASA Dryden Flight Research Centre utilised two F/A-18 aircraft, flying in a close proximity formation, to achieve an induced drag reduction of over 20% and a fuel saving of over 18% [2, 3]. Close proximity formation flight is, however, too hazardous for use in commercial aviation. A safer alternative is known as extended formation flight and is defined by stream-wise separation distances of more than 10 spans between the aircraft in the formation. Theoretical studies of extended formation flight have shown a drag reduction of approximately 30% and 40% for a 2-aircraft and 3-aircraft formation respectively [1, 4]. In order for long distance extended formation flight to be implemented practically, investigations into the control systems required have also been conducted. Such an investigation involved a field test utilising C-17 Globemaster aircrafts, with their current autopilot system, to achieve a fuel flow reduction of 7% – 8% [5].

The vast majority of all theoretical and experimental formation flight investigations have been conducted utilising turbojet propelled aircraft. Little is known about the wing and propeller wake interactions of a turboprop propelled aircraft formation. The following report therefore aims to explore the effect turboprop propelled aircraft have on the relative positioning of aircraft in a formation. The study makes use of an amalgamation of approximate aerodynamic models to determine whether the far field aircraft wing wake is noticeably affected by the helicoidal vortices shed from its turboprop engines. The computer model created, in order to facilitate such a study, is multivariable and thus highly versatile in allowing for a full range of turboprop aircraft to be modelled in the current and future investigations.

Chapter 2

2. Literature Review

2.1 The Theory of Formation Flight

Formation flight has been used in nature as a power saving method even before the invention of aircraft. During long flights, migratory birds employ V formations in order to reduce their heart rate and thus decrease their energy spent [1]. Biomimicry has thus resulted in this tactic being investigated in the field of aeronautics.

A wing generates lift by inducing a downward momentum into the surrounding air. This downward momentum of air creates a high pressure system beneath the wing and a subsequent low pressure system above the wing. The net imbalance of the pressure distribution results in the generation of lift [6]. As shown in the figure below, this pressure distribution also results in the flow curling around the wing tips. The air flowing over the bottom surface of the wing therefore travels towards the wing tip, from the high pressure system to the low pressure system, and the air flowing over the top surface of the wing travels inboard of the wing tip.

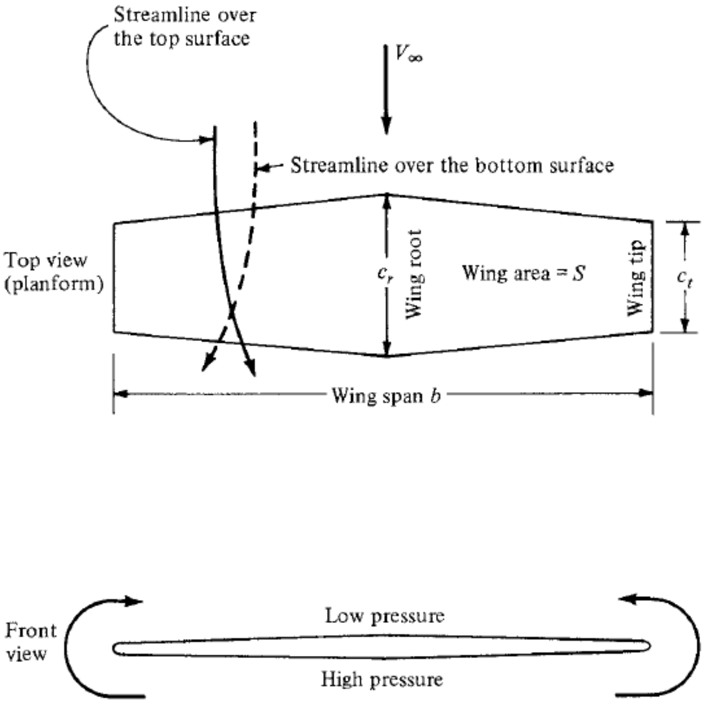

Figure 2.1 Pressure distribution over finite wing [6].

When the flow travelling over the top and bottom wing surfaces meets at the trailing edge of the wing, a vortex sheet is created. The tendency of the flow to curl around the wingtips results in the roll up of this vortex sheet into a pair of counter rotating vortices, trailing each wing slightly inboard of the wing tip. As shown in the figure below, this rolling up of the vortex sheet produces a downwash region inboard of the vortex and an upwash region outboard of the vortex [6].

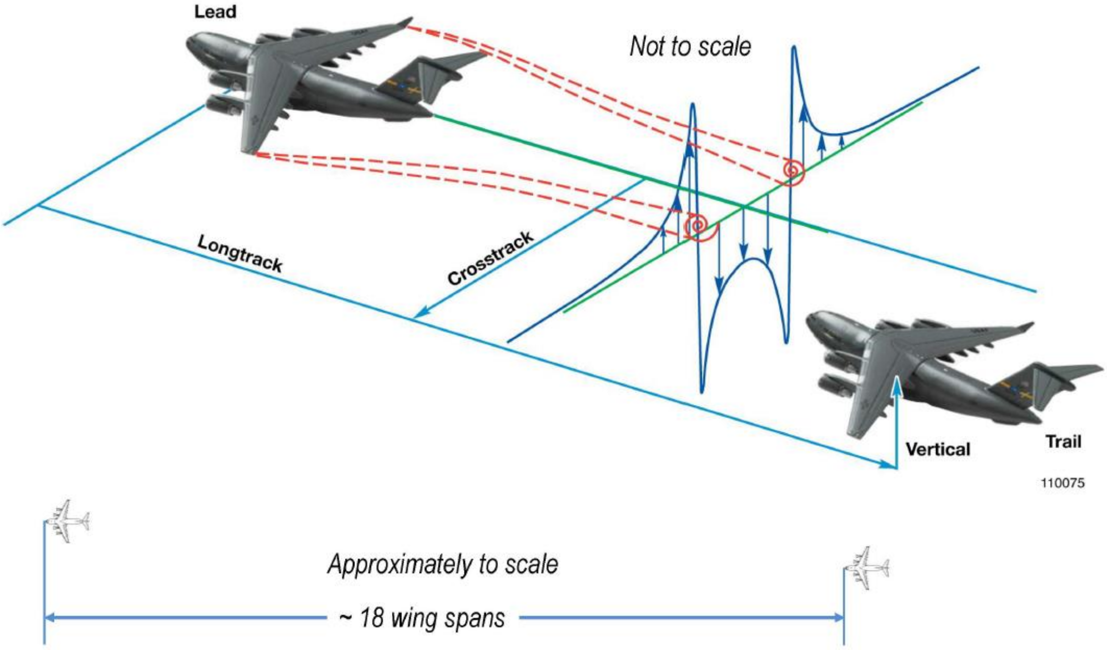

Figure 2.2 C-17 Globemaster Formation Flight Geometry [5].

When a trailing aircraft is positioned in the upwash field of a leading aircraft's wake, it sees an increase in its effective angle of attack. This increased angle of attack is a result of the rotation of the lift vector due to the upwash. As depicted by Ray et al. [3], the following figure shows how the nonformation flight lift and drag vectors (L and D) rotate by the change in angle of attack, $\Delta\alpha$, due to the upwash force, W, of the trailing vortex of the leading aircraft in formation flight.

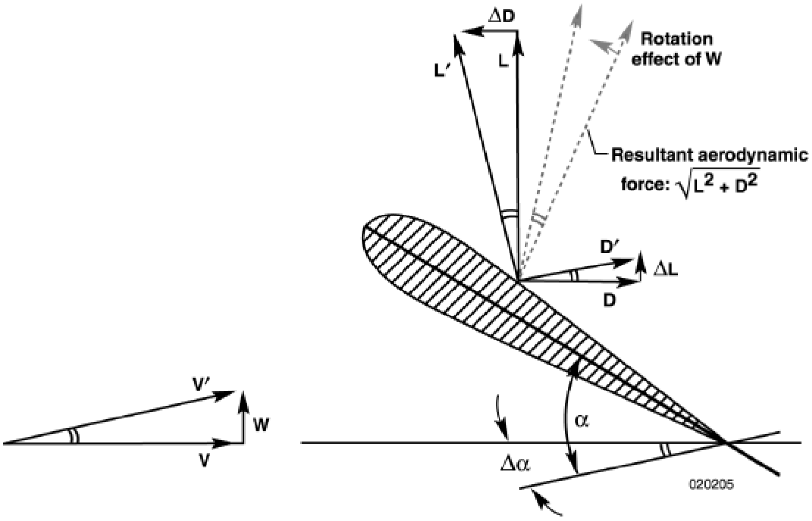

Figure 2.3 Rotation of lift and drag forces due to upwash induced by leading aircraft [3].

It is therefore evident that the drag reduction, ΔD, is obtained by the rotation of the original lift force from L to L'. The reduced drag during formation flight is therefore given by [3]:

$$D_F = D' \cos(\Delta\alpha) - \Delta D \tag{2.1.1}$$

where:

$$\Delta D = \sin(\Delta\alpha)\, L \tag{2.1.2}$$

Similarly, an increase in lift, ΔL , is obtained by the rotation of the drag force from D to D'. The increased lift during formation flight is therefore given by [3]:

$$L_F = L' \cos(\Delta\alpha) + \Delta L \tag{2.1.3}$$

where:

$$\Delta L = \sin(\Delta\alpha)\, D \tag{2.1.4}$$

In practice, the pilot will have to trim the trailing aircraft to ensure all forces acting on it remain in balance. This will ensure the trailing aircraft does not diverge from its flightpath in the upwash field of the leading aircraft. More specifically, the reduction in drag requires the pilot to reduce power in order to maintain speed, and the increase in lift requires the pilot to decrease the pitch of the aircraft in order to maintain altitude [3].

It is therefore this reduction in required power that results in the sought after decrease in fuel consumption obtained through formation flight.

2.2 Vortex Wake Characteristics

A vortex sheet is a planar array of parallel vortex filaments that translate in the direction of fluid motion [7]. As the vortex sheet is aligned with the velocity field of the fluid, there can exist no force acting upon it, no pressure gradient across it, and no discontinuity of normal velocity through it. There is, however, a discontinuity of tangential velocity, of which the magnitude is the vortex strength of the sheet [25].

The velocity field of an aircraft’s wake is dominated by the rolling up of this vortex sheet, at the

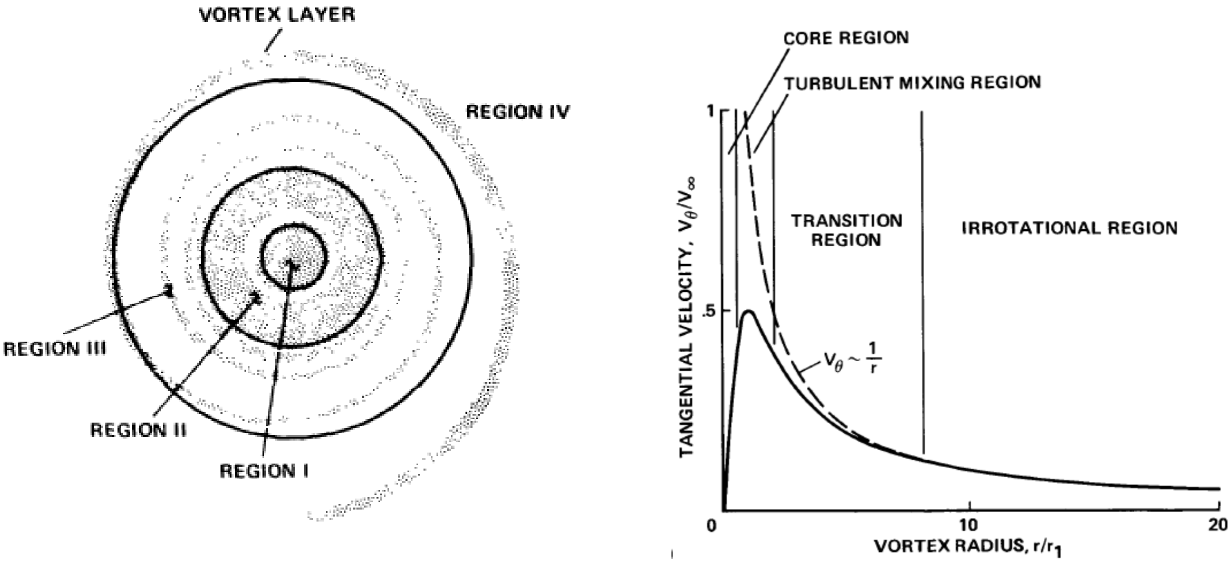

Figure 2.4 Regions of the roll up and merging of a vortex sheet along with the tangential velocity and position of each region [8, 9]

wingtips, in to two counter rotating vortices of equal strength. As shown by Tung et al. [8] these tip vortices consist of four distinct flow regions, which are as follows:

Region I – Viscous Core:

The inner most region is governed by laminar flow and solid body type rotation. The magnitude of the circulation in this region is proportional to the square of the distance from the centre.

Region II – Turbulent Mixing Region:

Within this region the flow is turbulent and the tangential velocity attains its maximum value at the maximum velocity radius, r1.

Region III – Transition Region:

The transitional region lies between the turbulent mixing region and the irrotational region and thus the flow here is extremely variable.

Region IV – Irrotational Region:

This region is governed by inviscid and irrotational flow in which circulation is constant.

Although the physical size and characteristics of these regions may vary, they remain distinct as the vortex ages. Conveniently labelled by Takahashi et al. [9], the aging of the vortex sheet in a wing's wake can be divided into three distinct regions as shown in the figure below:

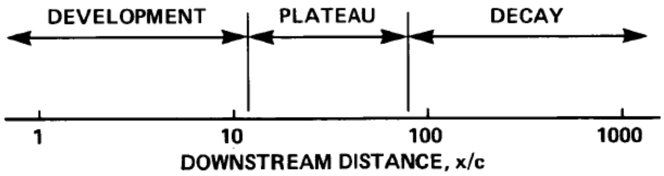

Figure 2.5 Longitudinal characterisation of wing wake vortex sheet [9].

The Development Region:

The development region is the region between the trailing edge of the wing and the point at which the wingtip wake has fully rolled up into two counter rotating vortices. For a simple wing, this point can occur almost instantaneously at the trailing edge of the wing, however, for a flapped wing this point is situated anywhere from 5 to 20 spans downstream [9, 10].

The Plateau Region:

The plateau region is typically situated more than 20 span lengths downstream. It is characterised by a pair of stable fully rolled up counter rotating vortices which begin to decay slowly.

The Decay Region:

The decay region is characterised by the decay of the vortices at a rate proportional to the square root of the downstream distance.

Once the vortices enter the decay region they no longer possess the energy required for the purpose of formation flight. Therefore, as aforementioned, Extended Formation Flight is conducted in the late stages of the development region or the early stages of the plateau region, more than 10 spans downstream of the leading aircraft [1, 4]. This ensures the vortices possess sufficient energy to maximise drag reduction whilst still ensuring the aircraft are positioned a safe following distance from one another.

2.3 Wake Modelling in Formation Flight

To date, a range of models have been utilised to accurately predict wake interactions in formation flight simulations. A highly accurate simulation which encompasses precise aerodynamic and turbulence models in conjunction with flight mechanics and control parameters would be extremely computationally expensive. In an extensive review of airplane trailing vortices, Spalart [11] states that a model capable of achieving an accuracy of 30% when predicting the trajectory and lifespan of vortices behind an aircraft would be extremely remarkable. As with all simulations, there is a trade-off between accuracy and computational cost. The type of model selected is, therefore, dependent on the type of formation being investigated, which aspects of formation flight the model is intended to most accurately simulate, as well as the computational processing power available. As a result, formation flight wake modelling makes use of either flat wake models or dynamic wake models.

Flat wake models involve rigid wake geometries without dynamic interaction between induced velocities and wake structure. For example, in a review of flat wake theory for predicting rotor inflow-wake velocities (with regards to helicopter rotors), Wilson [12] states that flat wake theory involves a rigid undeflected ribbon of vorticity shed by the lifting surface. With this model applied to helicopters, the vortices shed from the rotor blades are assumed to merge into a single ribbon of vorticity trailing behind the rotor.

Flat wake models, such as Prandtl's lifting line theory and the vortex lattice method, have been used extensively in modelling aircraft wakes in formation flight. Most notably, the predicted induced drag reduction obtained from both a single horseshoe (Prandtl's lifting line theory) model and a vortex lattice model was compared to flight test data presented by Vachon et al. [2] and Ray et al. [3]. The comparison showed the results of both models corresponded well with the flight test data around the position of maximum aerodynamic advantage. Flat wake models are effective in predicting the trends of the loads on the trailing aircraft, but their representation of the lead aircraft wake is poor. An investigation conducted by Blake and David [13] indicated that the vortex lattice model is capable of over predicting induced drag savings by an average of 15% when compared to data obtained through wind tunnel tests.

Flat wake models serve as reasonable approximations in close formation flight, as the trailing wake has had little time to develop. In extended formation flight, however; wake rollup, vortex motion, vortex interaction, and circulation and decay should be accounted for and thus more dynamic models are required [1].

Dynamic wake models involve either a Eularian or Lagrangian approach. Eularian based dynamic wake models involve a CFD approach of Large Eddy Simulation (LES), whereas Lagrangian dynamic wake models involve vortex filament methods (VFM). Each method is suited to particular aspects of formation flight, and both approaches have, therefore, been used extensively in such models. For example, in an investigation into aircraft drag reduction through extended formation flight, Ning [1] utilised a linearised vortex filament method in order to simulate wake propagation for various configurations of three aircraft formations. A high-fidelity CFD analysis was then conducted in order to investigate compressibility effects of a smaller two aircraft formation [1].

CFD is extremely computationally expensive in high gradient regions such as those found in vortices; however, it is unparalleled in accuracy and in providing a comprehensive view of fluid flow. CFD is therefore suited to more intricate investigations of smaller domains, where higher fidelity is required or where compressibility and viscosity are important considerations. Vortex filament models provide less comprehensive views of fluid flow than CFD, but they are less computationally expensive. VFM is therefore utilised in lower fidelity investigations of larger domains, and for comparative studies in which model parameters, such as formation configurations, can be rapidly compared to one another.

The current investigation, whose methods are presented in the following chapter, aims to determine the effect turboprop propulsion has on the aerodynamics of formation flight. The investigation therefore involves a large domain and comparative study of varying parameters, namely engine and propeller blade configurations. A dynamic wake model, the vortex filament method, has therefore been selected in order to model the wing wake and propeller wake interaction of the leading aircraft in the formation. VFM will allow for rapid engine configuration comparisons whilst providing a reasonably comprehensive fluid flow field view of the wing and propeller wake interaction. However, a flat wake model, Prandtl's lifting line theory, will be utilised to determine the starting parameters from which the vortex filament model will develop the trailing wake. Furthermore, in order to reduce computational costs, the propeller wake will employ a flat wake model type reduction to the VFM utilised in generating its trailing wake. The theory of vortex filament methods, Prandtl's lifting line theory and propeller wake modelling will, therefore, be detailed further in the subsequent sections of this literature review.

2.3.1 Lifting-Line Theory

The Prandtl Lifting-Line Theory is a mathematical model used to predict the spanwise lift distribution of a three-dimensional wing based on its geometry. The model involves the chordwise circulation, at any spanwise location, being replaced by a single concentrated vortex [16]. These local vortices of circulation are known as 'Bound Vortices' and are placed on the wing at the quarter-chord position along the entire span domain, $-b/2 < y < b/2$. At this stage Helmholtz's Vortex Theorems need to be introduced in order for the three-dimensional motion of fluid in the vicinity of vortex filaments to be described. The three vortex theorems, as presented by Lighthill [17], are as follows:

Helmholtz's first vortex theorem:

A vortex filament's strength remains constant along its entire length.

Helmholtz's second vortex theorem:

A vortex filament cannot start or end abruptly within a fluid; it must form a closed loop path or extend to the boundaries of the fluid.

Helmholtz's third vortex theorem:

If rotational external forces are not present, a fluid that is initially irrotational must remain irrotational.

It is to be noted that these theorems apply to inviscid flows or flows where the influence of viscous forces are negligible. This is due to the gradual dissipative effect of viscous forces on the strength of the vortices. According to Helmholtz's first vortex theorem, if a change in the circulation along the length of a vortex filament exists $\left(\frac{d\Gamma_{(y)}}{dy}\right)$, then a similar vorticity component must be introduced in a perpendicular direction (γ_x). Therefore, vortex filaments do not terminate but merely change direction in order to ensure the strength of the filaments remain constant along their entire length, which is in accordance with Helmholtz's second vortex theorem. The most basic filament arrangement that satisfies these conditions is a single "Horseshoe" vortex as shown in the following figure.

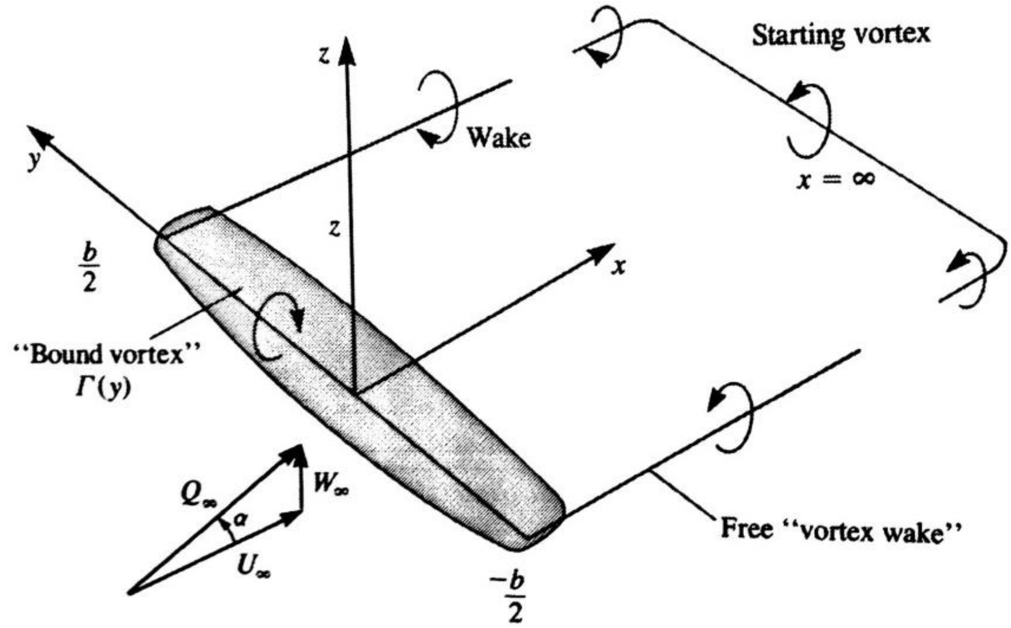

Figure 2.6 Far field horseshoe model of a finite wing [16].

According to the Kutta–Joukowski theorem $\left(L'_{(y)} = \rho\, V_\infty\, \Gamma_{(y)} \right)$, the single horseshoe vortex model implies constant lift due to its constant circulation at all sections on the wingspan. A more realistic model, therefore, is the lifting-line theory model in which the vortex strength, and thus the lift, varies along the wingspan. However, having a single bound vortex whose circulation varies along its length does not comply with Helmholtz first vortex theorem. Therefore, as the spanwise circulation (vortex strength) varies, so vortices are shed from the trailing edge of the wing in order to maintain a constant circulation per vortex filament. Thus, Prandtl's Lifting-Line Theory model uses a large number of spanwise horseshoe vortices; the bound vortices of which are all placed along the quarter-chord line as shown in the figure below.

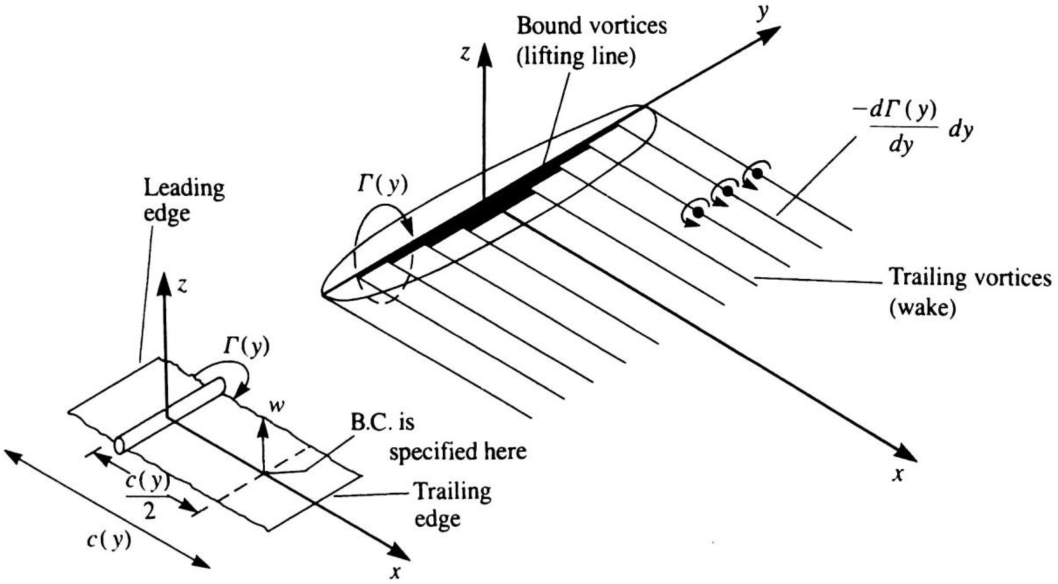

Figure 2.7 Lifting-line model consisting of several horseshoe vortices [16].

These shed vortices, whose strength is the derivative of the local wing circulation distribution $\left(\frac{d\Gamma_{(y)}}{dy} \right)$ influence the flow left and right of each wing section by either inducing an upwash or downwash at the neighbouring stations. The local magnitude of lift at each station is therefore affected by the lift generated at neighbouring wing sections. Thus in order to account for the influence of one section over its neighbours, the Lifting-Line Theory models the unknown (and sought-after) local lift in conjunction with the unknown local circulation. The detailed derivation of which is provided in Appendix A.1. With reference to Appendix A.1, the highlights and results of Prandtl's Lifting-Line Theory derivation are as follows [18]:

The first assumption is that the circulation of the wing varies along the span with a Fourier series function distribution. The spanwise locations (y) are therefore mapped to the angle (θ) using the following polar coordinate transformation:

$$y = s \cos\theta \qquad (2.3.1)$$

Where 's' is the semi-span of the wing geometry being mapped. In order to describe the general spanwise circulation, as opposed to assuming an elliptical lift and circulation distribution, the following Fourier series expansion, which makes use of the spanwise coordinate (θ), is selected:

$$\Gamma(y) = \Gamma(\theta) = \gamma = 4\, s\, V_\infty \sum_{n=1}^{\infty} A_n \sin(n\theta) \tag{2.3.2}$$

A plot of the first three symmetric terms in the expansion is shown in the following figure:

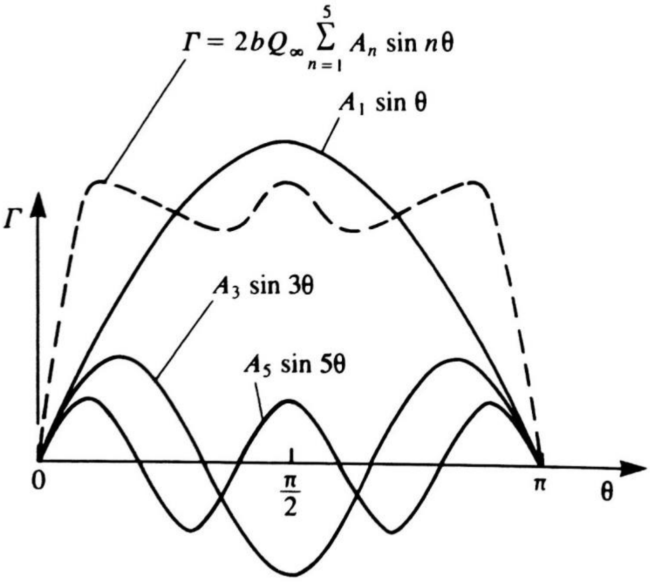

Figure 2.8 Fourier sine series representation of a symmetric spanwise circulation distribution $\boldsymbol{\Gamma(\theta)}$, n = 1, 3, 5 [16].

The boundary condition of zero flow normal to the lifting surface, $V_N = 0$, is then applied at several spanwise locations along the wing. This boundary condition requires that flow angles at each section be in balance. In three dimensional wing flow, the flow angles are set by the freestream direction, the wing surface angles and an additional flow angle component. This component is imparted by the trailing vortices and is a result of the downwash velocity they induce. As can be seen from the figure below, the effective angle of attack is therefore the sum of the wing's angle of attack, the section twist angle and the downwash induced angle.

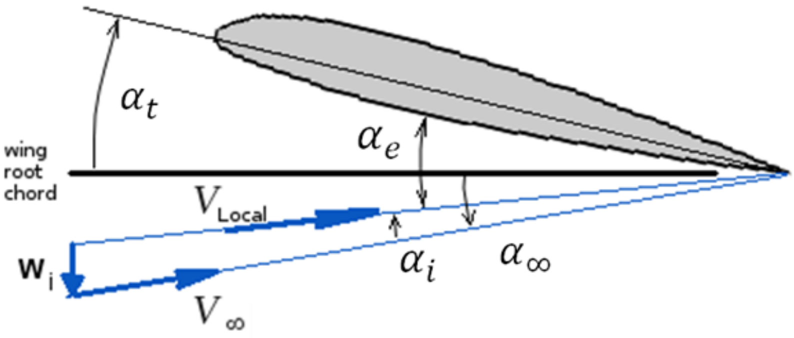

Figure 2.9 Two-dimensional section (in the y = const. plane) of a three dimensional wing, showing the effective angle of attack and local velocity (adapted from Houghton and Carruthers [18]).

The effective angle of attack is therefore given by the following equation:

$$\alpha_e = \alpha_\infty + \alpha_t - \alpha_0 - \alpha_i \tag{2.3.3}$$

Where α_∞ is the freestream angle of attack for the three-dimensional wing, α_0 is the zero-lift angle of attack of the current wing section, α_t is the local change in angle of attack due to geometric twist of the wing, and α_i is the change in angle of attack due to downwash. At each wing section, in the $y = const.$ plane, the 2-D lift coefficient is a function of this effective angle of attack, as shown by Equation A.1.4 of Appendix A.1. The 2-D section lift coefficient is, however, also a function of the bound vortex strength at each wing section, as shown by Equation A.1.5 of Appendix A.1. Equating equation A.1.4 and A.1.5, and rearranging in terms of the vortex strength, yields the following equation:

$$\gamma = \frac{1}{2} V_\infty\, c\, C_{l\alpha} \left(\alpha_\infty + \alpha_t - \alpha_0 - \alpha_i\right) \tag{2.3.6}$$

In the above equation both circulation, γ, and the induced angle of attack, α_i , are unknown. From Figure 2.9 above, however, it can be seen that, by assuming small angles, this induced angle of attack is given by:

$$\alpha_i = \frac{w_i}{V_\infty} \tag{2.3.7}$$

The downwash velocity here is a result of the shed vortex filaments and is thus a function of circulation only. The value of, α_i, can therefore be determined in terms of $\Gamma(y)$ and thus Equation 2.3.6 can be reduced to having a single unknown. This is done by integrating the influence of each differential shed vortex filament over the entire span domain of the wing, the process of which is detailed by Equation A.1.8 – A.1.10 of Appendix A.1. The result is the following equation for the total downwash at any spanwise position:

$$w_i = V_\infty \sum_{n=1}^{\infty} \frac{n\, A_n \sin(n\theta)}{\sin(\theta)} = V_\infty \sum_{n=1}^{\infty} n\, A_n \sin(n\theta) \tag{2.3.11}$$

Substitution of this downwash equation, as well as the Fourier series bound vortex distribution function, into the modified equation 2.3.6 ($\Gamma = \frac{1}{2} V_\infty\, c\, C_{l\alpha} \left(\alpha_\infty + \alpha_t - \alpha_0 - \frac{w_i}{V_\infty}\right)$) yields the relationship of Equation A.1.12 of Appendix A.1, which after rearranging results in the following final boundary equation:

$$\sum_{n=1}^{\infty} A_n \sin(n\theta) \left(\sin(\theta) + \frac{n\, c\, C_{l\alpha}}{8\, s}\right) = \frac{c\, C_{l\alpha}}{8\, s} \sin(\theta)\; (\alpha_\infty + \alpha_t - \alpha_0) \tag{2.3.13}$$

By selecting a number of spanwise locations (θ) and values for n, equation 2.3.13 can be expressed in matrix form. The left-hand side of the equation represents each element in the matrix, with each row representing a different spanwise position and each column representing a different value for n. The right-hand side of the equation represents the right hand side of the matrix form and thus the A_n coefficients can be solved by simple matrix algebra:

$$x = A_n = \frac{b}{A} \tag{2.3.14}$$

Once the A_n coefficients have been determined they can be substituted back into Equation 2.3.2 in order to determine the circulation distribution of the wing. Subsequently, the spanwise lift distribution of the wing can be determined by substituting the circulation distribution and spanwise station mapping into:

$$\frac{dL}{dy} = \rho\, V_\infty\, \Gamma(y) \tag{2.3.15}$$

Yielding:

$$dL(\theta) = \rho\, {V_\infty}^2\, b^2 \sum_{n=1}^{\infty} A_n\, \sin(n\theta)\, \sin(\theta)\, d\theta \tag{2.3.16}$$

Other parameters of importance are the coefficient of lift and the coefficient of induced drag. The coefficient of lift can be obtained by integrating and reducing equation 2.3.16 above. Yielding:

$$C_L = \pi\, AR\, A_1 \tag{2.3.17}$$

Where A_1 is the first of the solved A_n coefficients. Similarly the coefficient of induced drag can be obtained from reducing:

$$D_i = \rho\, V_\infty \int_{-s}^{+s} \Gamma(y)\, sin\, \alpha_i\, dy \tag{2.3.18}$$

to:

$$C_{Di} = \pi\, AR\, \sum_{n=1}^{\infty} n\, A_n^2 \tag{2.3.19}$$

2.3.2 Vortex Filament Method

As aforementioned, vortex filament methods involve a Lagrangian approach to dynamic wake models. This modelling technique has been used successfully in simulating roll up, plateau and decay wake regions for both single and multiple aircraft configurations [1, 4, 19]. Most notably, a linearised vortex filament method was utilised by Ning [1] in order to simulate wake propagation for various configurations of three aircraft formations, and a three dimensional vortex filament method was developed by Ehret and Oertel [19] in order to investigate the distribution of exhaust gases in the wake of a cruising Boeing 747.

Within the wake of an aircraft; inviscid, incompressible fluid flow which contains regions of concentrated vorticity, results in the development of a velocity potential field throughout the flow. Vortex filament methods model this flow field domain by discretising the flow's vorticity distribution as a set of discrete filaments and tracking this discretisation in a Lagrangian reference frame [19]. As detailed in Prandtl's lifting line method above; according to the theorems of Kelvin and Helmholtz, this vorticity distribution is a result of the change in circulation distribution $\Gamma(y)$ along the wingspan, y-axis, of the aircraft. This change in circulation results in a vortex sheet being shed from the trailing edge of the wing. The strength of this shed vortex sheet per unit span is equal to the negative of the strength of the bound vorticity per unit span [25, 26]:

$$\frac{d\Gamma_{Free}}{dy} = -\frac{d\Gamma_{Bound}}{dy} \tag{2.3.20}$$

The proof of which is detailed in Appendix A.2 and follows the same procedure outlined by Wald [25] in his study of the aerodynamics of propellers.

As aforementioned, a vortex sheet is a planar array of parallel vortex filaments that translates in the direction of the velocity field of the fluid. As a result of its alignment with the fluid's motion, there can exist no force acting upon it, no pressure gradient across it, and no discontinuity of normal velocity through it, which causes it to roll up into a complex topology of trailing vortices.

Vortex filament methods discretise this vortex sheet into a set of discrete vortex filaments as shown by Figure 2.10 below.

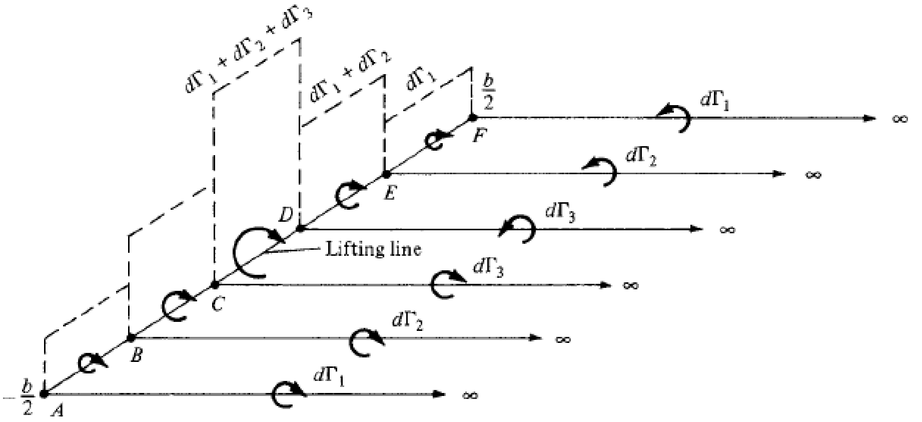

Figure 2.10 Shed vortex filaments as a result of changes in bound vorticity along the span of the wing [15].

Within the velocity field of an aircraft's wake there exists an inversely proportional relationship between the induced velocity and the distance from the origin of vorticity (the vortex filament core). One of the commonly utilised methods of computing the local velocity field in an aircraft's wake is the integration of the Biot-Savart law over the set of discrete vortex filaments, which make up the trailing vortex sheet.

The Bio-Savart Law:

The Bio-Savart law is rooted in describing the electromagnetic fields of electrical potential theory, however, the theory extends to describing the potential flow fields of inviscid, incompressible fluids. Within the vortex sheet of an aircraft's trailing wake, each vortex filament induces a flow field in the surrounding space.

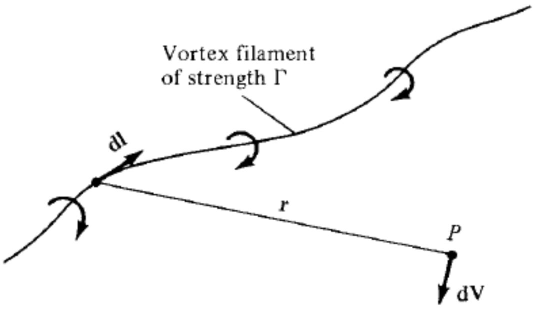

Figure 2.11 Illustration of the Bio-Savart law with regards to vortex filaments [15]

A constant vortex strength value (Γ) is obtained if the circulation is taken about any path enclosing a single filament. As shown in the figure above; a differential directed segment of a vortex filament (dl), with a constant vortex strength (Γ), induces a differential velocity at an arbitrary point (P) in accordance with the following equation known as the Bio-Savart law [15]:

$$d\vec{V} = \frac{\Gamma}{4\,\pi}\frac{d\vec{l} \times \vec{r}}{|\vec{r}|^3} \tag{2.3.21}$$

Where $\vec{r}$ is the radius vector from $d\vec{l}$ to the arbitrary point P. The derivation of equation 2.3.21 can be found in the work of Katz and Plotkin [22] as well as Karamcheti [22] and will therefore not be covered here. The induced velocity at point P is obtained by integrating equation 2.3.21 over the entire length of the vortex filament. From Appendix A.3 (Vortex Filament Induced Velocity Derivation) it can be seen that for a vortex filament of infinite length, the magnitude of the induced velocity is given by:

$$V = \frac{\Gamma}{2\,\pi\,h} \tag{2.3.22}$$

Where h is the perpendicular distance from point P to the vortex filament as shown in Figure A.5 of Appendix A.3. Similarly, from Appendix A.3 and Figure A.6 the following general equation for the magnitude of the induced velocity was obtained:

$$V = -\frac{\Gamma}{4\,\pi\,h}\,(\cos\theta_1 - \cos\theta_2) \tag{2.3.23}$$

Where θ_1 and θ_2 are the angles between the end point radius vectors to point P and the vortex filament direction, as shown in Figure A.6 of Appendix A.3.

Although the Biot-Savart law is computationally inexpensive for numerical simulations; it is, however, unstable under certain simulation parameters. In three-dimensional simulations, a curved line vortex with an infinitesimal core radius would induce itself a logarithmically infinite velocity as the vortex filament is approached, and would therefore result in a singularity [19]. This singularity, at the centre of a Biot-Savart filament, cannot exist in a fluid and prevents stable wake forms, in numerical schemes, from converging. Furthermore, as aforementioned in section 2.2 Vortex Wake Characteristics, the vortices shed from an aircraft's wing consist of irrational flow around a viscous core of rotational flow [8]. Therefore, in order to more accurately model these vortices, trailing vortex profile models, such as the Lamb-Oseen model and the Burnham-Hallock model, incorporate finite viscous cores into the modelling scheme.

The Lamb-Oseen vortex profile model involves the temporal addition of viscous effects of increasing core diameter, and has been utilised in vortex decay investigations of far wake fields. However, according to Tipping-Woods [20], the Lamb-Oseen model over estimates the viscous effects of vortex decay. Furthermore, the complexity of the model would render it impractical for the modelling of wake roll-up processes through numerical methods.

Burnham-Hallock Vortex Profile Model:

The Burnham-Hallock model is a low order algebraic model similar to a model based off of the Biot-Savart law, however, unlike the Biot-Savart law; the Burnham-Hallock model assigns a finite viscous core to the vortex filaments in an aircraft's shed wake. According to Fischenberg [23] and Burnham and Hallock [24], values obtained via the use of the Burnham-Hallock model correlate well with experimental measurements obtained in investigations of the rolled up wake of cruising aircraft.

Following a similar process to that described in Appendix A.3, 'Vortex Filament Induced Velocity Derivation', the induced velocity from an infinite vortex with core radius r_c , is given by the following equation known as the Burnham-Hallock model:

$$V = \frac{\Gamma}{2\,\pi}\left(\frac{h}{h^2 + r_c^2}\right) \tag{2.3.24}$$

Similarly, according to the Burnham-Hallock model, the induced velocity as a result of a vortex filament of finite length is given by:

$$V = \frac{\Gamma}{4\,\pi}\left(\frac{h}{h^2 + r_c^2}\right)(\cos\theta_1 - \cos\theta_2) \tag{2.3.25}$$

Where θ_1, θ_2 and h are identical geometries to those expressed in the vortex filament induced velocity derivation of the Bio-Savart law depicted above and shown in Figure A.6 of Appendix A.3.

As there exists a singularity within a numerical scheme of the Biot-Savart law, the Burnham-Hallock model is a justifiable substitute as its results correlate well with the Biot-Savart velocity profile outside of the core region.

Numerical Computation:

Appendix A.3.1 outlines the method utilised in rewriting the Burnham-Hallock model in vector form for numerical computation. The procedure follows the methodology described by Katz and Plotkin [22] in which the Biot-Savart model is rewritten in vector form. The resultant form of the Burnham-Hallock model derived by Equations A.3.10 – A.3.17 is as follows:

$$\vec{V} = \frac{\Gamma}{4\,\pi}\left(\frac{\frac{|\vec{r}_1 \times \vec{r}_2|}{|\vec{r}_0|}}{\left(\frac{|\vec{r}_1 \times \vec{r}_2|}{|\vec{r}_0|}\right)^2 + r_c^2}\right)\left(\frac{\vec{r}_0 \cdot \vec{r}_1}{|\vec{r}_0||\vec{r}_1|} - \frac{\vec{r}_0 \cdot \vec{r}_2}{|\vec{r}_0||\vec{r}_1|}\right)\frac{\vec{r}_1 \times \vec{r}_2}{|\vec{r}_1 \times \vec{r}_2|} \tag{2.3.26}$$

The variables of which are shown in Figure A.6 of Appendix A.3 and the figure below.

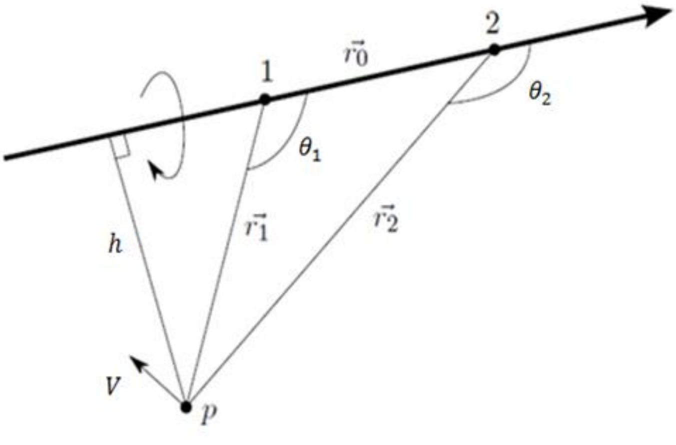

Figure 2.12 Velocity induced at point P by a straight vortex filament of finite length (Adapted from Katz and Plotkin [22]).

Within numerical schemes utilising either the Burnham-Hallock model or the Biot-Savart law, the induced velocities of the vortex filaments are used to discretise the velocity field in the aircraft's shed wake. As a vortex sheet cannot sustain a force imbalance, a discontinuity of pressure, or a discontinuity of normal velocity, the filaments making up the vortex sheet have to align with the velocity field they induce. The shed vortex sheet of the aircraft is therefore iteratively adjusted to align with its induced velocity field until a stable wake formation is attained. The explicit procedure is detailed further in section 3.3 - 3.6 of Chapter 3, 'Simulation Design and Methodology'.

2.4 The Trailing Vortex System of a Propeller

2.4.1 The Dynamics of the Helicoidal Vortex Sheet

A propeller is a propulsive devise that transmits power by converting rotational motion into thrust through the use of a number of rotating lifting surfaces. The lifting surfaces, blades, are positioned radially about a shaft that is aligned approximately with the direction of motion of the aircraft (free stream velocity).

Analogous to finite wing theory and Helmholtz's Vortex Theorems presented above, if the bound vorticity on a propeller blade varies in magnitude along its span, a free vortex filament, with circulation equal to the change in bound vorticity, must emanate from the trailing edge of the propeller blade. The proof of which is presented in Appendix A.2 and follows the procedure presented by Wald [25] in his study of the aerodynamics of propellers. The free vortex strength per unit length is therefore related to the bound vorticity as follows [26]:

$$\frac{d\Gamma_{Free}}{dr} = -\frac{d\Gamma_{Bound}}{dr} \tag{2.4.1}$$

Where r is the distance from the centreline axis of the propeller.

A collection of these free vortex filaments shed from the trailing edge of the blade results in a vortex sheet emanating from the trailing edge of the blade. The vortex sheet shed from each propeller blade results in a set of interleaved helicoidal sheets as shown in the figure below.

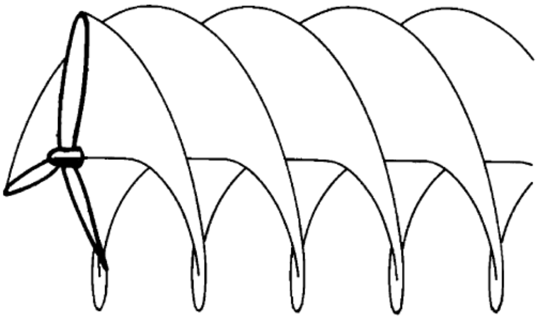

Figure 2.13 The trailing helicoidal vortex sheets of a propeller [25].

Similar to wing wake vortices, the outer region of each blade's shed vortex sheet rolls up and is absorbed into a single helicoidal blade tip vortex. The inner region of each blade's vortex sheet is similarly absorbed into a single vortex of opposite sense lying on the propeller's centreline axis. These helicoidal vortices translate uniformly downstream parallel to the propeller's centreline axis as a rigid body without further deformation [25].

Both Goldstein and Theodorsen's propeller wake theories, as well as more modern propeller wake models, are based on undeformed helicoidal vortex sheets in order to relate the loading of the propeller to the induced velocities of the trailing wake [29]. The seemingly unrealistic use of helicoidal vortex sheets as adequate representations of propeller trailing vortex systems in theoretical models can, however, be justified by the following two principles:

1. If there exists no external forces acting on a fluid, hydrodynamic impulse is conserved in the evolution of a free vortex sheet. That is, the rolling-up of a free vortex sheet conserves both hydrodynamic impulse (even in the presence of viscosity) and circulation [25, 27].

2. In an unbounded fluid at rest at infinity, replacing the vortex system of the fluid with another vortex system of the same impulse will result in identical velocity fields at large distances [25, 28].

It can therefore be inferred, from the above two principles, that the induced velocity at the propeller imparted by downstream undeformed helicoidal vortex sheets is identical to the velocity that would be induced by downstream portions of a fully rolled-up helicoidal vortex system. Hence, for a propeller with an ideal load distribution, it is justifiable to use either a mathematical model in which the helicoidal vortex sheets translate backward without deformation or a mathematical model in which the vortex sheet is completely rolled up into distinct helicoidal vortices [25].

2.4.2 Propeller Vortex Theories

Propeller vortex theories prescribe the shape of the propeller wake and utilise its geometry in order to calculate the velocity it induces at the propeller blades. The following three propeller vortex theories have been utilised extensively in propeller design: the theory of Betz, Glauert and Prandtl; the theory of Goldstein and the theory of Theodorsen. All three theories utilise a propeller wake model that is based on a minimum induced loss blade loading distribution [29]. The theories differ in complexity as a result of the varying detail in which the propeller wake is described.

Betz, Glauert and Prandtl Propeller Vortex Theory:

In Betz, Glauert and Prandtl propeller vortex theory the propeller is modelled as a disk due to the assumption that the propeller has an infinitely large number of blades. Furthermore, the bound circulation along the bladespan is assumed constant. It is therefore implied that the blade's shed vorticity is concentrated at the edge of the propeller disk. As shown in the figure below, the shed vorticity of the infinite number of propeller blades results in a cylinder of spiralling vortices and the propeller wake is thus treated as a rigid cylinder. Furthermore, in order to close the vortex loop of the cylinder, there exists a centreline vortex (root vortex) with magnitude equal to the summation of all vortex lines spanning the propeller wake.

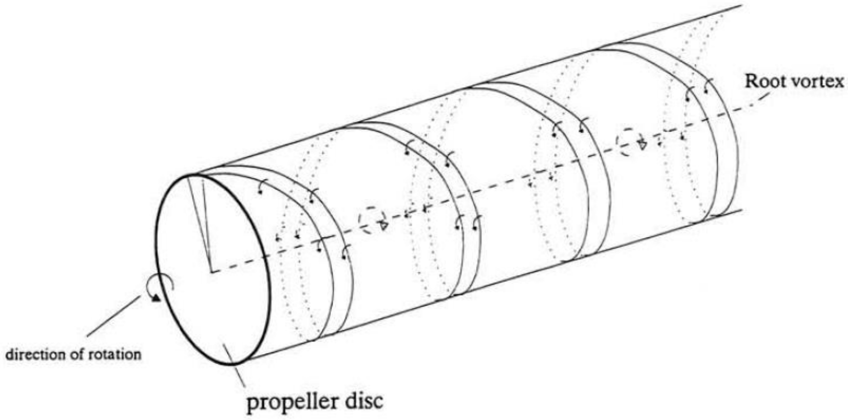

Figure 2.14 Betz, Glauert and Prandtl Propeller Wake Model [29].

The Betz, Glauert and Prandtl propeller vortex theory has been utilised in the design of minimum loss propeller blades in order to achieve the highest efficiency for a given thrust. According to the theorem, this condition of minimal energy loss is related to a certain optimal distribution in the far wake, which is in turn identical to the circulation distribution around the propeller blades if a light propeller loading is assumed.

Goldstein Propeller Vortex Theory:

In contrast to the infinite number of propeller blades in the Betz, Glauert and Prandtl propeller vortex theory; the Goldstein propeller theory utilises a finite number of blades. Goldstein's propeller vortex theory makes use of a lifting line model in which each blade is modelled by a single bound vortex line of varying circulation in the radial direction. The propeller wake is therefore modelled by a helicoidal vortex sheet shed from the trailing edge of each propeller, as shown in Figure 2.13 above.

The helicoidal vortex sheet has a constant slope due to its geometry being prescribed by the free stream velocity and the rotational velocity of the propeller. Furthermore, within Goldstein's propeller wake model it is assumed that the helicoidal vortex sheets translate backwards from the propeller as rigid bodies without roll-up deformation or contraction of the slipstream tube of the propeller. These three-dimensional helicoidal vortex sheets induce velocities in the slipstream of the aircraft. According to Goldstein's propeller vortex theory, the equation of the helicoidal vortex sheet of a single blade far behind the propeller is given by [25, 29]:

$$\theta - \frac{\Omega\, z}{V_\infty} - \frac{2\pi(n-1)}{B} = 0 \qquad \text{for } r < R \tag{2.4.2}$$

Where θ, r and z are the cylindrical polar coordinates referred to the helix axis, Ω is the rotational velocity of the propeller and V_∞ is the unperturbed onset flow velocity (free stream velocity) of the propeller. Furthermore, B is the number of blades, R is the propeller radius, r is the radial position vector and n is the position number of each blade ($n = 1, 2, \ldots, B$). Similar to the propeller theory of Betz, Glauert and Prandtl; the Golstein propeller theory assumes a light propeller loading.

Theodorsen Propeller Vortex Theory:

The Theodorsen propeller vortex theory, which is largely based on Goldstein's propeller vortex theory, extends the lightly loaded propeller assumption of both the Betz, Glauert and Prandtl theory and the Goldstein theory to heavily loaded propellers. Theodorsen's theory shows that Betz, Glauert and Prandtl's theorem of optimum distribution of circulation applies to heavily loaded propellers if the shape of the helix infinitely far behind the propeller is referred to. Furthermore, the radial distribution of circulation in the far field wake behind a lightly loaded propeller, obtained using Goldstein's theorem, was shown to be identical to the radial distribution of circulation of a heavily loaded propeller, obtained using Theodorsen's theorem, by comparing the results for the same value of helix angle. In Theodorsen's theory the heavily loaded propeller is equivalent to an infinite number of lightly loaded propellers, with optimum circulation distributions, placed in series [29].

According to Theodorsen's propeller vortex theory, the equation of the helicoidal vortex sheet of a single blade far behind the propeller is given by [25, 29]:

$$\theta - \frac{\Omega\, z}{V_\infty + w} - \frac{2\pi(n-1)}{B} = 0 \qquad \text{for } r < R \qquad (2.4.3)$$

Where all variables, with the exception of w, are identical to those of Equation 2.4.2 of Goldstein's propeller vortex theorem above. w is the axial displacement velocity of the helicoidal vortex sheets in the far field wake of the propeller, with respect to the surrounding fluid, and is an independent parameter on which all other quantities depend. Within Theodorsen's propeller vortex theory, the value of w and all subsequent dependent variables must be obtained iteratively. Theodorsen's theory therefore requires computation of its numerical schemes in order to be utilised effectively. The theory is, however, the most sophisticated and complete propeller vortex model [29].

The ensuing theory presented within the current literature review is, therefore, that of Theodorsen's propeller vortex theory with inputs from Goldstein's theory, on which Theodorsen's theory is based.

2.4.3 The Kinematics of Propeller Blades

As a result of a propellers motion through a fluid, the blades are subject to several components of relative velocity of the fluid: the axial velocity due to the free stream velocity, V_∞, through the fluid and the rotational velocity, Ωr_0 , imparted on the blades by the rotation of the shaft of the propeller. In addition to these velocities, the blades are subject to an induced velocity due to the disturbance of the fluid by the propeller. This induced velocity is a result of the entire system of bound and free vorticity of the lifting surfaces of the propeller [25].

The symmetrical placement of blades, radially about a propeller's hub, results in no net velocity being induced on one blade by another. This is due to the radial vortex lines along the blades being equally spaced and of equal strength, for steady flow and a propeller of ideal load distribution. Therefore, the only contribution to the resultant velocity at a blade is the trailing vorticity. Furthermore, according to Wald [25], propellers are almost always adequately represented by the lifting line assumption of two-dimensional airfoil theory. This is due to the induced velocity not varying significantly along the chord of the blade, as most propeller blades have sufficiently small chord lengths. Furthermore, for blades of sufficiently small chord, the blade section forces are the same as would occur in a uniform velocity field. Thus, as in two-dimensional airfoil theory, the lift on the blade element is related to the angle of attack with regards to the local relative velocity. For blades with large chord lengths, such as marine propellers, vortex lattice or other lifting surface representations are more appropriate for blade kinematics and force analyses.

2.4.4 The Kinematics of Helicoidal Vortex Sheets

According to the theory of Theodorsen [31], for a point on each of B undeforming sheets shed from B equally spaced propeller blades the equation for the angular coordinate of the vortex sheet, with respect to time, is given by:

$$\theta = \Omega t + \frac{2\pi(n-1)}{B} \tag{2.4.4}$$

Where all variables are identical to those described in Section 2.4.2 'Propeller Vortex Theories' above. The equation for the horizontal displacement of the vortex sheet, with respect to time, is given by:

$$z = (V_\infty + w)t \tag{2.4.5}$$

Substituting Equation 2.4.5 into 2.4.4 in order to eliminate the time variable, the equation for the angular coordinate of the vortex sheet with respect to the vortex sheet length is given by the following equation:

$$\theta - \frac{\Omega z}{V_\infty + w} - \frac{2\pi(n-1)}{B} = 0 \tag{2.4.6}$$

Where, as aforementioned; w is the backward velocity of the sheet, induced by the propeller, with respect to the surrounding fluid. The resultant velocity diagram for each vortex sheet is shown in the figure below.

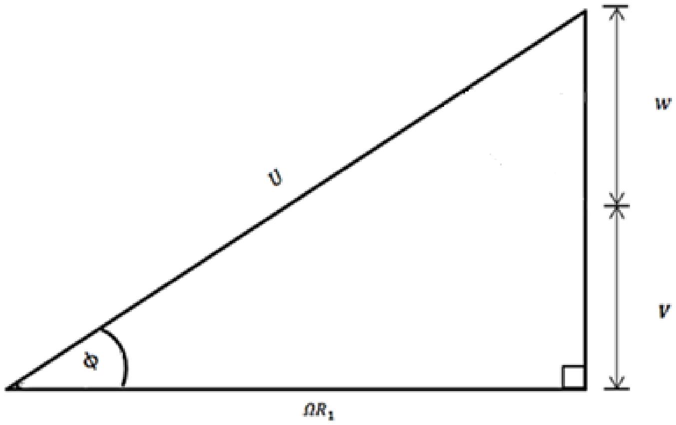

Figure 2.15 Velocity Components of the Helicoidal Vortex Sheet (Adapted from Wald [25]).

In the figure above; U is the resultant velocity, R_1 is the radius to the edge of the vortex sheet and ϕ is the angular pitch of the sheet. Furthermore, for all subsequent uses, the subscript 1 is used for all coefficients and variables that are referred to the helicoidal trailing vortex system. From Figure 2.15 above, it can be seen that the angular pitch is given by:

$$\phi = \tan^{-1}\left(\frac{dz}{rd\theta}\right) = \tan^{-1}\left(\frac{(V_\infty + w)}{\Omega r}\right) = \tan^{-1}\left(\frac{\lambda_2}{x_1}\right) \quad (2.4.7)$$

Where, as prescribed by Wald [25], λ_2 is the advance ratio $\frac{(V_\infty + w)}{\Omega R_1}$ and x_1 is the dimensionless radial coordinate $\frac{r}{R_1}$ on the trailing vortex system. Similarly, the linear pitch of the helicoidal vortex sheet can be obtained as follows:

$$P = 2\pi r \tan\phi = \frac{2\pi(V_\infty + w)}{\Omega} = 2\pi R_1 \lambda_2 \quad (2.4.8)$$

The velocity normal to any point on the surface of the helicoidal sheet is the velocity with which it is convected freely by the induced velocity of the propeller [25]. This velocity is therefore the normal component of the displacement velocity of the sheet and is given by $w cos\phi$. Thus, the axial and tangential components of this convective velocity of the sheet are respectively:

$$u_{z1} = w\cos^2\phi \quad (2.4.9)$$

$$u_{\theta 1} = \cos\phi \sin\phi \tag{2.4.10}$$

Representing these convective velocity components on Figure 2.15 results in the following velocity diagram for each helicoidal vortex sheet:

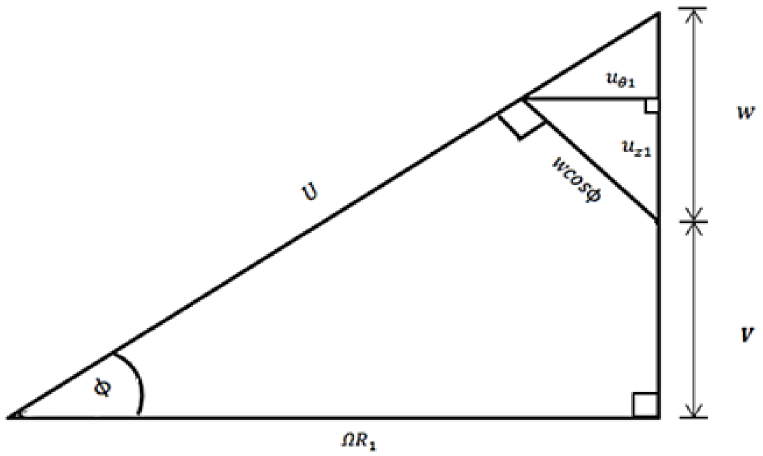

Figure 2.16 Velocity Components of the Helicoidal Vortex Sheet (Adapted from Wald [25]).

It is therefore evident that the angular pitch of the helicoidal sheet can also be obtained utilising the convective velocity components as follows:

$$\phi = \tan^{-1} \frac{(V + u_{z1})}{\Omega r - u_{\theta 1}} \tag{2.4.11}$$

Equating both angular pitch equations (Equation 2.4.11 and Equation 2.4.7) to one another, the axial and tangential convective velocity components can be represented solely by the helicoidal velocity components of Figure 2.15 as follows:

$$u_{z1} = \frac{w}{1+\left(\frac{\lambda_2^2}{x_1^2}\right)} \tag{2.4.12}$$

and

$$u_{\theta 1} = \frac{w\left(\frac{\lambda_2}{x_1}\right)}{\left(1+\frac{\lambda_2^2}{x_1^2}\right)} \tag{2.4.13}$$

According to Larrabee [30], in his work on the practical design of minimum induced loss propellers, helicoidal vortex sheets are locally convected normal to their surfaces and therefore possess both rotational and translational velocity about their centreline axis. A vortex sheet is a sheet of velocity discontinuity in the fluid and does not contain fluid particles. Thus, if a helicoidal vortex sheet rotates about its axis, translates along its axis or both simultaneously, the motion of the sheet will be identical. Therefore, according to Wald [25], distinguishing between rotation and translation is futile as the momentum transport and flow around the helicoids is in either case identical to a simple axially translating helicoidal surface.

2.4.5 The Goldstein Circulation Function

The Goldstein circulation function was developed in order to determine the distribution of vorticity on the helicoidal vortex sheet; and deduce from this free vorticity distribution, the bound circulation on the propeller. The function is based on the representation of the shed vortex system as a regular helicoidal vortex sheet moving uniformly backward in the fluid.

In order to describe the fluid flow in the wake of a propeller, the determination of the velocity potential function φ is required. Consequentially, the partial differential equation that must be satisfied by the potential function is:

$$\nabla^2 \varphi = 0 \tag{2.4.14}$$

Furthermore, an imposed boundary condition on the surface of the helicoidal vortex sheet, defined by Equation 2.4.6, is that the normal velocity on the surface is given by:

$$\frac{\partial \varphi}{\partial n} = w \cos \Phi \tag{2.4.15}$$

(Note, here capital letter phi (Φ) is the pitch angle of the helicoidal sheet, as defined in Equation 2.4.7 above, and lower case phi (φ) represents the velocity potential function.)

By considering a lightly loaded propeller, Goldstein [26] succeeded in calculating the potential function for two and four-bladed propellers over a wide range of advance ratios. However, through the use of a rheoelectrical analog to evaluate the circulation function, Theodorsen [31] was able to show that Goldstein's theory extended to the case of heavily loaded propellers. This is due to the circulation function being dependant only on the geometry of the helicoidal vortex sheet at a distance behind the propeller. Thus, it is not a requirement that the pitch of the helicoidal sheet be equal to the pitch at the propeller blade, which is true for the case of a lightly loaded propeller.

The Goldstein circulation function, expressed as a dimensionless factor, is given by the following equation:

$$G(r_1) = \frac{\Gamma(r_1)}{hw} \tag{2.4.16}$$

Where $\Gamma(r_1)$ is the circulation distribution in the free vortex sheet, h is the axial distance between successive turns of the helicoidal vortex sheets and w is the axial displacement velocity of the sheets with respect to the surrounding fluid. As h is dependent on the geometry of the helicoidal sheet, it can be represented in terms of the pitch of the helicoid and the number of interleaved sheets B as follows:

$$h = \frac{P}{B} = \frac{2\pi(V+w)}{\Omega B} \tag{2.4.17}$$

Where P is the linear pitch of the helicoid, as expressed in Equation 2.4.8 above. Substituting Equation 2.4.17 into the Goldstein circulation function of Equation 2.4.16 results in Equation 2.4.18 below:

$$G(r_1) = \frac{B\,\Gamma\,\Omega}{2\,\pi\,w\,(V_\infty + w)} = \frac{B\,\Gamma}{2\,\pi\,R_1\,w\,\lambda_2} \tag{2.4.18}$$

(Note that the original Goldstein Circulation function, which assumed light propeller loading, did not include the induced axial displacement velocity w which has been introduced as a result of the work of Theodorsen [31].)

In a more recent study, Ribner and Foster [32] employed a numerical scheme in order to update and extend Theodorsen's rheoelectric analog evaluation of the parameters governing the ideal efficiency of propellers. Their propeller wake model represented the trailing sheets by a set of discrete helicoidal vortex filaments and was utilised in order to generate Goldstein functions. Although their representation was a more physical one, the results were less accurate and only a limited range of variables were covered.

Accurate tabulated values of $G(r)$ for two to ten-blade propellers with an advance ratio λ_2 from 1/12 to 4 were, however, computed by Tibery and Wrench Jr [33]. Their tabulated function $K(r)$ is defined as the ratio of the circulation $\Gamma(r_1)$ to the circulation of a Betz type model in which there are an infinite number of sheets emanating from an infinite number of blades. The resulting circulation function is as follows:

$$K(r_1) = \frac{B\,\Gamma}{\Gamma_\infty} = \frac{B\,\Gamma}{2\,\pi\,r_1\,u_{\theta 1}} \tag{2.4.19}$$

Representing the tangential velocity in terms of the axial displacement velocity and advance ratios by use of Equation 2.4.13 $\left(u_{\theta 1} = \frac{w\left(\frac{\lambda_2}{x_1}\right)}{\left(1+\frac{\lambda_2^2}{x_1^2}\right)} \right)$, the Tibery and Wrench circulation function *K(r)* can be represented in terms of the Goldstein circulation function as follows:

$$K(r_1) = G(r_1)\left(1 + \frac{\lambda_2^2}{x_1^2}\right) \tag{2.4.20}$$

In contrast to the Tibery and Wrench circulation function *K(r)*, the Goldstein circulation function *G(r)* is a more graphic representation as the shape of the circulation distribution with respect to radius is shown. Thus, the tabulated values of Tibery and Wrench must be divided by $\left(1 + \frac{\lambda_2^2}{x_1^2}\right)$ to obtain the Goldstein circulation function *G(r)*. Tables of the Goldstein circulation function for two to six-bladed propellers, obtained by Wald's [25] conversion of Tibery and Wrench's tables, is presented in Appendix B.1.

2.4.6 The Thrust of a Propeller with Ideal Load Distribution

Goldstein and Theodorsen's vortex theories prescribe the shape of the trailing propeller wake and utilise its geometry to calculate the induced effects at the propeller. A result of such modelling techniques, conducted by Theodorsen [31], is an equation for the thrust of a propeller expressed entirely as a function of the characteristics of the trailing helicoidal vortex sheets. A detailed derivation of the thrust equation, which precisely follows that described by Theodorsen [31] and Wald [25], is presented in Appendix A.4. A brief overview of this derivation will, however, be presented here.

Beginning with the general momentum theory of Betz, the propeller is modelled as an infinitely thin actuator disc exerting a distributed force on the flow field. By applying an Eulerian approach to the momentum integral theorem, the axial force required to produce the continuous motion of the helicoidal vortex sheet can be obtained. Within this Eulerian approach, the propeller is placed within a closed control surface S, depicted in the figure below, through which the fluid flows.

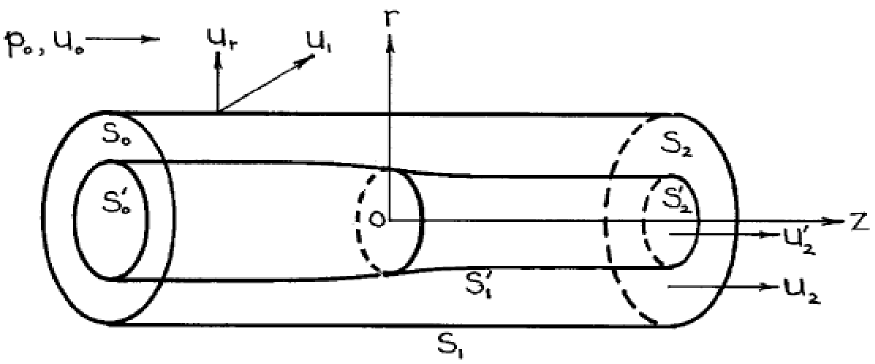

Figure 2.17 Momentum Integral Control Surface [25].

As shown by Equation A.4.5 and A.4.6 of Appendix A.4, by placing the propeller at the origin on the z-axis and considering the Eulerian cylindrical control surface depicted above, the resultant force (F) acting on the fluid, imparted by the propeller, and thus the positive forward thrust (T) of the propeller is given by:

$$T = \int_{S_2'} [(p_2 - p_0) + \rho\, u_2'(u_2' - u_0)] dS_2' \tag{2.4.21}$$

By application of the generalised Bernoulli equation for conservative force fields, Betz [29] derived an expression for the pressure increase over the propeller disc as outlined in Equation A.4.1 to A.4.4 of Appendix A.4. Substitution of the velocity terms derived in Section 2.4.4, 'The Kinematics of Helicoidal Vortex Sheets', into Equation 2.4.21 as well as by assuming a constant density and substituting the derived pressure equation of Equation A.4.4, yields the following thrust integral:

$$T = \rho \int_S \left[(V + w)\, u_{z1} + u_{z1}^2 - \frac{u^2}{2}\right] dS \tag{2.4.22}$$

Where the integration is to be conducted over a Trefftz plane, which is a fixed plane normal to the axis of the helicoidal vortex sheet. In order to evaluate the thrust integral, Theodorsen [31] derived two dimensionless variables that are functions of the pitch of the helicoidal vortex sheet and the Goldstein circulation function. The two variables are known as the mass transport factor κ and the axial energy tip loss factor ε.

In order to derive the mass transport and axial tip loss factors, Theodorsen made use of rheoelectric analog experiments in which a physical model of the helicoidal vortex sheets were placed in an electrolytic tank [29]. The electrical potential (voltage distribution) within the tank is analogous to the potential flow (velocity potential) of the helicoidal vortex sheets. The mass transport factor κ can be compared physically to the blocking effect of the helical surface and was thus obtained by measuring the change in resistance caused by inserting the physical helicoidal vortex sheet model into the electrolytic tank. The mass transport factor κ is therefore a function of the axial velocity u_{z1} as follows:

$$\kappa = \int_S \left(\frac{u_{z1}}{wS}\right) dS \tag{2.4.23}$$

Through the derivation outlined in Equation A.4.9 to A.4.16 of Appendix A.4, the first term of the thrust integral of Equation 2.4.22 above can be represented in terms of the mass transport factor κ as follows:

$$\rho \int_S^{\cdot} [(V+w)\, u_{z1}\; dS = \kappa \rho \pi R_1^2\, (V+w)\, w \tag{2.4.24}$$

Furthermore, by Equation A.4.14 of Appendix A.4, the mass transport factor κ can be computed from tabulated values of the Goldstein circulation function by the following relation:

$$\kappa = \int_0^1 2\, G(x_1)\; x_1\, dx_1 \tag{2.4.25}$$

Similarly, the axial energy transport factor ε is a function of u_{z1}^2 as follows:

$$\varepsilon = \int_S^{\cdot} \frac{u_{z1}^2\, dS}{\pi\, R_1^2\, w^2} \tag{2.4.26}$$

And thus the second term of the thrust integral of Equation 2.4.22 can be represented in terms of the axial energy transport factor ε as follows:

$$\rho \int_S^{\cdot} u_{z1}^2\; dS = \varepsilon \rho \pi R_1^2 w^2 \tag{2.4.27}$$

Due to the mass transport and the axial energy transport factors' mutual dependence on the axial component of the helicoids convective velocity u_{z1}, Wald [25] developed an expression for $\varepsilon(\lambda_2)$ as a function of $\kappa(\lambda_2)$:

$$\varepsilon = \kappa + \frac{1}{2}\lambda_2\, \frac{d\kappa}{d\lambda_2} \tag{2.4.28}$$

Where, as aforementioned, λ_2 is the helicoidal vortex sheet advance ratio $\frac{(V_\infty + w)}{\Omega R_1}$. Equation 2.4.28 thus provides a means of obtaining the axial energy transport factor ε by numerical differentiation of tabulated values of the mass transport factor κ. Tabulated values of ε and κ, generated by Wald [25] for two to six-bladed propellers, can be found in Table B.2.1 and B.2.2 of Appendix B.2.

In order to evaluate the last term of the thrust integral of Equation 2.4.22, $-\frac{1}{2}\rho \int_S^{\cdot} u^2 dS$, a circuitous method is employed in which the integral is first transformed into a volume integral contained between two Trefftz planes, as shown in Equation A.4.20 of Appendix A.4. Application of Green's theorem, which transforms a volume integral into a surface integral, transforms this volume integral back into a more manageable surface integral on the original Trefftz plane S. After which, the circulation term of the resulting integral, Equation A.4.25 of Appendix A.4, is expressed in terms of the Goldstein circulation function. This allows Equation 2.4.25 above, which defines the relationship between the mass transport factor κ and the Goldstein circulation function $G(r_1)$, to be utilised in order to express the last term of the thrust integral in terms of the mass transport factor and other helicoidal vortex sheet characteristic variables. This entire circuitous process is described in Equations A.4.20 to A.4.27 of Appendix A.4 and yields the following expression for the last term of the thrust integral:

$$-\frac{1}{2}\rho \int_S u^2 dS = -\frac{1}{2}\rho\, \pi\, R_1^2 w^2 \kappa \tag{2.4.29}$$

Summing all the relevant terms of the thrust integral equation (Equation 2.4.24, 2.4.27 and 2.4.29) yields an equation for the thrust of the propeller expressed entirely as a function of the characteristics of the trailing helicoidal vortex sheet:

$$T = \kappa\rho\pi R_1^2 V^2 \overline{w}\left[1 + \overline{w}\,\left(\frac{1}{2} + \frac{\epsilon}{\kappa}\right)\right] \tag{2.4.30}$$

Where, as prescribed by Theodorsen [31], $\overline{w}$ is the nondimensional ratio of the induced helicoid axial velocity to the free stream velocity $\left(\overline{w} = \frac{w}{V_\infty}\right)$, ρ is the density of the air and R_1 is the radius of the helicoidal vortex sheet.

As can be seen from the derivation above; the mass transport factor κ, the axial energy factor ϵ and the Goldstein circulation function are all interrelated and depend on the unknown induced axial displacement velocity w of the helicoidal vortex sheets. An iterative process, beginning with an initial assumption of w, is therefore required in order to determine κ, ϵ and $G(r_1)$; and subsequently all other helicoidal vortex sheet characteristics of a given propeller for a specific aircraft. The algorithm for this iterative process is detailed fully in Section 3.2 ‘Propeller Wake Characteristics Model’.

2.4.7 The Helicoidal Vortex Sheet Radius

The free vorticity in the trailing helicoidal vortex sheet system at a radius r_1 is uniquely related to the bound circulation $\Gamma(r_0)$ about an element of the propeller blade at a corresponding radius r_0 as shown by the following derivation. Consider a closed loop line integral of the velocity along the path depicted in the figure below. It is evident that the path of integration does not encompass any vortex lines nor cut any vortex sheet and the line integral over the entire path is equivalently zero.

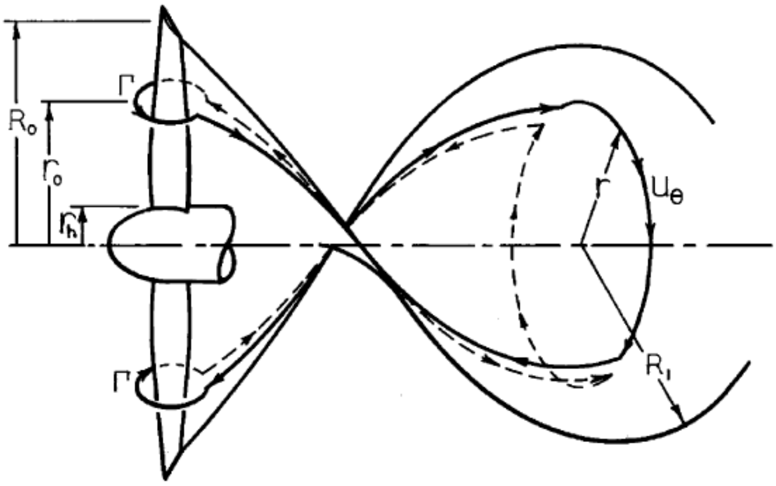

Figure 2.18 Relationship of Propeller Characteristics to Helicoidal Vortex Sheet Characteristics [25].

Moving from left to right in Figure 2.18 above and dividing the line integral into segments, it is clear that around each blade element the line integral is equal to the bound circulation, and the integral along the path of the vortex sheets is zero due to the equal yet opposite contributions of each side. The final path along the two arcs at radius r_1, within the helicoidal vortex sheet, is equal to the line integral of the tangential component of velocity at this position. The summation of these sections of the closed loop integral, which is equivalently zero, results in the following relationship:

$$B\Gamma(r_0) = \int_0^{2\pi} u_{\theta 1}(r_1)\ r_1\ d\theta \tag{2.4.31}$$

Thus consequentially, the total bound circulation of an element at radius r_0 on the propeller blades must be equal to the free vorticity within a circle of radius r_1 which passes through the vortex filament shed from the r_0 position on the propeller blades [25].

$$B\Gamma(r_0) = B\Gamma(r_1) \tag{2.4.32}$$

Now, in order to obtain an expression relating the dimensionless radial coordinate of the propeller and the dimensionless radial coordinate of the trailing vortex system, a continuity relation between the fluid flow through the propeller and the fluid flow through the trailing slipstream must be considered as follows:

$$(V_\infty + u_{z0})2\pi r_0 dr_0 = (V_\infty + u_{z1})2\pi r_1 dr_1 \tag{2.4.33}$$

Assuming that the ratio of the velocity terms remains constant, the integration of the above relation, detailed in Equation A.5.5 to A.5.10 of Appendix A.5, yields the following equation for the relation between the dimensionless radial coordinates of the propeller and helicoidal vortex sheet reference frame:

$$x_0^2 = x_h^2 + x_1^2\left(1 - x_h^2\right) \tag{2.4.34}$$

Where x_0 is the dimensionless radial coordinate of the propeller, x_1 is the dimensionless radial coordinate of the helicoidal vortex sheet and x_h is the dimensionless radial coordinate of the hub of the propeller. Note that the limits of integration for Equation 2.4.33 for the propeller reference frame, presented in Equation A.5.7 of Appendix A.5, are from the radius of the propeller hub to the radius of the blade tip, whereas for the helicoidal vortex sheet reference frame the limits of integration are from the helicoid centreline axis to the radius of the edge of the vortex sheet. According to Wald [25], this is due to the shed vortex system closing behind the hub or nacelle as a result of the ideal bound circulation distribution on the propeller blades, assuming the propeller has been designed in accordance with minimal energy dissipation criteria. Thus, the configuration of the vortex system some distance from the propeller containing a hub is identical to that of a hypothetical propeller which does not contain a central body.

By equating the thrust at the propeller plane, generated by the bound circulation, with the thrust resulting in the backward motion of the helicoidal vortex system, Equation 2.4.30, a ratio of the propeller radius to the radius of the heicoidal vortex sheet can be obtained.

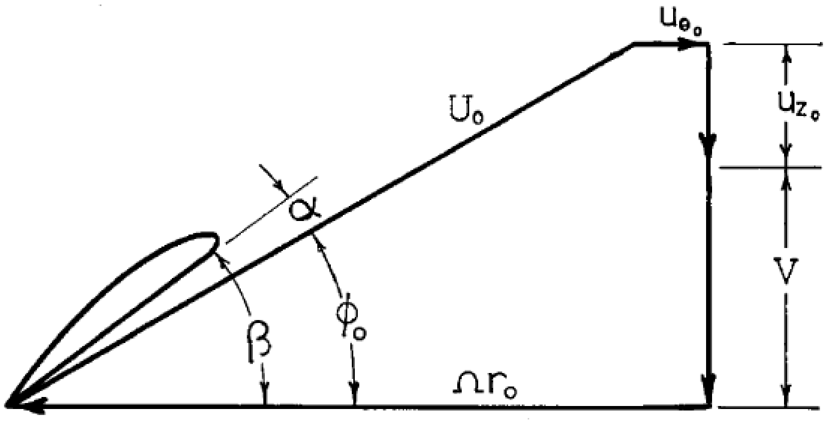

Figure 2.19 Blade Element Velocity Diagram [25].

Considering the blade element velocity diagram above and by application of the Kutta-Joukowsky theorem, it can be seen that the thrust of a blade element is proportional to the cross product of circulation and the component of relative velocity normal to the thrust. Thus the elemental thrust is given by:

$$dT = \rho\Gamma(\Omega r - u_{\theta 0})\, dr \tag{2.4.35}$$

By the derivation from Equation A.5.1 to A.5.15 of Appendix A.5 and the utilisation of the relation between the dimensionless radial coordinates of the propeller and helicoidal vortex sheet reference frame, Equation 2.4.34, the thrust at the propeller plane can be obtained from the elemental thrust equation above and represented entirely by the characteristics of the helicoidal vortex sheet as follows:

$$T_{0=}\ \rho\pi R_0^2 V_\infty^2 \overline{w}(1+\overline{w})\left[\kappa\left(1-x_h^2\right)-\frac{1}{2}\overline{w}(1+\overline{w})\lambda^2 I_1\right] \tag{2.4.36}$$

This thrust equation does, however, contain the radius of the propeller R_0. Thus, by equating this thrust at the propeller plane with the thrust of the helicoidal vortex system, Equation 2.4.30, which contains the radius of the helicoidal vortex sheet R_1, the following equation for the ratio of the propeller radius to the radius of the helicoidal vortex sheet can be obtained:

$$\left(\frac{R_0}{R_1}\right)^2 = \frac{\frac{\left[1+\overline{w}\left(\frac{1}{2}+\frac{\varepsilon}{\kappa}\right)\right]}{(1+\overline{w})}}{\left(1-x_h^2\right)-\frac{1}{2}\overline{w}(1+\overline{w})\lambda^2\frac{I_1}{\kappa}} \tag{2.4.37}$$

Where:

$$I_1 \equiv \int_0^1 \frac{2G(x_1)x_1^3 dx_1}{\left(x_1^2+\lambda_2^2\right)\left(x_1^2+c\right)} \tag{2.4.38}$$

and:

$$c = \frac{x_h^2}{\left(1-x_h^2\right)} \tag{2.4.39}$$

as defined by Wald [25]. By rearranging Equation 2.4.37, the expression for the helicoidal vortex sheet radius is as follows:

$$R_1 = \frac{R_0\left[(1+\overline{w})\left[\left(1-x_h^2\right)-\frac{1}{2}\overline{w}(1+\overline{w})\lambda^2\left(\frac{I_1}{\kappa}\right)\right]\right]^{1/2}}{\left[1+\overline{w}\left(\frac{1}{2}+\frac{\varepsilon}{\kappa}\right)\right]^{1/2}} \tag{2.4.40}$$

Where the Goldstein circulation function $G(x_1)$ must be obtained from the tables presented in Appendix B.1 and the value I_1 must, subsequently, be obtained by numerical integration.

Chapter 3

3. Simulation Design and Methodology

In order to determine if the wake produced by turboprop engines effects the relative positioning of aircraft in formation flight, a computer model was developed in MatLab to carry out such simulations. The multivariable program allows for a large range of turboprop aircraft to be simulated; the scope of which will be detailed in the following sections. The model consists of three major function groups: the initial wing and propeller characteristic functions, the Vortex Filament Method functions, and the 3D VFM and downwash graphic plot functions.

The initial wing characteristic function group is further divided into the Lifting Line Model function and the Vortex Filament Model Starting Position and Initial Setup functions. These functions are responsible for transforming the aircraft geometry and flight condition parameters, inputted by the user, into initial wake parameters to be used by the Vortex Filament Method model.

Similarly, the initial propeller characteristic function is responsible for transforming the turboprop geometry and engine parameters, specified by the user, into the initial helicoidal wake parameters. This function allows for one, two or four turboprop engines with two, three, four, five or six bladed configurations to be entered into the wake simulation depending on the type of aircraft that is to be modelled.

The Vortex Filament Method functions are then responsible for calculating the induced velocity of these two wake systems. The influence of the propeller and wing wake on itself as well as the influence these two wake systems have on each other is modelled within this function group. This function group involves iterative loops, in which the wake's velocity field is calculated and the trailing wake filaments are adjusted to align with this new velocity field, until such a time as convergence has been attained and the wake's current position is a near reflection of the velocity field it will induce.

The 3D VFM graphic plot is a visual quantitative representation of the final wake positions once convergence has been obtained. This graphic not only shows the wake geometry but a representation of the wing and propeller geometry and the relative positioning of the turboprop engines along the span of the wing.

Lastly, the downwash plot function allows for a cross-sectional plane to be taken at any point in the wake. This cross-section depicts the velocity field at the selected point in the wake by use of a vector plot graphic. The function also allows for the comparison of wakes from two separate aircraft simulations on the same figure.

A functional block diagram summarising the entire program, as well as depicting the variable progression, is shown in the following figure. Note the blue coloured arrows show the path of the wing wake and the red coloured arrows show the path of the helicoidal propeller wake.

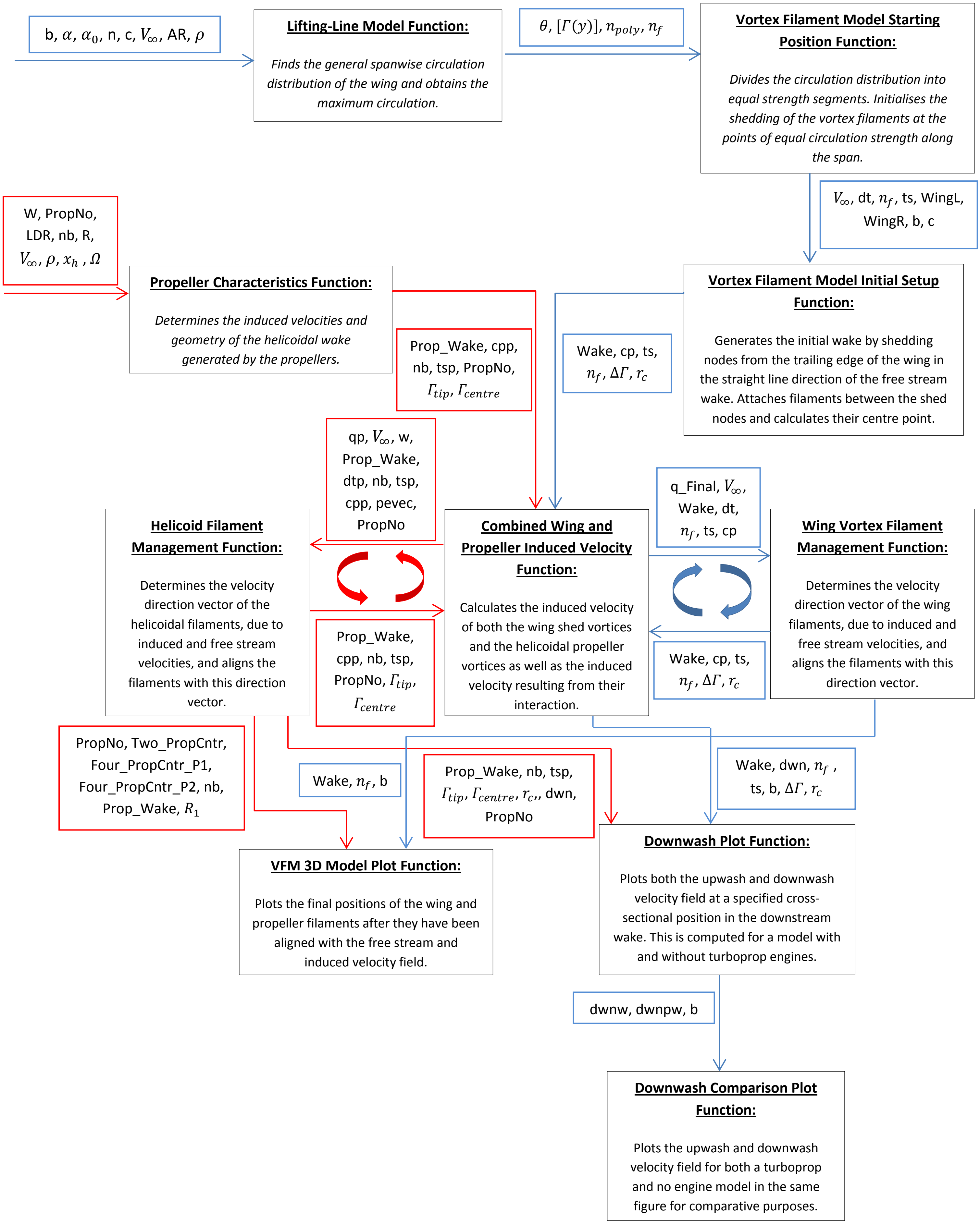
b, α, α_0, n, c, V_∞, AR, ρ
Lifting-Line Model Function:
Finds the general spanwise circulation distribution of the wing and obtains the maximum circulation.
θ, $[\Gamma(y)]$, n_{poly}, n_f
Vortex Filament Model Starting Position Function:
Divides the circulation distribution into equal strength segments. Initialises the shedding of the vortex filaments at the points of equal circulation strength along the span.
V_∞, dt, n_f, ts, WingL, WingR, b, c
W, PropNo, LDR, nb, R, V_∞, ρ, x_h , Ω
Propeller Characteristics Function:
Determines the induced velocities and geometry of the helicoidal wake generated by the propellers.
Prop_Wake, cpp, nb, tsp, PropNo, Γ_{tip}, Γ_{centre}
Wake, cp, ts, n_f, $\Delta\Gamma$, r_c
Vortex Filament Model Initial Setup Function:
Generates the initial wake by shedding nodes from the trailing edge of the wing in the straight line direction of the free stream wake. Attaches filaments between the shed nodes and calculates their centre point.
qp, V_∞, w, Prop_Wake, dtp, nb, tsp, cpp, pevec, PropNo
q_Final, V_∞, Wake, dt, n_f, ts, cp
Helicoid Filament Management Function:
Determines the velocity direction vector of the helicoidal filaments, due to induced and free stream velocities, and aligns the filaments with this direction vector.
Combined Wing and Propeller Induced Velocity Function:
Calculates the induced velocity of both the wing shed vortices and the helicoidal propeller vortices as well as the induced velocity resulting from their interaction.
Wing Vortex Filament Management Function:
Determines the velocity direction vector of the wing filaments, due to induced and free stream velocities, and aligns the filaments with this direction vector.
Prop_Wake, cpp, nb, tsp, PropNo, Γ_{tip}, Γ_{centre}
Wake, cp, ts, n_f, $\Delta\Gamma$, r_c
PropNo, Two_PropCntr, Four_PropCntr_P1, Four_PropCntr_P2, nb, Prop_Wake, R_1
Wake, n_f, b
Prop_Wake, nb, tsp, Γ_{tip}, Γ_{centre}, r_c,, dwn, PropNo
Wake, dwn, n_f , ts, b, $\Delta\Gamma$, r_c
VFM 3D Model Plot Function:
Plots the final positions of the wing and propeller filaments after they have been aligned with the free stream and induced field.
Downwash Plot Function:
Plots both the upwash and downwash velocity field at a specified cross-sectional position in the downstream wake. This is computed for a model with and without turboprop engines.
dwnw, dwnpw, b
Downwash Comparison Plot Function:
Plots the upwash and downwash velocity field for both a turboprop and no engine model in the same figure for comparative purposes.

3.1 Lifting Line Model

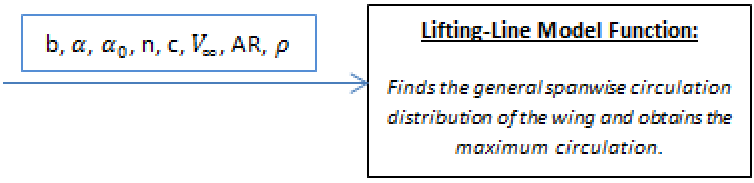

Figure 3.1 Flow diagram depicting input variables and mechanism of the Lifting-Line Model Function.

In order to obtain the starting positions of the shed vortex filaments, the general spanwise circulation of the wing needed to be found. This was obtained by making use of Prandtl's Lifting-Line Theory.

Firstly, the number of spanwise stations along the wing was selected after the wing had been mapped to polar coordinates by Equation 2.3.1 of Section 2.3.1 (Literature Review – Lifting-Line Theory). The choices for these positions, and thus θ, were chosen as a linear variation within the domain of $(0 < \theta < \pi)$. This range does, however, not include values for 0 or π as this would lead to a singular unsolvable matrix further on in the algorithm. Matrix A and vector b were then generated by use of the series of simultaneous equations of Equation 2.3.13 derived in Section 2.3.1:

$$\sum_{n=1}^{\infty} A_n \sin(n\theta)\left(\sin(\theta) + \frac{n\,c\,C_{l\alpha}}{8\,s}\right) = \frac{c\,C_{l\alpha}}{8\,s} \sin(\theta)\ (\alpha_\infty + \alpha_t - \alpha_0) \tag{2.3.13}$$

In order to generate a square matrix, the number of n values was selected to coincide with the number of spanwise stations previously specified. This resulted in an A matrix of the form:

$$Ax = \begin{bmatrix} \sin(1\theta_1)\left(\sin(\theta_1) + \frac{1\,c\,C_{l\alpha}}{8\,s}\right) & \cdots & \sin((n-1)\theta_1)\left(\sin(\theta_1) + \frac{(n-1)c\,C_{l\alpha}}{8\,s}\right) & \sin(n\,\theta_1)\left(\sin(\theta_1) + \frac{n\,c\,C_{l\alpha}}{8\,s}\right) \\ \vdots & \ddots & \vdots & \\ \sin(1\theta_n)\left(\sin(\theta_n) + \frac{1\,c\,C_{l\alpha}}{8\,s}\right) & \cdots & \sin((n-1)\theta_n)\left(\sin(\theta_n) + \frac{(n-1)c\,C_{l\alpha}}{8\,s}\right) & \sin(n\,\theta_n)\left(\sin(\theta_n) + \frac{n\,c\,C_{l\alpha}}{8\,s}\right) \end{bmatrix} A_n \tag{3.1.1}$$

And a b vector of the form:

$$b = \begin{bmatrix} \frac{c\,C_{l\alpha}}{8\,s} \sin(\theta_1)\ (\alpha_\infty + \alpha_t - \alpha_0) \\ \vdots \\ \frac{c\,C_{l\alpha}}{8\,s} \sin(\theta_{n-1})\ (\alpha_\infty + \alpha_t - \alpha_0) \\ \frac{c\,C_{l\alpha}}{8\,s} \sin(\theta_n)\ (\alpha_\infty + \alpha_t - \alpha_0) \end{bmatrix} \tag{3.1.2}$$

The A_n values were then obtained by simple matrix algebra. After which, they were substituted back into Equation 2.3.2 and 2.3.16 to obtain the spanwise circulation distribution and spanwise lift distribution respectively. The selection of the number of spanwise stations and A_n coefficients clearly determines the accuracy of both the circulation distribution and the lift distribution. A large number of spanwise stations and A_n coefficients should be utilised when the wing loading is highly non-eliptical. Analysing wings with part span flaps, for example, causes a discontinuity in the spanwise loading and therefore they require a much larger number of coefficients to accurately describe the circulation and lift distributions. Furthermore, where the wing loading is symmetric, as is the case with analysing steady trimmed flight, the even A_n coefficients are identically equal to zero and can therefore be dropped from the analysis.

Lastly, it should be noted that the use of Prandtl's Lifting-Line Theory as well as Helmholtz's Vortex Theorems, in the lifting-line model, imposes a number of limitations on the conditions of the model. The table below indicates the flow conditions to which each theory, and thus the model as a whole, is limited to.

Table 3.1: Theories utilised in the Lifting-Line Model and their associated limitations:

Theory:	**Limited to:**
Helmholtz's Vortex Theorems	• Inviscid flow
Prandtl's Lifting-Line Theory	• Inviscid flow • Incompressible flow • Unswept wings • High aspect ratio wings • Steady flows

3.2 Propeller Wake Characteristics Model

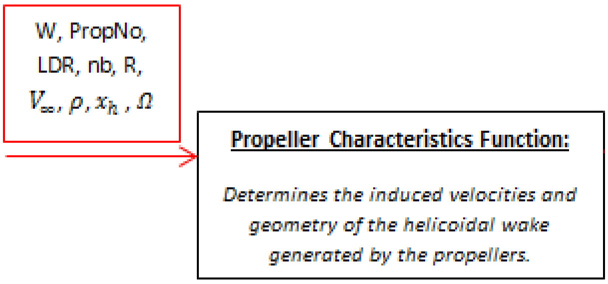

Figure 3.2 Flow diagram depicting input variables and mechanism of the Propeller Wake Characteristics Function.

As aforementioned, a helicoidal vortex sheet is shed from the trailing edge of propeller blades. In order to accurately model the wake of a turboprop driven aircraft, the vortices shed from both the wing and propeller lifting surfaces, as well as their interaction, need to be effectively modelled.

In order to determine the geometry and velocities of the helicoidal vortex, the thrust of each propeller had to first be obtained. This was initialised by first obtaining the lift to drag ratio of the aircraft to be modelled, acquired from experimental flight test data or design specifications if available. Further aircraft specifications required include the number of engines, the dry weight and typical payload. The net weight of the aircraft was, therefore, obtained from the summation of the dry (empty) weight and the typical payload.

Balancing the resultant forces on the aircraft, the approximate lift force generated by the aircraft was obtained by equating the lift to the net weight of the aircraft. Thereafter, the drag force of the aircraft was obtained by dividing the lift of the aircraft by the lift to drag ratio specification. Finally, by equating the drag force to the thrust force and dividing by the number of turboprop engines, the approximate thrust of each engine was obtained. This basic method of obtaining each engine's approximate thrust is shown in the flow diagram in the figure below:

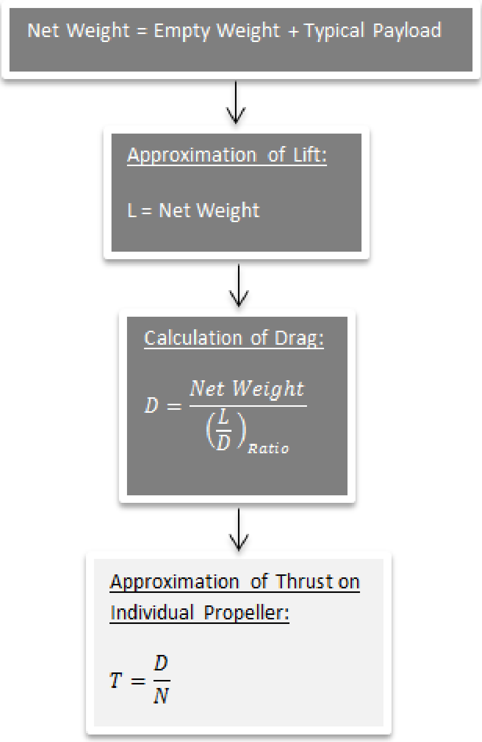

Figure 3.3 Turboprop Engine Thrust Flow Diagram.

As aforementioned, the propeller wake characteristics; such as the mass transport factor κ, the axial energy factor ϵ and the Goldstein circulation function; are all interrelated and depend on the unknown induced axial displacement velocity w of the helicoidal vortex sheets. By rearranging the thrust equation, Equation 2.4.30, the following equation for the induced axial displacement velocity w was obtained:

$$w = \frac{-\kappa\rho\pi R_1^2 V + \sqrt{\left(\kappa\rho\pi R_1^2 V_\infty\right)^2 + 4T\left(\kappa\rho\pi R_1^2\right)\left(\frac{1}{2}+\frac{\varepsilon}{\kappa}\right)}}{2\left(\kappa\rho\pi R_1^2\right)\left(\frac{1}{2}+\frac{\varepsilon}{\kappa}\right)} \tag{3.2.1}$$

In Equation 3.2.1 above, the thrust T has been previously obtained from the process described above. Furthermore, the air density ρ was obtained from the aircraft's cruising altitude and the free stream velocity V_∞ was set at the aircraft's cruising velocity. Thus, in order to calculate the helicoidal vortex sheet axial displacement velocity w the mass transport factor κ, the axial energy factor ε and the helicoidal sheet radius R_1 had to first be obtained as follows.

Each propeller's RPM, at the aircraft's cruising velocity, was obtained from general flight data and converted into angular velocity Ω. The inverse of the advance ratio λ_2, depicted in the equation below, was then obtained using the specified angular velocity and by assuming an initial value of the induced axial displacement velocity w.

$$\frac{1}{\lambda_2} = \frac{\Omega R_1}{(V_\infty + w)} \tag{3.2.2}$$

It was initially assumed that the helicoidal vortex sheet axial displacement velocity w was equal to the free stream velocity V_∞, and thus $w = V_\infty$. From the value obtained from Equation 3.2.2 above and by specifying the number of blades per turboprop engine, the corresponding mass transport factor κ and the axial energy factor ε values were obtained respectively from Table B.2.1 and Table B.2.2 of Appendix B.2. As the calculated inverse advance ratio $\frac{1}{\lambda_2}$ was not exactly equal to the tabulated values of $\frac{1}{\lambda_2}$ an interpolation function was generated and utilised in order to obtain the exact corresponding values of κ and ε for the calculated inverse advance ratio. It is to be noted that Tables B.2.1 and B.2.2 were entered and stored within the program as matrix arrays in order to automate the above process. Plots of the inverse exponential decay curves of the mass transport factor, κ, and the mass transport factor to axial energy factor ratio versus the inverse advance ratio, $\frac{1}{\lambda_2}$, are shown in Figure B.4 and B.5 of Apendix B.3 for a four-bladed propeller.

It is evident from Equation 2.4.40 that the induced axial displacement velocity w and the helicoidal vortex sheet radius R_1 are mutually dependent. Thus the helicoidal vortex sheet radius R_1 was initially assumed to be equal to the radius of the propeller R_0 in order to calculate an initial value for the induced axial displacement velocity w. The inverse advance ratio $\frac{1}{\lambda_2}$ was then recalculated utilising the new helicoidal vortex sheet axial displacement velocity w and compared to the previous calculated value. The process of calculating w was continuously repeated utilising the newly calculated value of the inverse advance ratio $\frac{1}{\lambda_2}$ until the difference between consecutive calculated values of $\frac{1}{\lambda_2}$ was less than an error tolerance of 10^{-4} .

Once this point had been reached the final inverse advance ratio $\frac{1}{\lambda_2}$ was utilised to calculate the helicoidal vortex sheet radius R_1 by firstly generating a corresponding Goldstein circulation function $G(x_1)$. This was achieved by selecting two Goldstein circulation function vectors, generated by storing the tables of Appendix B.1 in a matrix array of vectors, which bounded the Goldstein circulation function to be generated. These two selected Goldstein circulation functions were then utilised to interpolate values of the Goldstein circulation function corresponding to the calculated value of $\frac{1}{\lambda_2}$. This is more easily understood by noting that the inverse advance ratio $\frac{1}{\lambda_2}$ values serve as an index to selecting the required Goldstein circulation function. As this index value almost always falls between two indices, these indices are used to interpolate the required Goldstein circulation function. Plots of the seemingly parabolic Goldstein circulation function for a four-bladed propeller and a 0.75, 1 and 1.25 inverse advance ratio, $\frac{1}{\lambda_2}$, are shown in Figure B.1 to B.3 of Appendix B.3.

Once the Goldstein circulation function $G(x_1)$ was generated, the integral value I_1 of Equation 2.4.38 was obtained by use of MatLab's built in numerical integration scheme ODE45, which is a medium order nonstiff differential equation solver. Finally, the corresponding helicoidal vortex sheet radius was obtained from Equation 2.4.40, shown below.

$$R_1 = \frac{R_0\left[(1+\bar{w})\left[(1-x_h^2)-\frac{1}{2}\bar{w}(1+\bar{w})\lambda^2\left(\frac{I_1}{\kappa}\right)\right]\right]^{1/2}}{\left[1+\bar{w}\left(\frac{1}{2}+\frac{\varepsilon}{\kappa}\right)\right]^{1/2}} \tag{2.4.40}$$

The process of calculating R_1 was continuously repeated utilising the newly calculated value of the helicoidal vortex sheet radius R_1 until the difference between consecutive calculated values of R_1 was less than an error tolerance of 10^{-4}. If the final value of R_1 did not deviate from the previous calculation of R_1 by more than the specified error tolerance, the program terminated and the final values stored in all arrays were taken as the representative characteristics of the propeller's trailing helicoidal wake. If, however, convergence was not obtained, the calculated value of R_1 was utilised to calculate a new helicoidal vortex sheet axial displacement velocity w. The entire process was then continuously repeated until convergence was attained. The complete iterative algorithm, described above, is presented in the functional block diagram in the figure below.

Once the helicoidal vortex sheet axial displacement velocity w and the helicoidal vortex sheet radius R_1 had been obtained, the final advance ratio λ_2 was calculated from the following equation, as prescribed by Wald [25]:

$$\lambda_2 = \frac{(V_\infty+w)}{\Omega R_1} \tag{3.2.3}$$

Thereafter, this value was utilised to calculate the angular pitch and the axial and tangential convective velocity components by the respective use of Equations 2.4.7, 2.4.12 and 2.4.13 outlined in Section 2.4.4, 'The Kinematics of Helicoidal Vortex Sheets', and presented below.

$$\phi = \tan^{-1}\left(\frac{dz}{rd\theta}\right) = \tan^{-1}\left(\frac{(V_\infty+w)}{\Omega r}\right) = \tan^{-1}\left(\frac{\lambda_2}{x_1}\right) \tag{2.4.7}$$

$$u_{z1} = \frac{w}{1+\left(\frac{\lambda_2^2}{x_1^2}\right)} \tag{2.4.12}$$

$$u_{\theta 1} = \frac{w\left(\frac{\lambda_2}{x_1}\right)}{\left(1+\frac{\lambda_2^2}{x_1^2}\right)} \tag{2.4.13}$$

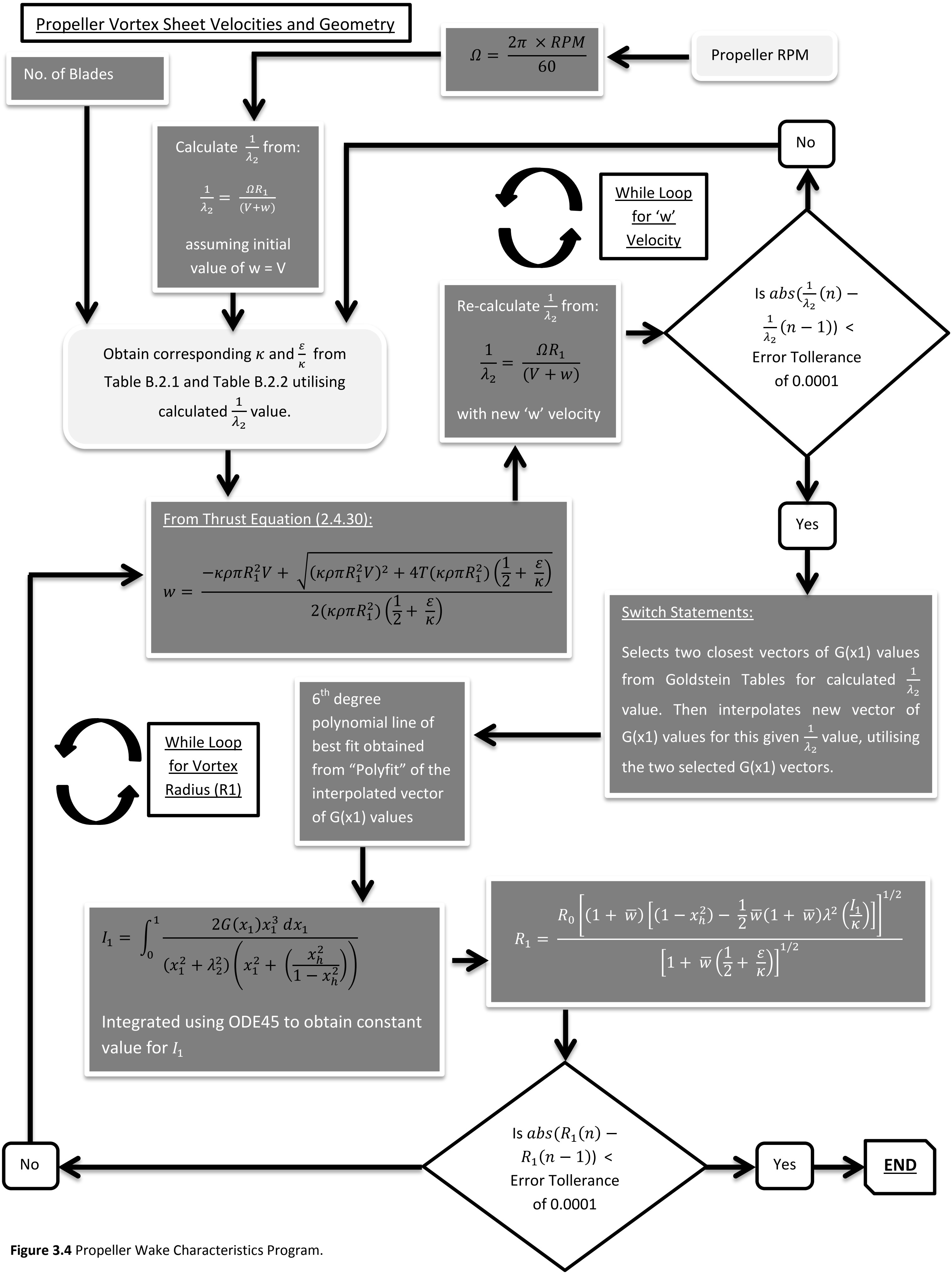

Figure 3.4 Propeller Wake Characteristics Program.

Although both Goldstein and Theodorsen's propeller vortex theories assume a rigid helicoidal vortex sheet that translates uniformly backward without further deformation, a vortex sheet with a free edge is a transient condition and will, thus, roll up into a set of helical blade tip vortices and a central vortex filament of opposite sense on the centreline axis [25]. Therefore, in order to more accurately model the trailing wake of the propeller, the Goldstein circulation function equation, Equation 2.4.18, was utilised in order to determine the approximate circulation of the rolled up helicoidal blade tip vortices. This calculation was performed by rearranging Equation 2.4.18 as follows:

$$\Gamma_{Tip} = \frac{2\,\pi\,R_1\,w\,\lambda_2 G(x_1)}{B} \tag{3.2.4}$$

Here the value of $G(x_1)$ was taken at the blade tips where $x_1 = 1$. The centreline vortex strength was obtained by multiplying the negative of the tip vortex strength by the number of tip vortices (i.e. the number of blades) as follows:

$$\Gamma_{Centre} = -\Gamma_{Tip} \times B \tag{3.2.5}$$

All the calculated propeller wake characteristic values were then utilised in order to generate the 3D model of the propeller trailing wake before the influence of the wing wake was introduced. The following table shows the initial position of each blade at time $t = 0$ in the simulation.

Table 3.2: Initial Blade Positions (at time $t = 0$):

Number of Blades:	**Position (Rad):**
Two-bladed Propeller:	$Pos = \frac{1}{2}\pi + (N_{Blade} - 1) \times \frac{2\pi}{B}$
Three-bladed Propeller:	$Pos = \frac{1}{6}\pi + (N_{Blade} - 1) \times \frac{2\pi}{B}$
Four-bladed Propeller:	$Pos = (N_{Blade} - 1) \times \frac{2\pi}{B}$
Five-bladed Propeller:	$Pos = (N_{Blade} - 1) \times \frac{2\pi}{B}$
Six-bladed Propeller:	$Pos = \frac{1}{6}\pi + (N_{Blade} - 1) \times \frac{2\pi}{B}$

Where N_{Blade} is the position number of the blade being modelled ($N_{Blade} = 1,2,3 \dots B$).

In order to model both the wing and propeller wake, a Vortex Filament Method model was employed. It was decided that the VFM model act on a predefined initial wake pattern in order to reduce the time to reach a converged wake formation and, thus, reduce computational cost. The predefined propeller wake formation was based on that defined by Goldstein and Theodorsen's propeller wake theory, however, rolled up blade tip vortices were generated as opposed to a rigid vortex sheet.

The predefined propeller wake formation, therefore, consists of helicoidal blade tip vortices and a centreline vortex filament as defined by Equations 3.2.4 and 3.2.5 above. The vortex filaments, which span the propeller wake domain, were generated by shedding nodes from the propeller blade tips and centreline axis at incremental time steps dt_p. Along the propeller wake axis (x-axis) these nodes were shed at the combined free stream and induced axial displacement velocity of the propeller wake ($V_\infty + w$). With each differential time step dt_p, the blade position changes from the initial position at time $t = 0$, shown in Table 3.2 above, due to the angular velocity of the turboprop blades and, thus, the position of the subsequent blade tip's shed node changes. Therefore, the y and z coordinates of the nodes were shed as a function of the angular velocity and the helicoidal vortex sheet radius R_1, obtained from Equation 2.4.40 in the algorithm described above. The vortex sheet edge at the propeller plane will, in reality, be shed at the propeller radius R_0. However, through contraction and roll up immediately after the propeller, the sheet will form a set of helicoidal vortices at radius R_1. Therefore, as only the far field wake is of concern and in order to reduce computational cost, the nodes were shed at the helicoidal vortex sheet radius R_1.

Once the nodes where shed from the blade tips and hub axis, they were linked by vortex filament segments to form a set of helicoidal filaments around a centreline hub filament. These filament segment objects stored the centre point node and the circulation strength (obtained from Equations 3.2.4 and 3.2.5 above) of each filament segment in the vortex filament model. The components and velocities used to discretise this prescribed helicodal vortex wake are shown in Figure 3.5 below.

Lastly, it should be noted that the use of Goldstein and Theodorsen's propeller vortex theory as well as the modelling techniques utilised to reduce computational cost, in the Propeller Characteristics Model, imposes a number of limitations on the conditions of the model. The table below indicates the flow conditions to which each theory, and thus the model as a whole, is limited to.

Table 3.3: Theories utilised in the Propeller Wake Characteristics Model and their associated limitations:

Theory:	**Limited to:**
Goldstein and Theodorsen Propeller Vortex Theory	• Inviscid flow • Incompressible flow • Steady flow • Only propeller and turboprop propulsive devices • Far field wake (eliminates development region of vortex aging)

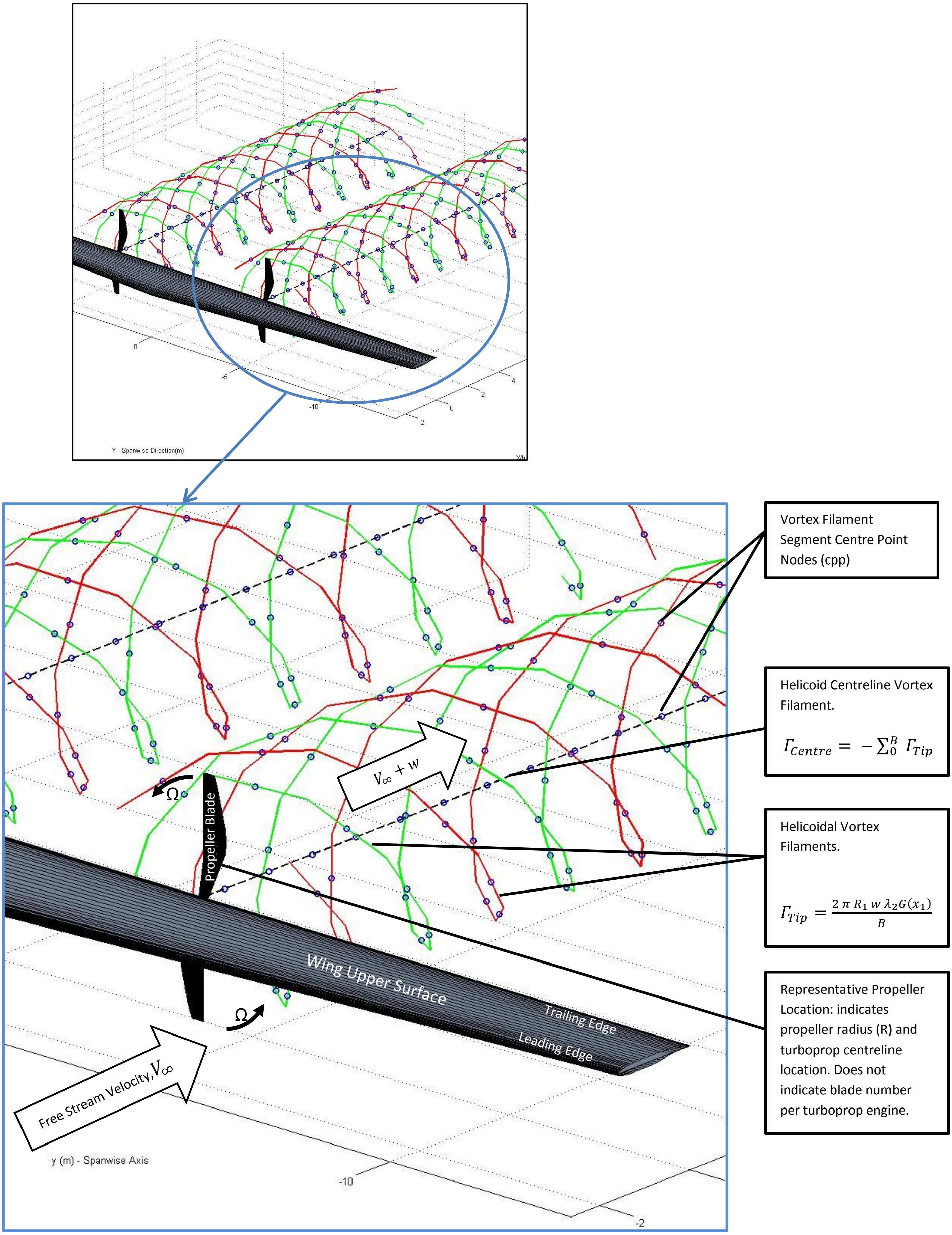

Figure 3.5 Prescribed Turboprop Trailing Wake.

3.3 Vortex Filament Method – Initial Wake

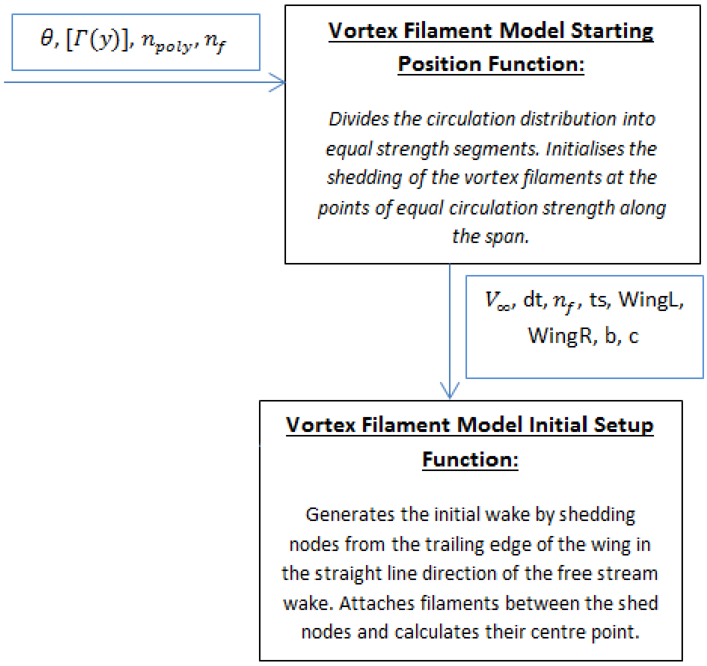

Divides the circulation distribution into equal strength segments. Initialises the shedding of the vortex filaments at the points of equal circulation strength along the span.

Generates the initial wake by shedding nodes from the trailing edge of the wing in the straight line direction of the free stream wake. Attaches filaments between the shed nodes and calculates their centre point.

Figure 3.6 Flow diagram depicting input variables and mechanism of the Vortex Filament Model Initial Wake functions.

As aforementioned, in order to reduce computational cost the VFM model acts on a predefined wake formation. Both the Vortex Filament Model Starting Position Function and Initial Setup Function are responsible for transforming the results of the Lifting-Line Model (LLM) into an initial wing wake formation.

Once the circulation distribution had been obtained by the LLM model, the VFM Starting Position Function obtained the maximum bound circulation value of the wing. This maximum circulation value was then divided by the number of filaments per semi-span nf, specified by the user, in order to obtain a constant filament circulation value $\Delta\Gamma$. For incremental steps from $\Delta\Gamma$ to $\Gamma = nf \times \Delta\Gamma$, where $\Gamma_{Max} = (nf + 1) \times \Delta\Gamma$, the positions on the span correlating to the constant filament circulation value $\Delta\Gamma$ were found. These locations on the span mark the starting positions of each vortex filament which discretises the wing wake of the aircraft. Note that as $\Gamma_{Max} = (nf + 1) \times \Delta\Gamma$, the centre span filament positions are omitted from the simulation. This is due to the fuselage of the aircraft occupying this location, the fact that the bound circulation gradient is zero at this position and due to the two vortex filaments occupying this position cancelling each other out as a result of their circulation being equal in magnitude but opposite in direction. The bound circulation gradient increases as the wing tips are approached, thus, by the method mentioned above, the density of shed vortex filaments increases in the spanwise direction towards the wing tips. The method of dividing the bound circulation into equal circulation increments ensures that the corresponding shed vortex filaments have a higher span wise density in the roll up region. This guarantees that the simulation has a higher resolution in the areas of interest. The method of determining the constant circulation vortex filament positions, described above, is depicted in the figure below.

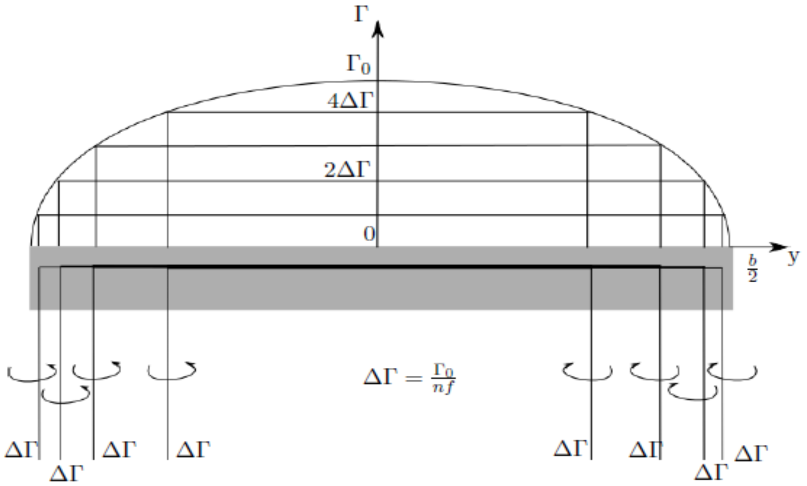

Figure 3.7 Lifting Line Method to Wake Formation Conversion [20].

The wing wake axis was then set by the VFM Initial Setup Function. The origin was placed at the centre of the wing span and, in accordance with the ‘Right hand rule’, the y-axis was positioned along the span, the positive x-axis was positioned in the direction of the shed wake and the z-axis was positioned in correlation with a positive lift direction. The vortex filament positions obtained in radians by the process mentioned above were then converted by Equation 2.3.1, $y = s\cos\theta$, into physical y-coordinate positions along the span. The z-coordinate was initially fixed at zero for all nodes spanning the predetermined wake. In order to generate the initial wake, at simulation time $t = 0$, nodes were shed from the vortex filament starting positions on the trailing edge of the wing. The shed node’s y and z coordinates were set to the values specified above. The x-coordinate of the nodes were generated by shedding the nodes at the trailing edge of the wing by a displacement length equivalent to the product of the free stream velocity V_∞ and the differential time step dt of the total simulation time t. The number of shed nodes and, thus, the length of the trailing wake was determined by the total simulation time specified by the user.

Once the coordinates of the nodes were determined, they were linked together to form vortex filament segments. The position number and coordinate position of these generated vortex filament segments were stored in a multidimensional array such as that depicted in the figure below.

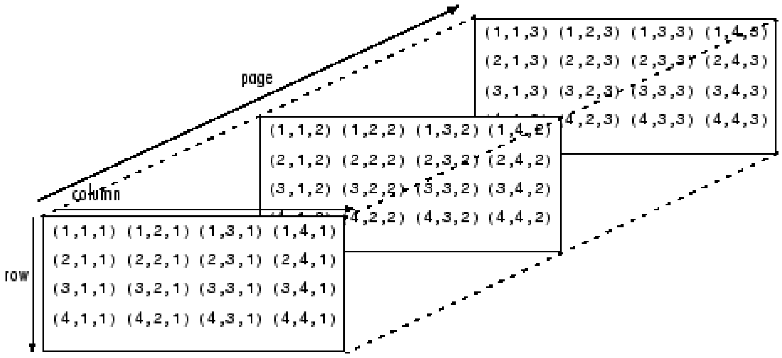

Figure 3.8 Multidimensional Array [35].

Where the rows of the multidimensional array denote the filament number, the columns denote the node position numbers and the pages denote the x,y and z coordinates respectively. Thereafter, the centre point of each vortex filament segment was determined and the initial predetermined wake, including node and centre point positions, was plotted. The components and velocities used to discretise this prescribed wing trailing vortex sheet are shown in Figure 3.9 below.

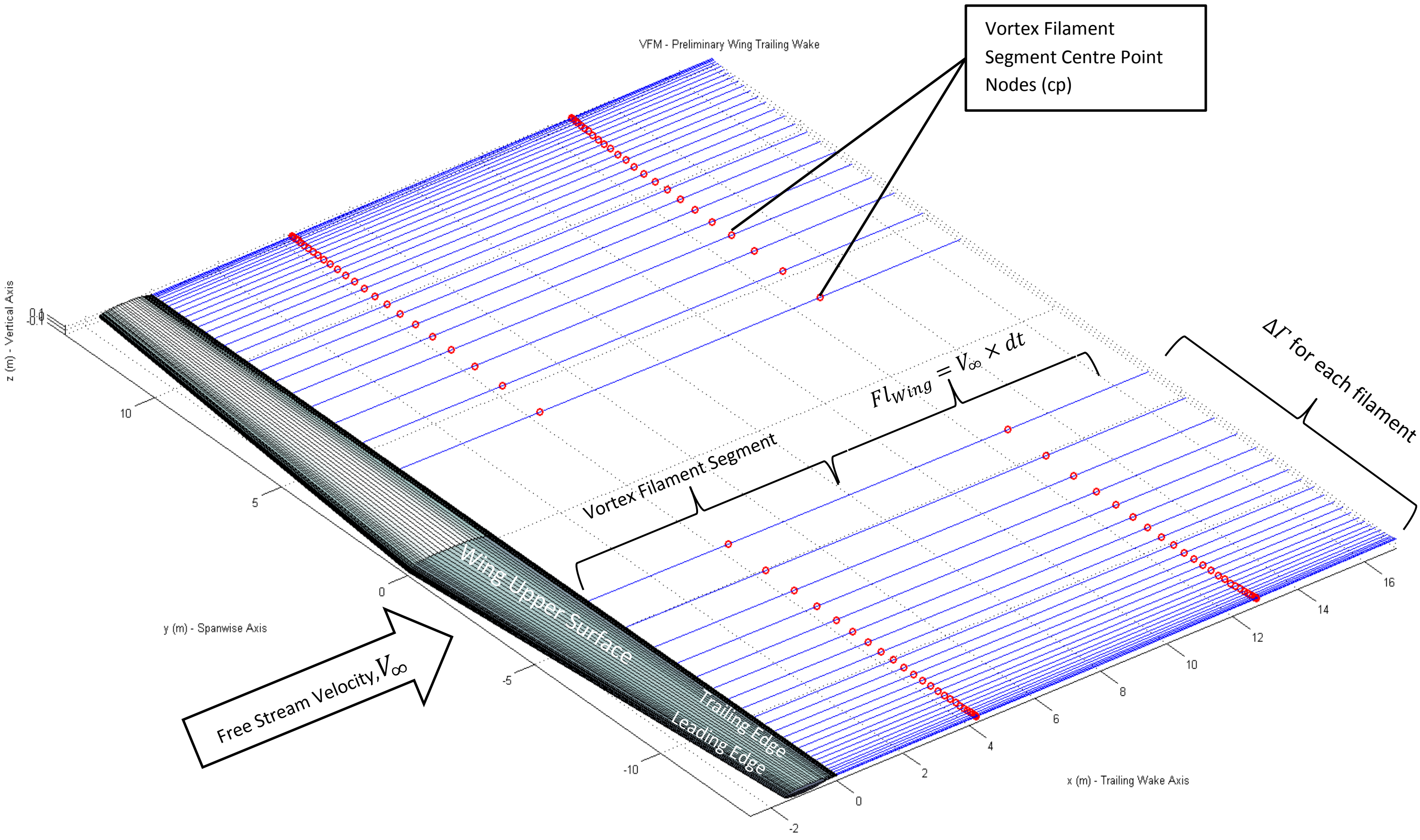

Figure 3.9 Preliminary Wing Trailing Vortex Sheet.

3.4 Combined Wing and Propeller Wake Induced Velocity

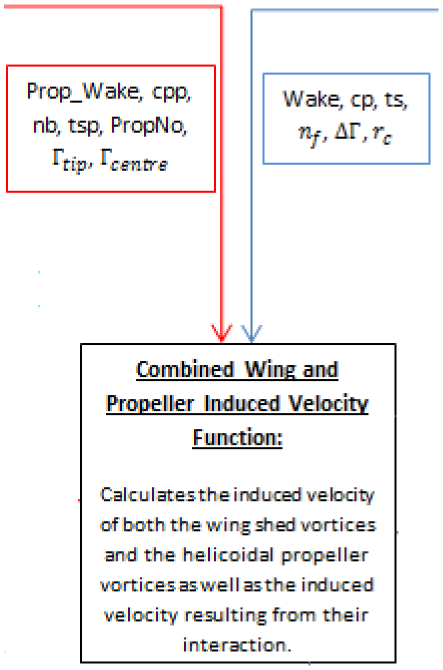

Calculates the induced velocity of both the wing shed vortices and the helicoidal propeller vortices as well as the induced velocity resulting from their interaction.

Figure 3.10 Flow diagram depicting input variables and mechanism of the Combined Wing and Propeller Wake Induced Velocity.

The Combined Wing and Propeller Induced Velocity Function is responsible for calculating the induced velocity of both the wing shed vortices and the helicoidal propeller vortices as well as the induced velocity resulting from their interaction.

The wing wake induced velocity was calculated first by cycling through each vortex filament segment and calculating its effect on the centre point of all vortex filament segments discretising the wing wake. The numerical computation form of the Burnham-Hallock induced velocity model (Equation 2.3.26), derived in Equations A.3.10 – A.3.17 of Appendix A.3.1, was utilised in calculating this induced velocity and is shown below:

$$\vec{V} = \frac{\Gamma}{4\,\pi}\left(\frac{\frac{|\vec{r}_1 \times \vec{r}_2|}{|\vec{r}_0|}}{\left(\frac{|\vec{r}_1 \times \vec{r}_2|}{|\vec{r}_0|}\right)^2 + E^2}\right)\left(\frac{\vec{r}_0 \cdot \vec{r}_1}{|\vec{r}_0||\vec{r}_1|} - \frac{\vec{r}_0 \cdot \vec{r}_2}{|\vec{r}_0||\vec{r}_1|}\right)\frac{\vec{r}_1 \times \vec{r}_2}{|\vec{r}_1 \times \vec{r}_2|} \qquad (2.3.26)$$

Where $\vec{r}_0$ is the vortex filament segment inducing the velocity and falls between two shed nodes (i.e. node 1 and 2 in Figure 3.11 below). $\vec{r}_1$ and $\vec{r}_2$ are the distance vectors from the nodes bounding the vortex filament segment inducing the velocity to the centre point of the vortex filament segment on which the induced velocity is acting.

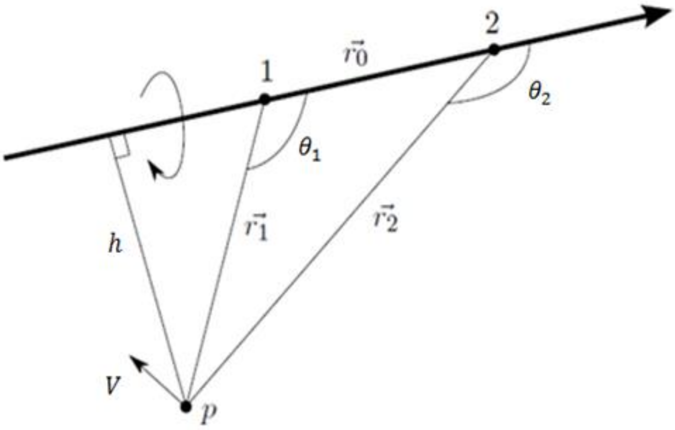

Figure 3.11 Velocity induced at point P by a straight vortex filament of finite length (Adapted from Katz and Plotkin [22]).

Once all $\vec{r}_0$ wing wake vortex filament segments were cycled through, and their induced velocity on the predetermined wing wake had been calculated, the same procedure was carried out for the helicoidal propeller vortex filament segments. The Burnham-Hallock induced velocity model was utilised once again in order to determine the induced velocity of each propeller wake vortex segment on the helicoidal propeller wake. Note, however, that in order to obtain a smooth propeller wake profile the differential time step for the propeller wake dtp was selected to be one tenth the value of the wing wake differential time step dt and, thus, the propeller wake contains ten times the number of nodes as the wing wake.

Thereafter, the wing vortex filament segments were cycled through once again and their induced velocity on the helicoidal propeller wake was calculated. Similarly, the propeller wake vortex filament segments were cycled through once again and their induced velocity on the wing wake was calculated. Thus, the influence of all vortex filaments on all wake formations, shed in the wake of a turboprop propelled aircraft, was calculated.

The use of the Burnham-Hallock induced velocity model, in the Combined Wing and Propeller Induced Velocity Function, imposes a number of limitations on the conditions of the model. The table below indicates the flow conditions to which this induced velocity model and the Bio-Savart Law, from which the model is derived, is limited to.

Table 3.4: Theories utilised in the Combined Wing and Propeller Induced Velocity Function and their associated limitations:

Theory:	**Limited to:**
Bio-Savart Law and Burnham-Hallock Model	• Inviscid flow • Incompressible flow

3.5 Vortex Filament Management

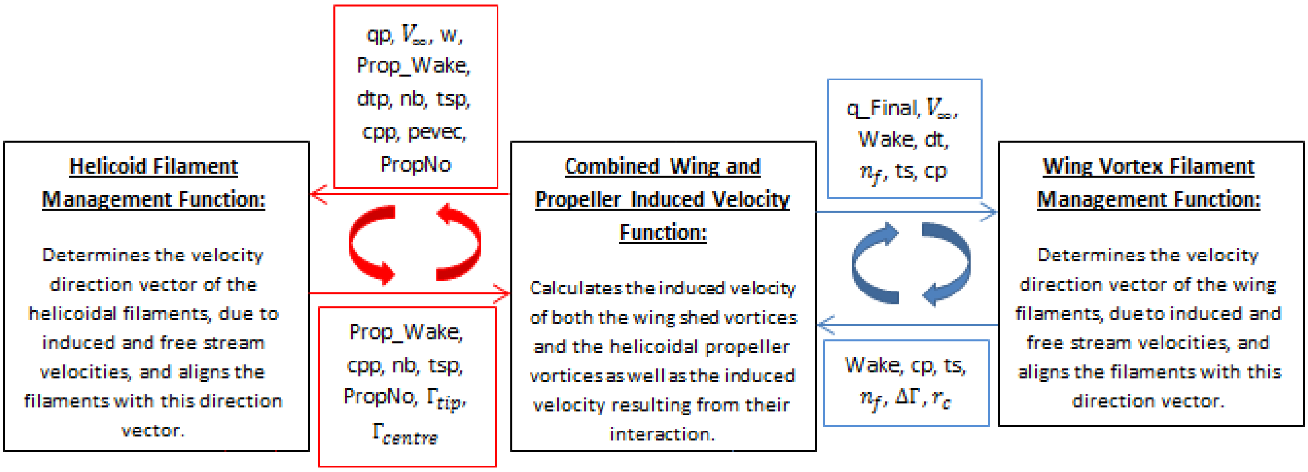

Figure 3.12 Vortex Filament Management Function and Induced Velocity Function Relationship.

Once the induced velocity field of the aircrafts trailing wake has been determined, the vortex filaments were adjusted to align with this velocity field. The Wing Vortex Filament Management Function and the Propeller Filament Management Function were responsible for carrying out this operation and are identical in procedure but differ in filament length calculations.

Both filament management functions first calculate the velocity field of the wake by the summation of the induced velocity and the free stream velocity. For the wing wake the free stream velocity is the aircraft's cruising velocity V_∞ in the positive x-axis direction. The propeller wake velocity field is, however, comprised of the summation of the free steam velocity V_∞, the vortex filament induced velocities, as well as the propeller's induced axial displacement velocity w obtained from 'The

Propeller Wake Characteristics Model' above. The total velocity seen by each vortex filament segment, referred to the filament segment centre point, was therefore calculated in this regard.

From this total velocity, the velocity unit direction vector was calculated for each filament segment at its centre point. Thereafter, the new direction of the filament segment was calculated by multiplying the unit vector for each filament segment by the filament segment length, Fl. Where:

$$Fl_{Wing} = V_{\infty} \times dt \tag{3.5.1}$$

for wing filament segments and:

$$Fl_{Prop} = (V_{\infty} + w) \times dt_p \tag{3.5.2}$$

for propeller filament segments. Once the filament segments were aligned with the wake's velocity field, the new positions of their centre points were calculated. These centre point coordinates and new filament segment position coordinates were then inputted once again into the Combined Wing and Propeller Induced Velocity Function in order to determine the new induced velocity field of the adjusted wake. This cyclic process of constantly realigning the vortex filaments, discretising the wake, with the velocity field they induce, was carried out until convergence was attained and the vortex filament positions accurately represented the velocity field of the wake. This circuitous relationship between the Vortex Filament Management Function and the Induced Velocity Function, in ensuring the accurate graphical representation of the wake by vortex filaments, is shown in Figure 3.12 above.

3.6 Vortex Filament Method – 3D Graphic Model

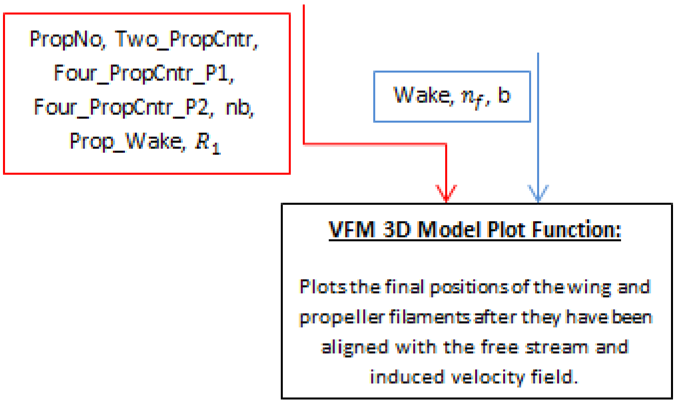

Figure 3.13 Flow diagram depicting input variables and mechanism of the 3D VFM Graphic Plot.

Once convergence between the Filament Management and Induced Velocity functions was attained and, thus, the final position of each vortex filament was determined, the VFM 3D Graphic Plot was called.

The wing surface was plotted first by reading in coordinate points of the NACA profile of the specified aircraft wing. These points were stored in Microsoft Xcel and were automatically entered into arrays when the plot function was called. These coordinates were then surface mapped using MatLab's built in surface plotting function. Thereafter, a similar process was carried out in order to plot the blades of the turboprop engine(s) and fix these to the relevant positions on the specified aircraft's wing. Once again the propeller blade profile coordinates were stored in Microsoft Xcel and were automatically entered into the MatLab program when the plot function was called.

Once the propeller surface had been mapped, the wing trailing wake vortex filaments and propeller trailing wake vortex filaments were plotted by use of their respective filament segment node coordinates. Note that in order to distinguish between the blade tip vortices, alternating line colours were utilised.

3.7 Upwash and Downwash Model

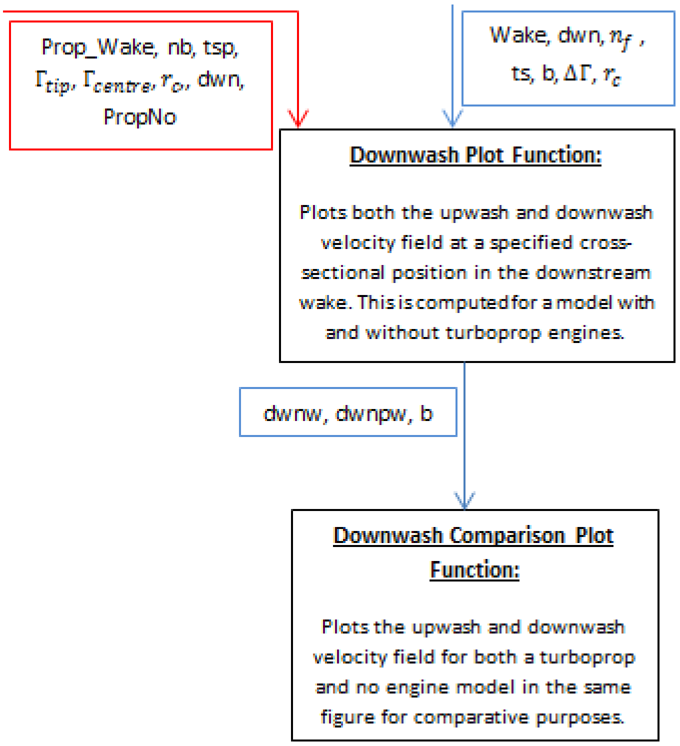

Figure 3.14 Flow diagram depicting input variables and mechanism of the Upwash and Downwash Velocity Model.

The 3D VFM wake model was then segmented at regions specified by the user in order to determine the upwash and downwash velocity fields at various locations in the wake. In order to achieve this, the wake was cross sectioned along the x-axis by a y-z plane. Points were then generated on the y-axis along the span of the aircraft, with a half span length extension of points beyond the wing tips. The Induced Velocity function was then called in order to determine the velocity at these points by all the filaments discretising the aircraft's wake. Thereafter, the y-direction velocity components were filtered out to obtain only the distribution and magnitude of vertical velocity components at these points.

The resulting upwash and downwash velocity components were subsequently plotted. In order to investigate the effects of helicoidal vortices on the upwash and downwash velocity field of an aircraft, this plot was generated for aircraft with and without turboprop engines and the resulting plots were superimposed on one another by the Downwash Comparison Plot function.

Chapter 4

4. Results and Discussion

4.1 Lifting Line Method and Vortex Filament Method Model Validation

In order to validate the LLM and VFM model programs, a test was derived in order to determine if the numerical schemes within the models converged. Based on this convergence test and the associated Mean Relative Percentage Error results, the induced velocity model within the VFM was also selected. Thereafter, both the LLM and VFM models were utilised to reproduce the results of Ehret and Oertel [19] in their calculation of wake vortex structures in the near-field wake behind a cruising Boeing 747 aircraft. Furthermore, the models were subsequently validated against the experimental results of Burnham et al. [36] by comparing the simulated results with those obtained during their ground-based measurements of the wake vortex characteristics of a B747 aircraft in various configurations. The results and discussion of said validation is detailed below.

Convergence Test:

In order to determine if the iterative numerical scheme of the Vortex Filament Method, utilising either the Burnham-Hallock induced velocity model or the Biot-Savart induced velocity model, achieved a converged solution, a relative error function was derived as follows:

The Relative Error (RE) between two vectors is given as follows:

$$\varepsilon_i = \sum_{i=1}^{N} \frac{|\vec{a_i} - \vec{b_i}|}{|\vec{a_i}|} \tag{4.1.1}$$

Where $\vec{a_i}$ and $\vec{b_i}$ are the vectors being compared and N is the number of vectors in each vector set. A more meaningful comparison, however, is the Mean Relative Percentage Error (MRPE) obtained as follows:

$$\varepsilon_{MPi} = \frac{1}{N} \sum_{i=1}^{N} \frac{|\vec{a_i} - \vec{b_i}|}{|\vec{a_i}|} \times 100 \tag{4.1.2}$$

Within the current investigation, the two vectors ($\vec{a_i}$ and $\vec{b_i}$) are the direction unit vector of the current wake ($\vec{e_i}$) and the induced velocity vector ($\vec{v_i}$) respectively. The direction unit vector of the current wake ($\vec{e_i}$) is the direction of each VFM segment at the current iteration loop, and the induced velocity vector ($\vec{v_i}$) is the velocity induced by each of these VFM segments within this same current iteration loop. When the direction of the induced velocity vector ($\vec{v_i}$) coincides with the direction unit vector of the current wake, the numerical scheme has converged and, thus, the wake formation is stable and representative of the actual trailing wake of the aircraft. In order to determine the degree of correlation between the direction of the respective vectors ($\vec{e_i}$ and $\vec{v_i}$) the difference method within the MRPE was replaced with the cross product between the two vectors. The cross product is a function of sine of the angle between the two vectors, thus as the angle between the two vectors approaches zero, so the cross product approaches zero. Therefore, the final resultant MRPE equation for vectors $\vec{e_i}$ and $\vec{v_i}$ is as follows:

$$\varepsilon_{MPi} = \frac{1}{N}\sum_{i=1}^{N}\frac{|\vec{v_i}\times\vec{e_i}|}{|\vec{v_i}|}\times 100 \tag{4.3.3}$$

Where N is the number of VFM segments in the trailing aircraft wake and is thus equal to the product of the number of filaments and time steps ($N = nf \ \times ts$).

Selection of Induced Velocity Model:

Although the Burnham-Hallock induced velocity model should, theoretically, result in a more accurate representation of the trailing wake than the Biot-Savart induced velocity model, a test for convergence of both schemes was conducted in order to determine their respective numerical stability. The relative accuracy as well as numerical stability, obtained by use of the MRPE equation, was therefore utilised in the selection of the induced velocity model.

An identical simulation, 10 filaments per semi-span generating a trailing wake approximately 4.3 wingspans long in the streamwise direction, was conducted for both the Biot-Savart and Burnham-Hallock induced velocity models. The results are as follows:

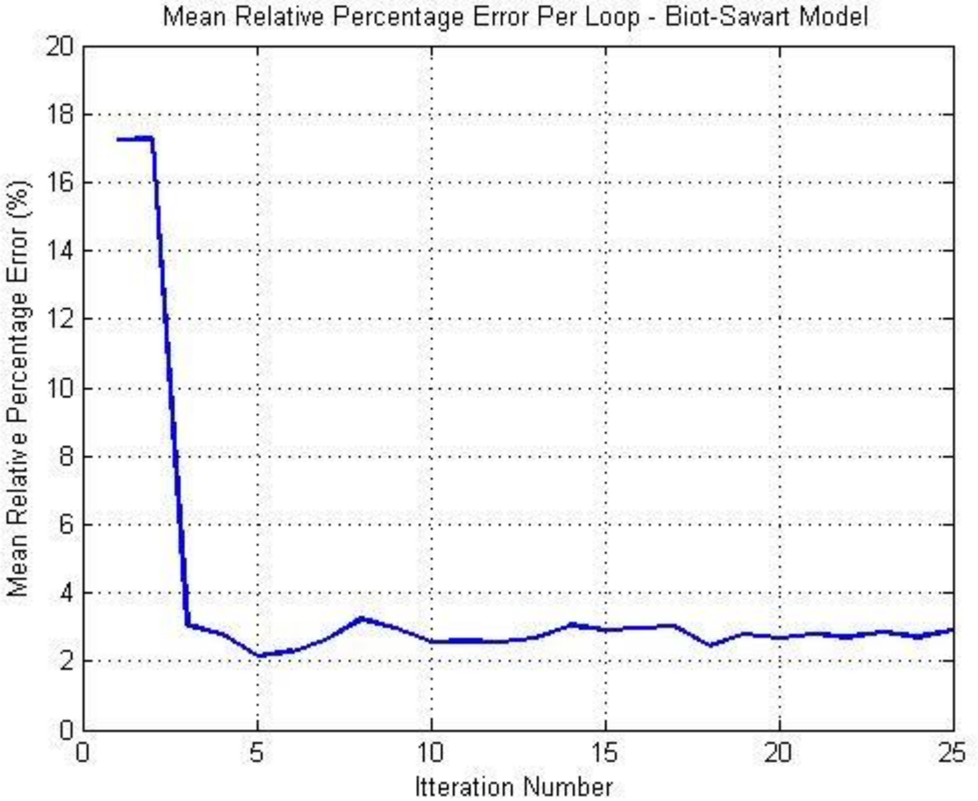

Figure 4.1 Mean Relative Percentage Error - Biot-Savart Induced Velocity Model.

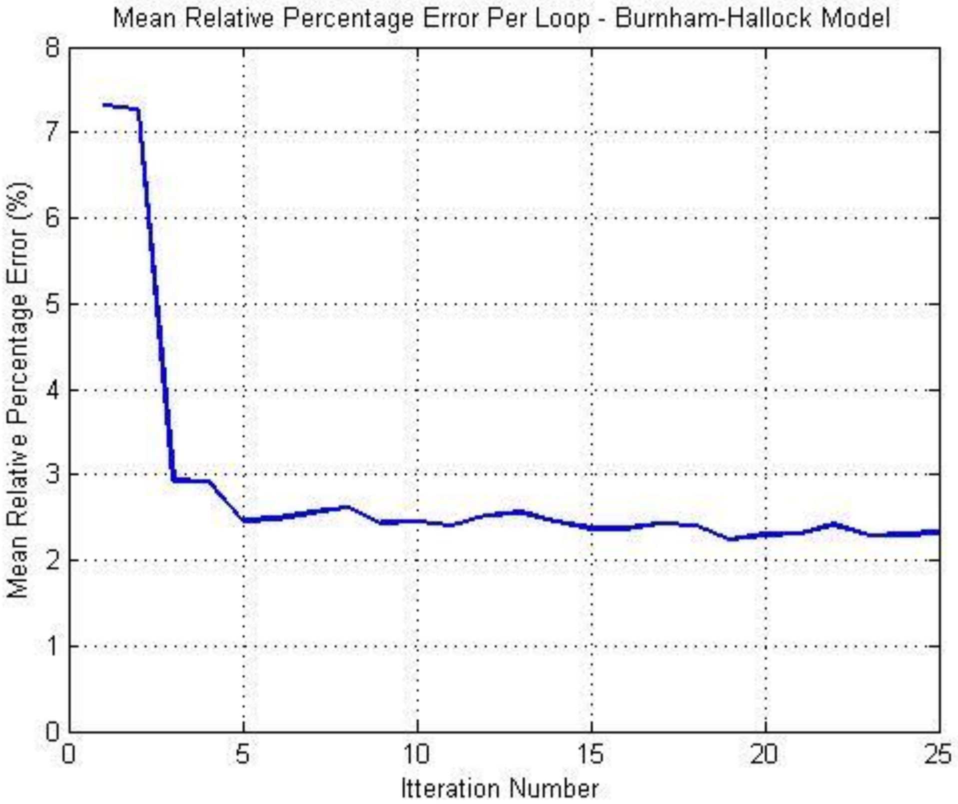

Figure 4.2 Mean Relative Percentage Error - Burnham-Hallock Induced Velocity Model.

From the MRPE plots above, it is evident that both induced velocity models reach a converged solution with relative stability fluctuations of 0.3%. The Biot-Savart Model reaches its lowest MRPE value of 2.139% after just 5 iterative loops of the numerical scheme whereas the Burnham-Hallock Model reaches its lowest MRPE value of 2.241% at 19 iterations. However, after 5 iterations the Burnham-Hallock Model attains a 2.457% MRPE just 0.318% higher than the Biot-Savart Model.

It is therefore evident that the Biot-Savart Model is only marginally faster at achieving a representative trailing wake than the Burnham-Hallock Model. This is, however, to be expected as the Biot-Savart Model is a more approximate induced velocity model than the Burnham-Hallock Model. Although upscaling the simulation, and introducing the turboprop trailing wake, will further increase the time taken for the Burnham-Hallock Model to achieve a minimum MRPE value, the Burnham-Hallock Model will result in a far more accurate representation of the trailing wake as each vortex filament contains a finite viscous core. Furthermore, according to the work of Fischenberg [23] and Burnham and Hallock [24], values obtained via the use of the Burnham-Hallock model correlate well with experimental measurements obtained in investigations of the rolled up wake of cruising aircraft. The Burnham-Hallock Model was therefore selected over the Biot-Savart Model to compute the induced velocities of the VFM model due to its superior accuracy outweighing its lengthier computational time.

VFM Validation:

In order to validate the programmed VFM Burnham-Hallock model, the simulation proposed by Ehret and Oertel [19] for a cruising Boeing 747 was carried out. The results of which were then compared to results obtained by Ehret and Oertel [19] as well as experimental results obtained by

Burnham et al. [36] in their ground-based measurements of the wake vortex characteristics of a B747 aircraft.

Ehret and Oertel [19] utilised an integrated Biot-Savart law VFM, incorporating a finite vortex core for each vortex filament in order to eliminate self-induction singularities. The conditions for their simulation, utilised in order to calculate the distribution of exhaust gases behind a cruising aircraft, are presented in the table below:

Table 4.1: Ehret and Oertel Simulation Conditions [19]:

Flight Condition:	**Input Data:**
Aircraft type	Boeing 747
Wingspan (b)	60 m
Wing Sweep Angle (Φ)	37°
Wing Aspect Ratio (AR)	7.4
Aircraft Net Weight	2.87×10^6 N
Cruising Velocity (Free Stream Velocity - V_∞)	250 m/s
Altitude (H)	11.3 km
Air Density at Altitude (ρ)	0.35 kg/m^3
Air Pressure (P)	215.9 hPa
Air Temperature (T)	214.3 K
Vortex Filaments per Semi-span	50
Finite Filament Core Radius (r_c)	3 m
Wake Length (L_w)	750 m
Timestep (Δt)	0.06 s
Vortex Age (t)	3 s
Velocity Field Cross-section x-position	750 m

In order to obtain the circulation distribution of the B747 wing, Ehret and Oertel assumed an elliptically loaded wing for which the circulation distribution is given by [16, 19]:

$$\Gamma(y) = \Gamma_{max}\sqrt{1 - \left(\frac{2\,y}{b}\right)^2} \qquad (4.3.4)$$

Consequently, as a result of assuming an elliptically loaded wing, the spanwise integral of the lift distribution is simply half the area of an ellipse (with semi-axes Γ_{max} and $\frac{b}{2}$). Thus the lift can be evaluated as [16]:

$$L = \rho\, V_\infty \int_{-b/2}^{b/2} \Gamma(y)dy = \frac{\pi b}{4}\, \rho\, V_\infty\, \Gamma_{max} \qquad (4.3.5)$$

In order to determine the maximum circulation, Ehret and Oertel [19] equated the lift of the B747 at cruising velocity and altitude to the weight of the aircraft (shown in Table 4.1) as follows:

$$W = L = \frac{\pi b}{4} \rho V_{\infty} \Gamma_{max} \tag{4.3.6}$$

$$L = 2.87 \times 10^6 = \frac{\pi(60)}{4} (0.35)(250) \Gamma_{max}$$

$$\Gamma_{max} = 700 \, m^2/s$$

Substituting this result into Equation 4.3.4 yields the following equation utilised by Ehret and Oertel for the circulation distribution of the B747 at cruise [19]:

$$\Gamma(y) = 700\sqrt{1 - \left(\frac{y}{30}\right)^2} \tag{4.3.7}$$

In order to replicate this circulation distribution utilising the programmed General Spanwise Circulation Lifting Line Method as opposed to assuming the above equation for the circulation distribution of an elliptically loaded wing, the following additional input data for the B747 at cruise was required:

Table 4.2: Additional simulation conditions of B747 at cruise:

Flight Condition:	**Input Data:**
Wing Angle of Attack (α)	2.4 deg
Wing Zero Lift Angle (α_0)	-3.019 deg
2D Lift Slope Coefficient (CL_{α})	5.5
Wing Root Chord (C_{Root})	14.63 m
Wing Tip Chord (C_{Tip})	4.06 m

Inputting this data into the General Spanwise Circulation Distribution LLM program, which makes use of the Fourier series expansion of Equation 2.3.2, yields the following circulation distribution comparison for the B747 at cruise:

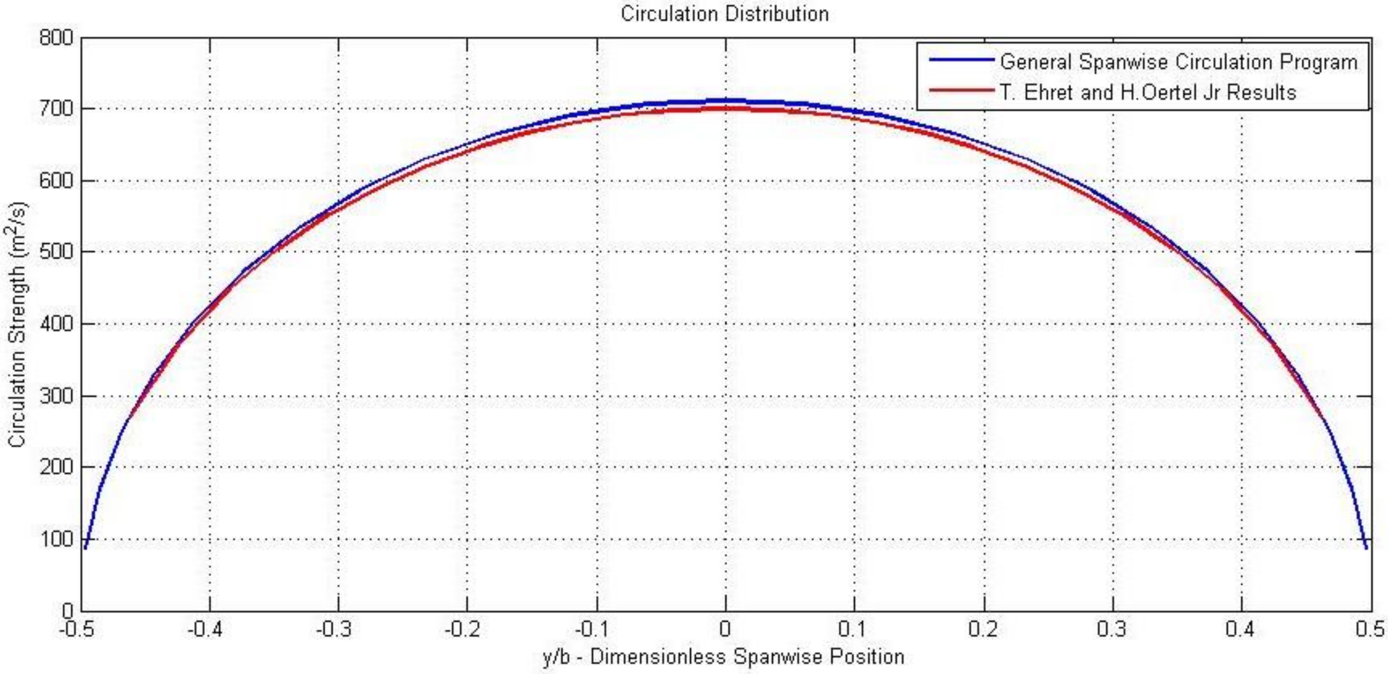

Figure 4.3 Circulation Distribution of a Boeing 747 Aircraft at Cruise.

In the above circulation distribution plot, the blue curve represents the spanwise circulation along the wing as a result of the use of the General Spanwise Circulation LLM program, whereas the red curve represents the spanwise circulation distribution resulting from the work of Ehret and Oertel. As can be seen from the figure above, the circulation distribution results of the General Spanwise Circulation LLM program compare extremely well with that of Ehret and Oertel [19]. It is to be noted, however, that the General Spanwise Circulation LLM program achieves a maximum circulation of 712.4 m^2/s as opposed to the 700 m^2/s achieved by Ehret and Oertel [19]. Substituting this result into Equation 4.3.6 above, yields a total lift force of 2.937 x 10^6 N. As the lift force of the aircraft at cruise should equal the weight of the aircraft, to maintain a constant altitude of 11.3 km, the lift force result compares relative well to the weight of the aircraft quoted at 2.87 x 10^6 N [19]. It is to be noted, however, that in order to replicate the exact circulation distribution of Ehret and Oertel [19] for the B747, the following wing planform had to be utilised in the General Spanwise Circulation LLM program [16]:

$$c(y) = c_{root}\left[1 - \left(\frac{2\,y}{b}\right)^2\right]^{1/2} \tag{4.3.8}$$

Where c_{root} is the chord length at the wing root. The following equation is, however, a more accurate local chord function of the spanwise position variable for the B747 and other trapezoidal wing planforms [37]:

$$c(y) = c_{root}\left[1 - (1 - \lambda)\,\frac{2y}{b}\right] \tag{4.3.9}$$

Where λ is the wing taper ratio, $= c_{tip}/c_{root}$, and c_{tip} is the chord length at the wing tip.

The ability of the General Spanwise Circulation LLM program in reproducing the circulation distribution utilised by Ehret and Oertel [19] indicates that the program is indeed accurate at producing circulation distribution profiles for a variety of wing planforms, in which variable local chord and wing geometric twist are incorporated.

Using the above aforementioned circulation distribution, Ehret and Oertel [19] utilised a three-dimensional Vortex Filament Method in order to visualise the wake behind a B747 for a wake length of $L_w = 600\,m$ discretised by 40 filaments at a vortex age of $t = 2.4\,s$. The result, obtained by utilisation of their integrated Biot-Savart law VFM is shown in the figure below:

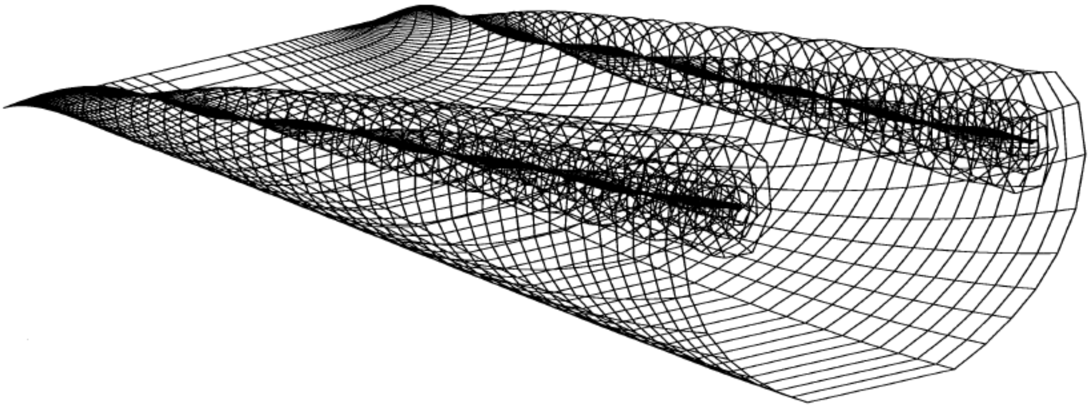

Figure 4.4 Three-Dimensional View of the Wake Vortex Structure of the B747 under Cruising Conditions [19].

As the above result provided by Ehret and Oertel [19] does not include numerical values, only a qualitative comparison can be undertaken with regards to the wake vortex structure. Utilising the programmed VFM and the above aforementioned input parameters of Ehret and Oertel [19], the above three dimensional view of the wake vortex structure of a B747 at cruise was replicated using a Burnham-Hallock induced velocity VFM regime which yielded the following result:

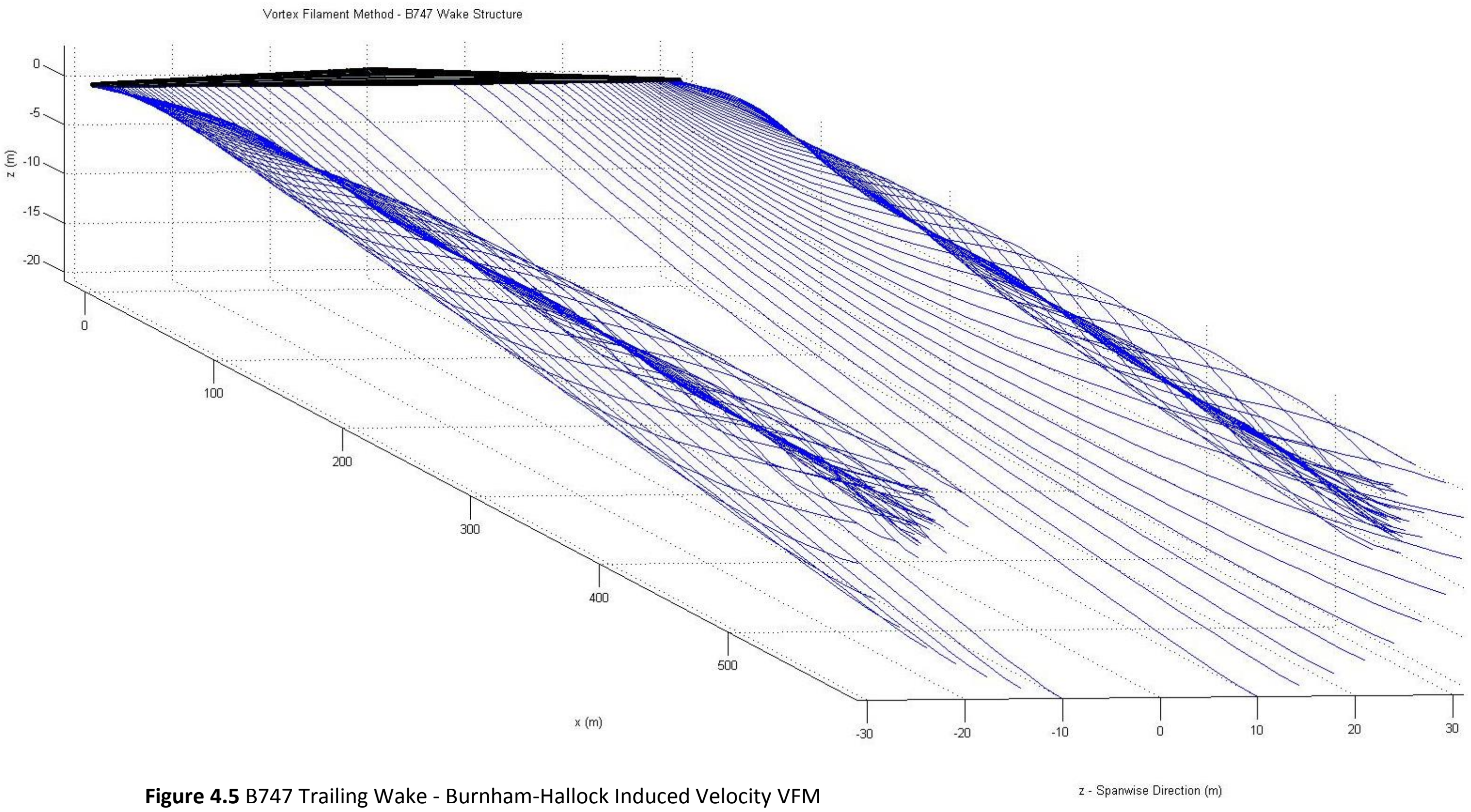

Figure 4.5 B747 Trailing Wake - Burnham-Hallock Induced Velocity VFM

By making use of their three-dimensional Vortex Filament Method, Ehret and Oertel [19] determined the vertical velocity profile (upwash and downwash velocity field) at an x-position of 750 m downstream of the wing. This wake length equates to a vortex age of t = 3 s and, thus, a time step number of ts = 50 for a differential time step of dt = 0.06 s. Their resulting vertical velocity field profile is shown in the following figure below:

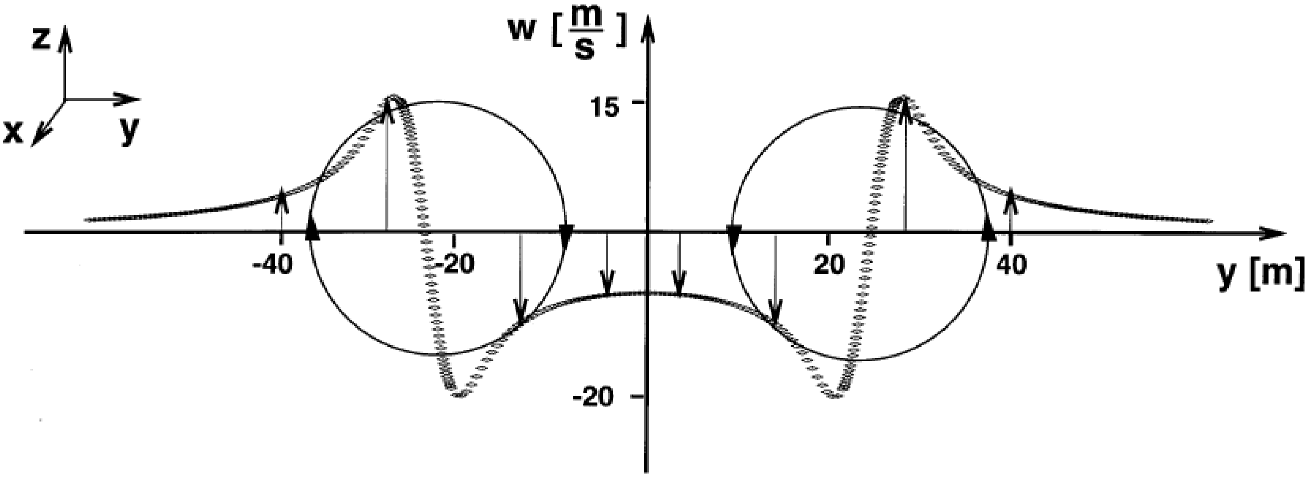

Figure 4.6 Vertical Velocity Field Profile of Cruising B747 Wake [19].

From the figure above it can be seen that the vertical velocity profile reaches a maximum value (upwash velocity) of $w_{max} = 16\,m/s$ and a minimum value (downwash velocity) of $w_{min} = -20\,m/s$. Furthermore, from the VFM results obtained by Ehret and Oertel [19] it is evident that the centres of the trailing vortex cores, where $w = 0\,m/s$, are located at vertical positions of $z = -6.2\,m$ relative to the aircraft wing located at $z = 0\,m$. From the vertical velocity profile above, it can be seen that the horizontal position of the vortex core centres, along the y-axis, is approximately 23.5 m from the centre of the wing and thus the distance between the centres is approximately 47 m or $\pi/4$ of the wingspan ($b = 60\,m$) [19].

Ehret and Oertel [19] validated their Biot-Savart VFM simulation by comparing the above results to the ground-based measurements of the wake vortex characteristics of a B747 aircraft conducted by Burnham et al [36]. These experimental results were obtained by flying a Boeing 747 aircraft at low level over a laser-Doppler velocimeter, an array of monostatic acoustic sounders, and an array of propeller anemometers in order to measure the vortex velocities of 54 passes of the aircraft [36]. Wake flow visualisation was also attained by use of smoke and balloon tracers [36]. The velocity field profile of the above experiment is shown in the figure below:

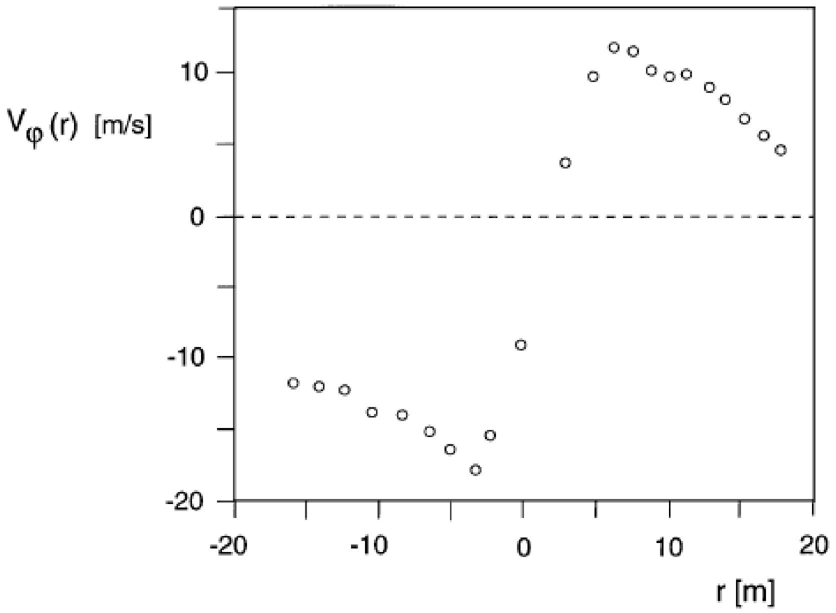

Figure 4.7 Measured Velocity Field Profile of B747 Wake [36].

Where $V_\varphi(r)$ denotes the tangential circumferential velocity and r denotes the radial distance from a trailing vortex centre where $V_\varphi(r = 0) = 0$.

The vertical velocity field profile generated as a result of utilising the above aforementioned flight conditions, presented in Table 4.1, within the constructed VFM Burnham-Hallock model is as follows:

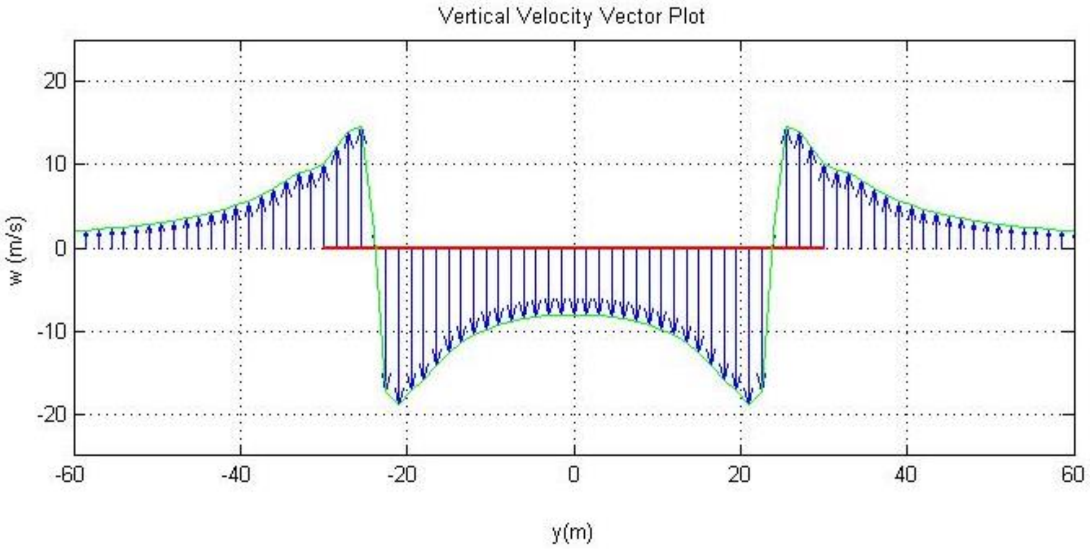

Figure 4.8 Burnham-Hallock VFM Vertical Velocity Profile.

From the figure above it can be seen that the vertical velocity profile reaches a maximum value (upwash velocity) of $w_{max} = 14.65\, m/s$ and a minimum value (downwash velocity) of $w_{min} = -18.94\, m/s$. By plotting this vertical velocity profile in conjunction with the numerically obtained vertical velocity profile of Ehret and Oertel [19] as well as the experimental results of Burnham et al.

[36], through use of the tabulated values presented in Appendix C, it can be seen from the figure below that the programmed Burnham-Hallock VFM results compare well with both approaches.

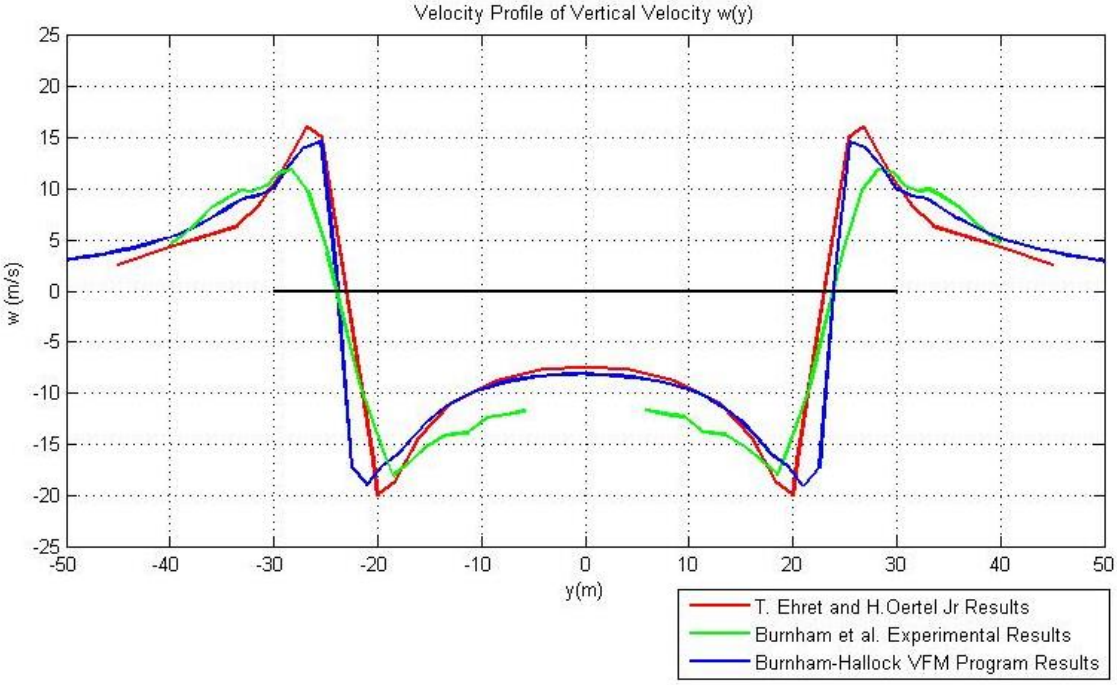

Figure 4.9 Numerical and Experimental Velocity Profile Comparison.

Moreover, a vertical profile of the wing wake, generated by use of the Burnham-Hallock VFM program, was taken at an x position of 750 m downstream of the aircraft in order to determine the location of the rolled-up trailing vortex cores. From this transverse vortex filament profile, shown in the figure below, it is evident that the centres of the vortex cores are located at a vertical position of approximately $z = -4.8\,m$, relative to the aircraft wing at $z = 0\,m$, and a spanwise position of $y = \mp 23.74\,m$. Thus, the horizontal distance between the centres is approximately 47.48 m and the vortex centre locations therefore compare well with the vortex centre locations obtained by the integrated Biot-Savart law VFM simulation conducted by Ehret and Oertel [19].

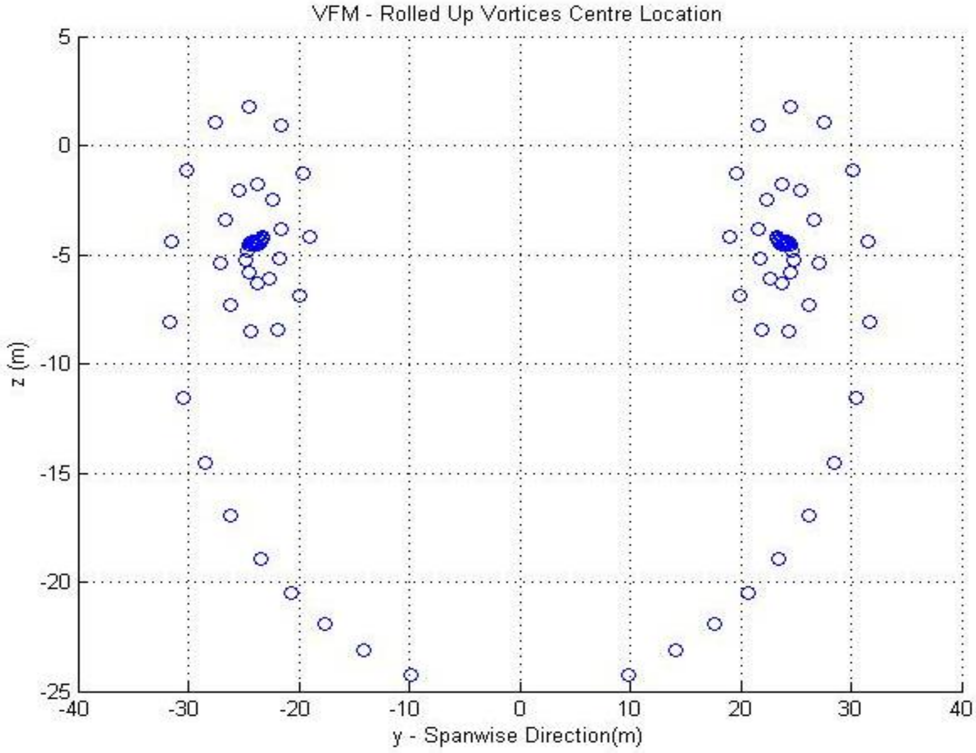

Figure 4.10 Trailing Wake Transverse Section at 750 m Downstream of Wing.

Lastly, it is to be noted that the programmed Burnham-Hallock VFM simulation reached a converged wake formation, as shown in the MRPE figure below. In contrast to Figure 4.1 & 4.2, the figure below reaches a converged numerical solution with a Mean Relative Percentage Error, between filament positions, of approximately 0%. This means that all filaments are orientated to accurately coincide with the velocity field they induce and will not deviate from their current positions with subsequent iterations of the numerical model. This converged wake formation is a consequence of utilising a finite filament core radius $r_c = 3\ m$, selected to coincide with the core radius utilised by Ehret and Oertel [19].

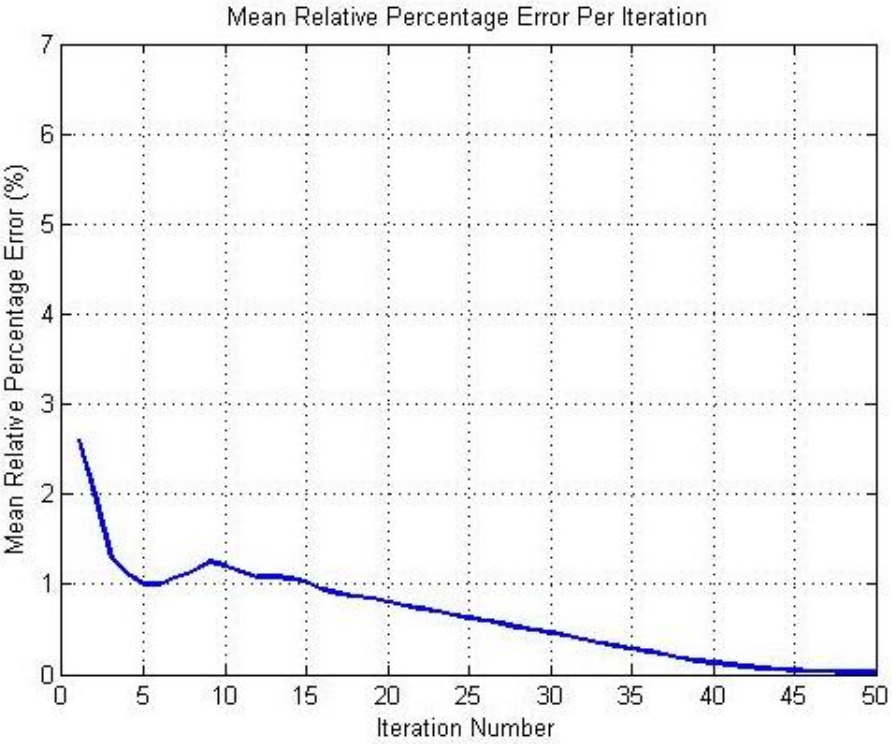

Figure 4.11 Convergence Plot.

Ehret and H.Oertel [19] defined the following relationship between the numerical parameters of the simulation in order to obtain numerical stability and convergence:

$$\frac{2r_cN_s}{L_w} > 0.4 \tag{4.3.10}$$

Where N_s is the number of filament segments and L_w is the length of the trailing wake. Utilising Equation 4.3.10 and the conditions of the B747 simulation above yields a minimum critical filament core radius of $r_c = 0.03\ m$. The reason Figure 4.1 & 4.2 do not reach a 0% MRPE convergence is due to the filament core radius being selected in accordance with Equation 4.3.10 above, which has been developed specifically for use in the integrated Biot-Savart law VFM of Ehret and Oertel [19] and not the utilised Burnham-Hallock VFM. Therefore a new relationship had to be developed in order to determine the critical ratio K_{Crit} (0.4 in Equation 4.3.10 above) above which the Burnham-Hallock VFM model reaches a stable and converged wake formation. Utilising the aforementioned B747 simulation parameters above and slowly decreasing the filament core radius from the utilised 3m, a minimum filament core radius of $r_c = 2.65\ m$ was observed to be the lowest possible core radius capable of achieving and maintaining numerical stability. Therefore Equation 4.3.10 can be expanded as follows to calculate the new value of K_{Crit} :

$$\frac{2r_cN_s}{L_w} > K_{Crit} \tag{4.3.11}$$

$$\frac{2(2.65)(2n_ft_s)}{(t_sV_\infty dt)} > K_{Crit}$$

$$K_{Crit} = \frac{2(2.65)(2(50))}{((250)(0.06))}$$

$$K_{Crit} = 35.\dot{3}$$

Therefore, the new modified convergence requirement equation, adapted for use by the Burnham-Hallock induced velocity VFM, is as follows:

$$\frac{2r_cN_s}{L_w} > 35.\dot{3} \tag{4.3.12}$$

As a result of the entire above positive validation process, the programmed VFM Burnham-Hallock (B-H) model was subsequently utilised to simulate turboprop aircraft wakes of a higher complexity.

4.2 The Effect of Turboprop Engine Trailing Wakes on the Wing Trailing Wake and Vertical Velocity Profile

In order to determine the degree to which the trailing helicoidal vortices, shed from turboprop engines, affect an aircraft's trailing wing wake, a variety of turboprop propelled aircraft were modelled for a variety of flight states. The influential factors that were investigated through these simulations were the number of turboprop engines, the number of blades per engine and the aircraft's wing loading.

The aircrafts selected for these simulations were the single turboprop engine, three-bladed Lancair Propjet; the double turboprop engine, six-bladed ATR 72; and the four engine, four-bladed Lockheed P-3 Orion. Table 4.3 below demonstrates the variety of turboprop propelled aircraft that can be modelled by the generated Burnham-Hallock VFM program as well as the spread of the selected aircrafts across the number of engines and blades that the program is capable of simulating. The aircrafts selected for the simulation are indicated by bold text within Table 4.3.

Table 4.4 below indicates the aircraft flight states in which each aircraft is modelled. The flight states vary from normal one g wing loading, such as during cruise conditions, to zero g wing loading with full propeller thrust, such as in vertical ascents in aerobatic formations. 'Full propeller thrust' denotes full engine power, and propeller RPM, at cruise and not the maximum power output the engine can achieve. For each aircraft in each flight state simulation, the VFM wake profile was generated. From this wake profile the vertical induced velocity field at 330 m downstream of the aircraft was obtained. According to the Autonomous Formation Flight project at NASA Dryden Flight Research Centre, which utilised two F/A-18 aircraft for formation flight experiments, downstream distances between the aircraft of 1.5 b to 6.6 b classify as close proximity formation flight [2, 3]. For extended formation flight, however, downstream distances greater than 10 span lengths are required according to Ning et al. [1, 4]. Therefore, in order to simulate extended formation flights, a downstream trailing wake distance of 330 m was selected as it equates to a downstream wingspan distance of 10.9 b for the Lockheed P-3 Orion, 12.4 b for the ATR 72 and 36.3 b for the Lancair Propjet.

Table 4.3: Aircraft Simulation Scope:

No. of Blades **No. of Engines**	**2**	**3**	**4**	**5**	**6**
1		• ***Lancair Propjet***	• Pilatus PC-12 • Epic E1000	• DAHER-SOCATA TBM 900	
2		• Diamond DA-42 • King Air 200	• Beechcraft C-12 Huron • Mitsubishi MU-2 • Transall C-160 • Dornier Do 228 • North American Rockwell OV-10 Bronco	• Let L-410 Turbolet • Let L-610	• Bombardier Q400 • EADS CASA C-295 • ***ATR 72*** • Saab 2000 • Ilyushin Il-114 • Alenia C-27J Spartan
4			• Lockheed AC-130H • ***Lockheed P-3 Orion*** • Ilyushin Il-38		• Lockheed Martin C-130J Super Hercules • Lockheed Martin KC-130

Table 4.4: Aircraft Flight States:

Wing Loading	**Engine Power (Engaged/Disengaged)**	**Flight State**
1 g	No propeller thrust	Aircraft preparing for a dive
1 g	Full propeller thrust	Normal Flight
0.75 g	No propeller thrust	
0.75 g	Full propeller thrust	
0.5 g	No propeller thrust	
0.5 g	Full propeller thrust	
0.25 g	No propeller thrust	
0.25 g	Full propeller thrust	
0 g	No propeller thrust	Stationary aircraft, no induced velocity
0 g	Full propeller thrust	Vertical ascent, relevant to aerobatic formations

4.2.1 Aircraft Simulation Input Parameters and Output Propeller and Wing Wake Data

The first aircraft simulated, for the flight conditions listed in Table 4.4 above, was the single turboprop engine aircraft, the Lancair Propjet. The specifications and dimensions of the Lancair Propjet, utilised within these simulations, is shown in Table 4.5 and Figure 4.12 below. Furthermore, 50 vortex filaments (25 per semi-span), were utilised in discretising the wing wake. Utilising Equation 4.3.12 above, the minimum vortex core radius required to achieve a converged wake formation is therefore 3.37 m. This is a greater core radius than the 3 m vortex core radius utilised in the B747 simulation even though the Lancair Propjet has a wingspan 1/6 of the B747. It is therefore evident that the equation to describe the conditions required for convergence of the VFM wake proposed by Ehret and Oertel [19], Equation 4.3.10 above, should take into account the wingspan of the aircraft. An aircraft with a smaller wingspan will have more closely spaced vortex filaments. A smaller vortex core radius should therefore be selected in order to accommodate the higher vortex filament density. A large vortex core radius results in adjacent filaments falling within one another's core radius location and, thus, the velocity they would induce on one another is greatly diminished. Selecting a vortex core radius in compliance with the vortex filament density (which is partly determined by the wingspan of the aircraft) will ensure the closely spaced adjacent filaments interact with one another to achieve a more 'realistic' representative rolled up wake formation.

Table 4.5: Lancair Propjet Specifications:

Specification:	
Empty Weight	1 045 kg [47]
Typical Pay Load	682 kg [47]
Net Weight	1 727 kg
Lift to Drag Ratio	14.2 [45]
Number of Turboprop Engines	1
Number of Blades per Engine	3
Cruise Speed	596 km/h [47]
Cruise Altitude	7 315 m [47]
Air Density at Altitude (ρ)	0.569 kg/m^3
Engine	Walter M601E-11 Turboprop Engine [50]
Maximum Propeller RPM	2080 rpm [51, 52, 53]
Propeller RPM at Cruise	1700 – 1900 rpm [51, 52]
Propeller Diameter (D)	1.981 m [48]
Wing Aspect Ratio (AR)	9.3 [54]
Mean Aerodynamic Chord (MAC)	0.99 m
Wing Chord at Root (c_r)	1.18 m [54]
Wing Chord at Tip (c_t)	0.77 m [54]

It is therefore proposed that a wingspan ratio factor, f_{WR}, be introduced into the modified Ehret and Oertel [19] convergence requirement equation, Equation 4.3.12, where:

$$f_{WR} = \frac{b_{sim}}{b_{B747}} \qquad (4.3.13)$$

In which b_{sim} is the wingspan of the aircraft to be simulated. Thus, the amended Equation 4.3.12 is as follows:

$$\frac{2r_cN_s}{L_w} f_{WR} > 35.\dot{3} \qquad (4.3.14)$$

Utilising Equation 4.3.14, the minimum vortex core radius which will ensure a stable and converged wake formation for the Lancair Propjet is 0.52 m. Therefore, a vortex core radius of 0.6 m (115% r_{c_MIN}) was selected in order to ensure stability and convergence of the numerical scheme.

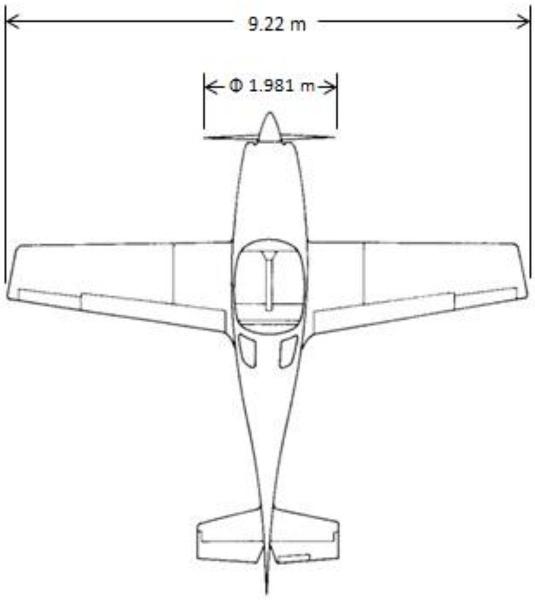

Figure 4.12 Lancair Propjet Dimensions (Adapted from [47, 48]).

As aforementioned, the Lifting Line Method and Propeller Wake Characteristics subroutines were utilised first in order to discretise the initial wake. The Lancair Propjet makes use of a single Walter M601E-11 Turboprop Engine rotating it's 1.981 m diameter three-bladed propeller at between 1700 and 1900 rpm during cruise to maintain a cruising speed of 596 km/h. Utilising these specifications and those presented in Table 4.5 above, the output parameters generated from the Propeller Wake Characteristics Model, outlined in Section 3.2, were utilised in generating the initial helicoidal vortex propeller wake. These aforementioned propeller output parameters are presented in Table 4.6 and 4.7 below.

Table 4.6: Lancair Propjet – Goldstein and Theodorsen Propeller Wake Output Results:

Helicoidal Wake Parameter Output:	
Axial Displacement Velocity of helicoidal vortex sheets (w)	27.68 m/s
Helicoidal Vortex Sheet Radius (R_1)	0.975 m
Difference between propeller radius and radius of vortex sheet ($R - R_1$)	0.016 m
Ratio of vortex sheet radius to propeller radius	0.984
Blade Tip Vortex Circulation (Γ_{tip})	2.129 m^2/s
Centreline Vortex Circulation (Γ_{centre})	-6.386 m^2/s

Table 4.6: Lancair Propjet – Goldstein and Theodorsen Propeller Wake Graphical Output Results:

α_i	**Helicoidal Vortex Sheet Induced Angle of Attack versus Dimensionless Radial Coordinate.** 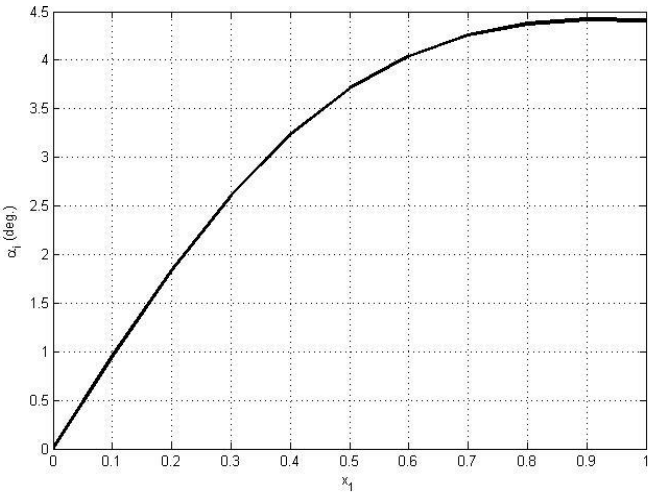 	ϕ	**Helicoidal Vortex Sheet Angular Pitch versus Dimensionless Radial Coordinate.** 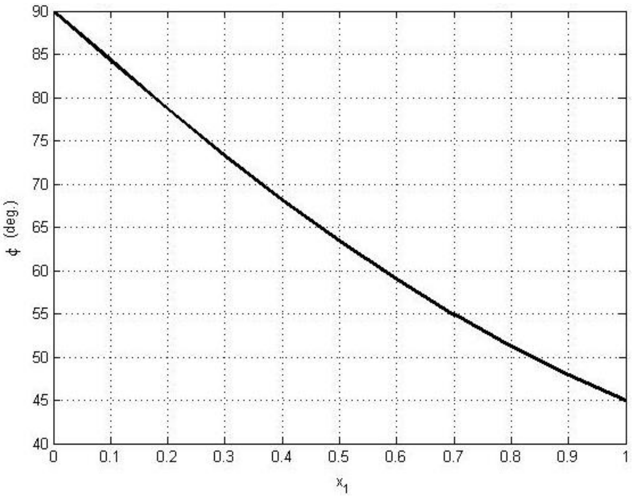
$u_{\theta 1}$	**Tangential Component of Convective Velocity versus Helicoidal Vortex Sheet Dimensionless Radial Coordinate.** 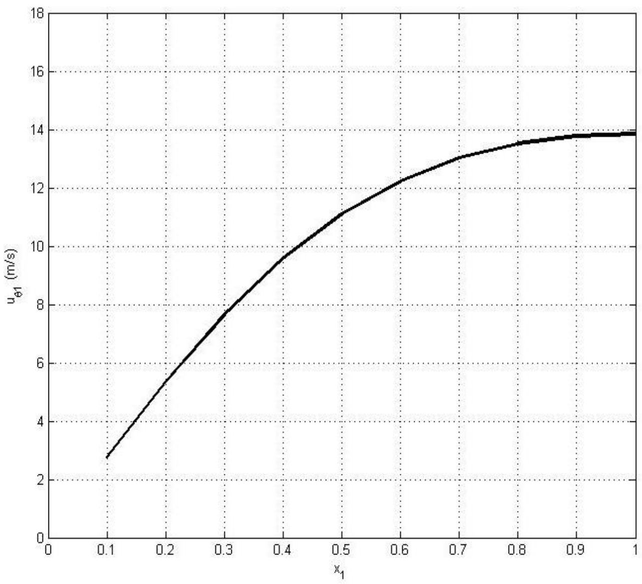 	u_{z1}	**Axial Component of Convective Velocity versus Helicoidal Vortex Sheet Dimensionless Radial Coordinate.** 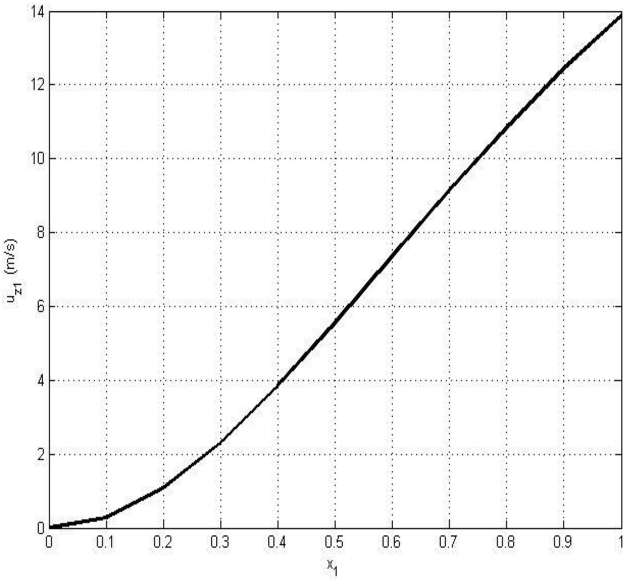

Utilising these propeller wake parameters, obtained via the use of the equations presented in Section 2.4.4, 'The Kinematics of Helicoidal Vortex Sheets', the kinematics and geometry of the initial helicoidal wake, depicted in the figure below, was established.

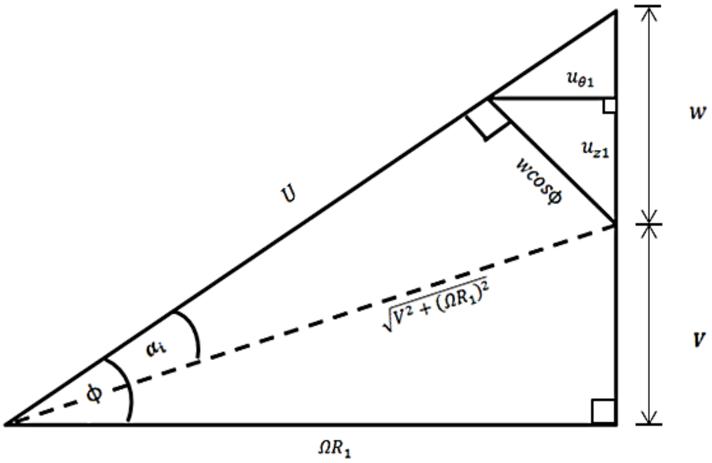

Figure 4.13 Kinematics and Geometry of the Helicoidal Vortex Sheet (Adapted from Wald [25]).

The result of the VFM model, for the Lancair Propjet, utilising all aforementioned subroutine data for a cruising wing loading of 1 g is shown in the figure below.

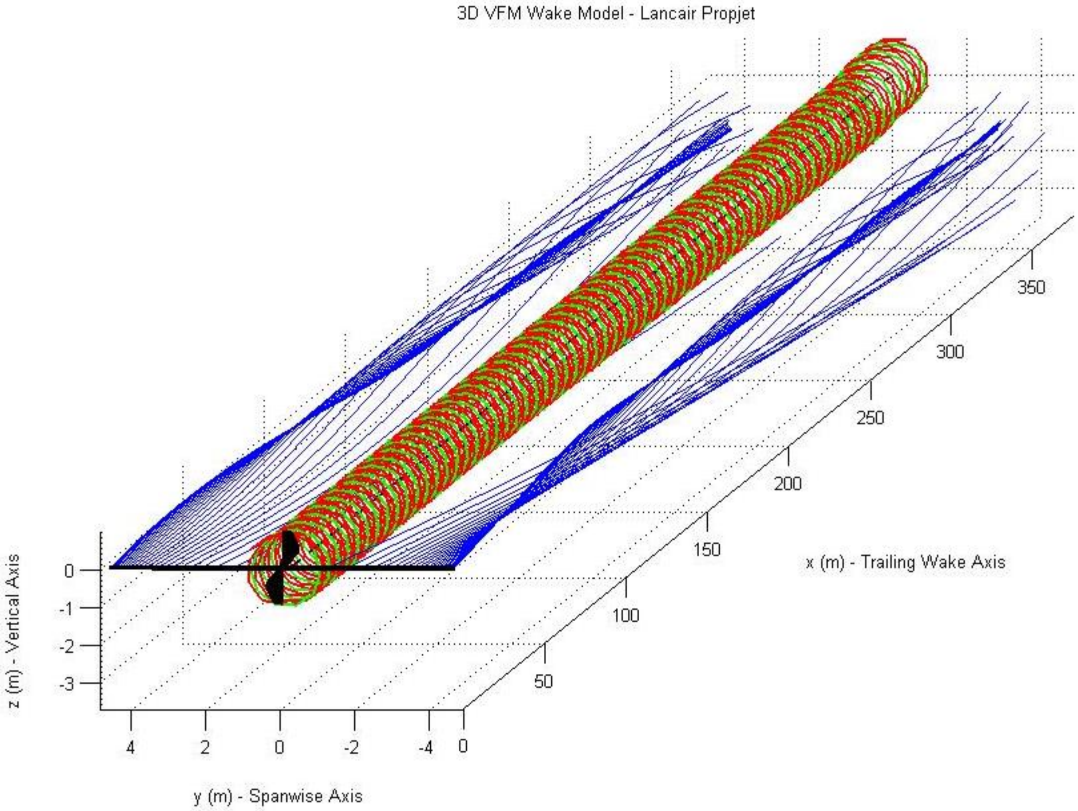

Figure 4.14 Vortex Filament Method 3D Model of Lancair Propjet Trailing Wake Formation – 1g Wing Loading.

The VFM model was utilised in order to simulate all flight states, presented in Table 4.4 above. The result of taking a transverse section of the induced velocity at 330 m downstream in the wake is shown in Table 4.7 below.

Table 4.7: Lancair Propjet Downwash Results:

Wing Loading	No Propeller Effects	Propeller-Wing Downwash Interaction
1g	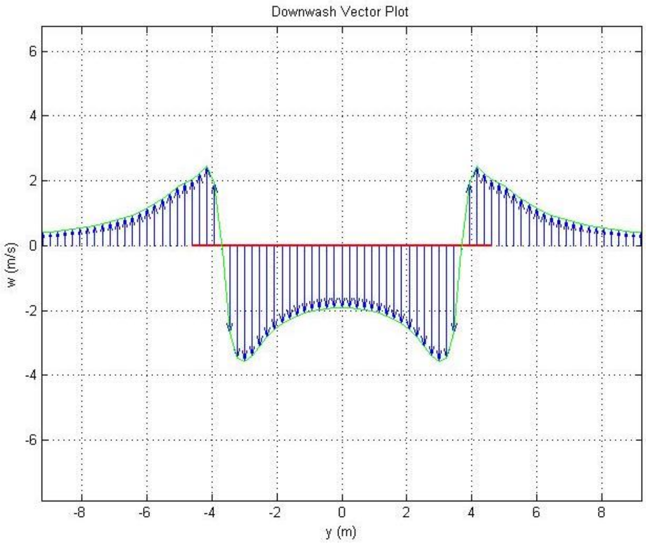	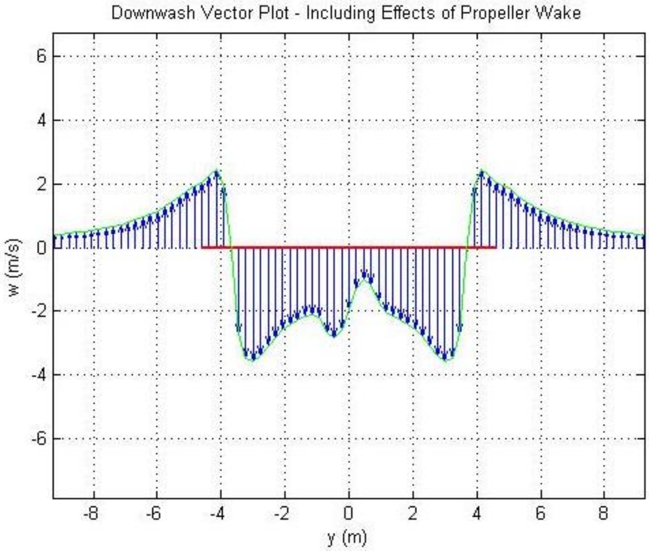
0.75g	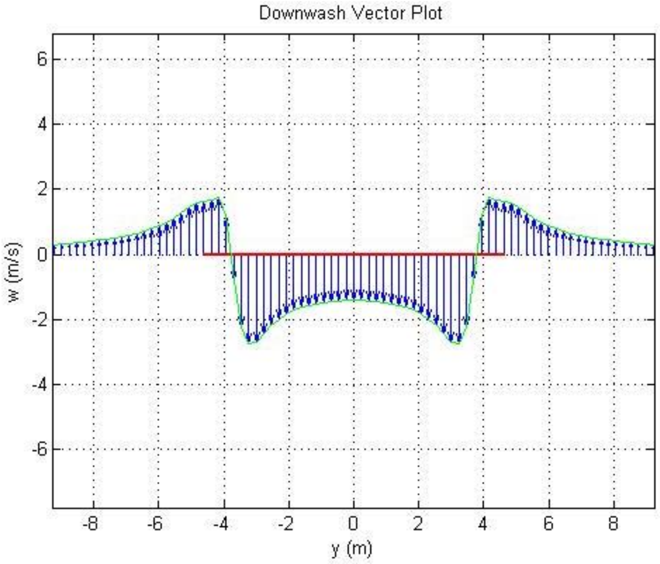	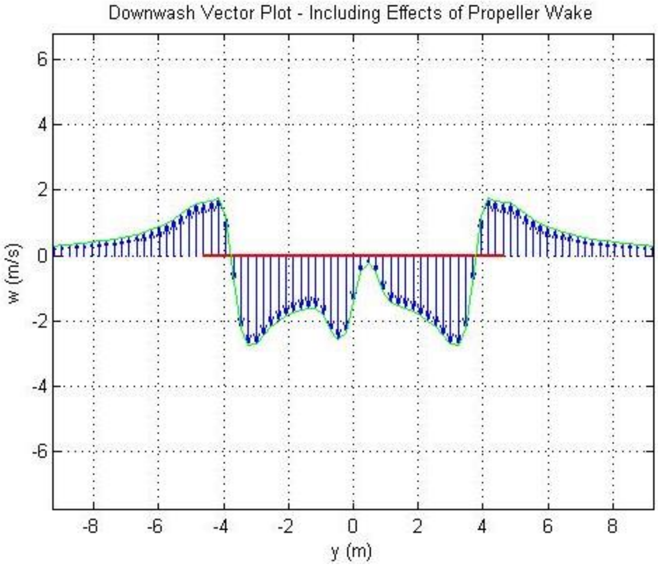

0.5g	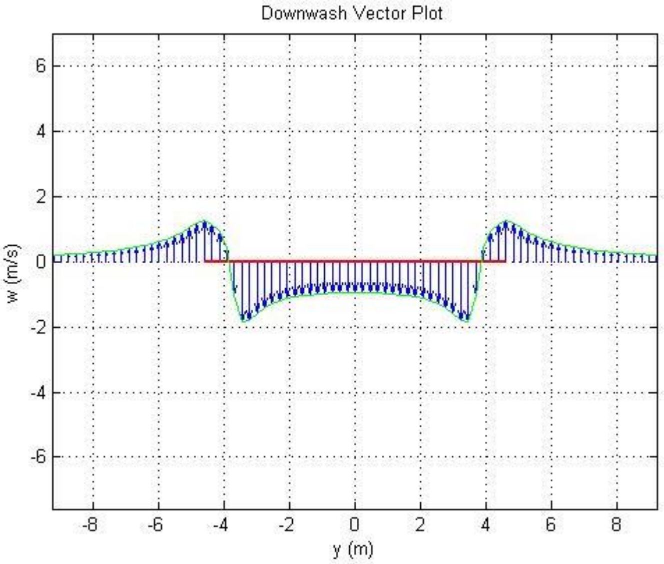Downwash Vector Plot w (m/s) y (m) 6 4 2 0 -2 -4 -6 -8 -6 -4 -2 0 2 4 6 8	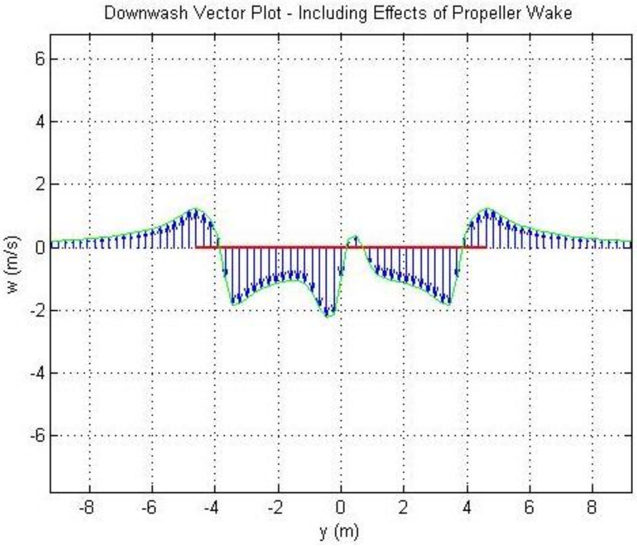Downwash Vector Plot - Including Effects of Propeller Wake w (m/s) y (m) 6 4 2 0 -2 -4 -6 -8 -6 -4 -2 0 2 4 6 8
0.25g	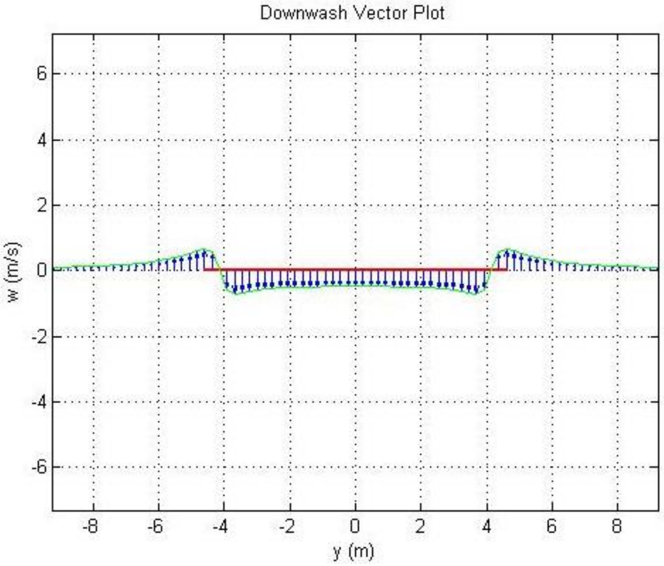Downwash Vector Plot w (m/s) y (m) 6 4 2 0 -2 -4 -6 -8 -6 -4 -2 0 2 4 6 8	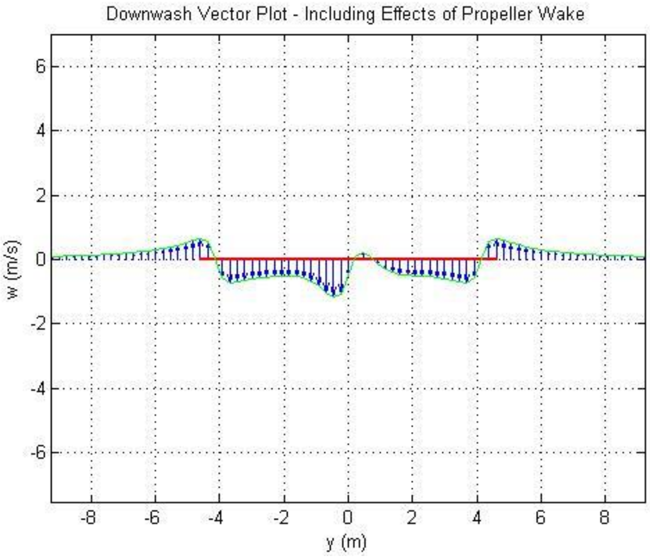Downwash Vector Plot - Including Effects of Propeller Wake w (m/s) y (m) 6 4 2 0 -2 -4 -6 -8 -6 -4 -2 0 2 4 6 8
0g		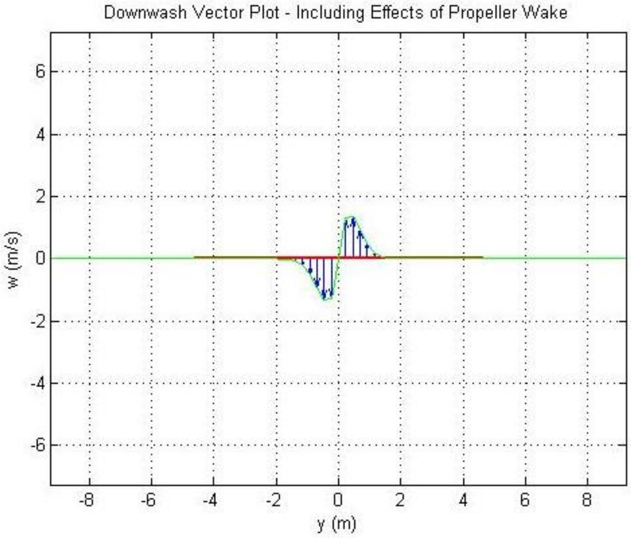Downwash Vector Plot - Including Effects of Propeller Wake w (m/s) y (m) 6 4 2 0 -2 -4 -6 -8 -6 -4 -2 0 2 4 6 8

Due to the turboprop engine being placed along the centreline of the aircraft, it can be seen from the above vertical induced velocity plots that the helicoidal vortex induced velocity only affects that region of the wake between approximately -0.33 b and 0.33 b in the spanwise domain (where b is the wingspan length of the aircraft). This region is characterised by a downwash (negative) velocity, and the helicoidal vortex induced velocity quite evidently disrupts this region causing a reduced downwash effect on the starboard wing between the aircraft centreline and approximately 0.1 b. Similarly, the port side wing experiences an increased downwash velocity between the aircraft centreline and approximately -0.1 b in the spanwise direction. The effects of the helicoidal vortices on the wing vertical velocity profile are verified by the downwash velocity profile for the 0 g wing loading flight state and full propeller thrust. Within this profile, the helicoidal vortices account for the entire induced velocity and result in a 1.3 m/s peak upwash and downwash respectively.

In addition to the velocity field generated directly by the helicoidal vortices, these vortices influence the 3D VFM wing wake vortex filaments and result in minor skewing of the vortex rollup transverse section in the starboard wing wake, as shown in Table D.1.1 of Appendix D. This influence of the helicoidal vortices results in the starboard wing's peak upwash velocity increasing marginally by an average of 0.003 m/s for all flight states.

It has been postulated that the helicoidal vortex induced velocity should become more pronounced with a decrease in wing loading, due to the decrease in wing induced downwash velocity. From the progression in Table 4.7 above, it can be seen however, that the effects of the helicoidal vortices do not have a greater effect on the downwash for both the 0.5 g and 0.25 g wing loading flight states. The reason for this reduced effect is due to the helicoidal vortices descending, under mutual induction, at a far slower rate than the rolled up wing vortices. For full propeller thrust the helicoidal vortices remain higher in the wake, descending to approximately -0.15 m in the vertical axis after a wake length of 330 m. The rolled up wing vortices descend to varying degrees with a variation in wing loading. This is due to the variable wing loading resulting in varying vortex filament strength. The position of the wing's rolled up vortex centres for all flight states are shown in Table D.1.1 of Appendix D. As the wing wake is the dominant wake, in magnitude and domain length, and the wake harnessed for extended formation flight, it forms the reference frame from which the ideal downwash position is obtained. Thus, the greater the distance between the centre location of the wing's rolled up vortices and the centre of the helicoidal vortices, the lower the effects of the propeller wake on the wing wake. However, in order to investigate the maximum effect the propeller wake is capable of imparting on the wing wake, a hypothetical 'worst case' scenario is derived in the subsequent section, Section 4.2.2, in which the vortex centres of the helicoidal vortex and the wing's rolled up vortices are aligned.

The second aircraft simulated, for the flight conditions listed in Table 4.4 above, was the two turboprop engine aircraft, the ATR 72. The specifications and dimensions of the ATR 72, utilised within these simulations, is shown in Table 4.8 and Figure 4.15 below. Utilising the modified convergence requirement equation, Equation 4.3.14, the minimum vortex core radius required to achieve a converged wake formation for the VFM model was calculated at 1.35 m. However, through experimental iteration a vortex core radius as low as 1.2 m (89% r_{c_MIN}) was selected for improved accuracy whilst still maintaining numerical stability of the model.

Table 4.8: ATR 72 Specifications:

Specification:	
Empty Weight	13 500 kg [44]
Typical Pay Load	7 500 kg [44]
Net Weight	21 000 kg [44]
Lift to Drag Ratio	17.143 [42, 43]
Number of Turboprop Engines	2
Number of Blades per Engine	6
Cruise Speed	509 km/h [44]
Cruise Altitude	7 620 m [44]
Air Density at Altitude (ρ)	0.5495 kg/m^3
Engine	Pratt & Whitney Canada PW127M [44]
Maximum Propeller RPM	1200 rpm [54,55]
Propeller RPM at Cruise	1008 - 1032 rpm (84% Np - 86% Np) [54]
Propeller Diameter (D)	3.93 m [44]
Propeller Rotation Direction	Clockwise for both engines [54]
Wing Aspect Ratio (AR)	12.01 [42, 56]
Mean Aerodynamic Chord (MAC)	2.25 m
Wing Chord at Root (c_r)	2.63 m [42]
Wing Chord at Tip (c_t)	1.59 m [56]

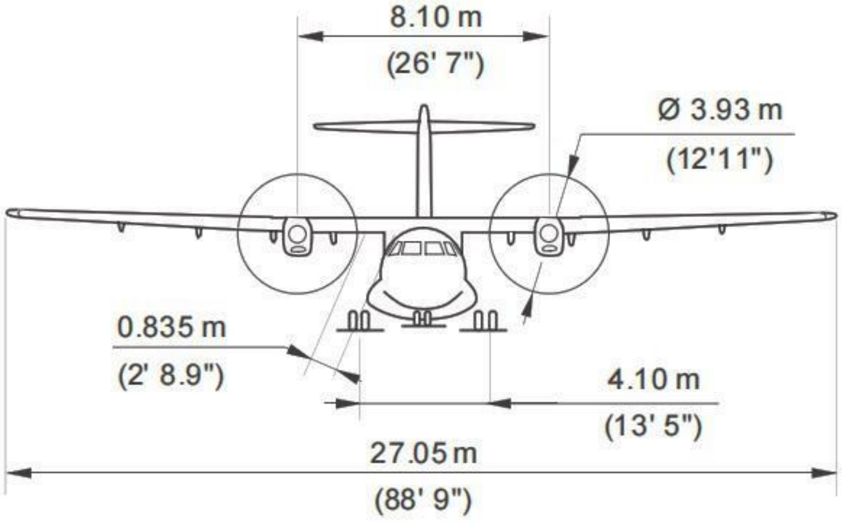

Figure 4.15 ATR 72 Dimensions [44].

The ATR 72 makes use of two Pratt & Whitney Canada PW127M turboprop engines which both rotate clockwise as viewed from the tailplane reference frame. These turboprop engines rotate the ATR 72's six-bladed, 3.93 m diameter, propellers at between 1008 and 1032 rpm during cruise to maintain a cruising speed of 509 km/h. Utilising these specifications and those presented in Table 4.8 above, the output parameters generated from the Propeller Wake Characteristics Model, outlined in Section 3.2, were utilised in generating the two initial helicoidal vortex propeller wakes. These aforementioned propeller output parameters are presented in Table 4.9 and 4.10 below.

Table 4.9: ATR 72 Propeller Output Specifications:

Outputs:	
Axial Displacement Velocity of helicoidal vortex sheets (w)	21.52 m/s
Helicoidal Vortex Sheet Radius (R_1)	1.932 m
Difference between propeller radius and radius of vortex sheet ($R - R_1$)	0.033 m
Ratio of vortex sheet radius to propeller radius	0.983
Blade Tip Vortex Circulation (Γ_{tip})	3.035 m^2/s
Centreline Vortex Circulation (Γ_{centre})	-18.209 m^2/s

Table 4.10: ATR 72 – Goldstein and Theodorsen Propeller Wake Graphical Output Results:

α_i	**Helicoidal Vortex Sheet Induced Angle of Attack versus Dimensionless Radial Coordinate.** 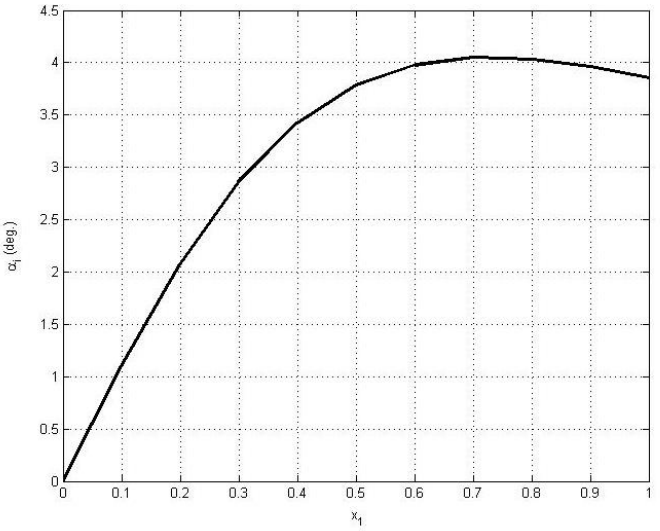	ϕ	**Helicoidal Vortex Sheet Angular Pitch versus Dimensionless Radial Coordinate.** 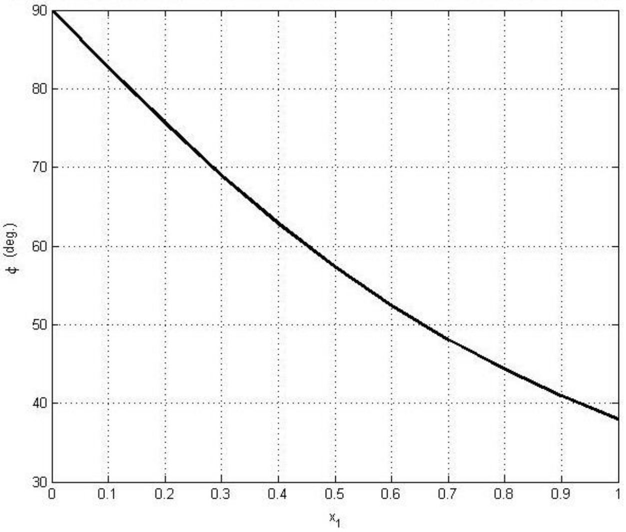
$u_{\theta 1}$	**Tangential Component of Convective Velocity versus Helicoidal Vortex Sheet Dimensionless Radial Coordinate.** 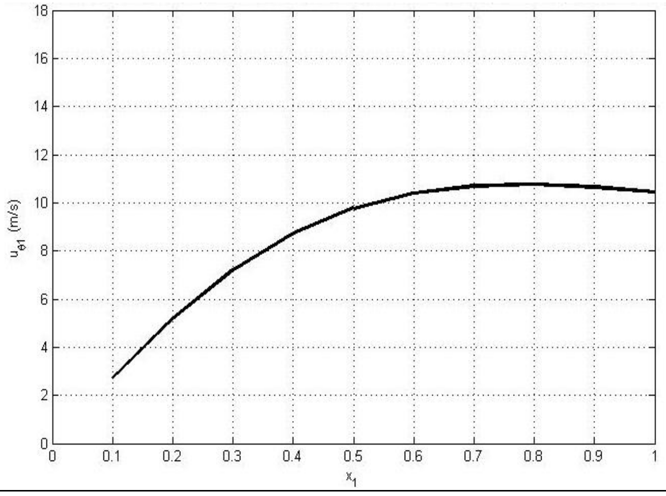	u_{z1}	**Axial Component of Convective Velocity versus Helicoidal Vortex Sheet Dimensionless Radial Coordinate.** 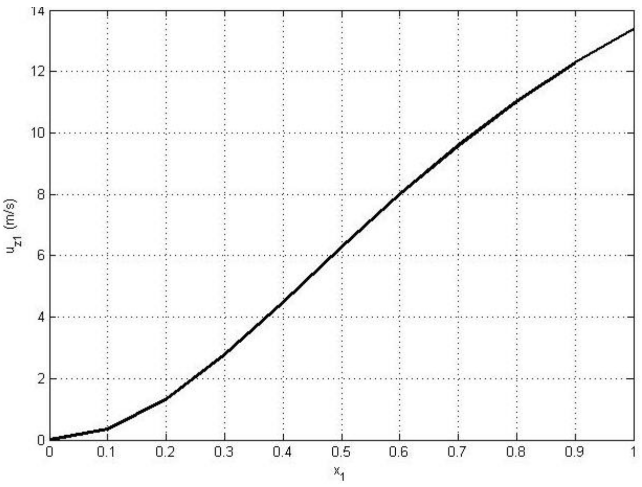

Utilising these propeller wake parameters, obtained via the use of the equations presented in Section 2.4.4, 'The Kinematics of Helicoidal Vortex Sheets', the kinematics and geometry of the initial helicoidal wake was established. The result of the VFM model, for the ATR 72, utilising all aforementioned subroutine data for a cruising wing loading of 1 g is shown in the figure below.

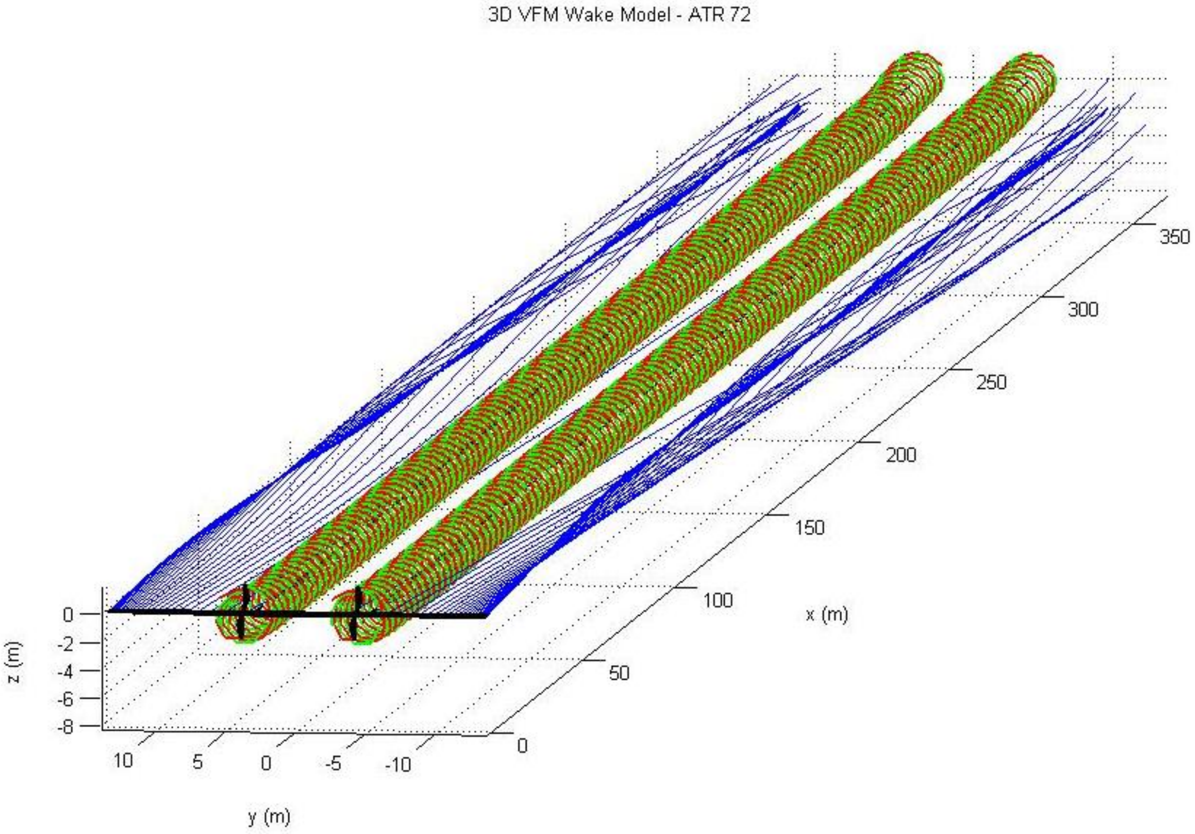

Figure 4.16 Vortex Filament Method 3D Model of ATR 72 Trailing Wake Formation.

In order to compare the effects of counter rotating propeller pairs with conventional unidirectional rotating propellers on twin-engine aircraft, a hypothetical model of the ATR 72 was generated in which the turboprop engines rotate in opposite directions. As with conventional counter rotating twin-engine aircraft, the propeller rotation direction for each turboprop engine within the hypothetical model was clockwise for the port side engine and counter-clockwise for the starboard engine, as viewed from a tailplane reference.

The 3D VFM model for said hypothetical ATR 72 is shown in Figure 4.17. The differences between the 3D VFM model for the conventional and counter rotating engine ATR 72 are seemingly subtle when viewing both Figure 4.16 and 4.17. However, both the downwash velocity profile and vortex roll up transverse section plots (shown in Table 4.11, Table 4.12, Table D.1.2 and Table D.1.3 respectively) display vast dissimilarities between unidirectional and counter-rotating turboprop configurations, the intricacies of which are discussed below.

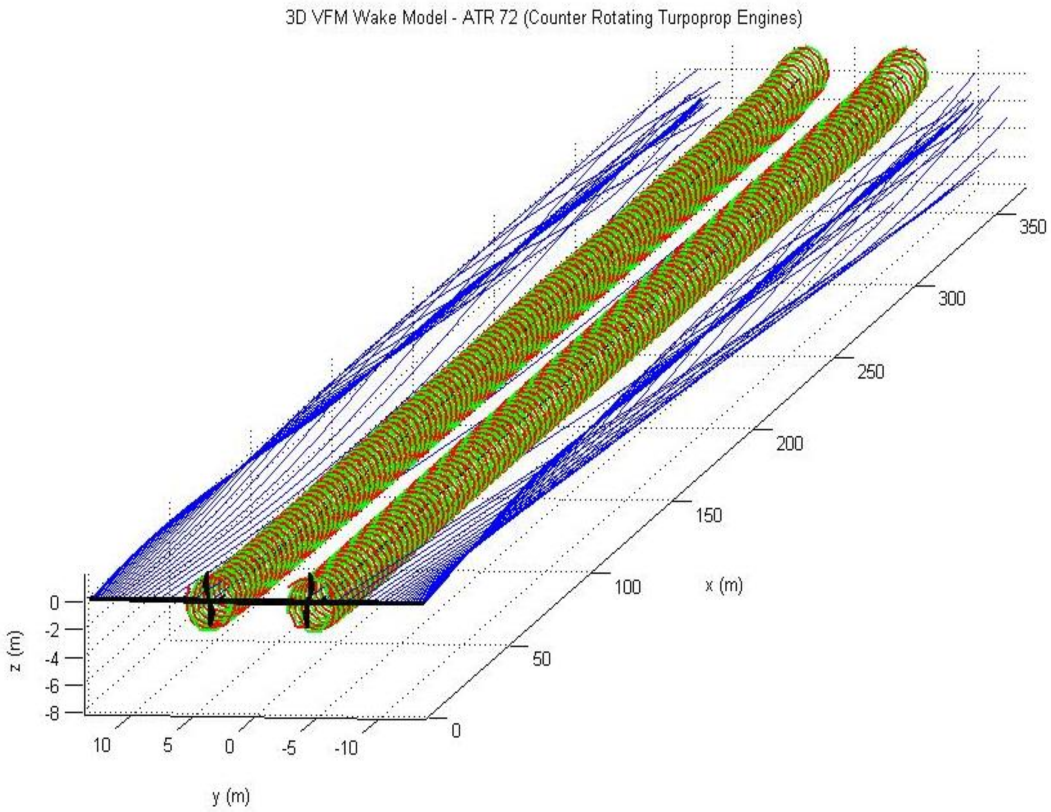

Figure 4.17 Vortex Filament Method 3D Model of ATR 72 (Counter Rotating Turboprop Engines) Trailing Wake Formation.

As aforementioned, the VFM B-H model was utilised in order to simulate all flight states, presented in Table 4.4 above, for both the conventional and hypothetical ATR 72. The result of taking a transverse section of the induced velocity at 12.4 span lengths (330 m) downstream in the respective wakes is shown in Table 4.11 and 4.12 below.

Table 4.11: ATR 72 (Conventional Unidirectional Rotation Turboprop Engines) Downwash Results:

Wing Loading:	No Propeller Effects	Propeller-Wing Downwash Interaction
1g	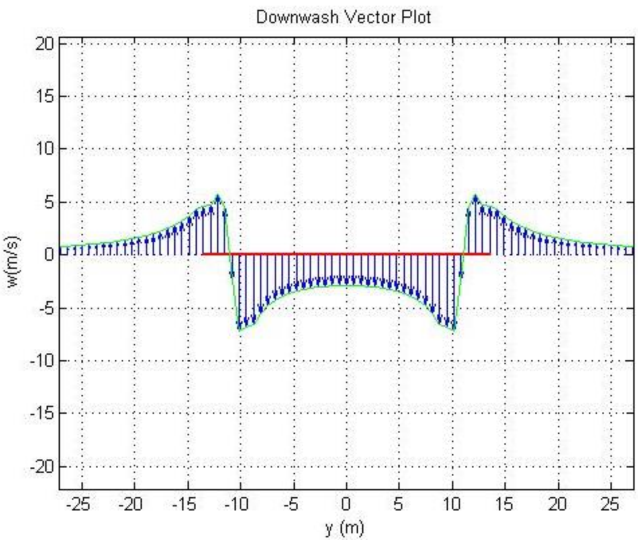	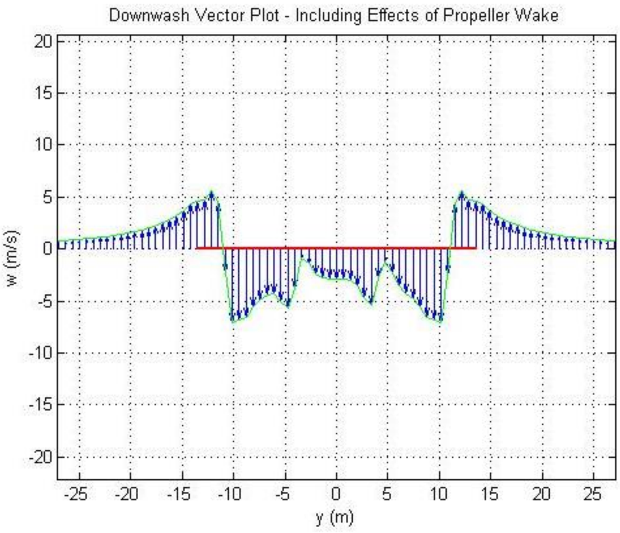

0.75g	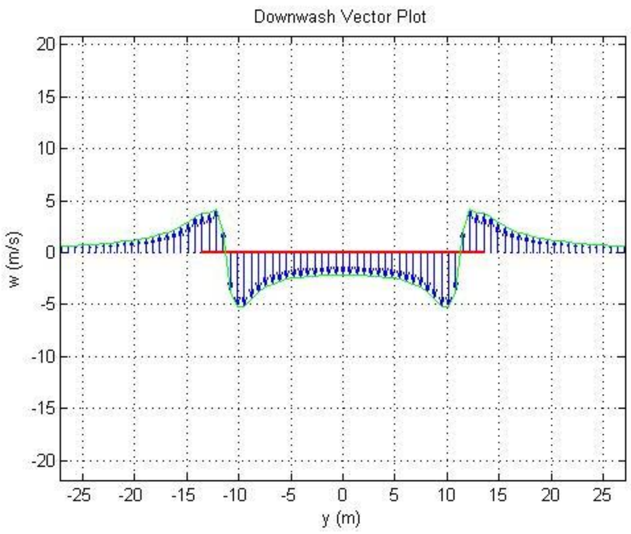 Downwash Vector Plot	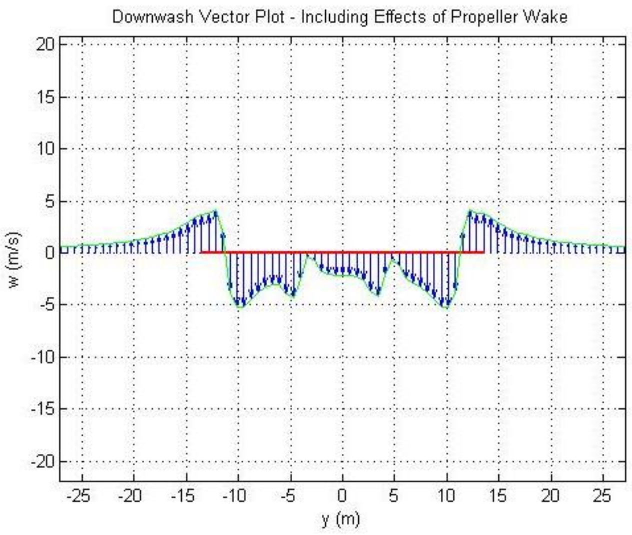 Downwash Vector Plot - Including Effects of Propeller Wake
0.5g	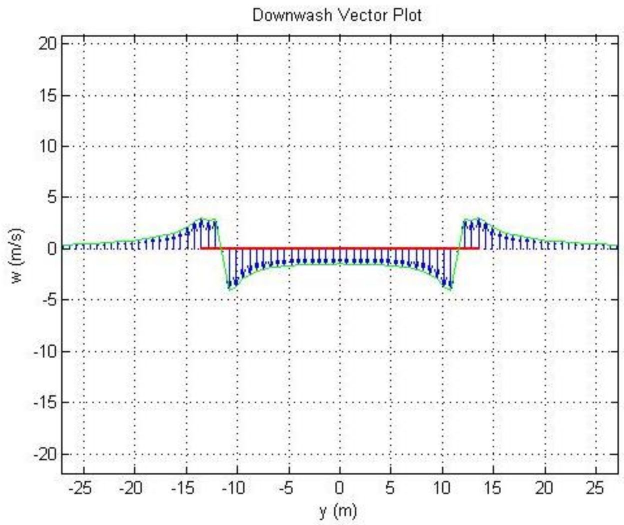 Downwash Vector Plot	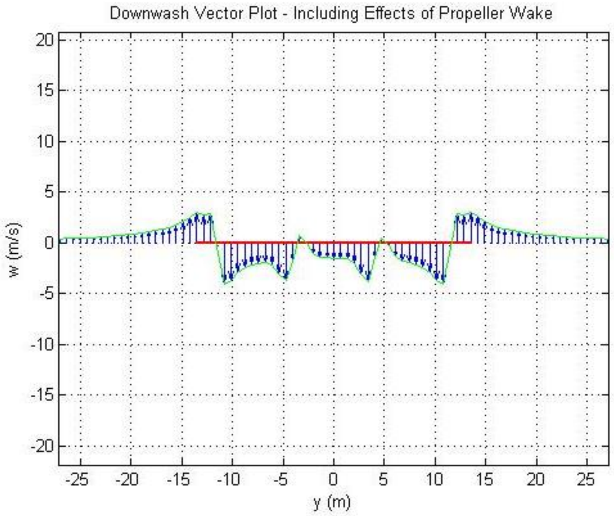 Downwash Vector Plot - Including Effects of Propeller Wake
0.25g	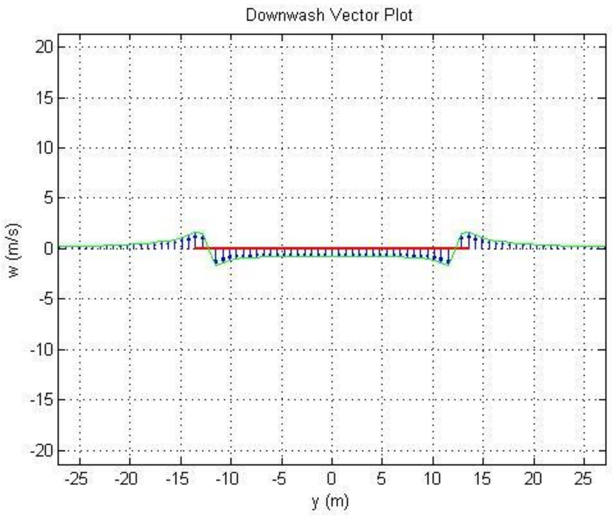 Downwash Vector Plot	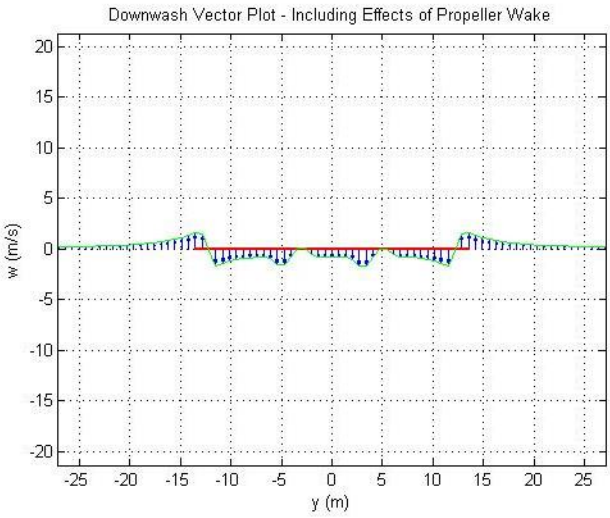 Downwash Vector Plot - Including Effects of Propeller Wake

0g		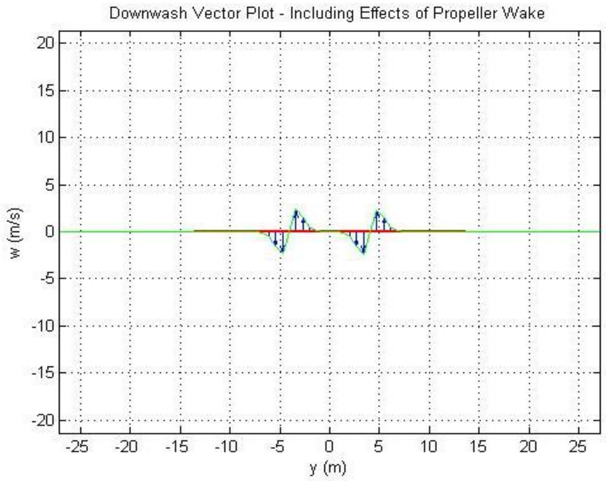

Table 4.12: ATR 72 (Counter Rotating Turboprop Engines) Downwash Results:

Wing Loading:	No Propeller Effects	Propeller-Wing Downwash Interaction
1g	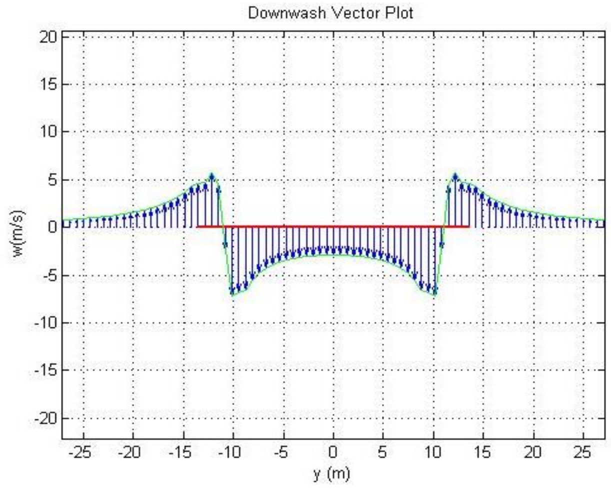	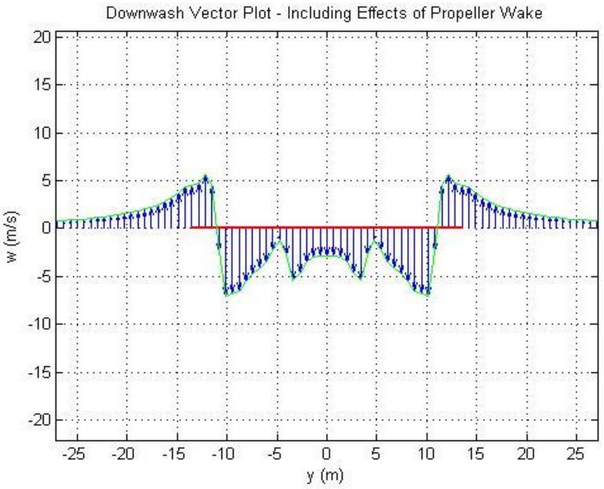
0.75g	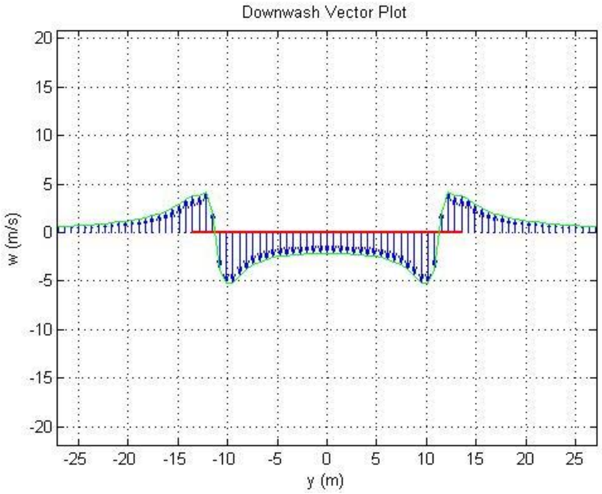	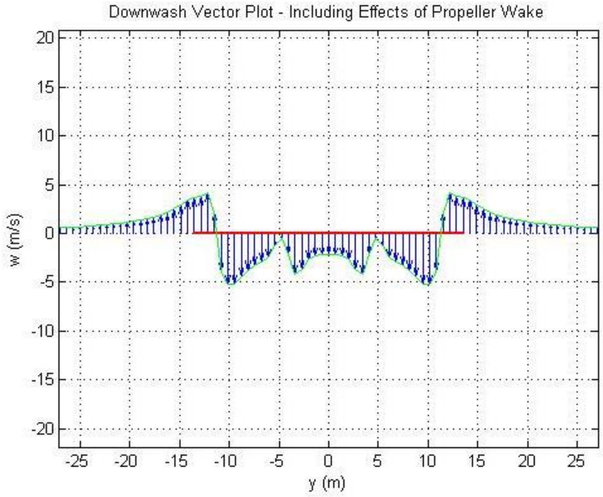

0.5g	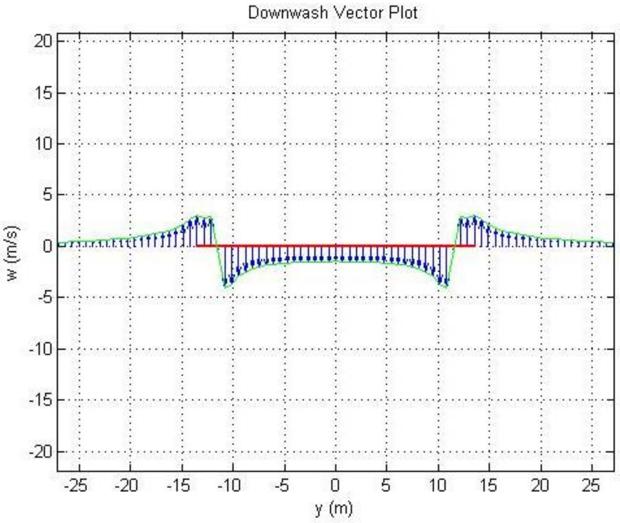Downwash Vector Plot w (m/s) y (m)	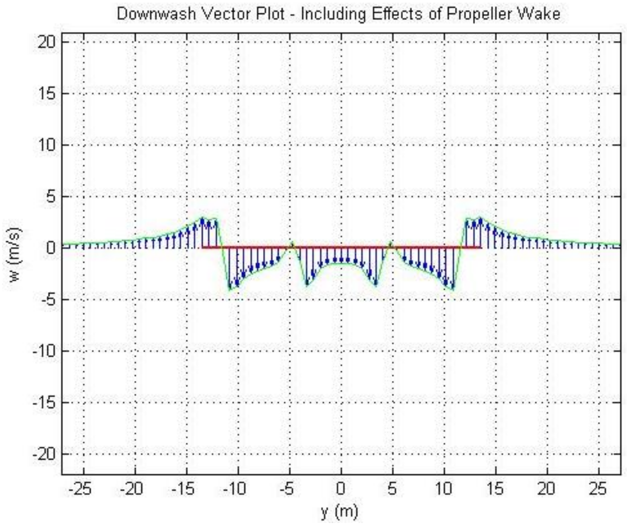Downwash Vector Plot - Including Effects of Propeller Wake w (m/s) y (m)
0.25g	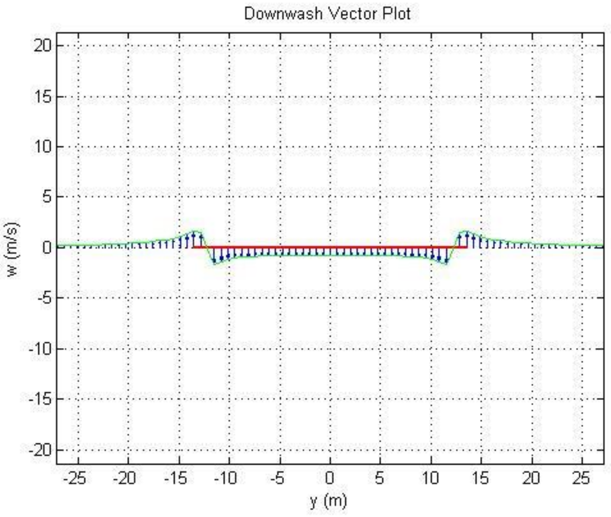Downwash Vector Plot w (m/s) y (m)	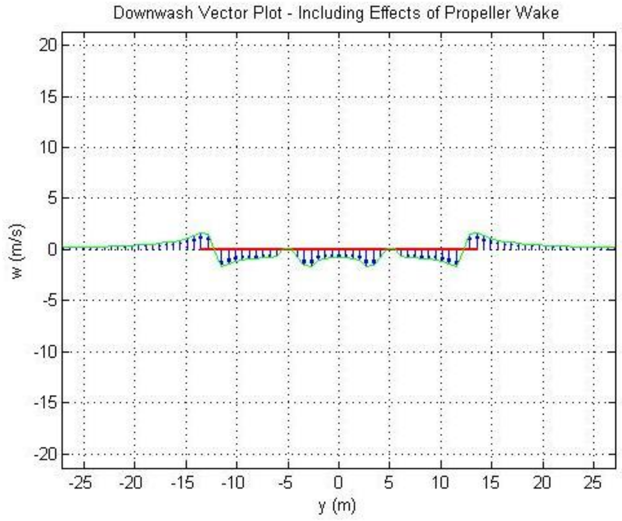Downwash Vector Plot - Including Effects of Propeller Wake w (m/s) y (m)
0g		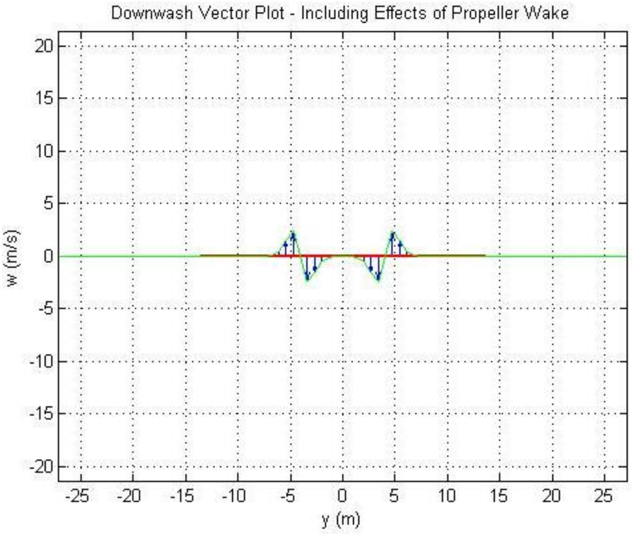Downwash Vector Plot - Including Effects of Propeller Wake w (m/s) y (m)

Due to the centreline of the two Pratt & Whitney Canada PW127M turboprop engines being located at ±0.15 *b* (±4.05 m) from the longitudinal centreline of the aircraft, as shown in Figure 4.15, it can be seen from the above vertical induced velocity plots, for both the conventional and counter rotating turboprop configurations, that the helicoidal vortex induced velocity only affects that region of the wake between approximately -0.37 *b* and 0.37 *b* in the spanwise domain. This region is characterised by a downwash (negative) velocity, and the helicoidal vortex induced velocity quite evidently disrupts this region causing a reduced downwash effect in the surrounding region of -0.125 *b* and 0.175 *b* for the conventional ATR 72 model. Similarly, the hypothetical (counter rotating turboprop configuration) ATR 72 experiences a reduced downwash velocity in the surrounding region of ±0.175 *b* in the spanwise domain. As the wing loading is decreased to 0.5 g and 0.25 g, these aforementioned locations of minimum downwash result in localised upwash regions between the wing wake dominant upwash peaks, for both turboprop configurations. The effects the helicoidal vortices are capable of imparting, at full propeller thrust, on the wing vertical velocity profile are most evident when viewing the downwash velocity profiles for the 0 g wing loading flight state and full propeller thrust. Within this profile, the helicoidal vortices account for the entire induced velocity and result in a ±2.35 m/s peak upwash and downwash respectively for both ATR 72 engine configurations.

Furthermore, from the comparison of both downwash velocity plots for the two ATR 72 versions, it is evident that the conventional ATR 72 has an asymmetrical induced velocity field, about the aircraft longitudinal centreline, whereas the hypothetical ATR 72 has a symmetrical induced velocity field mirrored about the aircraft centreline. This is, however, to be expected as the counter rotating turboprop engines will generate counter rotating, mirrored, helicoidal vortex sheets. These vortex sheets will in turn induce downwash velocity fields on each semi-span that are seemingly reflected about the aircrafts longitudinal axis.

In addition to the velocity field generated directly by the helicoidal vortices, these vortices influence the 3D VFM wing wake vortex filaments and, in the case of the conventional ATR 72, result in minor skewing of the vortex rollup transverse section in the starboard wing wake, as shown in Table D.1.2 of Appendix D. This influence of the helicoidal vortices results in the starboard wing's peak upwash velocity increasing marginally by an average of 0.01 m/s for all flight states. In the case of the counter rotating turboprop configured ATR 72, the influence of the helicoidal vortices results in a symmetrical influence on the wing wake, as shown in Table D.1.3 of Appendix D, which in turn marginally decreases the wing wake peak upwash velocity by an average of 0.002 m/s for all flight states.

Similar to the downwash velocity plots of the Lancair Propjet, the effects of the ATR 72's helicoidal vortices do not have a more pronounced influence on the wing wake downwash as the wing loading is reduced, as shown in Table 4.11 and 4.12 above. Once again, the reason for this reduced effect is due to the helicoidal vortices descending, under mutual induction, at a far slower rate than the rolled up wing vortices. For 1 g wing loading and full propeller thrust the helicoidal vortices remain higher in the wake, resulting in a vertical difference of approximately 0.16 m between the wing's rolled up vortex centres and the centreline of the helicoidal vortex sheets after a wake length of 330 m for both ATR 72 configurations. The position of the wing's rolled up vortex centres for all flight states are shown in Table D.1.2 and D.1.3 of Appendix D for the conventional and hypothetical ATR 72 variations respectively. In order to investigate the maximum effect the propeller wake is capable of imparting on the wing wake, a hypothetical ‘worst case’ scenario is derived in the subsequent section, Section 4.2.2, in which the vortex centres of the helicoidal vortices and the wing’s rolled up vortices are aligned for both variations of the ATR 72.

The final aircraft simulated, for the flight conditions listed in Table 4.4 above, was the four turboprop engine aircraft, the Lockheed Martin P-3 Orion. The specifications and dimensions of the P-3 Orion, utilised within these simulations, is shown in Table 4.13 and Figure 4.18 below. Once again, utilising the modified convergence requirement equation, Equation 4.3.14, the minimum vortex core radius required to achieve a converged wake formation for the VFM model was calculated at 1.74 m. However, similar to the ATR 72, experimental iteration reduced the vortex core radius to 1.5 m (86% r_{c_MIN}), improving accuracy of the model whilst still ensuring a converged wake formation. From the vortex core radius selection for all three simulated aircraft, it is evident that the modified convergence requirement equation, Equation 4.3.14, can further be refined by recalculation of the critical convergence factor, K_{Crit} . The result of which, is the final form of the convergence requirement equation adapted for use by the Burnham-Hallock induced velocity VFM, presented below:

$$\frac{2r_c N_s}{L_w} f_{WR} > 30 \tag{4.3.15}$$

Table 4.13: Lockheed P-3 Orion Specifications:

Specification:	
Empty Weight	35 000 kg [40]
Typical Pay Load	26 400 kg [40]
Net Weight	61 400 kg [40]
Lift to Drag Ratio	12.5 [38, 39]
Number of Turboprop Engines	4
Number of Blades per Engine	4
Cruise Speed	607.5 km/h [46]
Cruise Altitude	8 625 m [46]
Air Density at Altitude (ρ)	0.488 kg/m^3
Engine	Allison T-56-A-14 [46]
Maximum Propeller RPM	1173 rpm (115% of cruise rpm) [59]
Propeller RPM at Cruise	1020 rpm (Engine 13820 rpm, Reduction Gear 13.54:1) [57, 58, 59]
Propeller Diameter (D)	4.115 m [41]
Propeller Rotation Direction	Clockwise for all engines [61,62]
Wing Aspect Ratio (AR)	7.5 [60]
Mean Aerodynamic Chord (MAC)	4.05 m
Wing Chord at Root (c_r)	5.77 m [61]
Wing Chord at Tip (c_t)	2.31 m [61]

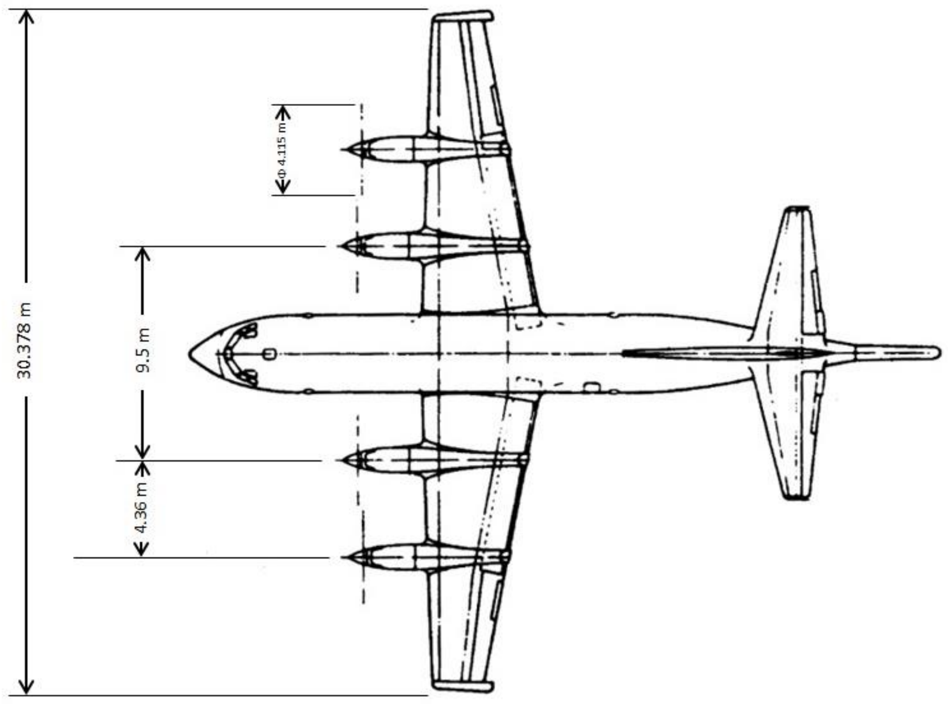

Figure 4.18 Lockheed P-3 Orion Dimensions (Adapted from [41]).

The P-3 Orion makes use of four Allison T-56-A-14 turboprop engines which all rotate clockwise as viewed from the tailplane reference frame. These turboprop engines rotate the P-3 Orion's four-bladed, 4.115 m diameter, propellers at 1020 rpm during cruise to maintain a cruising speed of 607.5 km/h. Utilising these specifications and those presented in Table 4.8 above, the output parameters generated from the Propeller Wake Characteristics Model, outlined in Section 3.2, were utilised in generating the four initial helicoidal vortex propeller wakes. These aforementioned propeller output parameters are presented in Table 4.14 and 4.15 below.

Table 4.14: P-3 Orion Propeller Output Specifications:

Outputs:	
Axial Displacement Velocity of helicoidal vortex sheets (w)	59.73 m/s
Helicoidal Vortex Sheet Radius (R_1)	2.031 m
Difference between propeller radius and radius of vortex sheet ($R - R_1$)	0.026 m
Ratio of vortex sheet radius to propeller radius	0.987
Blade Tip Vortex Circulation (Γ_{tip})	8.844 m^2/s
Centreline Vortex Circulation (Γ_{centre})	-35.376 m^2/s

Table 4.15: P-3 Orion – Goldstein and Theodorsen Propeller Wake Graphical Output Results:

α_i	**Helicoidal Vortex Sheet Induced Angle of Attack versus Dimensionless Radial Coordinate.** 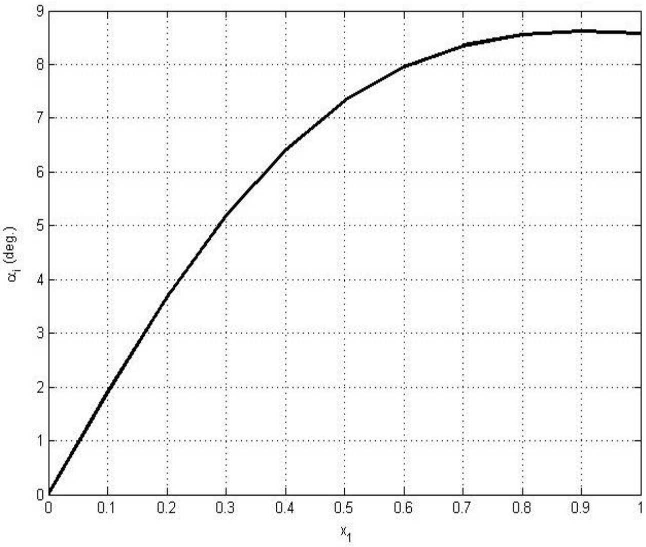 	ϕ	**Helicoidal Vortex Sheet Angular Pitch versus Dimensionless Radial Coordinate.** 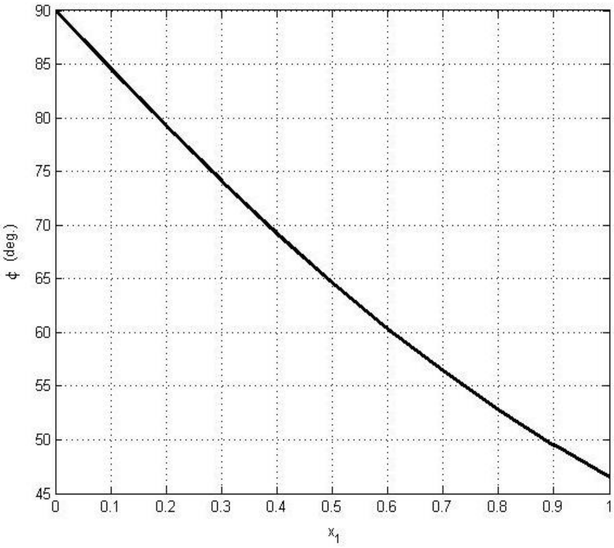
$u_{\theta 1}$	**Tangential Component of Convective Velocity versus Helicoidal Vortex Sheet Dimensionless Radial Coordinate.** 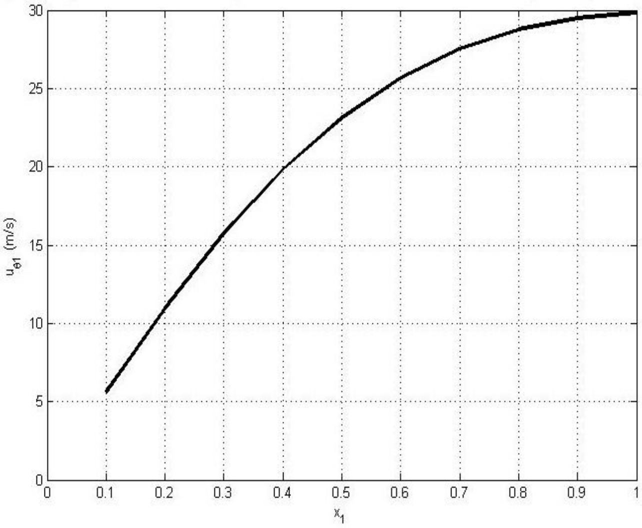 	u_{z1}	**Axial Component of Convective Velocity versus Helicoidal Vortex Sheet Dimensionless Radial Coordinate.** 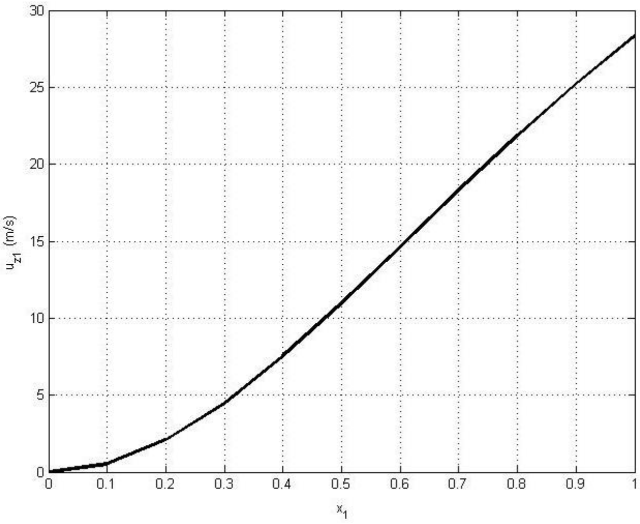

Comparing the propeller output results of the ATR 72 and P-3 Orion, it is evident that the axial displacement velocity of the helicoidal vortex sheets, w, is far greater for each of the 4 turboprop engines of the P-3 Orion than the ATR 72. Both the ATR 72 and P-3 Orion have similar propeller diameters, 3.93 m and 4.115 m respectively, and similar turboprop engine rpm at cruise, with the ATR 72 having a slightly higher rpm of 1032 rpm versus the P-3 Orion's 1020 rpm. It is therefore evident that the parameter which results in this increased helicoidal vortex sheet axial displacement velocity is the increased thrust of the turboprop engines. At cruise, the P-3 Orion's Allison T-56-A-14 turboprop engines produce double the thrust of the ATR 72's Pratt & Whitney Canada PW127M turboprop engines and, thus, result in a trivially higher cruise velocity as well as a higher helicoidal vortex sheet axial displacement velocity of 59.73 m/s versus the ATR 72's 21.52 m/s. This, however, is to be expected, as the helicoidal vortex sheet axial displacement velocity, w, is directly proportional to the free stream velocity and square root of the turboprop engine thrust, as shown in Equation 2.4.30 of Section 2.4.6.

Interestingly, the range for the ratio of vortex sheet radius to propeller radius (R_1/R) for all three aircrafts is surprisingly low, with the Lancair Propjet, ATR 72 and P-3 Orion propellers producing helicoidal vortex sheets with radii of 0.984, 0.983 and 0.987 of their propeller radii respectively. In quick approximate calculations, selecting a ratio of vortex sheet radius to propeller radius of 0.985 would, therefore, not only greatly reduce computational time but would yield fairly accurate helicoidal vortex sheet kinematics parameters, which are dependent on the determination of the helicoidal vortex sheet radius.

Lastly, the kinematic and geometric relationships presented by Wald [25], shown in Figure 4.13, are fortified by comparing the propeller output results of all three aircraft. It is evident that an increase in the helicoidal vortex sheet axial displacement velocity, w, and an increase in propeller rotational speed, results in an increase in the axial component of the helicoidal vortex sheet's convective velocity. Additionally, an increase in propeller rotational speed will also result in an increase in the tangential component of the helicoidal vortex sheet's convective velocity.

Utilising the propeller wake parameters for the P-3 Orion, obtained once again via the use of the equations presented in Section 2.4.4, 'The Kinematics of Helicoidal Vortex Sheets', the kinematics and geometry of the initial helicoidal wake was established. The result of the VFM model, for the Lockheed Martin P-3 Orion, utilising all aforementioned subroutine data for a cruising wing loading of 1 g is shown in the figure below.

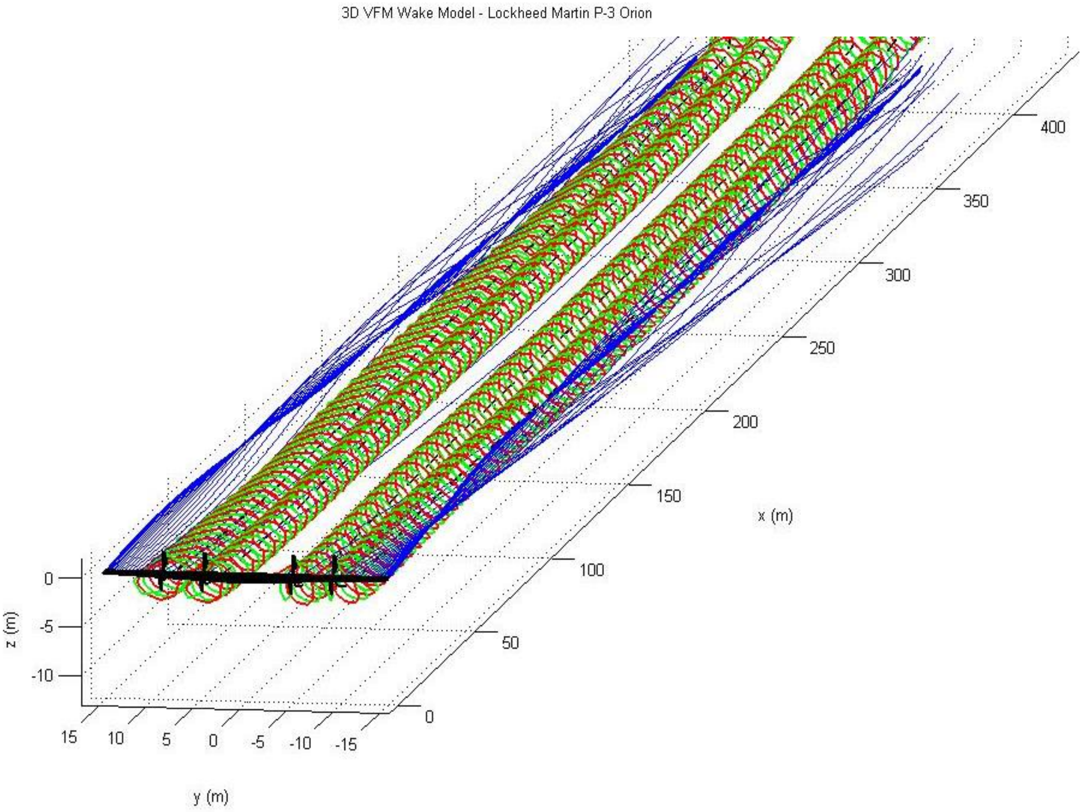

Figure 4.19 Vortex Filament Method 3D Model of Lockheed P-3 Orion Trailing Wake Formation.

As aforementioned, the VFM model was utilised in order to simulate all flight states, presented in Table 4.4 above, for the Lockheed Martin P-3 Orion. The result of taking a transverse section of the induced velocity at 10.9 span lengths (330 m) downstream in the respective wakes of each flight state is shown in Table 4.16 below.

Table 4.16: Lockheed Martin P-3 Orion Downwash Results:

Wing Loading:	No Propeller Effects	Propeller-Wing Downwash Interaction
1g	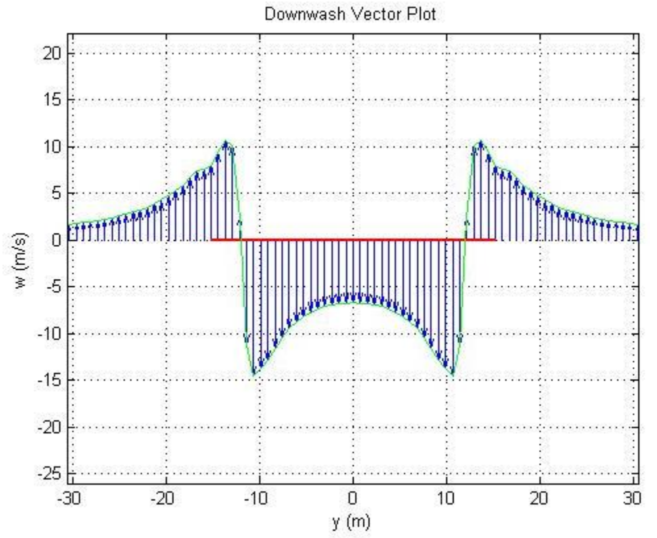	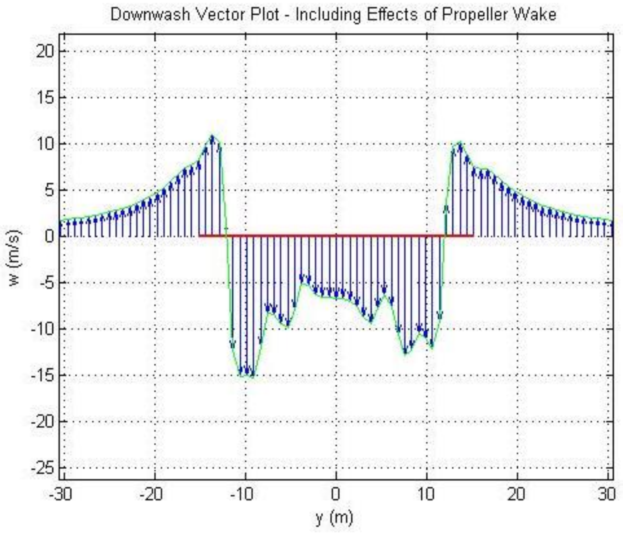
0.75g	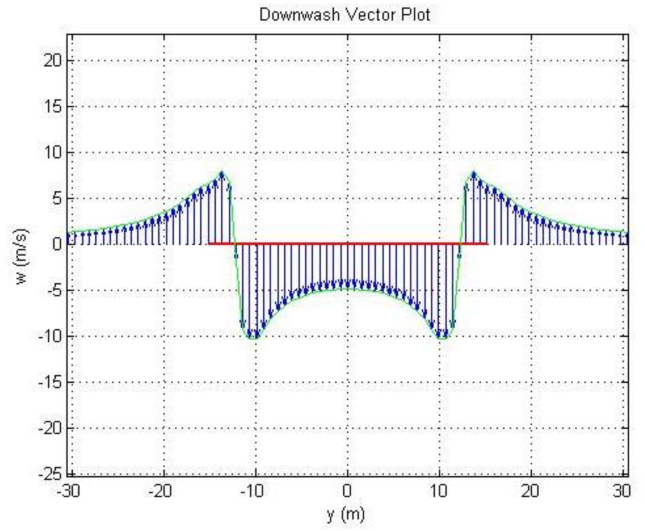	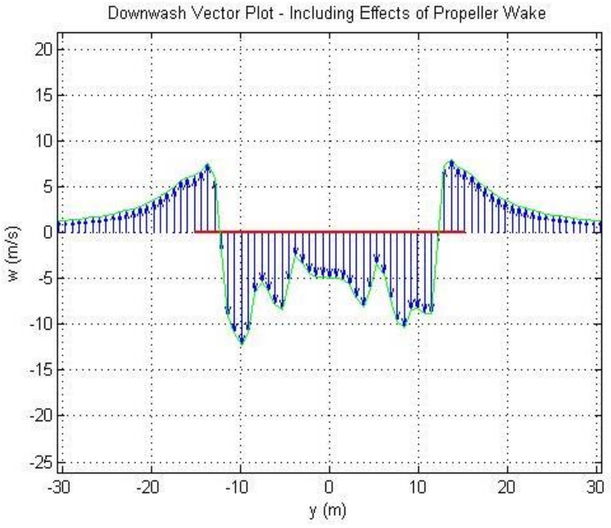

0.5g	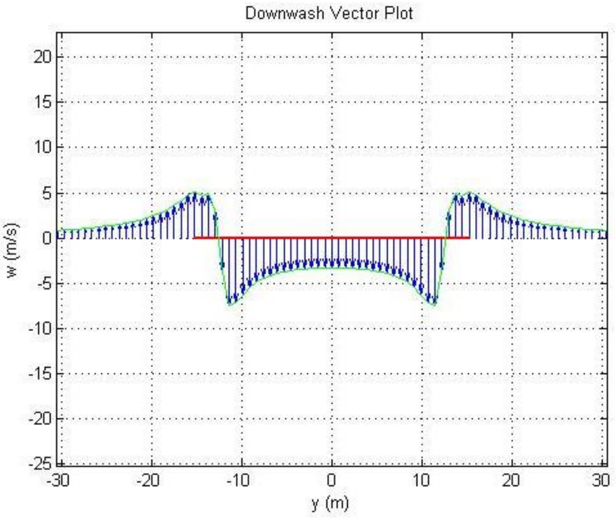Downwash Vector Plot w (m/s) y (m) 20 15 10 5 0 -5 -10 -15 -20 -25 -30 -20 -10 0 10 20 30	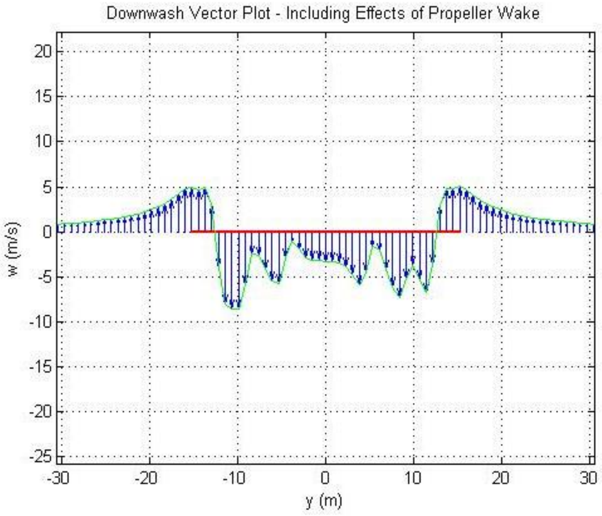Downwash Vector Plot - Including Effects of Propeller Wake w (m/s) y (m) 20 15 10 5 0 -5 -10 -15 -20 -25 -30 -20 -10 0 10 20 30
0.25g	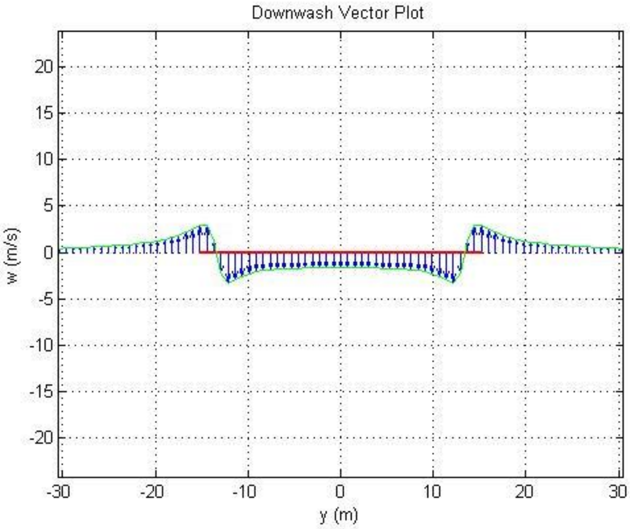Downwash Vector Plot w (m/s) y (m) 20 15 10 5 0 -5 -10 -15 -20 -30 -20 -10 0 10 20 30	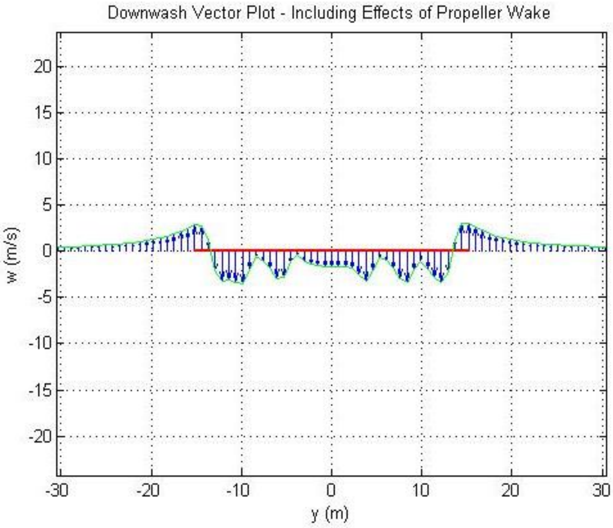Downwash Vector Plot - Including Effects of Propeller Wake w (m/s) y (m) 20 15 10 5 0 -5 -10 -15 -20 -30 -20 -10 0 10 20 30
0g		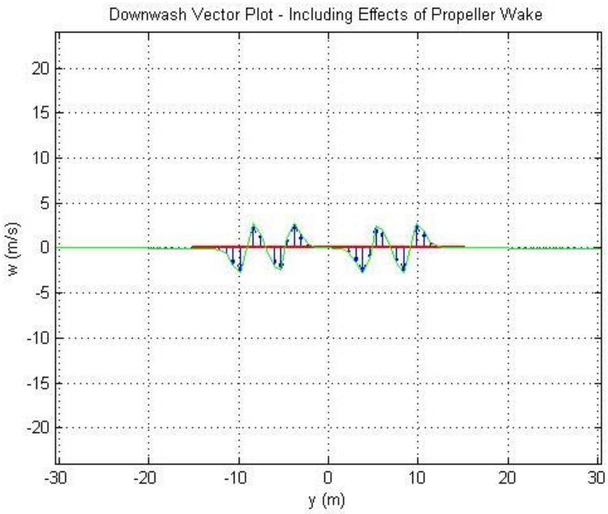Downwash Vector Plot - Including Effects of Propeller Wake w (m/s) y (m) 20 15 10 5 0 -5 -10 -15 -20 -30 -20 -10 0 10 20 30

It can be seen from the above vertical induced velocity plots that the helicoidal vortex induced velocity only affects that region of the wake between approximately -0.35 *b* and 0.375 *b*, in the spanwise domain, due to the outermost turboprop engine pairs being located at $\pm$0.3 *b*. This region is characterised by a downwash (negative) velocity, and the four helicoidal vortices quite evidently disrupt this region causing a reduction in the peak downwash velocity on the starboard wing, decreasing it from -14.57 m/s, produced in the absence of propeller effects, to -12.2 m/s during cruise conditions. The port side wing, however, experiences an increased peak downwash velocity of -15.21 m/s as opposed to the -14.57 m/s, during the 1 g wing loading flight state. This asymmetry in the propeller induced velocity effect on the trailing wing wake is a result of all four turboprops rotating clockwise, as seen from a tailplane reference. The effects of the helicoidal vortices on the wing vertical velocity profile are substantiated by the downwash velocity profile for the 0 g wing loading flight state and full propeller thrust. Within this profile, the helicoidal vortices account for the entire induced velocity and result in an asymmetric pattern of four upwash peaks, averaging 2.7 m/s and four downwash peaks, averaging -2.7 m/s, as a result of the four helicoidal vortex sheets.

In addition to the velocity field generated directly by the helicoidal vortices, these vortices influence the 3D VFM wing wake vortex filaments and result in minor skewing of the vortex rollup transverse section in the starboard wing wake, as shown in Table D.1.1 of Appendix D. This influence of the helicoidal vortices results in an increase in the starboard wing's rolled up vortex centre, which in turn results in the peak upwash velocity increasing marginally by an average of 0.03 m/s for all flight states.

Once again, from the progression in Table 4.16 above, it can be seen that the effects of the helicoidal vortices do not have a more pronounced effect, on the dominant wing wake induced velocity field, with a decrease in wing loading. This is due to the helicoidal vortices descending, under mutual induction, at a far slower rate than the rolled up wing vortices. In the case of 1 g wing loading and full propeller thrust, however, the difference between the centre of the rolled up wing vortices and the outermost helicoidal vortex pair centres is only 0.06 m after a wake length of 330 m. For the remaining decreasing wing loading flight states, this vertical difference between vortex centres increases, however, as a result of the decrease in the wing wake's vortex filament strengths. The position of the wing's rolled up vortex centres for all flight states are shown in Table D.1.4 of Appendix D. Once again, in order to investigate the maximum effect the propeller wake is capable of imparting on the wing wake, a hypothetical 'worst case' scenario is derived in the subsequent section, Section 4.2.2, in which the vortex centres of the helicoidal vortex and the wing's rolled up vortices are aligned for all flight states of the P-3 Orion.

From all downwash plots presented above, it is apparent that clockwise rotating turboprops result in a reduced peak downwash and an increased peak upwash on the starboard wing wake. This is an expected outcome when taking a reference point on one of the propeller blades and viewing it as a wing. From this propeller blade reference point, this 'wing' experience a culmination of the free stream velocity and the components of the propeller's rotational velocity. These velocity components will result in a more complex induced velocity field for the propeller blades' wakes; however, much the same as the wing downwash velocity profiles, the propeller blades will induce an upwash velocity slightly inboard of their blade tips. When the blade axis is parallel to the wing's spanwise axis, it is most evident that the superposition of the blade and wing upwash velocities will result in an increase in the aircraft's trailing wake peak upwash velocity and a decrease in the peak downwash velocity. These effects will be most pronounced when the turboprop engines are positioned further outboard of the wing root towards the wing tips. In the case of the P-3 Orion and ATR 72, the outermost engine placement that would result in the highest influence in peak wing upwash and downwash is $\pm 0.4\ b$ (80% of the wing's semi-span length). In aircraft design, however, wing mounted engines are placed in a more inboard position nearer the wing root. This reduces the force required by the vertical stabiliser (rudder) to produce a yawing moment about the aircraft's centre of mass. Thus, the rudder can be designed smaller and lighter due to the reduced force requirement. Furthermore, inboard location of wing mounted engines minimizes the yawing moment due to asymmetric thrust in the event of an engine failure [63]. It is therefore evident that this design convention has resulted in zero wing tip mounted turboprop propelled aircraft, and a maximum propeller wake influence on peak wing induced velocities will not be encountered.

4.2.2 Comparison of the Effects of Number of Turboprop Engines, Number of Blades per Engine and Aircraft Wing Loading on the Induced Downwash Velocity Profile

In order to more accurately compare the effects of increased number of turboprop engines and number of blades on the trailing wake of an aircraft, a post result processing routine was created in order to analyse and compare the characteristics of the downwash data for all aircrafts and flight conditions detailed above.

Firstly, the ratio of the average downwash velocity for full propeller thrust to no propeller thrust was analysed in order to investigate whether the helicoidal vortices produced a greater negative or positive velocity influence on the wing wake overall. The result of said investigation is shown in Figure 4.20 below.

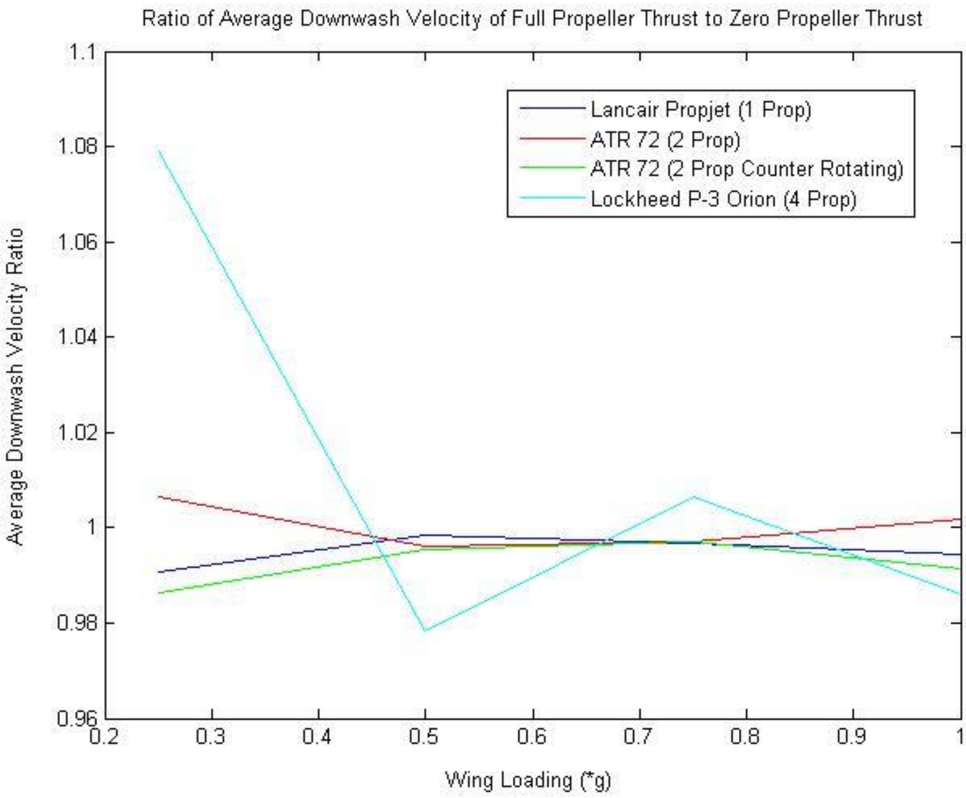

Figure 4.20 Comparison of Average Downwash Velocity Ratios for Full Propeller Thrust to Zero Propeller Thrust for all Simulated Aircraft.

From the above figure, it can be seen that at cruise, most aircraft experience a decrease in average upwash velocity as a result of the induced velocity imparted on the wake by the turboprop engines' trailing wake. This suggests that at cruise the helicoidal vortices have an accumulatively negative effect on the wing wake upwash velocity field. It is also apparent that all aircraft fluctuate about a 1:1 Average Velocity Ratio by only 2% of this equal ratio through all flight states. As aforementioned, in Section 4.2.2, this fluctuation is a result of the centre of the rolled up wing vortices approaching the centre line of the helicoidal vortices and then overshooting this position as the wing loading is reduced. The effects of the helicoidal vortices on the wing wake should increase with a decrease in the difference in vortex centre distance.

In order to investigate the absolute maximum effect the helicoidal vortices are capable of imparting on the wing wake's downwash velocity, the centre of the rolled up vortices and helicoidal vortices were aligned. The Average Downwash Velocity Ratio, as a result of this adjustment, is shown in the figure below.

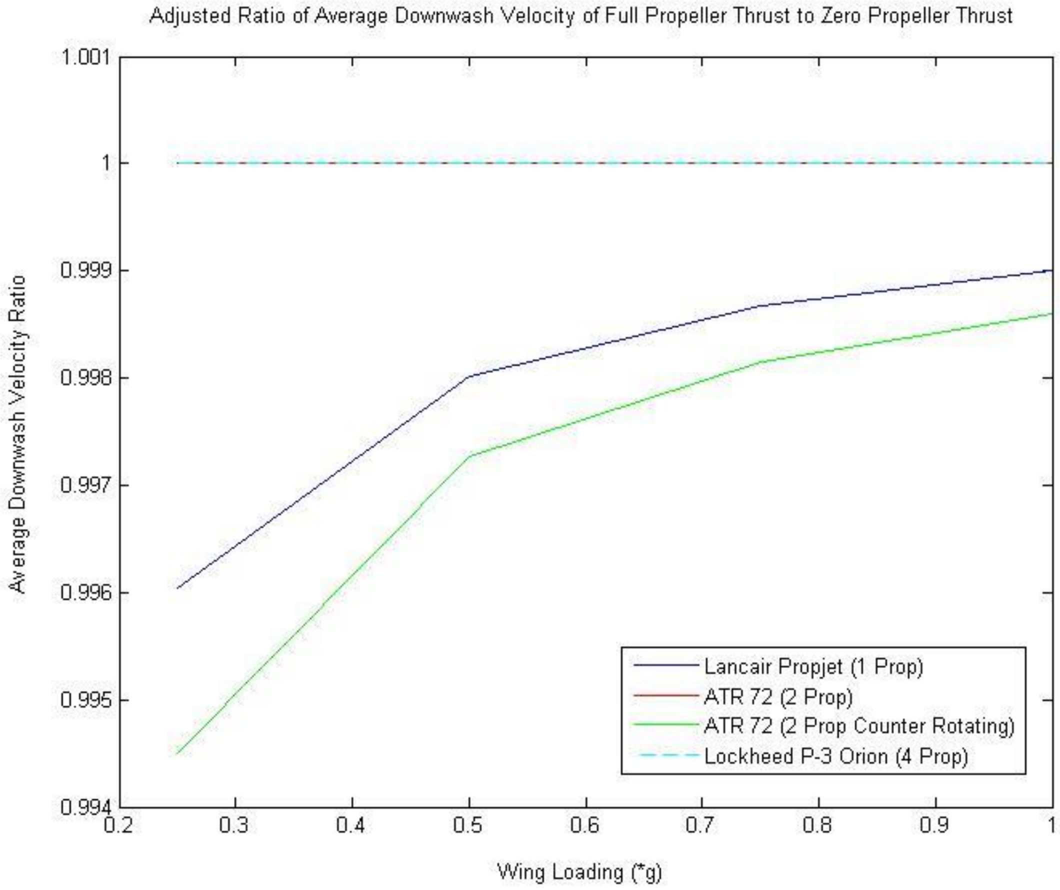

Figure 4.21 Hypothetical Average Downwash Velocity Ratio for Equivalent Helicoidal Vortex and Wing Rolled up Vortex Core Position.

Here the effects of the helicoidal vortices still remain relatively low, with the ATR 72 and P-3 Orion experiencing no changes in average downwash velocity, and the Lancair Propjet and ATR 72 (Counter Rotating Configuration) aircraft experiencing a 0.1% to 0.5% decrease in average velocity. By viewing the 0 g wing loading flight state (presented in Section 4.2.2 above) for all aircraft, it is apparent that the helicoidal vortices generate repetitive velocity field formations which are equal in magnitude but opposite in direction about the spanwise y-axis. The average effect of these induced velocity field patterns therefore equates to approximately zero, as seen in Figure 4.21 above. Figure 4.21 does not, however, incorporate the changes in wing wake induced velocity as a result of the helicoidal vortices altering the 3D VFM wing wake formation. The only meaningful conclusion that can therefore be drawn from Figure 4.20 and 4.21 above, is that the helicoidal vortices have a predominantly negative effect on the wing wake's average induced velocity, although, this effect is extremely low to almost negligible.

According to the work of Bower et al. [64], in both two and three aircraft formations, a 10% wing span overlap (outboard of a spanwise location of 0.4 *b*) between the aircraft results in a maximum fuel saving of approximately 10% to 16%. From the downwash velocity profiles, presented above, it is evident that this region is characterised by an upwash (positive) induced velocity region and incorporates the maximum peak upwash location for all simulated aircraft. The effect the turboprop engines impart on this peak upwash velocity is therefore of the utmost significance in determining whether the turboprop engine wake has a positive or negative influence on the already present fuel saving capabilities of formation flight. Thus, the ratio of peak downwash velocity for full propeller thrust to no propeller was investigated. The results of which are presented in the figure below.

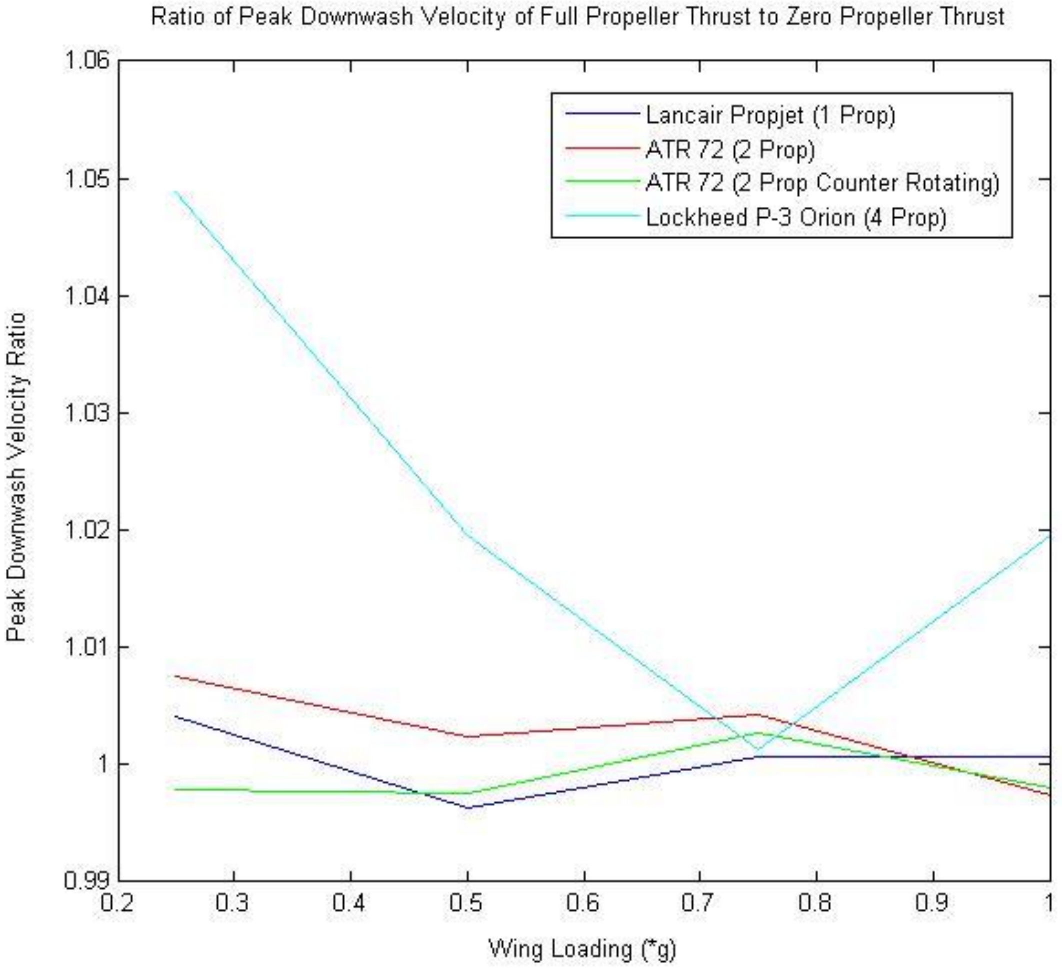

Figure 4.22 Comparison of Peak Downwash Velocity Ratios for Full Propeller Thrust to Zero Propeller Thrust for all Simulated Aircraft.

From the above figure it is apparent that the peak downwash velocity ratio at 0.25 g wing loading is greater than the peak downwash velocity ratio at 1 g wing loading for all simulated aircraft. This indicates that, as hypothesised, the helicoidal vortices do have a more pronounced effect with a reduction in wing loading. However, the difference in the peak downwash velocity ratio between these flight states is only around 1%, and thus the effect of the helicoidal vortices on the peak wing wake downwash is seemingly negligible.

By hypothetically aligning the vortex centres of both the propeller and wing wakes, once again, it is apparent that the induced velocity generated solely by the helicoidal vortex filaments will not influence the peak wing wake upwash velocity. This is due to the helicoidal vortex velocity field having an area of influence that does not intersect with the region in which the peak wing wake upwash velocity is located.

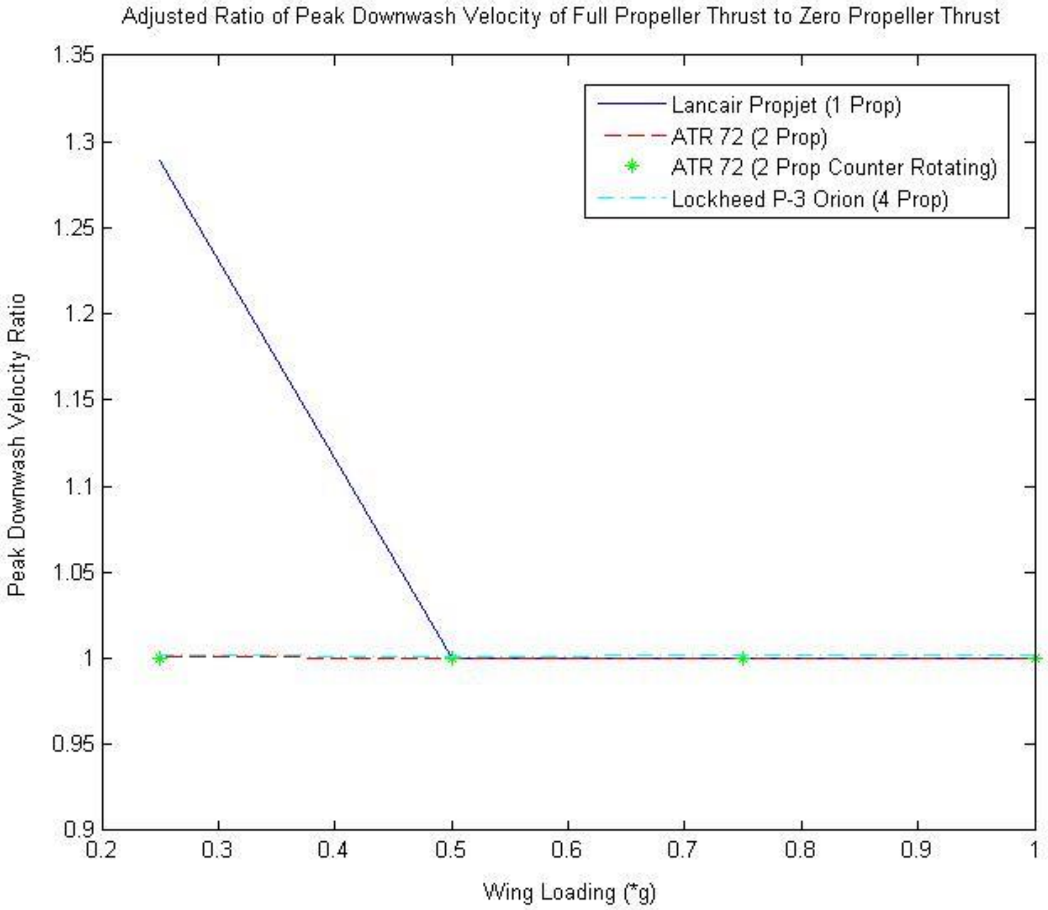

Figure 4.23 Hypothetical Peak Downwash Velocity Ratio for Equivalent Helicoidal Vortex and Wing Rolled up Vortex Core Position.

It can therefore be concluded from Figure 4.22 and 4.23 above that, due to the inboard position of the wing mounted engines, the induced velocity produced directly by the helicoidal vortices does not influence the peak downwash velocity generated by the rolled up wing wake vortices, which are located near the wing tips. This inboard position of the helicoidal vortices does influence the three dimensional wing wake to a marginal extent, as shown in Table D of Appendix D, however the change in the wing wake induced velocity as a result of this wing wake vortex sheet shift is almost negligible.

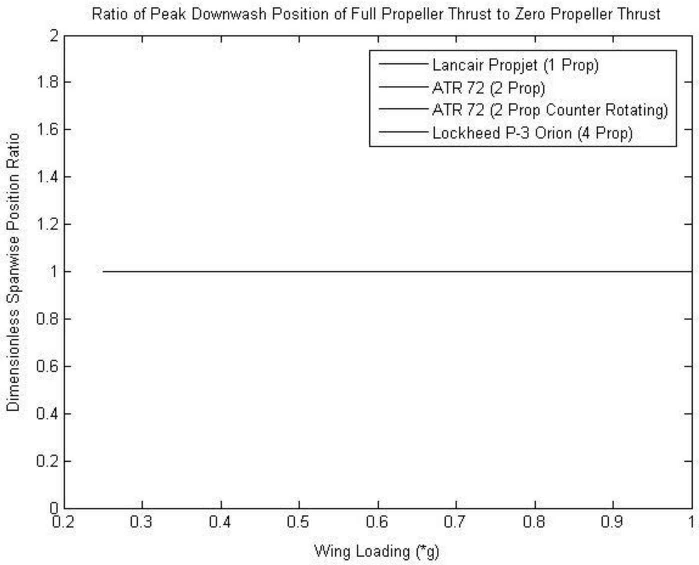

Figure 4.24 Peak Downwash Position Ratio for Full Propeller Thrust to Zero Propeller Thrust for all Simulated Aircraft.

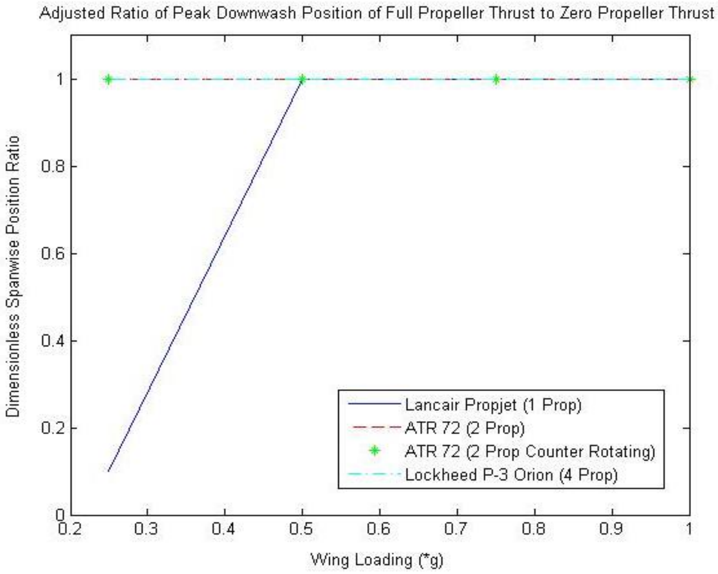

Figure 4.25 Hypothetical Peak Downwash Position Ratio for Equivalent Helicoidal Vortex and Wing Rolled up Vortex Core

Both Figure 4.24 and 4.25 verify that the distance between the wing tips and inboard location of the turboprop engines is too great to enable the helicoidal turboprop wakes to have a significant impact on the upwash regions of the wing trailing wake. Furthermore, it is evident that due to the helicoidal vortices area of influence remaining in the spanwise region about the engine mounting location, that the helicoidal vortices do not drift outboard to a far enough extent to influence the upwash region of the wing wake. Moreover, the vortex strengths of the wing wake filaments are much higher in magnitude than the vortex strengths of the helicoidal vortex filaments and thus the wing wake dominates the induced velocity field. Even at 0.25 g wing loading, the wing wake's peak induced velocity is greater than or equal to the peak induced velocity of the helicoidal vortex filaments, generated at full propeller thrust, and thus the peak upwash velocity location remains unchanged in the combined wing and propeller wake induced velocity plots.

Chapter 5

5. Conclusion

In order to determine the effect of turboprop propulsion on the aerodynamic benefits of formation flight, a three-dimensional aircraft wake model programme was produced. Within this programme, a Lifting Line Method numerical scheme was generated and utilised in order to determine the spanwise circulation distribution of a wing. This spanwise circulation distribution was employed in the discretization of a prescribed wing wake by use of shed vortex filaments of equal vortex strength. Similarly, a prescribed wake for the turboprop engines was generated by use of a numerical scheme based on the amalgamation of the propeller theory of Goldstein and Theodorsen. This prescribed helicoidal vortex sheet, trailing the turboprop propeller system, was similarly discretised by vortex filaments, with blade tip and propeller centreline vortex filament strengths determined through the Goldstein and Theodorsen propeller characteristics numerical scheme. A Vortex Filament Method, which made use of a Burnham-Hallock viscous core model, was then formulated and employed to model the three-dimensional progression and interaction of the wing and turboprop trailing wake.

In order to validate the VFM Burnham-Hallock model programme, it was initially utilised in the modelling of a B747 during cruise. The downwash velocity field obtained from said simulation was verified against both the simulation conducted by Ehret and Oertel [19] for a cruising Boeing 747 in which an integrated Biot-Savart law VFM, incorporating a finite vortex core, was utilised as well as against experimental results obtained by Burnham et al. [36] in their ground-based measurements of the wake vortex characteristics of a B747 aircraft. The downwash velocity results obtained via the use of the VFM Burnham-Hallock model programme compared extremely well to both the experimental and simulated results for the B747. The VFM Burnham-Hallock model produced peak upwash and downwash velocities which matched those obtained by Ehret and Oertel to within 95% accuracy. Furthermore, a distance of 47.48 m between the rolled up vortex centres was achieved utilising the programmed VFM Burnham-Hallock model, which differed from the vortex centre displacement of the Ehret and Oertel model by only 0.48 m, as a 47 m displacement was attained by said model. Qualitatively, the downwash velocity plots of both the models and the experimental results compared exceptionally well with only slight variations in peak upwash to peak downwash transition gradients. Likewise, the 3D VFM Burnham-Hallock plot displayed similar degrees of roll-up and descent when compared to the 3D VFM plot of Ehret and Oertel [19]. From this positive validation process, the programmed VFM Burnham-Hallock model was therefore considered to produce significantly accurate results of a respectable quality, and could thus be utilised to simulate turboprop aircraft wakes of a higher complexity.

In order to compare the effects of the number of turboprop engines and number of blades per engine on the aerodynamic benefits of formation flight, three turboprop propelled aircraft were selected for comparative simulations. These aircraft where the three-bladed single turboprop engine Lancair Propjet, the six-bladed twin turboprop engine ATR 72 and the four-bladed four engine Lockheed Martin P-3 Orion. In order to simulate extended formation flight, which makes use of aircraft downstream separation distances of more than 10 wingspan lengths, a wake length of 330 m for all aircraft was selected. This trailing wake length equated to a downstream distance of 10.9 span lengths for the Lockheed P-3 Orion, 12.4 span lengths for the ATR 72 and 36.3 span lengths for the Lancair Propjet. All aircraft were simulated via the use of the VFM Burnham-Hallock model programme for a range of flight states from normal one g wing loading, such as during cruise conditions, to zero g wing loading with full propeller thrust, such as in vertical ascents in aerobatic formations. The downwash induced velocity fields at 330 m downstream in the wake were then generated. Theses plots were utilised in order to investigate the effects of the inclusion of turboprop engines on the wing wake and, thus, their effect on the aerodynamic benefits of formation flight.

From the vortex core radius selection for all three simulated aircraft, a novel wake convergence requirement equation was formulated through the adaptation of the convergence requirement inequality presented by Ehret and Oertel [19]. Through experimentation with varying vortex core radii for all aforementioned aircraft simulations, the convergence requirement equation was refined and tailored to the programmed VFM Burnham-Hallock model with notable accuracy.

Comparing the propeller output results of the ATR 72 and P-3 Orion, it was found that the parameter which resulted in an increased helicoidal vortex sheet axial displacement velocity was the increased thrust of the turboprop engines. At cruise, the P-3 Orion's Allison T-56-A-14 turboprop engines produce double the thrust of the ATR 72's Pratt & Whitney Canada PW127M turboprop engines and, thus, resulted in a trivially higher cruise velocity as well as a higher helicoidal vortex sheet axial displacement velocity of 59.73 m/s versus the ATR 72's 21.52 m/s. This, however, was to be expected, as the helicoidal vortex sheet axial displacement velocity, w, is directly proportional to the free stream velocity and square root of the turboprop engine thrust. Interestingly, the range for the ratio of helicoidal vortex sheet radius to propeller radius (R_1/R) for all three aircrafts was surprisingly low, with the Lancair Propjet, ATR 72 and P-3 Orion propellers producing helicoidal vortex sheets with radii of 0.984, 0.983 and 0.987 of their propeller radii, respectively. In quick approximate calculations, selecting a ratio of vortex sheet radius to propeller radius of 0.985 would, therefore, not only greatly reduce computational time but would yield fairly accurate helicoidal vortex sheet kinematics parameters, which are dependent on the determination of the helicoidal vortex sheet radius. Lastly, it was verified that an increase in the helicoidal vortex sheet axial displacement velocity, w, and an increase in propeller rotational speed, results in an increase in the axial component of the helicoidal vortex sheet's convective velocity. Similarly, an increase in propeller rotational speed will also result in an increase in the tangential component of the helicoidal vortex sheet's convective velocity.

From the generated downwash induced velocity plots it was found that clockwise rotating turboprops result in a reduced peak downwash and an increased peak upwash on the starboard wing wake. This is an expected outcome, however, as the propeller blades induce an upwash velocity slightly inboard of their blade tips and when the blade axis is parallel to the wing's spanwise axis, it is most evident that the superposition of the blade and wing upwash velocities will result in an increase in the aircraft's trailing wake peak upwash velocity and a decrease in the peak downwash velocity. These effects will be most pronounced when the turboprop engines are positioned further outboard of the wing root towards the wing tips. In the case of the P-3 Orion and ATR 72, the outermost engine placement that would result in the highest influence in peak wing upwash and downwash is ± 0.4 *b* (80% of the wing's semi-span length). In aircraft design, however, wing mounted engines are placed in a more inboard position nearer the wing root in order to reduce the vertical stabiliser (rudder) strength and material requirements in producing a yawing moment about the aircraft's centre of mass. Furthermore, the inboard location of wing mounted engines minimizes the yawing moment due to asymmetric thrust in the event of an engine failure. It is therefore evident that this design convention has resulted in the production of zero wing tip mounted turboprop propelled aircraft, and a maximum propeller wake influence on peak wing induced velocities will not be encountered.

Moreover, from the generated downwash induced velocity plots, it was found that the helicoidal vortices affected that region of the wake inboard a mean value of approximately 35% of the wingspan (-0.35 *b* to 0.35 *b*), measured from the fuselage symmetry plane, for all simulated turboprop aircraft. This region is characterised by a downwash (negative) velocity, and the helicoidal vortices' induced velocity quite evidently disrupts this negative (downwash) induced velocity region. These helicoidal vortices' areas of influence are a result of said aforementioned aircraft design convention, in which engines are mounted in an inboard-most position along the wing, as well as the helicoidal vortices having minimal spanwise drift in the trailing wake. Additionally, the helicoidal vortices have a much lower vortex strength and filament density than the wing wake vortex filaments and, thus, the induced velocity field is dominated by the wing trailing wake. The regions of the wing wake dominated by upwash (positive) induced velocities are outboard of an average value of approximately 40% of the wingspan (-0.4 *b* to 0.4 *b*), measured from the fuselage symmetry plane, for all simulated aircraft. It is this region in which the fuel saving, drag reduction benefits of extended formation flight are harnessed. Therefore, as a result of engine mounting convention in aircraft design as well as marginal outboard drift of the helicoidal vortices, the effect of the helicoidal vortices, generated by the turboprop engines, have minimal to negligible effect on the 10% wing overlap outboard-most region that sees positive fuel savings of 10% to 16% for previously simulated echelon and inverted-V formations.

Chapter 6

6. Limitations and Future Work

6.1 Limitations

The table below is a summary of the limitations imposed on the 3-D aircraft wake model by the constituent theories and models utilised.

Table 6.1: Summary of the limitations of the utilised theories and models:

Theory:	**Limited to:**
Helmholtz's Vortex Theorems	• Inviscid flow
Prandtl's Lifting-Line Theory	• Inviscid flow • Incompressible flow • Unswept wings • High aspect ratio wings • Steady flows
Goldstein and Theodorsen Propeller Vortex Theory	• Inviscid flow • Incompressible flow • Steady flow • Only propeller and turboprop propulsive devices • Far field wake (eliminates development region of vortex aging)
Bio-Savart Law and Burnham-Hallock Model	• Inviscid flow • Incompressible flow

In addition to the limitations tabulated above, the subroutine Propeller Wake Characteristics Model was limited to a maximum blade number of six per turboprop engine, as shown in Table 4.3 of Section 4.2 above. This limitation is a result of Wald's [25] conversion of Tibery and Wrench's tables [33] to Goldstein circulation function tables only being available for up to six-bladed propellers, as shown in Appendix B.

Furthermore, vortex filament density for the trailing wing wake, was limited to 50 - 100 nodes per vortex sheet when four turboprop engines were introduced into the model. The 3D VFM B-H model is capable of a far greater number of vortex filaments, however, the limiting factor was computational processing power. For example, the one g wing loading full propeller thrust simulation of the Lockheed P-3 Orion required in excess of 50 hrs to compute when utilising a 50 vortex filament wake discretisation.

6.2 Recommendations and Future Work

It is recommended that coding practice which prioritises reduced computational cost be employed in models with high data processing routines. Utilising conservative coding regimes would have greatly reduced the computational requirements of the programmed VFM B-H model.

The programmed 3D VFM Burnham-Hallock model is easily upgradeable and modifiable. Therefore, an investigation into the effects of the inclusion of the tailplane, vertical stabiliser and fuselage on the propagation of the helicoidal vortex sheets could prove extremely interesting. The interaction of the helicoidal wake propagating over the wing bounding surface was omitted from the above investigations, due to computational and time constraints. However, according to Wald [25], the shed helicoidal vortex system closes behind a hub or nacelle as a result of the ideal bound circulation distribution on the propeller blades, assuming the propeller has been designed in accordance with minimal energy dissipation criteria. Thus, the configuration of the vortex system some distance from the propeller containing a nacelle is identical to that of a hypothetical propeller which does not contain a central body. It is therefore hypothesized that the effects of the wing surface would have limited effects on the geometry and kinematics of the helicoidal sheet in the far field wake. An investigation into the disruption of the far field helicoidal trailing wake as a result of the wing surface could therefore also prove to be a somewhat fascinating study. Analogous to the above aforementioned investigations would be the utilisation of computational fluid dynamic software to obtain comparative downwash velocity profiles for all simulated aircraft.

Furthermore, the conversion of accurate Tibery and Wrench [33] tabulated values for seven to ten-bladed propellers to Goldstein circulation function $G(r)$ tables would aid in future investigations of turboprop aircraft with higher blade numbers, such as the eight-bladed Airbus A400M. An amalgamation of all aforementioned possible future work could comprise as an interesting future Master’s or Ph.D. thesis.

Bibliography

[1] S. Ning, “Aircraft drag reduction through extended formation flight”, Ph.D. dissertation, Dept. Aeronautics and Astronautics, Stanford Univ., Stanford, CA., 2011.

[2] M. J. Vachon, R. J. Ray, K. R. Walsh, and K. Ennix. “F/A-18 Performance Benefits Measured During the Autonomous Formation Flight Project,” in *AIAA Atmospheric Flight Mechanics Conference and Ehhibit*, Monterey, CA., 2002, AIAA 2002-4491.

[3] R. J. Ray, B. R. Cobleigh, M. J. Vachon, and C. St.John. “Flight Test Techniques Used to Evaluate Performance Benefits During Formation Flight,” in *AIAA Atmospheric Flight Mechanics Conference and Exhibit*, Monterey, CA., 2002, AIAA 2002-4492.

[4] S. A. Ning, T. C. Flanzer, and I. M. Kroo. “Aerodynamic Performance of Extended Formation Flight,” in *48th AIAA Aerospace Sciences Meeting Including the New Horizons Forum and Aerospace Exposition*, Orlando, FL., 2010, pp. 855–865.

[5] J. Pahle, D. Berger, M. Venti, C. Duggan, J. Faber, and K. Cardinal. “An Initial Flight Investigation of Formation Flight for Drag Reduction on the C-17 Aircraft,” in *AIAA Atmospheric Flight Mechanics Conference*, Minneapolis, MN., 2012, AIAA 2012-4802.

[6] J. D. Anderson, “Introduction: Downwash and Induced Drag,” in *Fundamentals of Aerodynamics*, 5th ed. New York: McGraw-Hill, 2011, ch. 5, sec. 1, pp. 415–417.

[7] Prof. R. Fitzpatrick. (2016, January 22). *Fluid Mechanics* [Online]. Available: https://farside.ph.utexas.edu

[8] C. Tung, S. L. Pucci, F. X. Caradonna and H. A. Morse. “The Structure of Trailing Vortices Generated by Model Rotor Blades,” NASA, Moffett Field, CA, NASA Tech. Memo. 81316, 1981.

[9] R. K. Takahashi and K. W. Mcalister. “Preliminary Study of a Wing-Tip Vortex Using Laser Velocimetry,” NASA, Moffett Field, CA, NASA Tech. Memo. 88343, 1987.

[10] M. Czech, G. Miller, J. Crouch, and M. Strelets. “Predicting the near-field evolution of airplane trailing vortices,” in *Comptes Rendus Physique, vol. 6*, Elsevier, 2005, pp. 451–466.

[11] P. R. Spalart. “Airplane Trailing Vortices,” in *Annual Review of Fluid Mechanics, Vol. 30*, Seattle, WA: BCAG., 1998, pp. 107–138.

[12] J. C. Wilson. “Experimental Evaluation of a Flat Wake Theory for Predicting Rotor Inflow-Wake Velocities,” NASA Langley Research Centre, Hampton, VA, NASA Tech. Memo. 4334, 1992.

[13] W. B. Blake and David R. Gingras. “Comparison of Predicted and Measured Formation Flight Interference Effects,” in *Journal of Aircraft, Vol. 41, No. 2*, 2001, pp. 201-207.

[14] L. J. Clancy, “Lanchester-Prandtl Lifting Line Theory,” in *Aerodynamics*. London, England: Pitman Publishing Limited, 1975, ch. 8, sec. 11, pp. 185-188.

[15] J. D. Anderson, “Incompressible Flow over Finite Wings,” in *Fundamental of AERODYNAMICS*, 5th ed. Boston: McGraw-Hill, 2001, ch. 5.

[16] J. Katz and A. Plotkin, “Three-Dimensional Small Disturbance Solutions,” in *Low-Speed Aerodynamics*, 2nd ed. New York: Cambridge University Press, 2001, ch. 8, sec. 1, pp. 167-184.

[17] M. J. Lighthill, *An Informal Introduction to Theoretical Fluid Mechanics*, Oxford, UK: Clarendon Press, 1986.

[18] E. L. Houghton and N.B. Carruthers, *Aerodynamics for engineering students*, 3rd Ed. London, England: Arnold, 1982.

[19] T. Ehret and H. Oertel Jr., “Calculation of Wake Vortex Structures in the Near-Field Wake Behind Cruising Aircraft,” in *Atmospheric Environment, Vol 32, No. 18*, UK: Elsevier Science Ltd., 1998, pp. 3089-3095.

[20] W. Tipping-Woods, “Wing Trailing Vortex Paths In Formation Flight,” M.Sc. thesis, Dept. Mech. Eng. EBE, UCT, Cape Town, South Africa, 2014.

[21] K. Karamcheti, *Principles of Ideal Fluid Aerodynamics.* New York, NY: John Wiley & Sons Inc., 1966.

[22] J. Katz and A. Plotkin, “Fundamentals of Inviscid, Incompressible Flow,” in *Low-Speed Aerodynamics*, 2nd ed. New York: Cambridge University Press, 2001, ch. 2, sec. 11 and sec. 12, pp. 36-41.

[23] D. Fishenberg, “A Method to Validate Wake Vortex Encounter Models From Flight Test Data,” in *27th International Congress of the Aeronautical Sciences*, Nice, France, 2010.

[24] D. Burnham and J. Hallock. "Decay Characteristics of Wake Vortices from Jet Transport Aircraft,” in *Journal of Aircraft*, Vol. 50, No. 1, 2013, pp. 82-87.

[25] Q. R. Wald, “The aerodynamics of propellers,” in *Progress of Aerospace Sciences,* Vol. 42, Port Townsend, W.A, 2006, pp. 85 – 128.

[26] S. Goldstein, “On the Vortex Theory of Screw Propellers,” in *Series A, Containing Papers of a Mathematical and Physical Character, Vol. 123, Issue 792*, London, England: Proceedings of the Royal Society of London, 1929, pp. 440 – 465.

[27] P. G. Saffman, “Vortex Dynamics”. Cambridge, England: Cambridge University Press, 1992, pp. 99 – 103.

[28] G. K. Batchelor, “An Introduction to Fluid Dynamics”. Cambridge, England: Cambridge University Press, 1967, pp. 517 – 520.

[29] G. J. D. Zondervan, “A Review of Propeller Modelling Techniques Based on Euler Methods,” in *Series 01, Aerodynamics, Vol. 5*, Delft, Netherlands: Delft University Press, 1998.

[30] E. Larrabee, "Practical Design of Minimum Induced Loss Propellers," in *SAE Technical Paper 790585*, 1979.

[31] T. Theodorsen, “Theory of Propellers”. New York: McGraw-Hill Book Company Inc., 1948.

[32] H. S. Ribner and S.P. Foster, “Ideal Efficiency of Propellers – Theodorsen Revisited,” in *Journal of Aircraft*, Vol. 27, No. 9, Hampton, V.A: NASA Langley Research Centre, 1990, pp. 810 – 819.

[33] C. L. Tibery, J.W. Wrench Jr., “Tables of the Goldstein Factor,” in *Report 1534.* Washington, D.C: David Taylor Model Basin Applied Mathematics Laboratory, 1964.

[34] G. M. Andrew, M.S. Cahn, J.R. Garcia, and J.R. Stevens. "Stability Derivatives by Rheoelectric Analog," in *Journal of Aircraft*, Vol. 3, No. 6, 1966, pp. 590-591.

[35] The MathWorks, Inc. (1994-2016). *Multidimensional Arrays* [Online]. Available: http://www.mathworks.com/help/matlab/math/multidimensional-arrays.html

[36] D. C. Burnham, J. N. Hallock, I. H. Tombach, M. R. Brashears and M. R. Barber. “Ground-Based Measurements of the Wake Vortex Characteristics of a B747 aircraft in Various Configurations,” in *AIAA 15th Aerospace Sciences Meeting,* Los Angeles, C.A: NASA, US, 1977.

[37] D. A. Caughey. “Introduction to Aircraft Stability and Control,” in *M&AE 5070 Course Notes*, Ithaca, N.Y: Sibley School of Mechanical & Aerospace Engineering, Cornell University, 2011.

[38] A. G. Lee. “P-3 Orion Fuel Saving Modification Wind Tunnel Study,” in *Aviation and Surface Effects Department Report DTNSRDC/ASED-80/14*, Bethesda, M.D: David W. Taylor Naval Ship Research and Development Centre, 1980.

[39] L. K. Loftin Jr., “Design Trends,” in Quest *for Performance: The Evolution of the Modern Aircraft. NASA SP-468.* Washington, D.C: NASA History Office, 1985.

[40] Lockheed Martin Corporation. (2016). *P-3 Orion Specifications* [Online]. Available: http://www.lockheedmartin.com/us/products/p3/p-3-specifications.html

[41] Aerospaceweb.org. (2012). *Lockheed P-3 Orion Maritime Patrol/Anti-Submarine Plane* [Online].Available: http://www.aerospaceweb.org/aircraft/maritime/p3

[42] M.F. Nita, “Aircraft Design Studies Based on the ATR 72,” M.S. thesis, Dept. of Automotive and Aeronautical Eng., Hamburg University of Applied Sciences, Hamburg, Germany, 2008.

[43] R. Babikian, “The Historical Fuel Efficiency Characteristics of Regional Aircraft from Technological, Operational and Cost Perspectives,” M.S. thesis, Dept. of Aeronautics and Astronautics, MIT, Cambridge, M.A, 2001.

[44] Elio Baino. (2015, June). *ATR 72-600 Quick View Brochure* [Online]. Available: http://www.atraircraft.com/products/list.html

[45] G. Harloff, “Light Sport and General Aviation Airpplane Comparison and Harloff Performance Factor” in *ResearchGate*. Westlake, O.H: Harloff Inc., 2013.

[46] Chief of Information US Navy. (2016, May). *P-3C Orion Long Range ASW Aircraft* [Online]. Available: http://www.navy.mil/navydata/fact_display

[47] Lancair. (2016). *Lancair ES, ES-P, IV, IV-P* [Online]. Available: http://www.lancair.com/lancair-es-es-p-iv-iv-p/

[48] Hartzell Propeller. (2015). *Lancair IV, IV-P TSIO-550-B, E* [Online]. Available: http://hartzellprop.com/pilots/kit-builders/lancair-iv-iv-p-tsio-550-be/

[49] National Oceanic and Atmospheric Administration, "U.S. Standard Atmosphere 1976," Rockville, M.D: NASA, 1976.

[50] Graphiq. (2016). *Lancair Propjet Private Turboprop-driven Propeller Plane Specifications* [Online]. Available: http://planes.axlegeeks.com/l/712/Lancair-Propjet

[51] J. Waugh. (2016). *Walter Turbine Otter Conversion* [Online]. Available: http://www.stolairus.com/product/WALT001

[52] Air Support Inc. (2016). *Walter Turbine Otter Conversion* [Online]. Available: http://www.dhc3otter.com/walterturbineaog.htm

[53] *TSLM for Walter M601 Engines Operational & Install Manual*, VR Avionics, East London, South Africa, 2016, pp. 9 & 26.

[54] G. L. Horton, "Aero International [Regional] ATR-42 and 72 Series Aircraft Report," St. Paul Airlines, 2012.

[55] H. Tarquinio Jr., "ATR Certificate Data Sheet," Agencia Nacional de Aviacao Civil, Brazil, Type Certificate No. EA-9312, 2012.

[56] P. Jackson, "ATR 72," in *Jane's All the World's Aircraft 1995-96*. Coulsdon: Alexandria, 1995, pp. 158.

[57] *CNATT Training Manual –Turboprop Engines and Propellers,* CNATT, Pensacola, FL, Ch. 8.

[58] A. Myrick. (2014). *T56-A-14 Turboprop Aircraft Engine* [Online]. Available: https://prezi.com/p8jan1ldutcm/t56-a-14-turboprop-aircraft-engine/

[59] Course Hero, Inc. (2016). *P-3 Limits, Pressures, and Quantities* [Online]. Available: https://www.coursehero.com/flashcards/456698/P-3-Limits-Pressures-and-quantities/

[60] P-3 Orion Research Group The Netherlands. (2015). *Lockheed Martin P-3 Orion Technical Data* [Online]. Available: http://www.p3orion.nl/technical.html

[61] J. Pike. (1999). *FAS Military Analysis Network – P-3 Orion* [Online]. Available: http://fas.org/man/dod-101/sys/ac/p-3.htm

[62] OGMA. (2014). *Defence Aviation Services, Lockheed Martin P-3 Orion* [Online]. Available: http://www.ogma.pt/index.php?page=p3_en

[63] Ilan Kroo, "Propulsion – Engine Placement," in *Aircraft Design: Synthesis and Analysis*, Version 0.9. Stanford, C.A: Dept. of Aero/Astro Stanford University, 2016, ch. 9, sec. 2.1.

[64] G.C. Bower, T.C. Flanzer and I.M. Kroo. “Formation Geometries and Route Optimization for Commercial Formation Flight,” in *27th AIAA Applied Aerodynamics Conference*, San Antonio, TX., 2009, AIAA 2009-3615.

Appendix A

Aerodynamics Derivations and Proofs

A.1 Prandtl's Lifting-Line Theory Derivation

The first assumption is that the circulation of the wing varies along the span with a Fourier series function distribution. The spanwise locations (y) are therefore mapped to the angle (θ) using the following polar coordinate transformation:

$$y = s\cos\theta \tag{A.1.1}$$

Where 's' is the semi-span of the wing geometry being mapped. In order to describe the general spanwise circulation, as opposed to assuming an elliptical lift and circulation distribution, the following Fourier series expansion, which makes use of the spanwise coordinate (θ), is selected:

$$\Gamma(y) = \Gamma(\theta) = \gamma = 4\,s\,V_\infty \sum_{n=1}^{\infty} A_n \sin(n\theta) \tag{A.1.2}$$

A plot of the first three symmetric terms in the expansion is shown in the following figure:

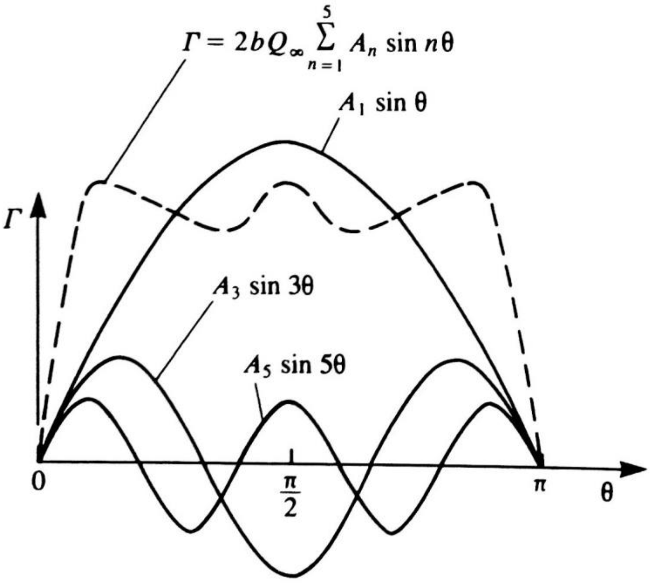

Figure A.1 Fourier sine series representation of a symmetric spanwise circulation distribution $\boldsymbol{\Gamma(\theta)}$, n = 1, 3, 5 [16].

The boundary condition of zero flow normal to the lifting surface, $V_N = 0$, is then applied at several spanwise locations along the wing. This boundary condition requires that flow angles at each section be in balance. In three dimensional wing flow, the flow angles are set by the freestream direction, the wing surface angles and an additional flow angle component. This component is imparted by the trailing vortices and is a result of the downwash velocity they induce. As can be seen from the figure below, the effective angle of attack is therefore the sum of the wing's angle of attack, the section twist angle and the downwash induced angle.

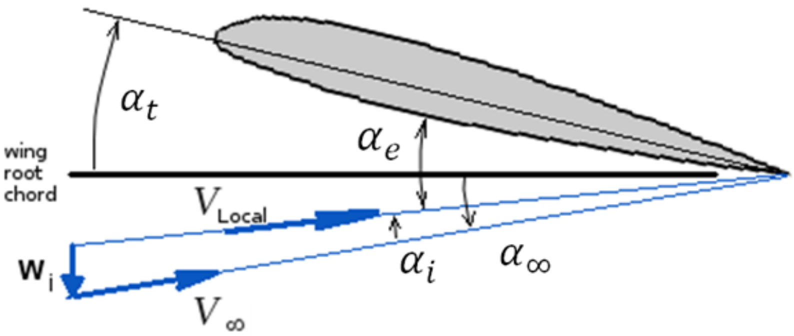

Figure A.2 Two-dimensional section (in the y = const. plane) of a three dimensional wing, showing the effective angle of attack and local velocity (adapted from [18]).

The effective angle of attack is therefore given by the following equation:

$$\alpha_e = \alpha_\infty + \alpha_t - \alpha_0 - \alpha_i \tag{A.1.3}$$

Where α_∞ is the freestream angle of attack for the three-dimensional wing, α_0 is the zero-lift angle of attack of the current wing section, α_t is the local change in angle of attack due to geometric twist of the wing, and α_i is the change in angle of attack due to downwash. At each wing section, in the $y = const.$ plane, the 2-D lift coefficient is a function of this effective angle of attack:

$$C_l = C_{l\alpha}\,(\alpha_\infty + \alpha_t - \alpha_0 - \alpha_i\,) \tag{A.1.4}$$

The 2-D section lift coefficient is, however, also a function of the bound vortex strength at each wing section and thus:

$$C_l = \frac{2\,\gamma}{V_\infty\, c} \tag{A.1.5}$$

Where γ is the two-dimensional circulation at each section. Equating Equation A.1.4 and A.1.5, for the 2-D lift coefficient and rearranging in terms of the vortex strength, yields the following equation:

$$\gamma = \frac{1}{2}\, V_\infty\, c\, C_{l\alpha}\,(\alpha_\infty + \alpha_t - \alpha_0 - \alpha_i\,) \tag{A.1.6}$$

In the above equation both circulation, γ, and the induced angle of attack, α_i , are unknown. From Figure A.2 above, however, it can be seen that, by assuming small angles, this induced angle of attack is given by:

$$\alpha_i = \frac{w_i}{V_\infty} \tag{A.1.7}$$

The downwash velocity here is a result of the shed vortex filaments and is thus a function of circulation only. The value of, α_i, can therefore be determined in terms of $\Gamma(y)$ and thus Equation A.1.6 can be reduced to having a single unknown. This is done by integrating the influence of each differential shed vortex filament over the entire span domain of the wing.

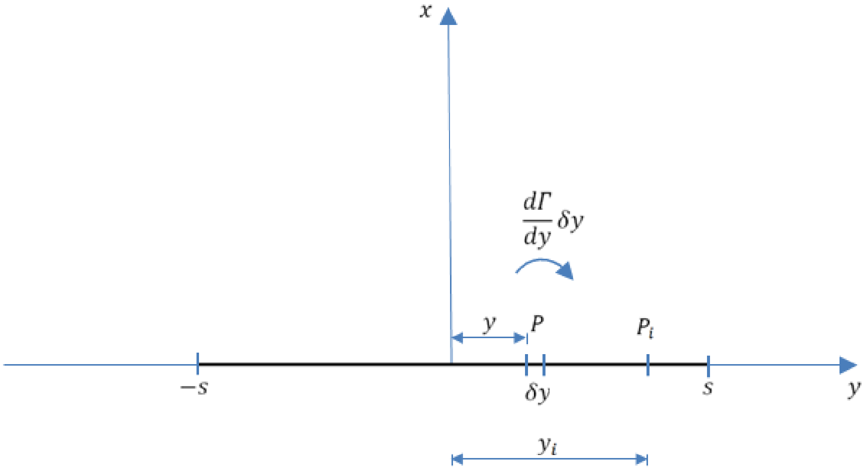

Figure A.3 Differential circulation on span domain. (Adapted from [14])

From the figure above it can be seen that the bound vorticity at any point P on the lifting line is $\Gamma(y)$ and there is consequently a trailing vortex of strength per unit length $\frac{d\Gamma}{dy}$ shed at this point. Therefore the differential downwash velocity induced at another point P_i , on the lifting line, by this trailing vorticity of strength $\frac{d\Gamma}{dy}\delta y$ at point P is:

$$dw_i = \frac{\frac{d\Gamma}{dy}\delta y}{4\pi\, r} \tag{A.1.8}$$

Where each sheet element behaves like half of an infinite vortex line and where r is the distance, along the lifting line, between the vortex element and the point at which the downwash is being calculated and is therefore given by $r = (y - y_i)$. Thus the total downwash at point P_i , or any arbitrary point, is:

$$w_i = \frac{1}{4\pi} \int_{-s}^{+s} \frac{1}{(y - y_i)}\, d\Gamma \tag{A.1.9}$$

By differentiating the Fourier series bound vortex distribution function (Equation A.1.2) and making use of the mapping function of Equation A.1.1, the differential element of circulation is given by:

$$\frac{d\Gamma}{dy} dy = d\Gamma = 4\, s\, V_\infty \sum_{n=1}^{\infty} n\, A_n\, \cos(n\theta)\, d\theta \tag{A.1.10}$$

Substitution of equation A.1.10 into A.1.9 and integrating yields an equation for the total downwash at any span position. By making use of Glauert’s integral this equation simplifies to [16]:

$$w_i = V_\infty \sum_{n=1}^{\infty} \frac{n\, A_n\, \sin(n\theta)}{\sin(\theta)} = V_\infty \sum_{n=1}^{\infty} n\, A_n\, \sin(n\theta) \tag{A.1.11}$$

Substitution of this result, as well as the Fourier series bound vortex distribution function, into the modified equation A.1.6 ($\Gamma = \frac{1}{2}\, V_\infty\, c\, C_{l\alpha} \left(\alpha_\infty + \alpha_t - \alpha_0 - \frac{w_i}{V_\infty}\right)$) yields the following relationship:

$$4\, s\, V_\infty \sum_{n=1}^{\infty} A_n \sin(n\theta) = \frac{1}{2} V_\infty\, c\, C_{l\alpha} \left(\alpha_\infty + \alpha_t - \alpha_0 - \sum_{n=1}^{\infty} n\, A_n \sin(n\theta)\right) \qquad \text{(A.1.12)}$$

After rearranging, the relationship is described by the final boundary equation:

$$\sum_{n=1}^{\infty} A_n \sin(n\theta) \left(\sin(\theta) + \frac{n\, c\, C_{l\alpha}}{8\, s}\right) = \frac{c\, C_{l\alpha}}{8\, s} \sin(\theta)\ (\alpha_\infty + \alpha_t - \alpha_0) \qquad \text{(A.1.13)}$$

By selecting a number of spanwise locations (θ) and values for n, Equation A.1.13 can be expressed in matrix form. The left-hand side of the equation represents each element in the matrix, with each row representing a different spanwise position and each column representing a different value for n. The right-hand side of the equation represents the right hand side of the matrix form and thus the A_n coefficients can be solved by simple matrix algebra:

$$x = A_n = \frac{b}{A} \qquad \text{(A.1.14)}$$

Once the A_n coefficients have been determined they can be substituted back into Equation A.1.2 in order to determine the circulation distribution of the wing. Subsequently, the spanwise lift distribution of the wing can be determined by substituting the circulation distribution and spanwise station mapping into:

$$\frac{dL}{dy} = \rho\, V_\infty\, \Gamma(y) \qquad \text{(A.1.15)}$$

Yielding:

$$dL(\theta) = \rho\, {V_\infty}^2\, b^2 \sum_{n=1}^{\infty} A_n \sin(n\theta)\ \sin(\theta)\, d\theta \qquad \text{(A.1.16)}$$

A.2 Dynamics of Trailing Vortex Sheets Proof

The derivative in the spanwise (or radial) direction of the strength of the free vortex sheet must be equal to the negative derivative of the strength of the bound vorticity in the spanwise (or radial) direction [25].

$$\frac{d\Gamma_{Free}}{dy} = -\frac{d\Gamma_{Bound}}{dy} \quad \text{For finite wings.} \qquad \text{(A.2.1)}$$

$$\frac{d\Gamma_{Free}}{dr} = -\frac{d\Gamma_{Bound}}{dr} \quad \text{For propeller blades.} \qquad \text{(A.2.2)}$$

This is due to the potential difference across a trailing vortex sheet, at a point on the sheet, being equal to the bound circulation at a corresponding point on the associated lifting surface, $\Delta\phi = \Gamma_{Bound}$ [25]. The proof of which is as follows:

Consider the placement of a point p on the lower surface of the vortex sheet and a point p^1 on the upper surface of the sheet vertically in line with point p, as shown in the figure below.

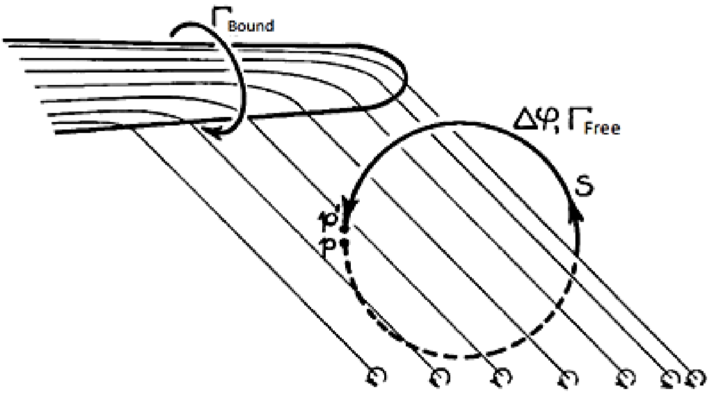

Figure A.4 Relationship between Bound and Free Vorticity [25].

By integrating along an arbitrary path s that connects both points by passing around the edge of the sheet and encompassing all the vorticity from point p to the edge of the sheet, the result is equal to the difference in potential between points p and p^1:

$$\int_{p}^{p^{1}} u.ds = \Delta\phi \tag{A.2.3}$$

If the vertical distance between point p and p^1 is allowed to reach zero, the integral around the closed path would equate to the total vortex strength between the now point pp^1 and the free edge of the vortex sheet:

$$\oint u.ds = \Gamma_{Free} \tag{A.2.4}$$

This is due to the path of integration encompassing all of the vortex filaments in the specified portion of the vortex sheet. Since the path of integration is unchanged, the above integrals are identical in magnitude and therefore:

$$\Delta\phi = \Gamma_{Free} \tag{A.2.5}$$

Thus the potential difference across a specified region of a vortex sheet is equal to the total circulation of that specified vortex sheet region. The region must, however, enclose the tip vortex filament at the edge of the vortex sheet.

From Figure A.4 above, it can be seen that by considering a path of integration around the lifting surface in line with the points p and p^1, so that a line may be drawn from the trailing edge of the lifting surface to the points without crossing a vortex filament, the integration around the lifting surface encompasses the same vorticity as the path s around the trailing vortex sheet. Therefore, the potential difference across a portion of a trailing vortex sheet is also equal to the bound circulation at a point on the span that marks the beginning of the specified vortex sheet portion [25]:

$$\Delta\phi = \Gamma_{Bound} \tag{A.2.6}$$

Consequentially, the magnitude of the bound and free vorticity is therefore equal:

$$\Gamma_{Free} = \Gamma_{Bound} \tag{A.2.7}$$

A.3 Vortex Filament Induced Velocity Derivation

The ensuing vortex filament induced velocity derivation is an amalgamation of the processes described in Katz and Plotkin [22] as well as Anderson [15].

The differential induced velocity of a vortex filament is given in vector form by the Biot-Savart law described in the equation below:

$$d\vec{V} = \frac{\Gamma}{4\pi}\frac{d\vec{l}\times\vec{r}}{|\vec{r}|^3} \tag{A.3.1}$$

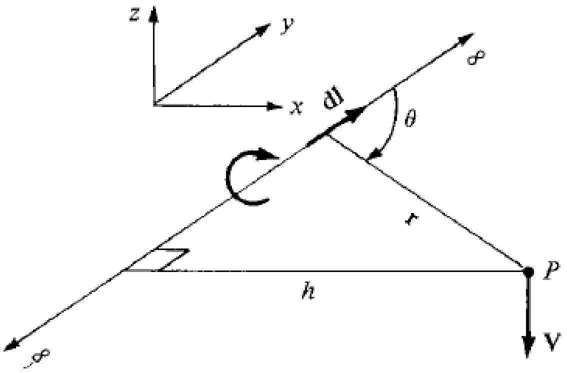

Figure A.5 Velocity induced at point P by a straight vortex filament of infinite length [15].

From the definition of a vector cross product, the cross product of the deferential directed vortex filament segment ($\vec{dl}$) and the radius vector ($\vec{r}$) of Equation A.3.1 can be written in the following scalar form:

$$\vec{dl} \times \vec{r} = |dl||r| \sin\theta \, \vec{n} \qquad \text{(A.3.2)}$$

Where $\vec{n}$ is the resulting unit vector of the cross product according to the right hand rule. Consequently, from Figure A.5 it can be seen that $\vec{n}$ is also therefore the unit vector of the induced velocity.

The velocity induced at point P by the entire vortex filament can be found by integrating Equation A.3.1. By substituting Equation A.3.2 into Equation A.3.1 and integrating along the length of an infinite vortex filament, the magnitude of the velocity, $V = |V|$, is given by:

$$V = \frac{\Gamma}{4\,\pi} \int_{-\infty}^{\infty} \frac{\sin\theta}{r^2} \, dl \qquad \text{(A.3.3)}$$

From the geometry in Figure A.5 it can be seen that:

$$r = \frac{h}{\sin\theta} \qquad \text{(A.3.4)}$$

$$l = \frac{h}{\tan\theta} \qquad \text{(A.3.5)}$$

$$dl = -\frac{h}{\sin^2\theta} \, d\theta \qquad \text{(A.3.6)}$$

Where h is the perpendicular distance from point P to the vortex filament. Substituting Equations A.3.4 – A.3.6 as well as the geometry for a finite vortex filament, shown in the figure below, into Equation A.3.3 yields Equation A.3.7.

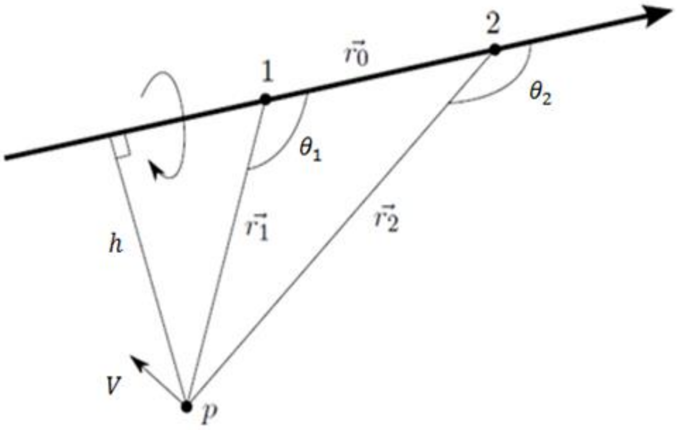

Figure A.6 Velocity induced at point P by a straight vortex filament of finite length (Adapted from Katz and Plotkin [22]).

$$V = -\frac{\Gamma}{4\,\pi\,h}\int_{\theta_1}^{\theta_2} \sin\theta\, d\theta \tag{A.3.7}$$

$$V = -\frac{\Gamma}{4\,\pi\,h}\left(\cos\theta_1 - \cos\theta_2\right) \tag{A.3.8}$$

As the length of the finite vortex filament increases, the angles θ_1 and θ_2 approach 0 degrees and 180 degrees respectively. Thus for a straight vortex filament of infinite length $\theta_1 = 0$ and $\theta_2 = \pi$, and equation A.3.8 reduces to:

$$V = \frac{\Gamma}{2\,\pi\,h} \tag{A.3.9}$$

A.3.1 Numerical Computation

The following derivation outlines the method utilised in rewriting the Burnham-Hallock model in vector form for numerical computation. The procedure follows the methodology described by Katz and Plotkin in which the Biot-Savart model is rewritten in vector form [22].

$$V = \frac{\Gamma}{4\,\pi}\left(\frac{h}{h^2 + r_c^2}\right)\left(\cos\theta_1 - \cos\theta_2\right) \tag{A.3.10}$$

Equation A.3.10 above is the result of applying the Burnham-Hallock model to a vortex filament of finite length and is derived in a similar method to Equation A.3.8 of the Biot-Savart law. From Figure A.6 above, the variables of Equation A.3.10 can be written in vector notation as follows:

$$\vec{r}_0 = \vec{r}_1 - \vec{r}_2 \tag{A.3.11}$$

$$h = \frac{|\vec{r}_1 \times \vec{r}_2|}{|\vec{r}_0|} \tag{A.3.12}$$

$$\cos\beta_1 = \frac{\vec{r}_0 \cdot \vec{r}_1}{|\vec{r}_0||\vec{r}_1|} \tag{A.3.13}$$

$$\cos\beta_2 = \frac{\vec{r}_0 \cdot \vec{r}_2}{|\vec{r}_0||\vec{r}_2|} \tag{A.3.14}$$

$$n = \frac{\vec{r}_1 \times \vec{r}_2}{|\vec{r}_1 \times \vec{r}_2|} \tag{A.3.15}$$

Where n is the direction unit vector of the resultant induced velocity. The substitution of Equation A.3.11 – A.3.14 into Equation A.3.10 and multiplication by the unit vector of Equation A.3.15, yields the following transformed equations of Equation A.3.8 and A.3.10 in vector form:

$$\vec{V} = \frac{\Gamma}{4\,\pi}\,\frac{|\vec{r_0}|}{|\vec{r}_1 \times \vec{r}_2|}\left(\frac{\vec{r}_0 \cdot \vec{r}_1}{|\vec{r}_0||\vec{r}_1|} - \frac{\vec{r}_0 \cdot \vec{r}_2}{|\vec{r}_0||\vec{r}_2|}\right)\frac{\vec{r}_1 \times \vec{r}_2}{|\vec{r}_1 \times \vec{r}_2|}$$

$$= \frac{\Gamma}{4\,\pi}\,\frac{\vec{r}_1 \times \vec{r}_2}{|\vec{r}_1 \times \vec{r}_2|^2}\,\vec{r}_0\left(\frac{\vec{r}_1}{|\vec{r}_1|} - \frac{\vec{r}_2}{|\vec{r}_2|}\right) \qquad \text{(A.3.16)}$$

$$\vec{V} = \frac{\Gamma}{4\,\pi}\left(\frac{\frac{|\vec{r}_1 \times \vec{r}_2|}{|\vec{r}_0|}}{\left(\frac{|\vec{r}_1 \times \vec{r}_2|}{|\vec{r}_0|}\right)^2 + r_c^2}\right)\left(\frac{\vec{r}_0 \cdot \vec{r}_1}{|\vec{r}_0||\vec{r}_1|} - \frac{\vec{r}_0 \cdot \vec{r}_2}{|\vec{r}_0||\vec{r}_2|}\right)\frac{\vec{r}_1 \times \vec{r}_2}{|\vec{r}_1 \times \vec{r}_2|} \qquad \text{(A.3.17)}$$

Where r_c is the core radius of the vortex filament.

A.4 Thrust of a Propeller with Ideal Load Derivation

The following derivation precisely follows that described by Theodorsen [31] and Wald [25] in their respective work on the aerodynamics of propellers.

By utilising the generalised Bernoulli equation for conservative force fields, $\frac{u^2}{2} + \Psi + \frac{p}{\rho} = const.$, the pressure equation for unsteady incompressible potential flow, in which there is no external force due to the absence of free surface effects is:

$$\frac{\partial \varphi}{\partial t} + \frac{u^2}{2} + \frac{p}{\rho} = const. \qquad \text{(A.4.1)}$$

Applying Equation A.4.1 to a helicoidal vortex sheet of infinite length and letting the pressure in the undisturbed fluid surrounding the helicoid (at a large radial distance from the helicoid axis) be p_∞, the pressure equation is thus:

$$\frac{\partial \varphi}{\partial t} + \frac{u^2}{2} + \frac{p}{\rho} = \frac{p_\infty}{\rho} \qquad \text{(A.4.2)}$$

As the undeforming helicoidal vortex sheet is assumed to translate axially backward by the induced displacement velocity in the positive z direction, the unsteady term of Equation A.4.1 can be represented as follows:

$$\frac{\partial\varphi}{\partial t} = -w\,\frac{\partial\varphi}{\partial z} = -w\,u_{z1} \qquad \text{(A.4.3)}$$

Where u_{z1} is the axial component of convective velocity of the vortex sheet as determined in Section 2.4.4. Substituting Equation A.4.3 into Equation A.4.2 and rearranging yields the following pressure equation for the rigid pattern flow of the helicoidal vortex sheet:

$$p - p_{\infty} + \frac{1}{2}\rho\,u^2 = \rho\,w\,u_{z1} \qquad \text{(A.4.4)}$$

By applying an Eulerian approach to the momentum integral theorem, the axial force required to produce the continuous motion of the helicoidal vortex sheet can be obtained. Within this Eulerian approach, the propeller is placed within a closed control surface, S, through which the fluid flows. This control surface remains stationary with respect to the propeller. Thus, application of the momentum theorem for a steady flow applied to such a control surface yields the following equation:

$$\int_S^{\cdot}(p\,\vec{n} + \rho\,\vec{n}\ \cdot\vec{w}\,\vec{w})dS - \vec{F} = 0 \qquad \text{(A.4.5)}$$

Where $\vec{F}$ is the resultant force acting on the fluid, imparted by the propeller, and is thus the positive forward thrust, $\vec{T}$, of the propeller. Furthermore, $\vec{n}$ is the outward normal unit vector of the control surface and $\vec{w}$ is the velocity at the surface.

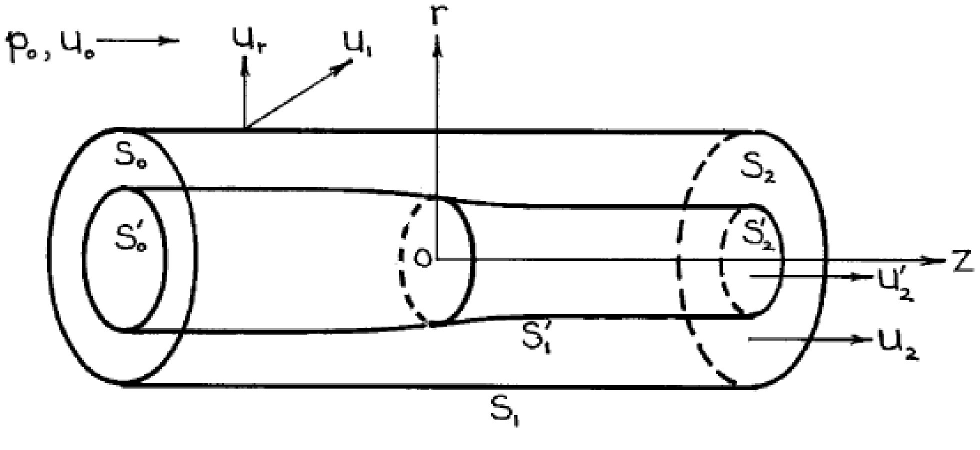

Figure A.7 Momentum Integral Control Surface [25].

By considering a cylindrical control surface, depicted in Figure A.7 above, in which the propeller is situated parallel to the onset flow u_0 and at the origin on the z-axis, the resulting thrust term of Equation A.4.5 is given by:

$$T = \int_{S_2'} [(p_2 - p_0) + \rho\, u_2'(u_2' - u_0)] dS_2' \qquad \text{(A.4.6)}$$

Here the cylindrical control surface is fixed to the axis of the propeller and therefore the end surfaces S_0 and S_2 are normal to the z-axis. These bounding surfaces are in fact the outer region of the bounding planes and are divided from the inner regions S_0' and S_2' by a stream surface S_1' which bounds the fluid that is subject to the direct forces imparted by the propeller. Both these curved and flat bounding surfaces are, however, assumed to be at large distances from the propeller. Furthermore, p_0 and p_2 respectively refer to the inlet and outlet pressure of the control surface S and u_0 and u_2 refer to the inlet and outlet velocity of the control surface. For a detailed derivation of Equation A.4.6 see Wald [25, pp. 90 - 91].

Substitution of the velocity terms derived in Section 2.4.4, ‘The Kinematics of Helicoidal Vortex Sheets’, into Equation A.4.6 yields the following:

$$T = \int_S (p - p_\infty)\, dS + \int_S \rho(V_\infty + u_{z1})u_{z1}\, dS \qquad \text{(A.4.7)}$$

Here the prime notation has been discarded since the integrand is zero outside of the slipstream and thus S is the entire exit plane of the control surface previously denoted as S_2 and S_2' . By assuming a constant density and substituting the derived pressure equation of Equation A.4.4 into the above, the thrust can be further represented as:

$$T = \rho \int_S \left[(V_\infty + w)\, u_{z1} + u_{z1}^2 - \frac{u^2}{2}\right] dS \qquad \text{(A.4.8)}$$

Theodorsen [31] developed two dimensionless variables κ and ε, which are functions of the pitch of the helicoidal vortex sheet and the Goldstein circulation function, in order to evaluate the above thrust equation entirely in terms of the characteristics of the helicoidal vortex sheet. Following the work of Theodorsen [31] and Wald [25], the derivation of the modified thrust equation is as follows.

Consider the triangle ABC, shown in the figure below, on the surface of a cylinder encapsulating the helicoidal vortex sheet.

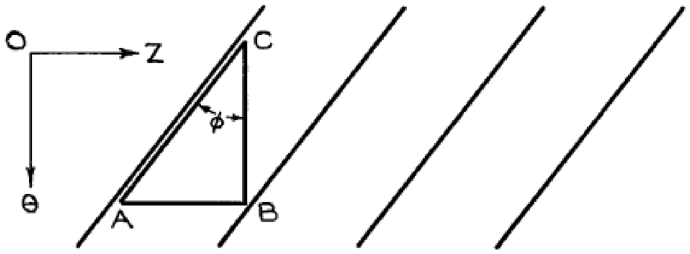

Figure A.8 Triangle Element [25].

Where ϕ is the angular pitch of the helicoidal vortex sheet, the side AC spans the distance between two successive helicoidal sheets and the triangle ABC moves with the helicoid. As no vortex element passes through the triangle:

$$\oint \vec{u} \cdot d\vec{s} = 0 \tag{A.4.9}$$

The velocity along CA is zero due to the path of integration moving with the helicoidal vortex sheet and thus:

$$\int_A^B u_{z1}\, dz + \int_B^C - u_{\theta 1}\, r_1\, d\theta = 0 \tag{A.4.10}$$

Due to screw symmetry the velocity is constant along lines parallel to AC and thus by replacing dz with $r_1 d\theta \tan\theta$ both integration terms can be computed from limits B to C. However, the limits B and C can be transformed in to the limits 0 and 2π by multiplying by the number of interleaved vortex sheets and thus Equation A.4.10 becomes:

$$\int_0^{2\pi} u_{z1}\, r_1\, d\theta = \left(\frac{1}{\tan\phi}\right) \int_0^{2\pi} u_{\theta 1}\, r_1\, d\theta \tag{A.4.11}$$

By substituting the relationship of bound to free vorticity as described in Section 2.4.6, $B\Gamma(r_0) = \int_0^{2\pi} u_{\theta 1}(r_1) r_1 d\theta$, as well as substituting the equation for angular pitch determined in Section 2.4.4, the result is:

$$\int_0^{2\pi} u_{z1}\, r_1\, d\theta = \frac{B\Gamma}{\left(\frac{\lambda_2}{x_1}\right)} \tag{A.4.12}$$

By substituting Equation A.4.12 as well as the Goldstein circulation function equation, Equation 2.4.18, the first term of the thrust equation of Equation A.4.8:

$$\int_S u_{z1}\ dS = \int_0^{2\pi} \int_0^{\infty} u_{z1}\, r_1\, dr_1\, d\theta \tag{A.4.13}$$

can be represented as follows:

$$\int_S u_{z1}\ dS = \int_0^{\infty} \left(\frac{B\Gamma}{\lambda_2}\right) R\, x\, dx = \lambda\, R_1^2\, w \int_0^1 2\, G(x_1)\ x_1\, dx_1 \tag{A.4.14}$$

Introducing Theodorsen's dimensionless mass transport coefficient κ, which is as follows:

$$\kappa = \int_S \left(\frac{u_{z1}}{wS}\right) dS \tag{A.4.15}$$

results in the following representation for the first term of the thrust equation of Equation A.4.8:

$$\rho \int_S\ [(V_\infty + w)\, u_{z1}\ dS = \kappa\rho\pi R_1^2\, (V_\infty + w)\, w \tag{A.4.16}$$

Furthermore, by Equation A.4.14, the value of κ can thus be computed as follows:

$$\kappa = \int_0^1 2\, G(x_1)\ x_1\, dx_1 \tag{A.4.17}$$

Introducing Theodorsen's axial energy transport factor:

$$\varepsilon = \int_S \frac{u_{z1}^2\, dS}{\pi\, R_1^2\, w^2} \tag{A.4.18}$$

results in the following representation for the second term of the thrust equation of Equation A.4.8:

$$\rho \int_S u_{z1}^2 \, dS = \varepsilon\rho\pi R_1^2 w^2 \tag{A.4.19}$$

In order to evaluate the last term of the thrust equation, $\int_S u^2 \, dS$, the integral over the plane normal to the axis, a Trefftz plane, can be converted into a volume integral by multiplying by the distance between two successive Trefftz planes as follows:

$$h \int_S u^2 dS = \int_\tau u^2 \, d\tau = \int_\tau (\nabla\varphi)^2 d\tau \tag{A.4.20}$$

Where h is the distance between successive vortex sheets, marked by the position of two Trefftz planes, $z = z_1$ and $z = z_2$. Thus the surface integral S has been transformed into the volume integral τ which is contained between the two Trefftz planes.

This allows for the application of Green's theorem which converts the volume integral τ into a surface integral σ now on the surface of the helicoidal vortex sheet:

$$\int_\tau [\varphi \, \nabla^2\varphi + (\nabla\varphi)^2] \, d\tau = \int_\sigma \varphi \left(\frac{d\varphi}{dn}\right) d\sigma \tag{A.4.21}$$

Here n is the outward normal unit vector of the surface σ, which is the complete inner and outer boundary of the volume τ. Since $\nabla^2\varphi = 0$, the application of Green's theorem to Equation A.4.20 yields the following:

$$h \int_S u^2 dS = \int_\sigma \varphi \left(\frac{d\varphi}{dn}\right) d\sigma = \int_\sigma \Delta\varphi \left(\frac{d\varphi}{dn}\right) d\sigma \tag{A.4.22}$$

As $\frac{d\varphi}{dn}$ is equal in magnitude on each side of the vortex sheet, $\Delta\varphi$, which is the difference in potential between the two sides, is introduced in order to perform the integration over just one side of the sheet.

As aforementioned, the normal velocity of the vortex sheet is the component of the axially induced displacement velocity w in the normal direction of the vortex sheet and thus:

$$\frac{d\varphi}{dn} = w \cos\phi \tag{A.4.23}$$

Therefore:

$$\left(\frac{d\varphi}{dn}\right) d\sigma = w \cos\phi \; d\sigma = w \; dS \qquad \text{(A.4.24)}$$

Substituting Equation A.4.24 into Equation A.4.22 yields the following integral for the last term of the thrust equation:

$$\int_S u^2 dS = \left(\frac{1}{h}\right) \int_S \Delta \varphi w \; dS = \left(\frac{1}{h}\right) \int_S \Gamma(r_1) w \; dS \qquad \text{(A.4.25)}$$

Expressing the circulation $\Gamma(r_1)$ in terms of the Goldstein circulation function of Equation 2.4.18 yields:

$$\int_S u^2 dS = \int_0^{2\pi} \int_0^R G(r) w^2 r \; dr \; d\theta = \pi R_1^2 \, w^2 \int_0^1 2G(x_1) \, x_1 \, dx_1 = \pi R_1^2 \, w^2 \kappa \qquad \text{(A.4.26)}$$

and thus the last term of the thrust equation is given by:

$$-\frac{1}{2}\rho \int_S u^2 dS = -\frac{1}{2}\rho \, \pi \, R_1^2 w^2 \kappa \qquad \text{(A.4.27)}$$

Summing all the relevant terms of the thrust equation (Equation A.4.16, A.4.19 and A.4.27) yields an equation for the thrust of the propeller expressed entirely as a function of the characteristics of the trailing helicoidal vortex sheet:

$$T = \kappa \rho \pi R_1^2 V_\infty^2 \overline{w}[1 + \overline{w} \left(\frac{1}{2} + \frac{\epsilon}{\kappa}\right)] \qquad \text{(A.4.28)}$$

Where, as prescribed by Theodorsen [31], $\overline{w}$ is the ratio of the induced axial velocity to the free stream velocity, $\overline{w} = \frac{w}{V_\infty}$.

A.5 Helicoidal Vortex Sheet Radius Derivation

Re-arranging the Goldstein circulation equation, Equation 2.4.18, the circulation distribution of the propeller's trailing vortex wake is given by:

$$B\Gamma = 2\pi R_1 w \lambda_2 G(x_1) = 2\pi R_0 V_\infty \overline{w}(1+\overline{w})\lambda G(x_1) \tag{A.5.1}$$

Where the subscripts 0 and 1 denote variables and coefficients referred to the propeller plane and helicoidal vortex system respectively.

Figure A.9 below depicts the velocities at the blade element. Utilisation of this velocity diagram and by application of the Kutta-Joukowsky theorem, it can be seen that the thrust of a blade element is proportional to the cross product of circulation and the component of relative velocity normal to the thrust [25]. Thus the elemental thrust is given by:

$$dT = \rho\Gamma(\Omega r - u_{\theta 0})\, dr \tag{A.5.2}$$

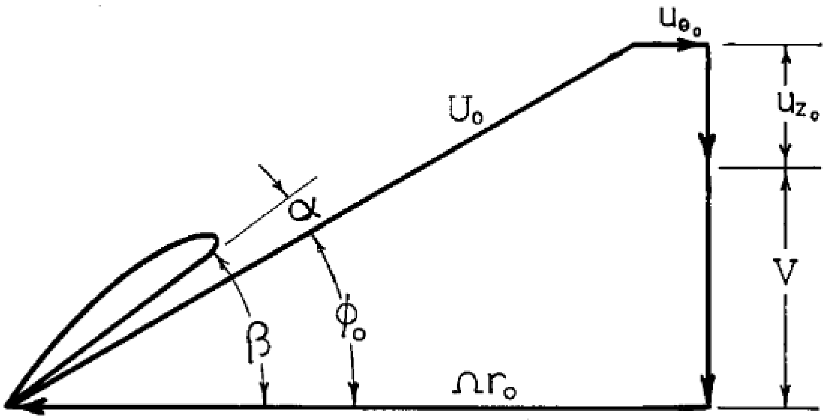

Figure A.9 Blade Element Velocity Diagram [25].

Substitution of Equation A.5.1 into A.5.2 and integrating over the diameter of the propeller yields the following expression for the thrust at the propeller plane:

$$T_0 = \rho\pi R_0^2 V_\infty^2 \overline{w}(1+\overline{w}) \int_{x_h}^{1} G(x_1)(x_0 - \lambda\overline{u}_{\theta 0})\, dx_0 \tag{A.5.3}$$

Where:

$$\bar{u}_{\theta 0} = \frac{\frac{1}{2}\bar{w}(1+\bar{w})\left(\frac{\lambda}{x_0}\right)}{(1+\frac{\lambda_2^2}{x_1^2})} \tag{A.5.4}$$

as defined by Wald [25, pp. 113].

Applying a continuity relation between the fluid flow through the propeller and the trailing slipstream yields:

$$(V_\infty + u_{z0})2\pi r_0 dr_0 = (V_\infty + u_{z1})2\pi r_1 dr_1 \tag{A.5.5}$$

Representing the ratio of the velocity terms by the constant K, assuming the ratio remains constant, results in the following integral relation:

$$K\int_{r_h}^{r_0} r_0 dr_0 = \int_0^{r_1} r_1 dr_1 \tag{A.5.6}$$

Or equivalently:

$$K\left(\frac{R_0}{R_1}\right)^2 \int_{x_h}^{x_0} x_0 dx_0 = \int_0^{x_1} x_1 dx_1 \tag{A.5.7}$$

Where x_h is the dimensionless radial coordinate at the hub. The result of the above integral is simply therefore:

$$x_0^2 = \frac{x_h^2 + x_1^2\left(\frac{R_1}{R_0}\right)^2}{K} \tag{A.5.8}$$

By applying the boundary condition at the tip of the propeller and the edge of the trailing slipstream where $x_0 = 1$ and $x_1 = 1$, results in the following:

$$\frac{\left(\frac{R_1}{R_0}\right)^2}{K} = 1 - x_h^2 \tag{A.5.9}$$

Finally an expression relating the dimensionless radial coordinates of the propeller and trailing vortex system is obtained:

$$x_0^2 = x_h^2 + x_1^2\left(1 - x_h^2\right) \tag{A.5.10}$$

By the application of Equation A.5.10 above, the first term of thrust integral of Equation A.5.3 can therefore be evaluated as following:

$$\int_{x_h}^{1} 2G(x_1)x_0 dx_0 = \left(1 - x_h^2\right)\int_0^1 2G(x_1)x_1 dx_1 = \left(1 - x_h^2\right)\kappa \tag{A.5.11}$$

Similarly, by application of Equation A.5.4 and A.5.10, the second term of the thrust integral can be evaluated as:

$$\int_{x_h}^{1} 2G(x_1)\bar{u}_{\theta 0}\, dx_0 = \tfrac{1}{2}\bar{w}(1 + \bar{w})\,\lambda\, I_1 \tag{A.5.12}$$

Where:

$$I_1 \equiv \int_0^1 \frac{2G(x_1)x_1^3 dx_1}{\left(x_1^2 + \lambda_2^2\right)\left(x_1^2 + c\right)} \tag{A.5.13}$$

and:

$$c = \frac{x_h^2}{\left(1 - x_h^2\right)} \tag{A.5.14}$$

as defined by Wald [25, pp. 114]

Substituting the results of Equation A.5.11 and A.5.12 into the thrust integral, Equation A.5.3, the thrust at the propeller plane is given by:

$$T_{0=}\ \rho\pi R_0^2 V_\infty^2 \bar{w}(1 + \bar{w})\left[\kappa\left(1 - x_h^2\right) - \tfrac{1}{2}\bar{w}(1 + \bar{w})\lambda^2 I_1\right] \tag{A.5.15}$$

Equating this thrust at the propeller plane, generated by the bound circulation, with the thrust resulting in the backward motion of the helicoidal vortex system, Equation A.4.28, yields the following equation for the ratio of the propeller radius to the radius of the helicoidal vortex sheet:

$$\left(\frac{R_0}{R_1}\right)^2 = \frac{\dfrac{\left[1 + \bar{w}\left(\frac{1}{2} + \frac{\varepsilon}{\kappa}\right)\right]}{(1 + \bar{w})}}{\left(1 - x_h^2\right) - \frac{1}{2}\bar{w}(1 + \bar{w})\lambda^2 \frac{I_1}{\kappa}} \tag{A.5.16}$$

Appendix B

Goldstein and Theodorsen Propeller Vortex Theory Tables

B.1 Goldstein Circulation Function Tables

Table B.1.1 Two-Bladed Propeller [25]:

The Goldstein function $G(x, \lambda_2)$ $B = 2$

x	0.2	0.3	0.4	0.5	0.6	0.7
$1/\lambda_2$						
0.25	.00385	.00562	.00719	.00847	.00936	.00972
0.50	.01500	.02181	.02779	.03258	.03581	.03691
0.75	.03248	.04703	.05954	.06929	.07548	.07706
1.00	.05517	.07941	.09976	.11506	.12410	.12538
1.25	.08188	.11706	.14583	.16660	.17789	.17794
1.50	.11152	.15826	.19541	.22114	.23394	.23194
1.75	.14308	.20148	.24658	.27656	.29011	.28547
2.00	.17572	.24547	.29782	.33128	.34497	.33735
2.25	.20873	.28922	.34799	.38419	.39757	.38683
2.50	.24158	.33198	.39628	.43457	.44732	.43351
2.75	.27382	.37321	.44215	.48197	.49392	.47721
3.00	.30518	.41254	.48529	.52617	.53722	.51785
3.25	.33542	.44974	.52553	.56708	.57722	.55549
3.50	.36444	.48472	.56284	.60474	.61400	.59023
3.75	.39215	.51744	.59725	.63924	.64770	.62222
4.00	.41854	.54794	.62889	.67076	.67850	.65163
4.25	.44357	.57628	.65788	.69946	.70657	.67877
4.50	.46734	.60258	.68440	.72555	.73212	.70341
4.75	.48989	.62696	.70862	.74923	.75536	.72614
5.00	.51120	.64953	.73071	.77069	.77646	.74698
5.25	.53140	.67043	.75086	.79013	.79562	.76610
5.50	.55052	.68978	.76923	.80773	.81300	.78363
5.75	.56869	.70770	.78598	.82366	.82878	.79974
6.00	.58589	.72432	.80125	.83808	.84310	.81452
7.00	.64642	.77971	.85021	.88336	.88830	.86263
8.00	.69603	.82137	.88463	.91400	.91913	.89725
9.00	.73713	.85326	.90927	.93500	.94032	.92240
10.00	.77150	.87807	.92726	.94964	.95507	.94083
11.00	.80045	.89762	.94063	.96005	.96545	.95445
12.00	.82497	.91324	.95078	.96760	.97286	.96460

The Goldstein function $G(x, \lambda_2)$ $B = 2$

x	0.8	0.85	0.90	0.925	0.950	0.975
$1/\lambda_2$						
0.25	.00929	.00864	.00754	.00673	.00564	.00405
0.50	.03502	.03244	.02818	.02512	.02104	.01510
0.75	.07236	.06668	.05764	.05124	.04283	.03074
1.00	.11649	.10679	.09186	.08148	.06798	.04879
1.25	.16376	.14944	.12800	.11332	.09440	.06775
1.50	.21172	.19250	.16433	.14526	.12087	.08674
1.75	.25889	.23471	.19984	.17646	.14670	.10526
2.00	.30437	.27535	.23399	.20645	.17153	.12307
2.25	.34766	.31402	.26652	.23501	.19518	.14006
2.50	.38851	.35055	.29727	.26207	.21760	.15617
2.75	.42683	.38488	.32625	.28757	.23878	.17141
3.00	.46262	.41704	.35347	.31158	.25874	.18579
3.25	.49596	.44710	.37903	.33416	.27755	.19938
3.50	.52697	.47518	.40301	.35539	.29529	.21223
3.75	.55575	.50139	.42551	.37538	.31203	.22438
4.00	.58248	.52587	.44666	.39422	.32785	.23589
4.25	.60730	.54874	.46655	.41199	.34283	.24683
4.50	.63035	.57014	.48528	.42880	.35703	.25724
4.75	.65178	.59018	.50297	.44472	.37054	.26716

Table B.1.1 Two-Bladed Propeller (Continued) [25]:

The Goldstein function $G(x, \lambda_2)$ $B = 2$

x	0.8	0.85	0.90	0.925	0.950	0.975
5.00	.67173	.60898	.51969	.45983	.38342	.27666
5.25	.69031	.62663	.53552	.47419	.39570	.28575
5.50	.70762	.64324	.55055	.48789	.40746	.29449
5.75	.72379	.65889	.56483	.50096	.41872	.30290
6.00	.73890	.67365	.57843	.51346	.42954	.31100
7.00	.79037	.72517	.62703	.55863	.46904	.34087
8.00	.83048	.76705	.66816	.59756	.50370	.36751
9.00	.86218	.79808	.70357	.63173	.53466	.39168
10.00	.88748	.83054	.73442	.66209	.56267	.41391
11.00	.90785	.85487	.76155	.68933	.58825	.43454
12.00	.92432	.87548	.78557	.71393	.61178	.45384

Table B.1.2 Three-Bladed Propeller [25]:

The Goldstein function $G(x, \lambda_2)$ $B = 3$

x	0.2	0.3	0.4	0.5	0.6	0.7
$1/\lambda_2$						
0.25	.00408	.00661	.00900	.01105	.01257	.01332
0.50	.01588	.02565	.03476	.04244	.04797	.05049
0.75	.03433	.05512	.07417	.08985	.10065	.10489
1.00	.05808	.09254	.12345	.14811	.16425	.16940
1.25	.08574	.13540	.17885	.21241	.23317	.23814
1.50	.11604	.18140	.23714	.27879	.30315	.30697
1.75	.14790	.22867	.29576	.34432	.37123	.37325
2.00	.18043	.27577	.35287	.40701	.43557	.43544
2.25	.21301	.32168	.40722	.46565	.49512	.49279
2.50	.24516	.36565	.45806	.51960	.54944	.54503
2.75	.27658	.40733	.50504	.56864	.59845	.59220
3.00	.30703	.44646	.54805	.61282	.64232	.63455
3.25	.33640	.48298	.58718	.65237	.68136	.67241
3.50	.36464	.51692	.62261	.68761	.71598	.70617
3.75	.39172	.54839	.65461	.71890	.74657	.73623
4.00	.41760	.57751	.68346	.74665	.77356	.76296
4.25	.44239	.60443	.70944	.77121	.79735	.78672
4.50	.46604	.62932	.73284	.79297	.81830	.80785
4.75	.48861	.65232	.75392	.81222	.83675	.82666
5.00	.51015	.67360	.77292	.82927	.85300	.84339
5.25	.53067	.69328	.79008	.84439	.86734	.85830
5.50	.55025	.71151	.80559	.85782	.87998	.87159
5.75	.56895	.72841	.81962	.86976	.89115	.88345
6.00	.58675	.74408	.83235	.88039	.90103	.89405
7.00	.65005	.79641	.87274	.91281	.93060	.92647
8.00	.70233	.83581	.90094	.93406	.94930	.94761
9.00	.74557	.86585	.92114	.94851	.96155	.96165
10.00	.78140	.88903	.93597	.95869	.96984	.97116
11.00	.81118	.90712	.94710	.96611	.97567	.97773
12.00	.83601	.92140	.95562	.97168	.97991	.98237

The Goldstein function $G(x, \lambda_2)$ $B = 3$

x	0.8	0.85	0.9	0.925	0.950	0.975
$1/\lambda_2$						
0.25	.01295	.01213	.01065	.00954	.00804	.00583
0.50	.04866	.04539	.03970	.03550	.02987	.02165
0.75	.10006	.09283	.08077	.07205	.06048	.04377

Table B.1.2 Three-Bladed Propeller (Continued) [25]:

The Goldstein function $G(x, \lambda_2)$ $B = 3$

x	0.8	0.85	0.9	0.925	0.950	0.975
1.00	.15992	.14762	.12780	.11373	.09527	.06886
1.25	.22276	.20473	.17652	.15681	.13113	.09468
1.50	.28501	.26106	.22441	.19907	.16628	.11998
1.75	.34456	.31485	.27008	.23937	.19978	.14411
2.00	.40032	.36523	.31290	.27717	.23124	.16679
2.25	.45179	.41184	.35264	.31232	.26054	.18796
2.50	.49890	.45466	.38930	.34484	.28773	.20763
2.75	.54176	.49383	.42306	.37486	.31290	.22593
3.00	.58062	.52960	.45411	.40259	.33625	.24296
3.25	.61581	.56225	.48270	.42824	.35794	.25885
3.50	.64764	.59207	.50908	.45202	.37815	.27373
3.75	.67646	.61933	.53346	.47412	.39703	.28769
4.00	.70256	.64431	.55606	.49472	.41106	.30086
4.25	.72623	.66725	.57708	.51399	.43139	.31332
4.50	.74773	.68835	.59666	.53208	.44712	.32515
4.75	.76729	.70782	.61498	.54910	.46200	.33642
5.00	.78512	.72580	.63214	.56515	.47615	.34718
5.25	.80139	.74246	.64827	.58034	.48961	.35749
5.50	.81626	.75790	.66346	.59475	.50247	.36739
5.75	.82987	.77226	.67779	.60844	.51477	.37693
6.00	.84235	.78564	.69134	.62148	.52655	.38613
7.00	.88294	.83081	.73888	.66807	.56939	.42005
8.00	.91222	.86559	.77792	.70747	.60666	.45030
9.00	.93362	.89271	.81042	.74131	.63957	.47772
10.00	.94941	.91403	.83774	.77067	.66897	.50283
11.00	.96113	.93090	.86086	.79632	.69542	.52603
12.00	.96989	.94430	.88050	.81884	.71937	.54758

Table B.1.3 Four-Bladed Propeller [25]:

The Goldstein function $G(x, \lambda_2)$ $B = 4$

x	0.2	0.3	0.4	0.5	0.6	0.7
$1/\lambda_2$						
0.25	.00393	.00698	.01007	.01286	.01505	.01628
0.50	.01530	.02707	.03882	.04926	.05725	.06150
0.75	.03308	.05803	.08251	.10378	.11949	.12711
1.00	.05595	.09706	.13652	.16990	.19356	.20378
1.25	.08255	.14134	.19638	.24159	.27230	.28391
1.50	.11166	.18842	.25834	.31408	.35043	.36232
1.75	.14231	.23638	.31960	.38403	.42452	.43588
2.00	.17371	.28379	.37826	.44940	.49265	.50304
2.25	.20533	.32969	.43322	.50912	.55397	.56322
2.50	.23674	.37350	.48390	.56281	.60835	.61649
2.75	.26766	.41491	.53013	.61056	.65607	.66325
3.00	.29790	.45373	.57200	.65272	.69766	.70406
3.25	.32734	.49002	.60974	.68976	.73374	.73957
3.50	.35583	.52375	.64368	.72222	.76495	.77040
3.75	.38340	.55507	.67414	.75063	.79191	.79716
4.00	.40995	.58412	.70148	.77548	.81519	.82038
4.25	.43547	.61102	.72601	.79725	.83531	.84053
4.50	.45996	.63592	.74805	.81634	.85272	.85805
4.75	.48344	.65896	.76787	.83310	.86780	.87329
5.00	.50595	.68029	.78570	.84787	.88089	.88657
5.25	.52742	.70003	.80180	.86091	.89230	.89817
5.50	.54795	.71831	.81633	.87245	.90225	.90831
5.75	.56752	.73523	.82948	.88269	.91096	.91721

Table B.1.3 Four-Bladed Propeller (Continued) [25]:

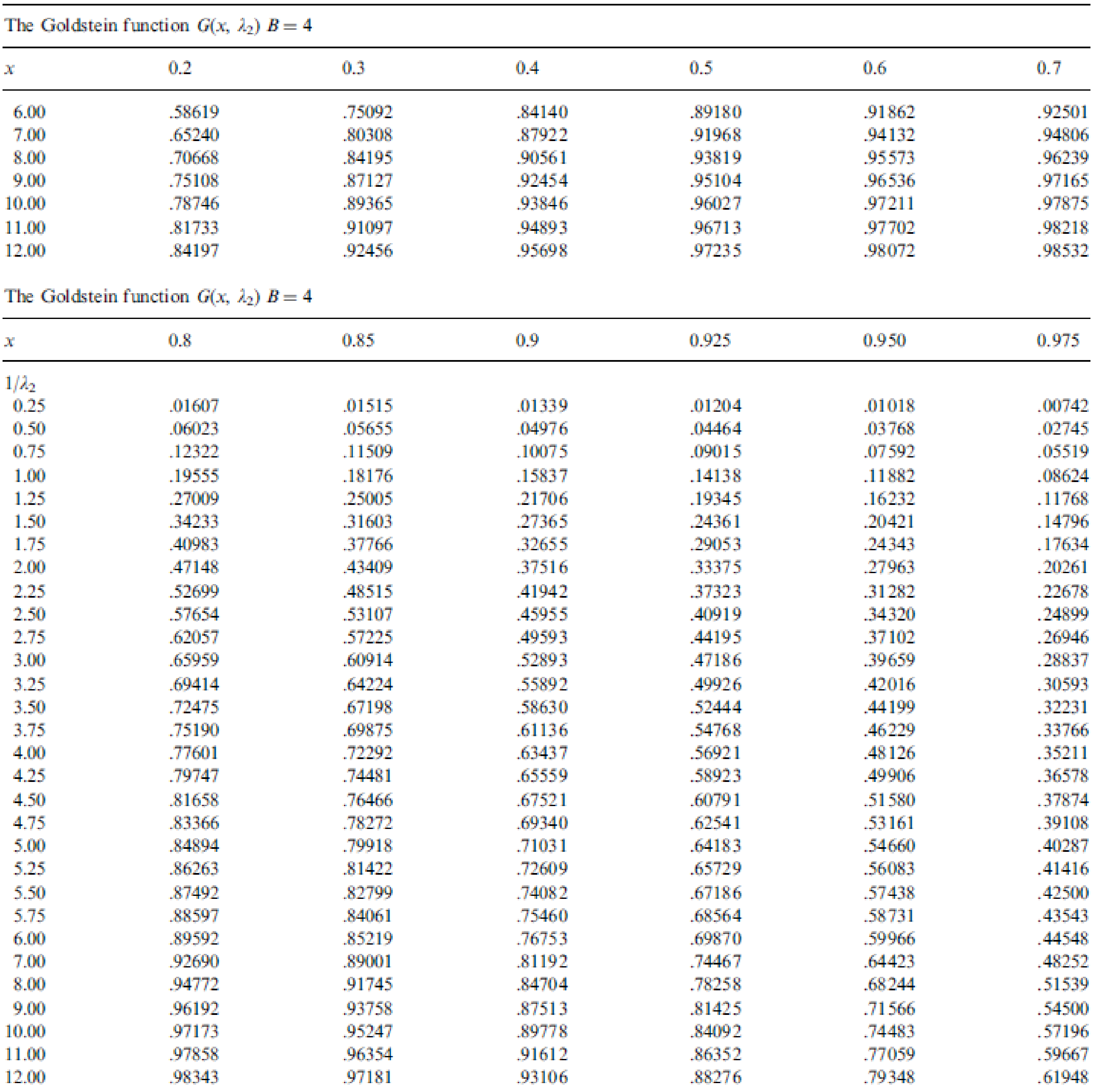

The Goldstein function $G(x, \lambda_2)$ $B = 4$

x	0.2	0.3	0.4	0.5	0.6	0.7
6.00	.58619	.75092	.84140	.89180	.91862	.92501
7.00	.65240	.80308	.87922	.91968	.94132	.94806
8.00	.70668	.84195	.90561	.93819	.95573	.96239
9.00	.75108	.87127	.92454	.95104	.96536	.97165
10.00	.78746	.89365	.93846	.96027	.97211	.97875
11.00	.81733	.91097	.94893	.96713	.97702	.98218
12.00	.84197	.92456	.95698	.97235	.98072	.98532

The Goldstein function $G(x, \lambda_2)$ $B = 4$

x	0.8	0.85	0.9	0.925	0.950	0.975
$1/\lambda_2$						
0.25	.01607	.01515	.01339	.01204	.01018	.00742
0.50	.06023	.05655	.04976	.04464	.03768	.02745
0.75	.12322	.11509	.10075	.09015	.07592	.05519
1.00	.19555	.18176	.15837	.14138	.11882	.08624
1.25	.27009	.25005	.21706	.19345	.16232	.11768
1.50	.34233	.31603	.27365	.24361	.20421	.14796
1.75	.40983	.37766	.32655	.29053	.24343	.17634
2.00	.47148	.43409	.37516	.33375	.27963	.20261
2.25	.52699	.48515	.41942	.37323	.31282	.22678
2.50	.57654	.53107	.45955	.40919	.34320	.24899
2.75	.62057	.57225	.49593	.44195	.37102	.26946
3.00	.65959	.60914	.52893	.47186	.39659	.28837
3.25	.69414	.64224	.55892	.49926	.42016	.30593
3.50	.72475	.67198	.58630	.52444	.44199	.32231
3.75	.75190	.69875	.61136	.54768	.46229	.33766
4.00	.77601	.72292	.63437	.56921	.48126	.35211
4.25	.79747	.74481	.65559	.58923	.49906	.36578
4.50	.81658	.76466	.67521	.60791	.51580	.37874
4.75	.83366	.78272	.69340	.62541	.53161	.39108
5.00	.84894	.79918	.71031	.64183	.54660	.40287
5.25	.86263	.81422	.72609	.65729	.56083	.41416
5.50	.87492	.82799	.74082	.67186	.57438	.42500
5.75	.88597	.84061	.75460	.68564	.58731	.43543
6.00	.89592	.85219	.76753	.69870	.59966	.44548
7.00	.92690	.89001	.81192	.74467	.64423	.48252
8.00	.94772	.91745	.84704	.78258	.68244	.51539
9.00	.96192	.93758	.87513	.81425	.71566	.54500
10.00	.97173	.95247	.89778	.84092	.74483	.57196
11.00	.97858	.96354	.91612	.86352	.77059	.59667
12.00	.98343	.97181	.93106	.88276	.79348	.61948

Table B.1.4 Five-Bladed Propeller [25]:

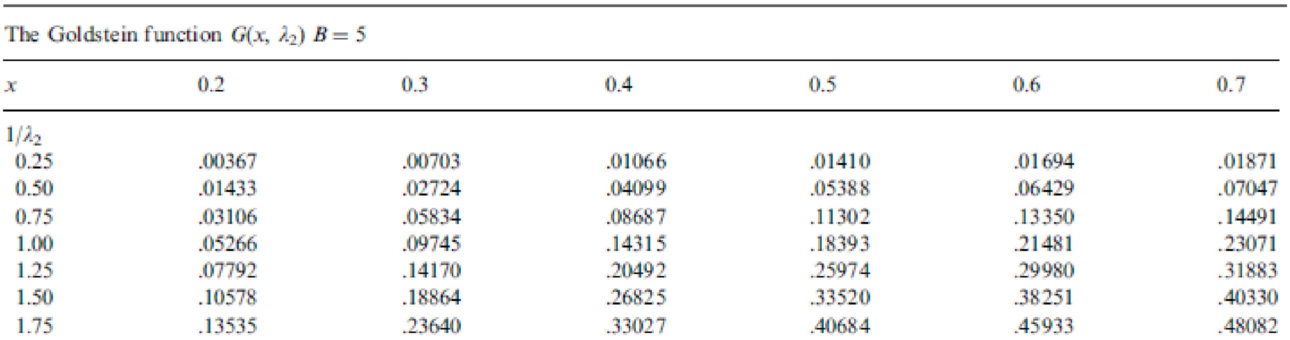

The Goldstein function $G(x, \lambda_2)$ $B = 5$

x	0.2	0.3	0.4	0.5	0.6	0.7
$1/\lambda_2$						
0.25	.00367	.00703	.01066	.01410	.01694	.01871
0.50	.01433	.02724	.04099	.05388	.06429	.07047
0.75	.03106	.05834	.08687	.11302	.13350	.14491
1.00	.05266	.09745	.14315	.18393	.21481	.23071
1.25	.07792	.14170	.20492	.25974	.29980	.31883
1.50	.10578	.18864	.26825	.33520	.38251	.40330
1.75	.13535	.23640	.33027	.40684	.45933	.48082

Table B.1.4 Five-Bladed Propeller (Continued) [25]:

The Goldstein function $G(x, \lambda_2)$ $B = 5$

x	0.2	0.3	0.4	0.5	0.6	0.7
$1/\lambda_2$						
2.00	.16593	.28366	.38919	.47273	.52847	.54996
2.25	.19701	.32951	.44401	.53203	.58941	.61049
2.50	.22816	.37336	.49429	.58463	.64237	.66283
2.75	.25912	.41491	.53997	.63087	.68389	.70776
3.00	.28964	.45400	.58124	.67128	.72701	.74613
3.25	.31953	.49061	.61835	.70649	.76035	.77884
3.50	.34862	.52474	.65168	.73713	.78879	.80668
3.75	.37688	.55647	.68156	.76381	.81305	.83040
4.00	.40422	.58593	.70837	.78706	.83379	.85063
4.25	.43056	.61323	.73240	.80737	.85157	.86792
4.50	.45588	.63849	.75398	.82516	.86684	.88272
4.75	.48016	.66185	.77338	.84077	.88002	.89543
5.00	.50345	.68346	.79083	.85452	.89142	.90637
5.25	.52569	.70342	.80656	.86667	.90134	.91583
5.50	.54689	.72187	.82075	.87744	.91000	.92402
5.75	.56712	.73892	.83358	.88701	.91759	.93114
6.00	.58638	.75469	.84521	.89555	.92427	.93736
7.00	.65444	.80681	.88202	.92183	.94429	.95556
8.00	.70979	.84530	.90764	.93947	.95728	.96686
9.00	.75471	.87409	.92601	.95183	.96619	.97427
10.00	.79119	.89595	.93951	.96079	.97256	.97939
11.00	.82094	.91281	.94969	.96748	.97729	.98308
12.00	.84530	.92601	.95753	.97259	.98088	.98583

The Goldstein function $G(x, \lambda_2)$ $B = 5$

x	0.8	0.85	0.9	0.925	0.950	0.975
$1/\lambda_2$						
0.25	.01876	.01781	.01583	.01427	.01211	.00886
0.50	.07011	.06626	.05866	.05277	.04468	.03266
0.75	.14273	.13422	.11823	.10610	.08962	.06538
1.00	.22503	.21065	.18474	.16544	.13946	.10158
1.25	.30845	.28771	.25151	.22490	.18934	.13776
1.50	.38777	.36085	.31485	.28131	.23666	.17213
1.75	.46036	.42791	.37310	.33330	.25834	.20424
2.00	.52529	.48817	.42578	.38048	.32021	.23306
2.25	.58254	.54172	.47306	.42305	.35634	.25961
2.50	.63262	.58906	.51536	.46140	.38910	.28385
2.75	.67624	.63083	.55324	.49601	.41890	.30605
3.00	.71416	.66768	.58725	.52733	.44610	.32651
3.25	.74714	.70025	.61787	.55582	.47107	.34545
3.50	.77583	.72911	.64555	.58184	.49411	.36308
3.75	.80083	.75475	.67067	.60570	.51547	.37959
4.00	.82266	.77758	.69356	.62769	.53535	.39511
4.25	.84176	.79796	.71448	.64802	.55394	.40979
4.50	.85850	.81622	.73365	.66688	.57139	.42369
4.75	.87321	.83261	.75129	.68445	.58781	.43693
5.00	.88616	.84735	.76756	.70083	.60333	.44955
5.25	.89757	.86062	.78258	.71616	.61802	.46164
5.50	.90766	.87260	.79648	.73054	.63194	.47323
5.75	.91658	.88344	.80938	.74404	.64520	.48437
6.00	.92449	.89325	.82135	.75674	.65781	.49509
7.00	.94829	.92420	.86155	.80075	.70286	.53446
8.00	.96344	.94540	.89206	.83600	.74084	.56919
9.00	.97330	.96011	.91547	.86457	.77326	.60022
10.00	.97986	.97042	.93355	.88787	.80118	.62826
11.00	.98435	.97771	.94756	.90699	.82537	.65378
12.00	.98749	.98291	.95847	.92272	.84643	.67711

Table B.1.4 Six-Bladed Propeller [25]:

The Goldstein function $G(x, \lambda_2)$ $B = 6$

x	0.2	0.3	0.4	0.5	0.6	0.7
$1/\lambda_2$						
0.25	.00343	.00693	.01093	.01493	.01840	.02072
0.50	.01341	.02685	.04202	.05693	.06960	.07779
0.75	.02915	.05753	.08886	.11899	.14388	.15919
1.00	.04963	.09614	.14606	.19275	.23014	.25186
1.25	.07378	.13991	.20854	.27078	.31904	.34555
1.50	.10067	.18647	.27228	.34758	.40419	.43378
1.75	.12948	.23400	.33448	.41973	.48201	.51322
2.00	.15959	.28120	.39344	.48543	.55095	.58274
2.25	.19043	.32716	.44814	.54407	.61077	.64245
2.50	.22160	.37130	.49831	.59572	.66210	.69315
2.75	.25275	.41325	.54385	.64087	.70574	.73592
3.00	.28363	.45284	.58497	.68016	.74273	.77186
3.25	.31400	.48993	.62196	.71428	.77405	.80205
3.50	.34366	.52459	.65516	.74392	.80059	.82742
3.75	.37253	.55683	.68492	.76969	.82313	.84876
4.00	.40051	.58674	.71159	.79214	.84232	.86679
4.25	.42746	.61443	.73549	.81175	.85876	.88205
4.50	.45338	.64003	.75694	.82892	.87287	.89502
4.75	.47827	.66367	.77619	.84401	.88505	.90609
5.00	.50210	.68549	.79349	.85732	.89561	.91559
5.25	.52485	.70562	.80907	.86908	.90482	.92377
5.50	.54653	.72418	.82311	.87953	.91288	.93085
5.75	.56719	.74130	.83579	.88883	.91999	.93700
6.00	.58684	.75711	.84727	.89713	.92626	.94238
7.00	.65602	.80912	.88353	.92275	.94525	.95821
8.00	.71198	.84727	.90872	.94005	.95776	.96825
9.00	.75711	.87570	.92677	.95220	.96645	.97500
10.00	.79357	.89722	.94005	.96103	.97271	.97978
11.00	.82314	.91379	.95008	.96764	.97738	.98328
12.00	.84727	.92677	.95781	.97272	.98095	.98594

The Goldstein function $G(x,\lambda_2)$ $B = 6$

x	0.80	0.85	0.90	0.925	0.950	0.975
$1/\lambda_2$						
0.25	.02110	.02015	.01802	.01629	.01386	.01018
0.50	.07861	.07479	.06660	.06009	.05102	.03741
0.75	.15929	.15082	.13368	.12032	.10193	.07459
1.00	.24965	.23537	.20778	.18665	.15783	.11533
1.25	.33985	.31941	.28122	.25232	.21313	.15561
1.50	.42418	.39795	.34993	.31383	.26500	.19346
1.75	.50001	.46881	.41226	.36983	.31238	.22817
2.00	.56659	.53149	.46791	.42008	.35515	.25968
2.25	.62427	.58634	.51726	.46496	.39363	.28824
2.50	.67386	.63411	.56095	.50504	.42829	.31418
2.75	.71632	.67567	.59967	.54092	.45964	.33788
3.00	.75263	.71185	.63412	.57320	.48814	.35965
3.25	.78372	.74341	.66486	.60235	.51419	.37979
3.50	.81033	.77101	.69242	.62882	.53814	.39850
3.75	.83319	.79521	.71722	.65295	.56027	.41600
4.00	.85284	.81649	.73961	.67505	.58080	.43245
4.25	.86980	.83525	.75990	.69537	.59993	.44797
4.50	.88446	.85184	.77835	.71411	.61782	.46267
4.75	.89715	.86652	.79516	.73143	.63461	.47664

Table B.1.4 Six-Bladed Propeller [25]:

The Goldstein function $G(x,\lambda_2)$ $B = 6$

x	0.80	0.85	0.90	0.925	0.950	0.975
5.00	.90818	.87956	.81052	.74751	.65039	.48995
5.25	.91778	.89116	.82457	.76244	.66529	.50268
5.50	.92616	.90148	.83745	.77635	.67936	.51487
5.75	.93348	.91071	.84929	.78931	.69269	.52656
6.00	.93991	.91894	.86017	.80143	.70532	.53780
7.00	.95879	.94414	.89583	.84266	.74996	.57888
8.00	.97043	.96059	.92179	.87469	.78689	.61482
9.00	.97789	.97149	.94089	.89983	.81780	.64673
10.00	.98284	.97884	.95504	.91968	.84390	.67531
11.00	.98626	.98389	.96557	.93544	.86603	.70109
12.00	.98871	.98740	.97343	.94797	.88487	.72446

B.2 Theodorsen Mass Coefficient and Axial Tip Loss Factor Tables

Table B.2.1 Mass Coefficient (κ) [25]:

$B =$	2	3	4	5	6
$1/\lambda_2$					
0.25	.00762	.01027	.01239	.01412	.01553
0.50	.02893	.03892	.04678	.05310	.05827
0.75	.06047	.08088	.09670	.1092	.1192
1.00	.09865	.1309	.1552	.1741	.1891
1.25	.1406	.1846	.2170	.2414	.2605
1.50	.1839	.2389	.2781	.3070	.3290
1.75	.2274	.2917	.3362	.3676	.3922
2.00	.2701	.3419	.3903	.4242	.4454
2.25	.3111	.3888	.4396	.4745	.4997
2.50	.3500	.4321	.4842	.5193	.5443
2.75	.3868	.4718	.5243	.5587	.5835
3.00	.4213	.5079	.5601	.5942	.6180
3.25	.4535	.5407	.5922	.6254	.6483
3.50	.4833	.5705	.6209	.6529	.6750
3.75	.5111	.5974	.6465	.6775	.6987
4.00	.5367	.6217	.6695	.6993	.7196
4.25	.5605	.6440	.6901	.7188	.7383
4.50	.5824	.6642	.7087	.7363	.7550
4.75	.6027	.6824	.7255	.7520	.7699
5.00	.6214	.6992	.7407	.7662	.7834
5.25	.6387	.7144	.7545	.7790	.7956
5.50	.6549	.7284	.7671	.7907	.8066
5.75	.6697	.7411	.7785	.8013	.8166
6.00	.6835	.7529	.7891	.8111	.8258
7.00	.7298	.7916	.8233	.8424	.8553
8.00	.7652	.8204	.8484	.8653	.8767
9.00	.7922	.8424	.8676	.8827	.8927
10.00	.8145	.8596	.8826	.8960	.9051
11.00	.8323	.8735	.8942	.9066	.9148
12.00	.8469	.8847	.9037	.9151	.9226

Table B.2.2 Tip Loss Factor to Mass Coefficient Ratio (ε/κ) [25]:

$B =$	2	3	4	5	6
$1/\lambda_2$					
0.75	.122	.132	.143	.152	.159
1.00	.179	.198	.215	.231	.242
1.25	.237	.263	.286	.305	.323
1.50	.289	.324	.354	.382	.394
1.75	.334	.380	.414	.441	.485
2.00	.379	.431	.470	.495	.518
2.25	.422	.478	.520	.550	.550
2.50	.459	.520	.563	.596	.619
2.75	.493	.558	.603	.632	.654
3.00	.525	.594	.637	.663	.686
3.25	.556	.624	.667	.696	.715
3.50	.583	.653	.695	.722	.739
3.75	.608	.680	.719	.744	.761
4.00	.632	.701	.740	.765	.781
4.25	.654	.720	.759	.782	.797
4.50	.674	.741	.776	.798	.812
4.75	.693	.757	.791	.812	.825
5.00	.711	.771	.805	.824	.836
5.50	.740	.799	.828	.845	.857
6.00	.766	.821	.847	.863	.873
7.00	.807	.854	.877	.890	.898
8.00	.840	.878	.897	.909	.916
9.00	.862	.897	.912	.923	.930
10.00	.878	.911	.926	.934	.940

B.3 Graphical Representation of Goldstein Circulation Function, Mass Coefficient and Axial Tip Loss Factor

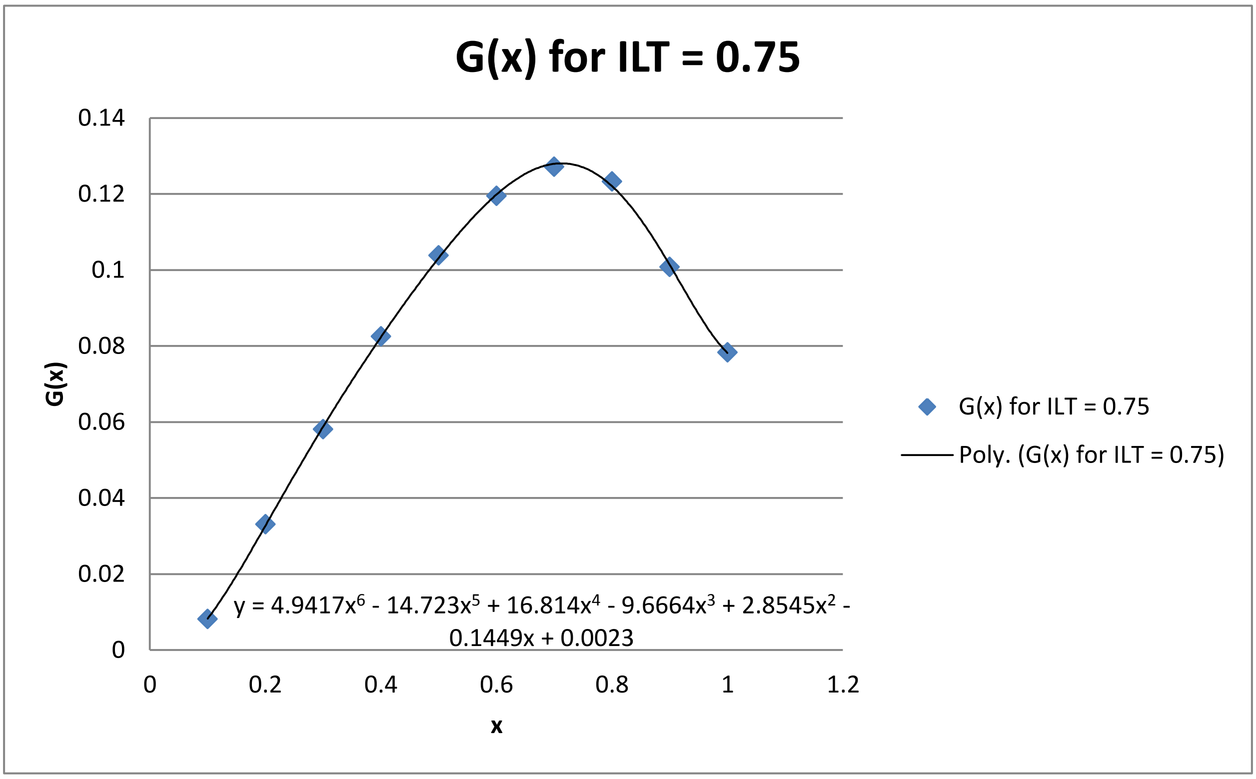

Figure B.1 Goldstein Circulation Function for an Inverse λ_2 Advance Ratio Value of 0.75 for a Four-Bladed Propeller.

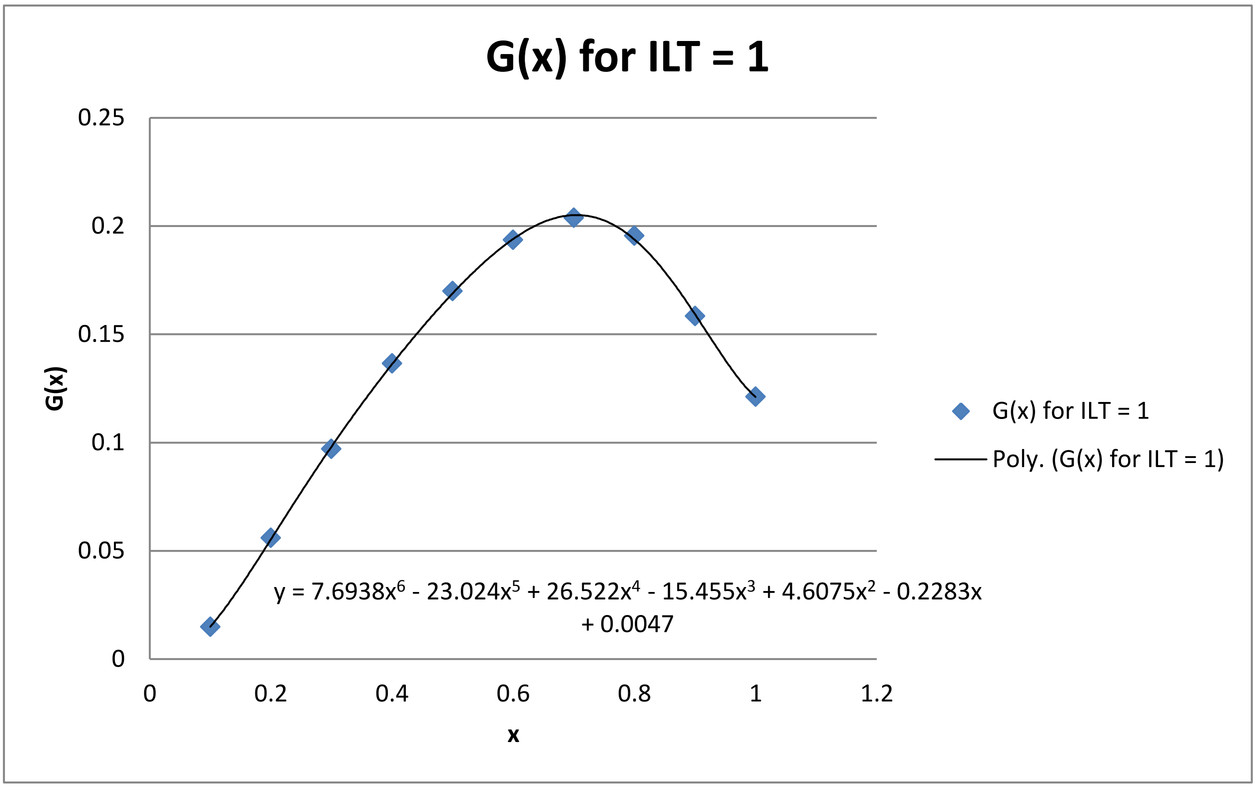

Figure B.2 Goldstein Circulation Function for an Inverse λ_2 Advance Ratio Value of 1 for a Four-Bladed Propeller.

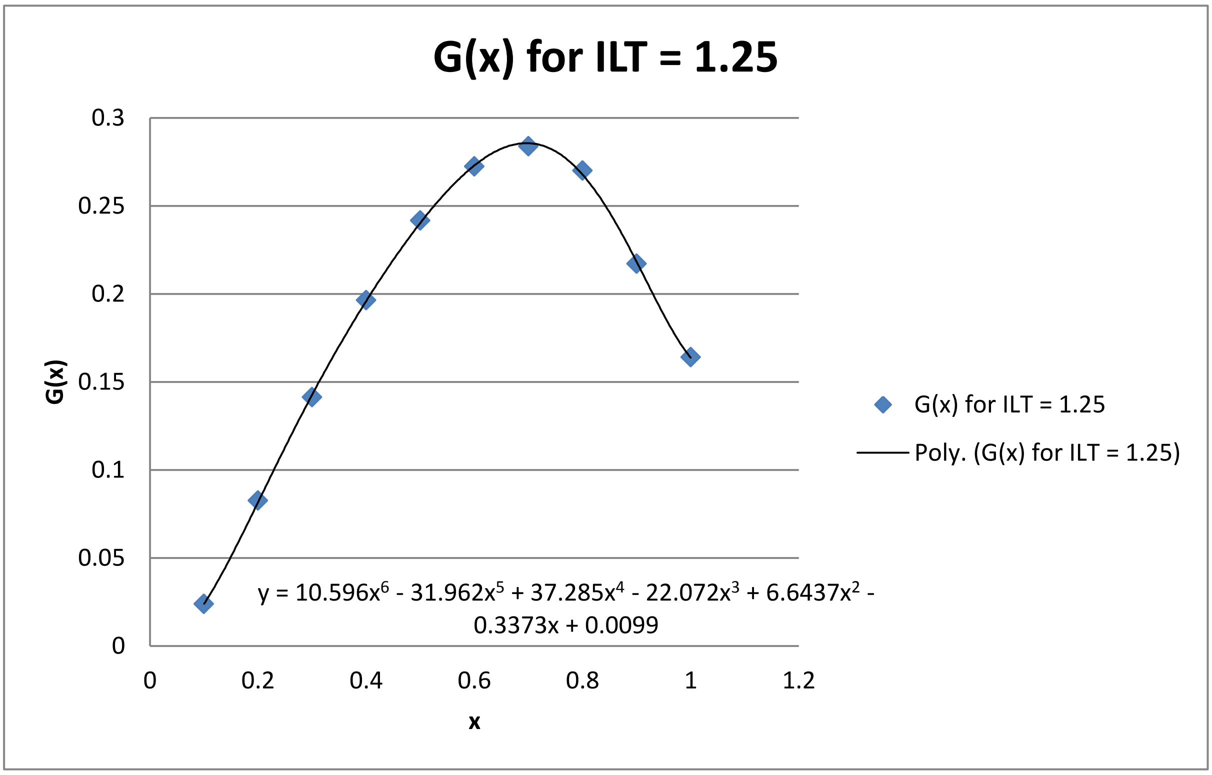

Figure B.3 Goldstein Circulation Function for an Inverse λ_2 Advance Ratio Value of 1.25 for a Four-Bladed Propeller.

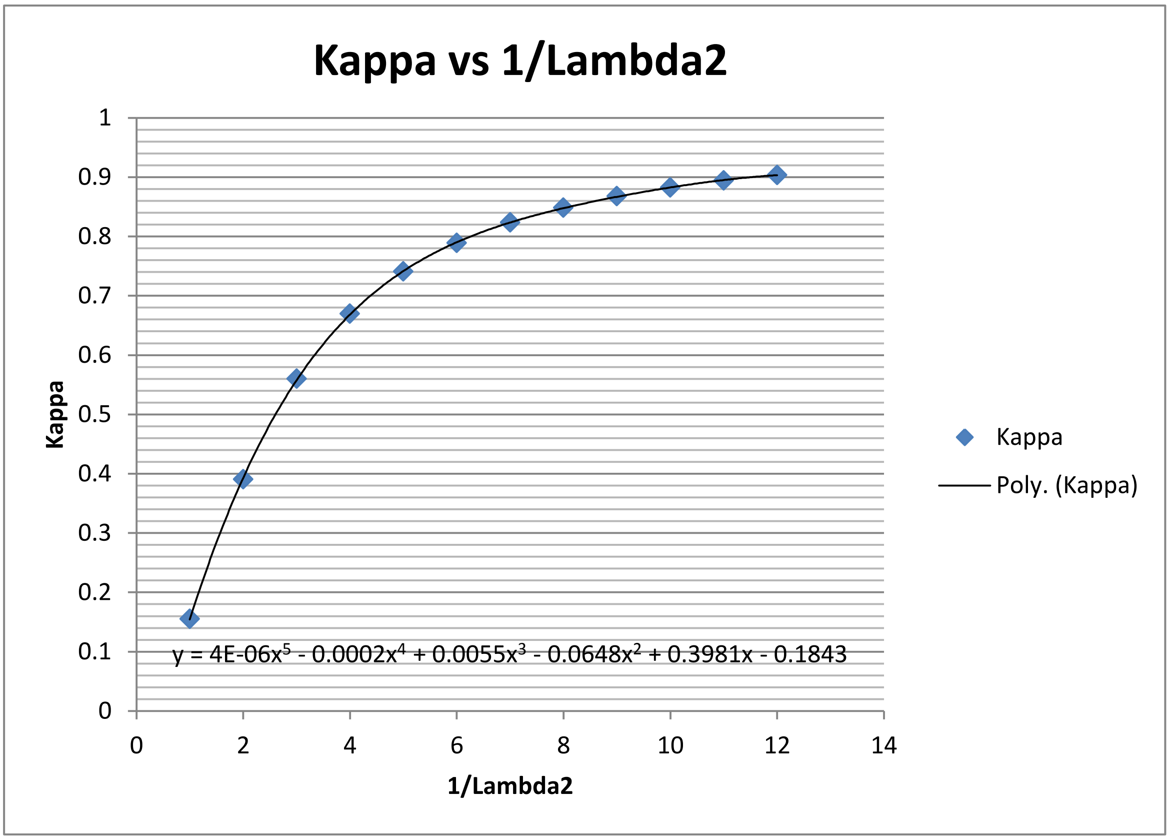

Figure B.4 Kappa versus the Inverse λ_2 Advance Ratio for a Four-Bladed Propeller.

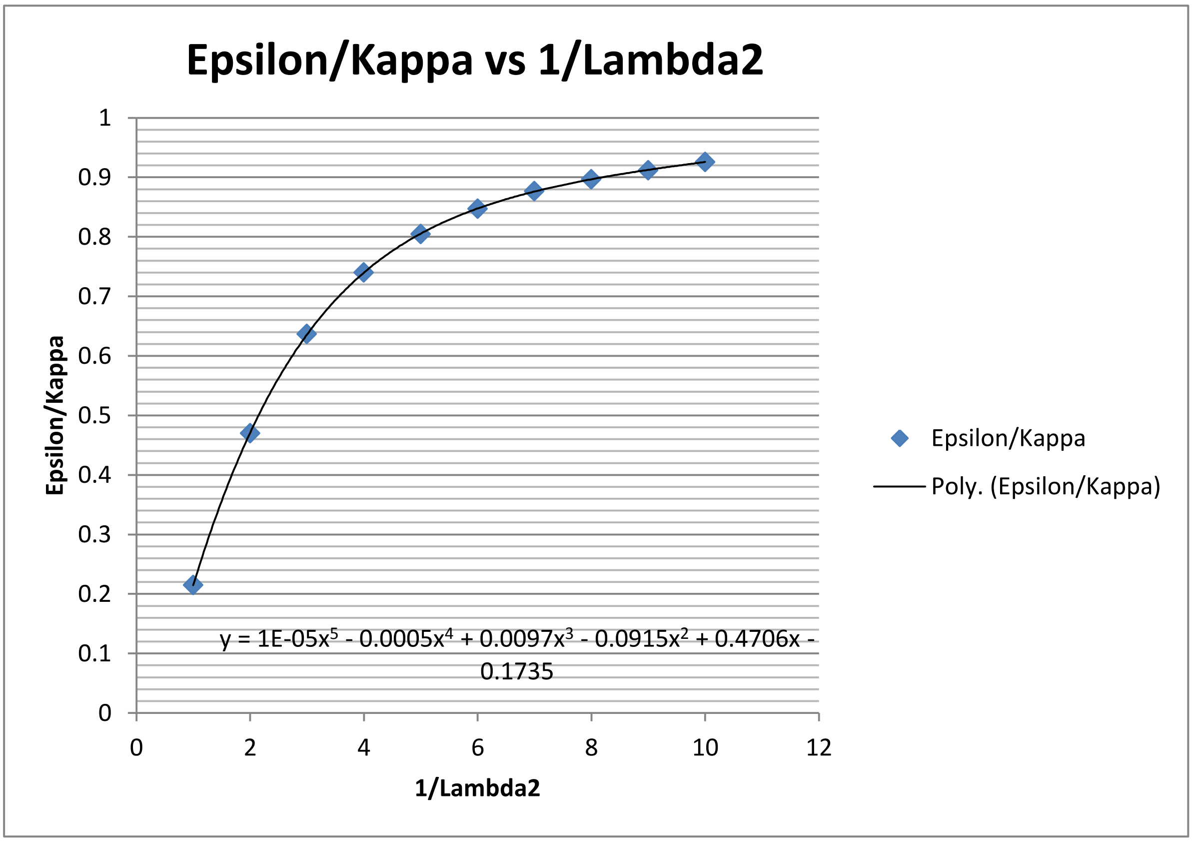

Figure B.5 Epsilon/Kappa versus the Inverse λ_2 Advance Ratio for a Four-Bladed Propeller.

Appendix C

Reference Tables

C.1 Validation Tables – Vertical Velocity Profiles

Table C.1.1 Ehret and Oertel B747 Numerical Vertical Velocity Profile [19]:

y(m)	**w(y)**
-45	2.548
-40	4.246242
-33.4628	6.37
-31.4944	8.281
-29.526	11.2112
-26.8128	16.0524
-25.4296	15.0332
-20.482	-16.562
-20	-20
-18.3008	-18.6004
-16.0664	-14.3325
-12.9808	-11.0838
-8.512	-8.7906
-4.0432	-7.644
0	-7.5166
4.0432	-7.644
8.512	-8.7906
12.9808	-11.0838
16.0664	-14.3325
18.3008	-18.6004
20	-20
20.482	-16.562
25.4296	15.0332
26.8128	16.0524
29.526	11.2112
31.4944	8.281
33.4628	6.37
40	4.246242
45	2.548

Table C.1.2 Burnham et al. Experimental B747 Vertical Velocity Profile [36]:

r(m)	**V(r)**
-15.92	-11.644
-14.16	-12.02612
-12.2672	-12.259
-10.48	-13.776
-8.2672	-14.022
-6.4	-15.17
-5.04	-16.4
-3.2	-17.958
-2.32	-15.498
-0.04	-8.938
3.04	3.854
4.96	9.84
6.48	11.89
7.88	11.562
9	10.25
10.4	9.758
11.46664	9.922
13.12	8.938
14.32	8.159
15.6	6.8306
16.88	5.658
18.2	4.674

C.2 Simulation Atmospheric Conditions

Table C.2.1 Temperature, pressure and density versus Geometric Altitude [49]:

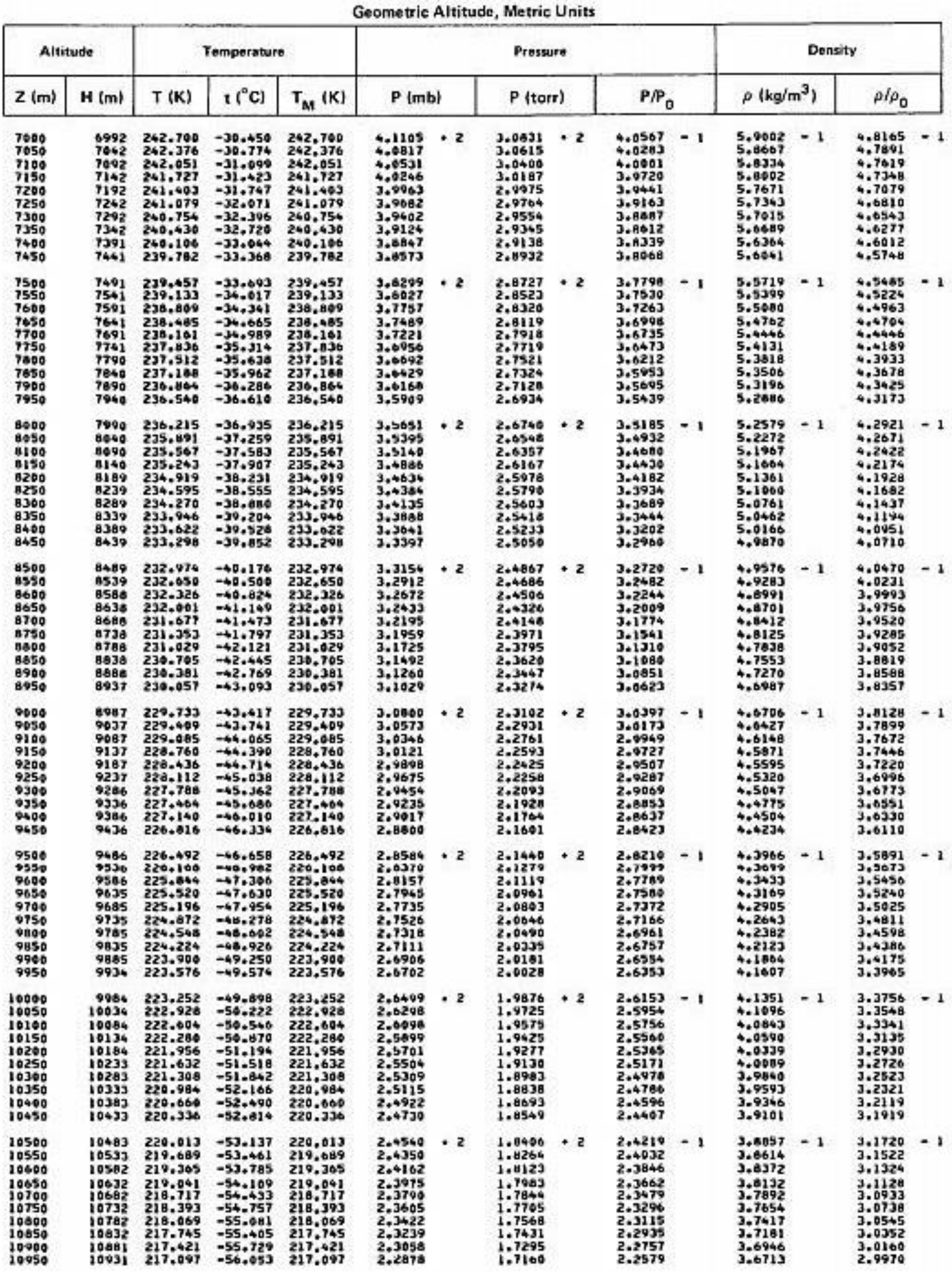

Geometric Altitude, Metric Units

Altitude		Temperature			Pressure			Density	
Z (m)	H (m)	T (K)	t (°C)	T_M (K)	P (mb)	P (torr)	P/P_0	ρ (kg/m^3)	ρ/ρ_0
7000	6992	242.700	-30.450	242.700	4.1105 + 2	3.0831 + 2	4.0567 - 1	5.9002 - 1	4.8165 - 1
7050	7042	242.376	-30.774	242.376	4.0817	3.0615	4.0283	5.8667	4.7891
7100	7092	242.051	-31.099	242.051	4.0531	3.0400	4.0001	5.8334	4.7619
7150	7142	241.727	-31.423	241.727	4.0246	3.0187	3.9720	5.8002	4.7348
7200	7192	241.403	-31.747	241.403	3.9963	2.9975	3.9441	5.7671	4.7079
7250	7242	241.079	-32.071	241.079	3.9682	2.9764	3.9163	5.7343	4.6810
7300	7292	240.754	-32.396	240.754	3.9402	2.9554	3.8887	5.7015	4.6543
7350	7342	240.430	-32.720	240.430	3.9124	2.9345	3.8612	5.6689	4.6277
7400	7391	240.106	-33.044	240.106	3.8847	2.9138	3.8339	5.6364	4.6012
7450	7441	239.782	-33.368	239.782	3.8573	2.8932	3.8068	5.6041	4.5748
7500	7491	239.457	-33.693	239.457	3.8299 + 2	2.8727 + 2	3.7798 - 1	5.5719 - 1	4.5485 - 1
7550	7541	239.133	-34.017	239.133	3.8027	2.8523	3.7530	5.5399	4.5224
7600	7591	238.809	-34.341	238.809	3.7757	2.8320	3.7263	5.5080	4.4963
7650	7641	238.485	-34.665	238.485	3.7489	2.8119	3.6998	5.4762	4.4704
7700	7691	238.161	-34.989	238.161	3.7221	2.7918	3.6735	5.4446	4.4446
7750	7741	237.836	-35.314	237.836	3.6956	2.7719	3.6473	5.4131	4.4189
7800	7790	237.512	-35.638	237.512	3.6692	2.7521	3.6212	5.3818	4.3933
7850	7840	237.188	-35.962	237.188	3.6429	2.7324	3.5953	5.3506	4.3678
7900	7890	236.864	-36.286	236.864	3.6168	2.7128	3.5695	5.3196	4.3425
7950	7940	236.540	-36.610	236.540	3.5909	2.6934	3.5439	5.2886	4.3173
8000	7990	236.215	-36.935	236.215	3.5651 + 2	2.6740 + 2	3.5185 - 1	5.2579 - 1	4.2921 - 1
8050	8040	235.891	-37.259	235.891	3.5395	2.6548	3.4932	5.2272	4.2671
8100	8090	235.567	-37.583	235.567	3.5140	2.6357	3.4680	5.1967	4.2422
8150	8140	235.243	-37.907	235.243	3.4886	2.6167	3.4430	5.1664	4.2174
8200	8189	234.919	-38.231	234.919	3.4634	2.5978	3.4182	5.1361	4.1928
8250	8239	234.595	-38.555	234.595	3.4384	2.5790	3.3934	5.1060	4.1682
8300	8289	234.270	-38.880	234.270	3.4135	2.5603	3.3689	5.0761	4.1437
8350	8339	233.946	-39.204	233.946	3.3888	2.5418	3.3444	5.0462	4.1194
8400	8389	233.622	-39.528	233.622	3.3641	2.5233	3.3202	5.0166	4.0951
8450	8439	233.298	-39.852	233.298	3.3397	2.5050	3.2960	4.9870	4.0710
8500	8489	232.974	-40.176	232.974	3.3154 + 2	2.4867 + 2	3.2720 - 1	4.9576 - 1	4.0470 - 1
8550	8539	232.650	-40.500	232.650	3.2912	2.4686	3.2482	4.9283	4.0231
8600	8588	232.326	-40.824	232.326	3.2672	2.4506	3.2244	4.8991	3.9993
8650	8638	232.001	-41.149	232.001	3.2433	2.4326	3.2009	4.8701	3.9756
8700	8688	231.677	-41.473	231.677	3.2195	2.4148	3.1774	4.8412	3.9520
8750	8738	231.353	-41.797	231.353	3.1959	2.3971	3.1541	4.8125	3.9285
8800	8788	231.029	-42.121	231.029	3.1725	2.3795	3.1310	4.7838	3.9052
8850	8838	230.705	-42.445	230.705	3.1492	2.3620	3.1080	4.7553	3.8819
8900	8888	230.381	-42.769	230.381	3.1260	2.3447	3.0851	4.7270	3.8588
8950	8937	230.057	-43.093	230.057	3.1029	2.3274	3.0623	4.6987	3.8357
9000	8987	229.733	-43.417	229.733	3.0800 + 2	2.3102 + 2	3.0397 - 1	4.6706 - 1	3.8128 - 1
9050	9037	229.409	-43.741	229.409	3.0573	2.2931	3.0173	4.6427	3.7899
9100	9087	229.085	-44.065	229.085	3.0346	2.2761	2.9949	4.6148	3.7672
9150	9137	228.760	-44.390	228.760	3.0121	2.2593	2.9727	4.5871	3.7446
9200	9187	228.436	-44.714	228.436	2.9898	2.2425	2.9507	4.5595	3.7220
9250	9237	228.112	-45.038	228.112	2.9675	2.2258	2.9287	4.5320	3.6996
9300	9286	227.788	-45.362	227.788	2.9454	2.2093	2.9069	4.5047	3.6773
9350	9336	227.464	-45.686	227.464	2.9235	2.1928	2.8853	4.4775	3.6551
9400	9386	227.140	-46.010	227.140	2.9017	2.1764	2.8637	4.4504	3.6330
9450	9436	226.816	-46.334	226.816	2.8800	2.1601	2.8423	4.4234	3.6110
9500	9486	226.492	-46.658	226.492	2.8584 + 2	2.1440 + 2	2.8210 - 1	4.3966 - 1	3.5891 - 1
9550	9536	226.168	-46.982	226.168	2.8370	2.1279	2.7999	4.3699	3.5673
9600	9586	225.844	-47.306	225.844	2.8157	2.1119	2.7789	4.3433	3.5456
9650	9635	225.520	-47.630	225.520	2.7945	2.0961	2.7580	4.3169	3.5240
9700	9685	225.196	-47.954	225.196	2.7735	2.0803	2.7372	4.2905	3.5025
9750	9735	224.872	-48.278	224.872	2.7526	2.0646	2.7166	4.2643	3.4811
9800	9785	224.548	-48.602	224.548	2.7318	2.0490	2.6961	4.2382	3.4598
9850	9835	224.224	-48.926	224.224	2.7111	2.0335	2.6757	4.2123	3.4386
9900	9885	223.900	-49.250	223.900	2.6906	2.0181	2.6554	4.1864	3.4175
9950	9934	223.576	-49.574	223.576	2.6702	2.0028	2.6353	4.1607	3.3965
10000	9984	223.252	-49.898	223.252	2.6499 + 2	1.9876 + 2	2.6153 - 1	4.1351 - 1	3.3756 - 1
10050	10034	222.928	-50.222	222.928	2.6298	1.9725	2.5954	4.1096	3.3548
10100	10084	222.604	-50.546	222.604	2.6098	1.9575	2.5756	4.0843	3.3341
10150	10134	222.280	-50.870	222.280	2.5899	1.9425	2.5560	4.0590	3.3135
10200	10184	221.956	-51.194	221.956	2.5701	1.9277	2.5365	4.0339	3.2930
10250	10233	221.632	-51.518	221.632	2.5504	1.9130	2.5171	4.0089	3.2726
10300	10283	221.308	-51.842	221.308	2.5309	1.8983	2.4978	3.9840	3.2523
10350	10333	220.984	-52.166	220.984	2.5115	1.8838	2.4786	3.9593	3.2321
10400	10383	220.660	-52.490	220.660	2.4922	1.8693	2.4596	3.9346	3.2119
10450	10433	220.336	-52.814	220.336	2.4730	1.8549	2.4407	3.9101	3.1919
10500	10483	220.013	-53.137	220.013	2.4540 + 2	1.8406 + 2	2.4219 - 1	3.8857 - 1	3.1720 - 1
10550	10533	219.689	-53.461	219.689	2.4350	1.8264	2.4032	3.8614	3.1522
10600	10582	219.365	-53.785	219.365	2.4162	1.8123	2.3846	3.8372	3.1324
10650	10632	219.041	-54.109	219.041	2.3975	1.7983	2.3662	3.8132	3.1128
10700	10682	218.717	-54.433	218.717	2.3790	1.7844	2.3479	3.7892	3.0933
10750	10732	218.393	-54.757	218.393	2.3605	1.7705	2.3296	3.7654	3.0738
10800	10782	218.069	-55.081	218.069	2.3422	1.7568	2.3115	3.7417	3.0545
10850	10832	217.745	-55.405	217.745	2.3239	1.7431	2.2935	3.7181	3.0352
10900	10881	217.421	-55.729	217.421	2.3058	1.7295	2.2757	3.6946	3.0160
10950	10931	217.097	-56.053	217.097	2.2878	1.7160	2.2579	3.6713	2.9970

Appendix D

Additional Results

D.1 Vortex Rollup Profiles

Table D.1.1 Lancair Propjet Vortex Rollup Transverse Section Results:

Wing Loading:	No Propeller Effects	Propeller-Wing Vortex Rollup Influence
1g	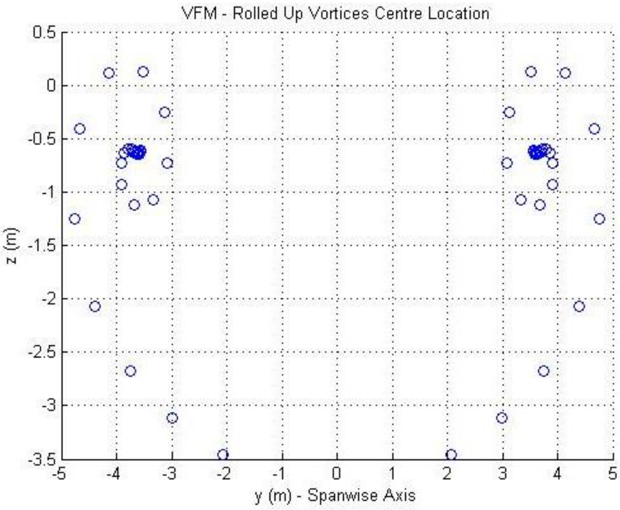	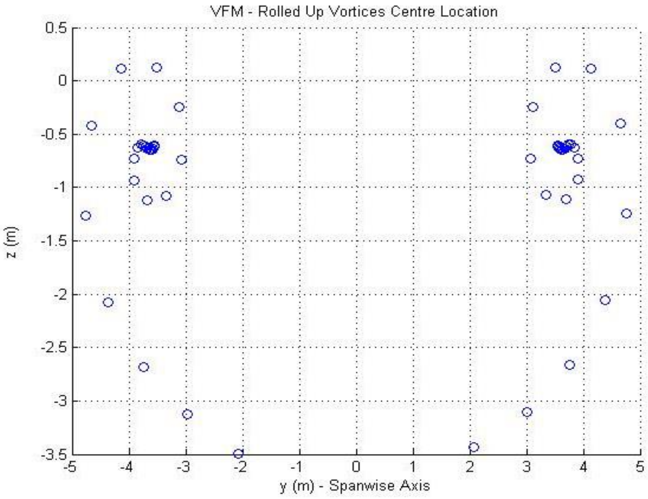
0.75g	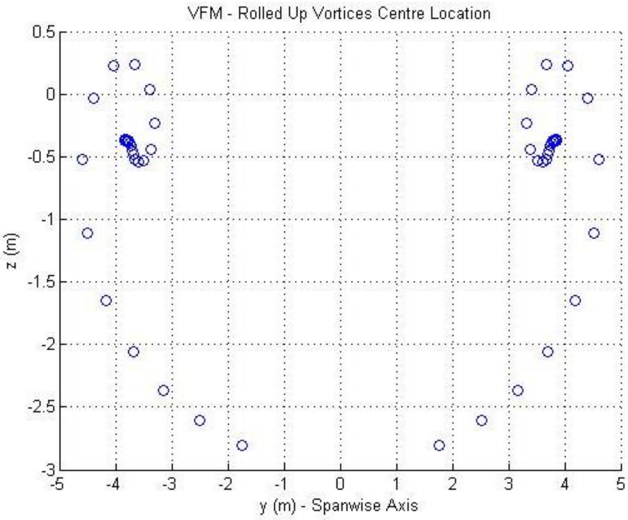	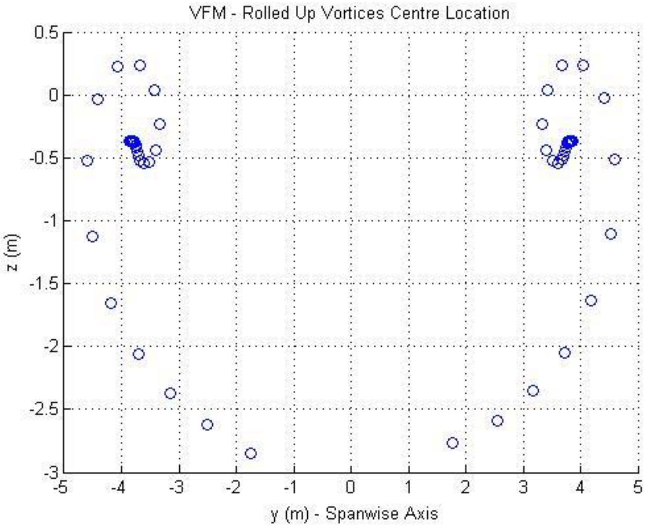

0.5g	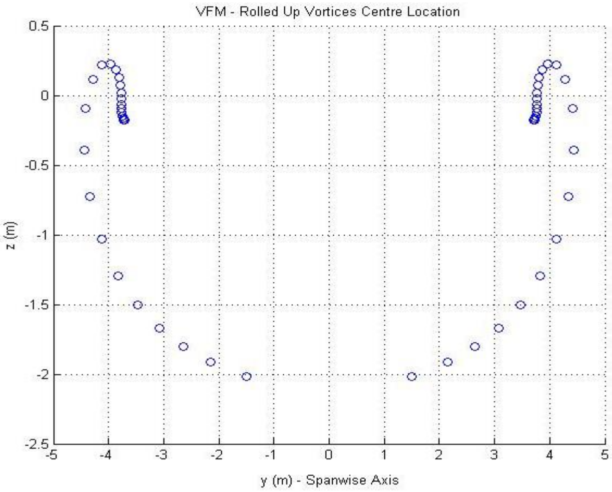	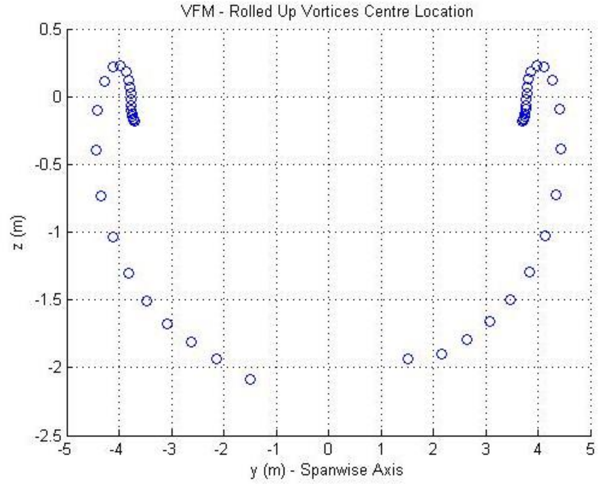
0.25g	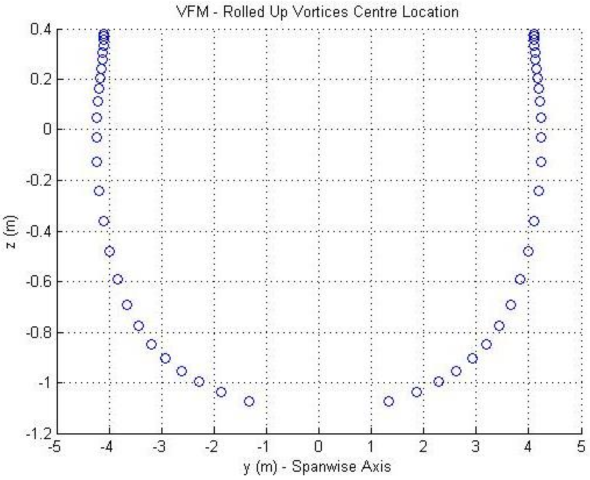	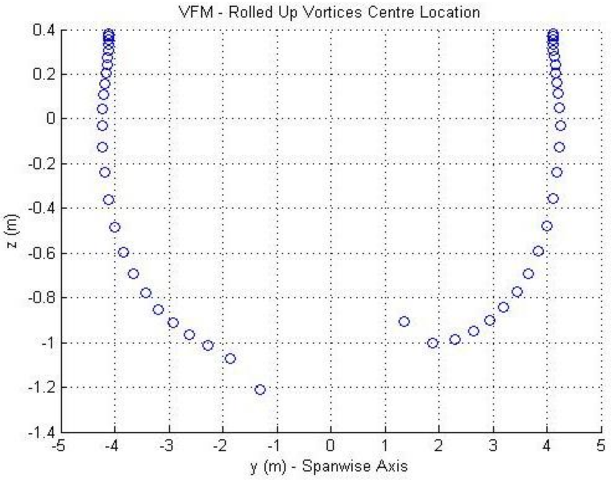

Table D.1.2 ATR 72 Vortex Rollup Transverse Section Results:

Wing Loading:	No Propeller Effects	Propeller-Wing Vortex Rollup Influence
1g	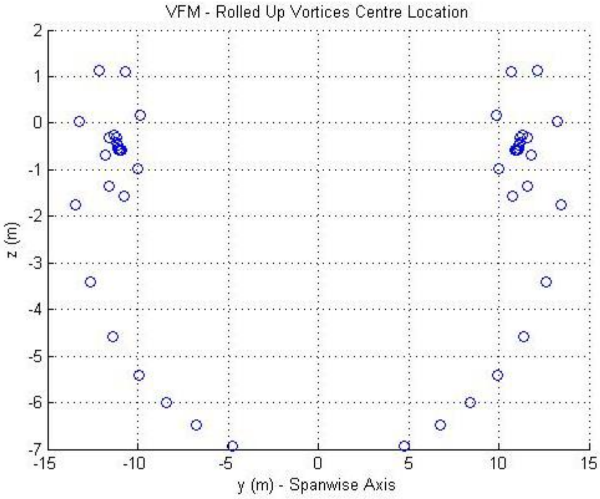	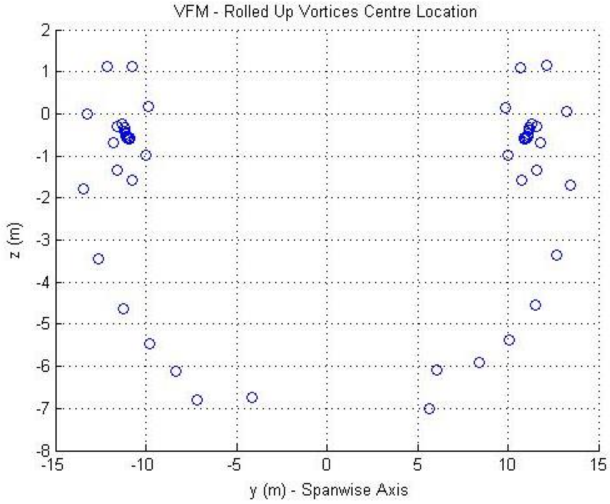

0.75g	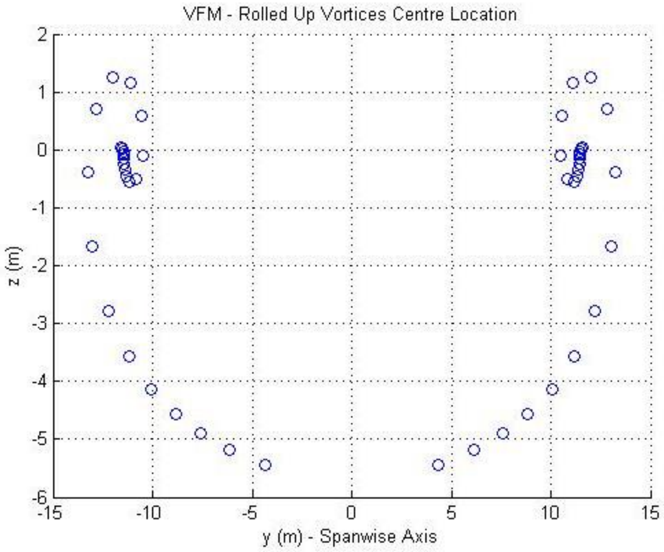	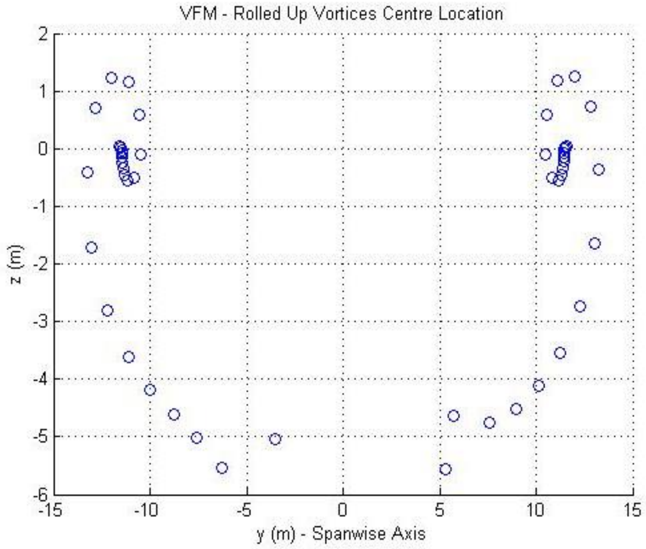
0.5g	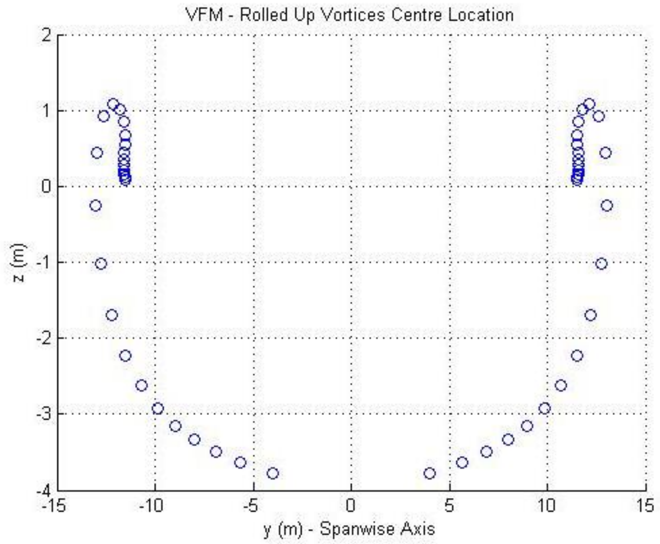	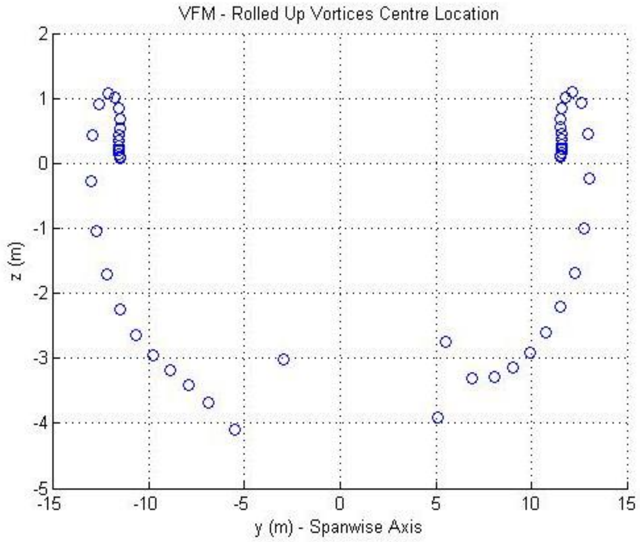
0.25g	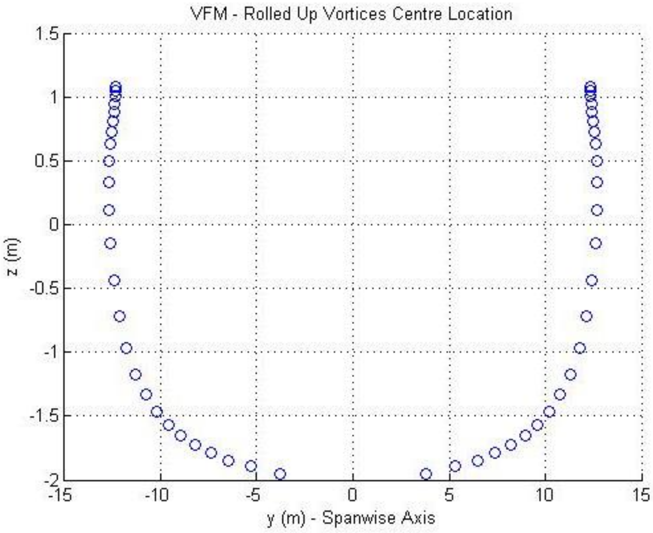	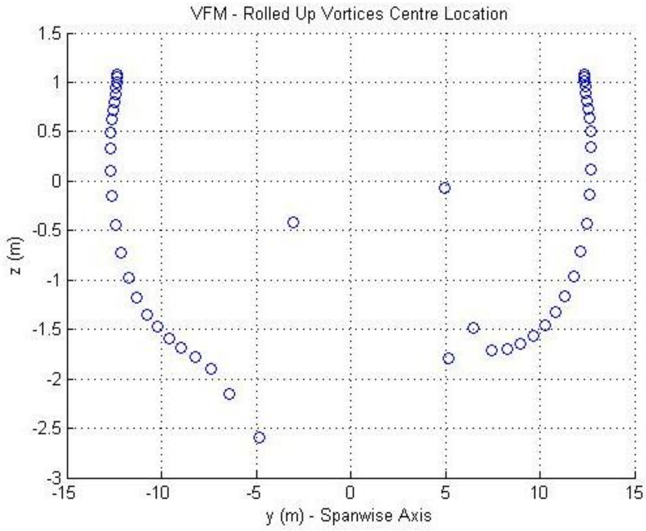

Table D.1.3 ATR 72 (Counter Rotating Turboprop Engines) Vortex Rollup Transverse Section Results:

Wing Loading:	No Propeller Effects	Propeller-Wing Vortex Rollup Influence
1g	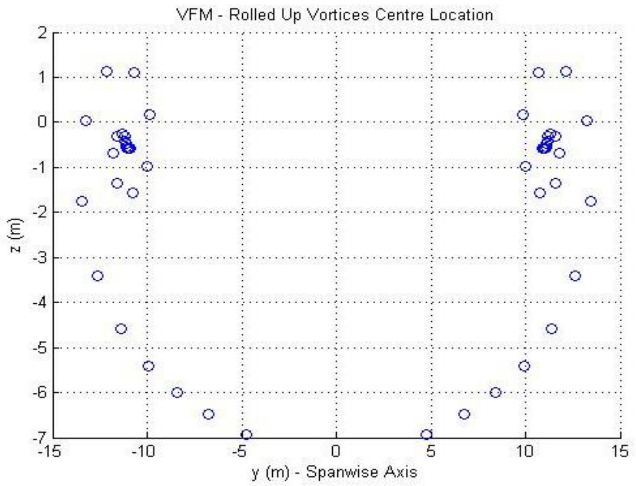	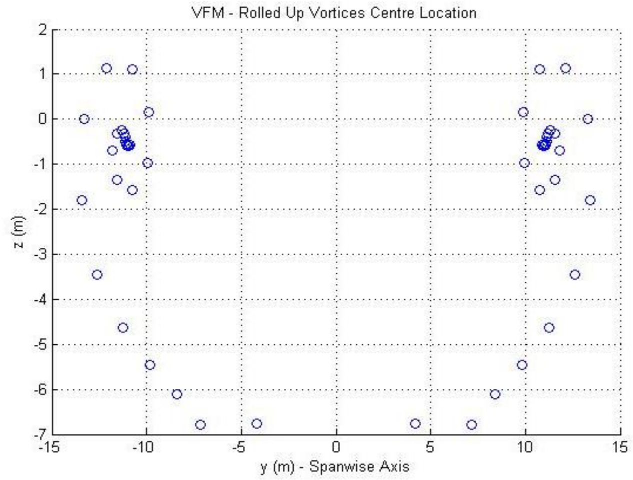
0.75g	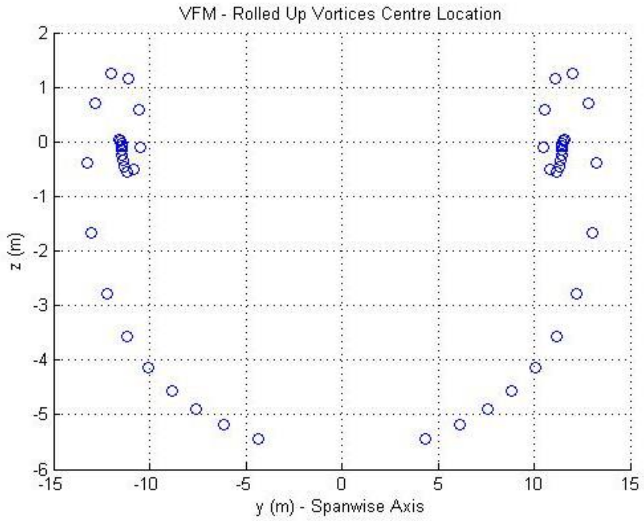	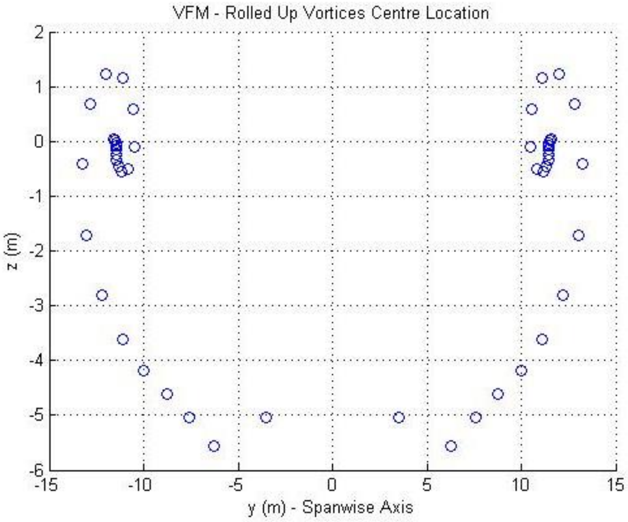
0.5g	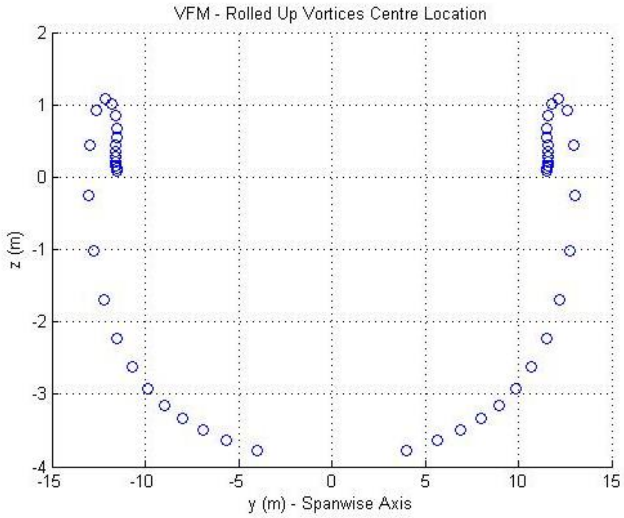	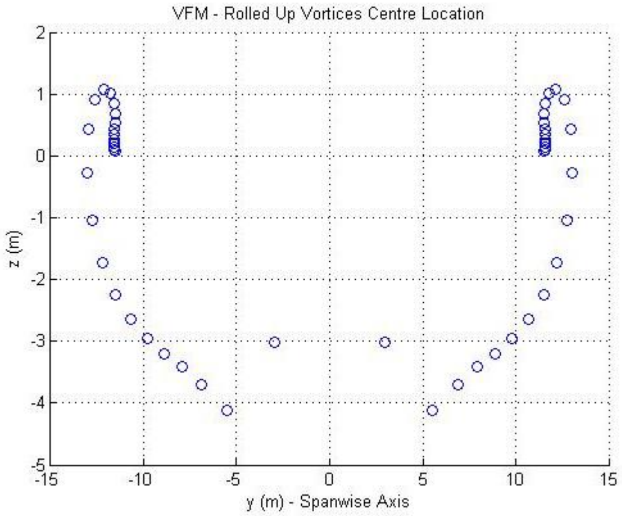

0.25g	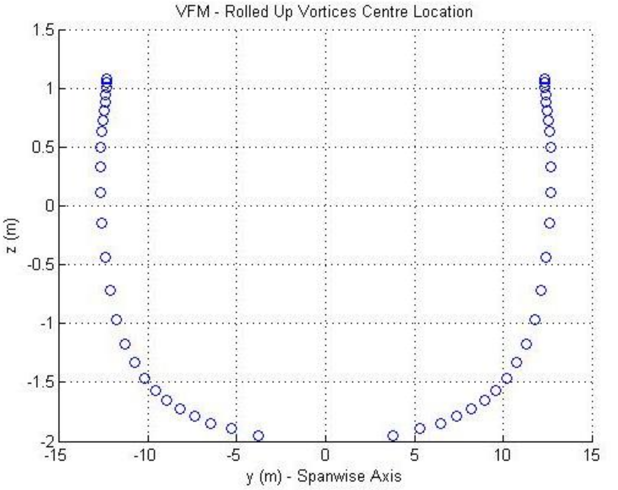	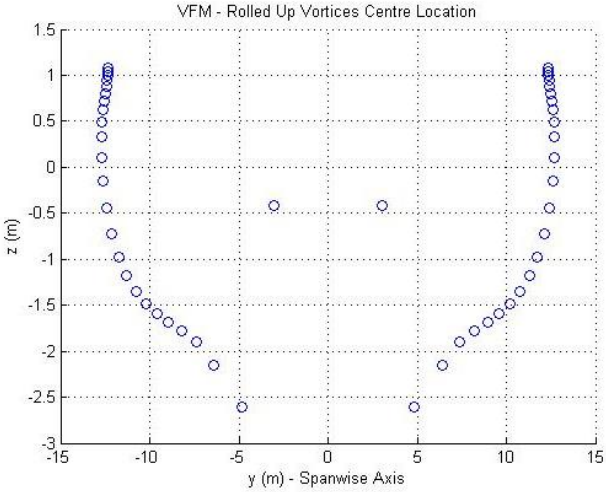

Table D.1.4 Lockheed Martin P-3 Orion Vortex Rollup Transverse Section Results:

Wing Loading:	No Propeller Effects	Propeller-Wing Vortex Rollup Influence
1g	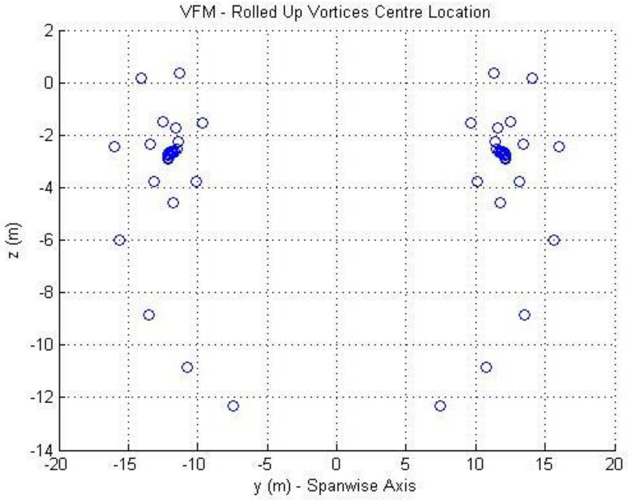	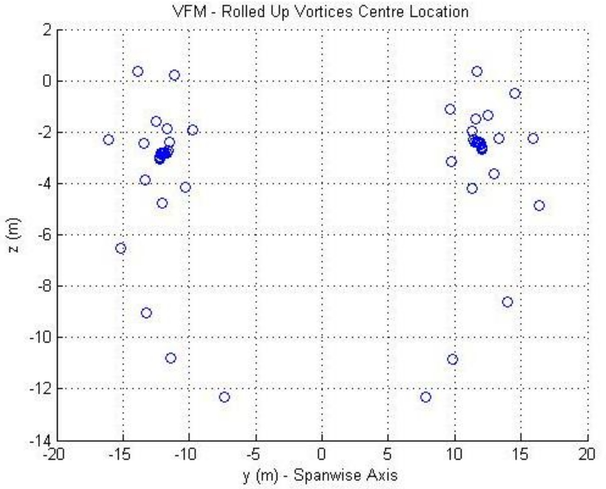
0.75g	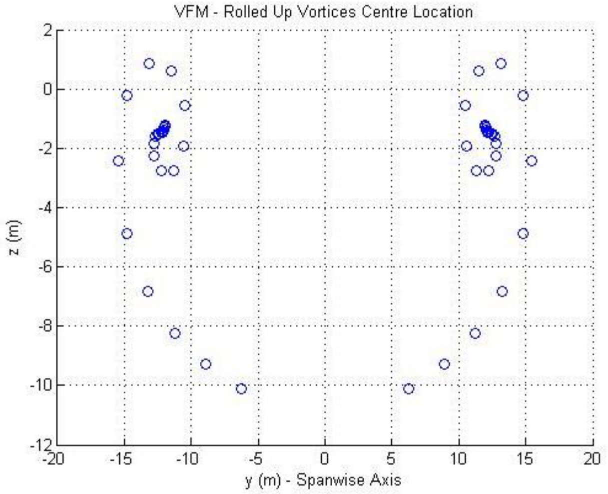	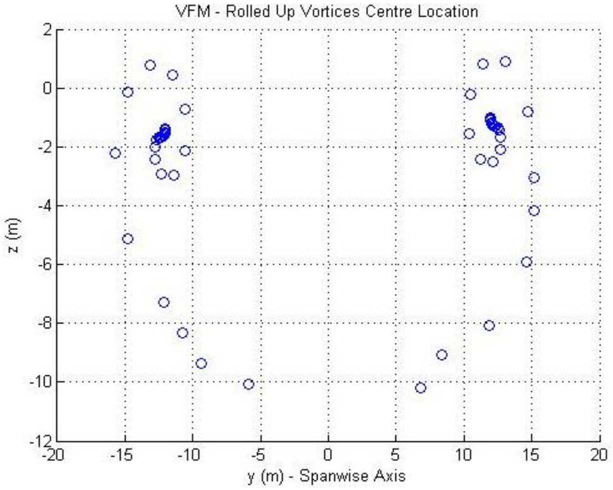

0.5g	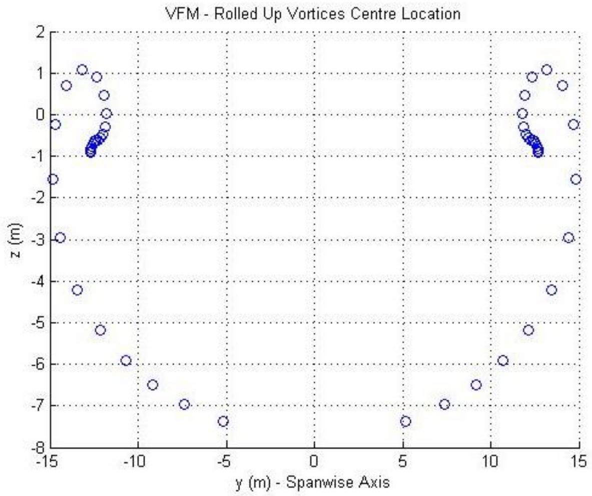VFM - Rolled Up Vortices Centre Location z (m) 2 1 0 -1 -2 -3 -4 -5 -6 -7 -8 -15 -10 -5 0 5 10 15 y (m) - Spanwise Axis	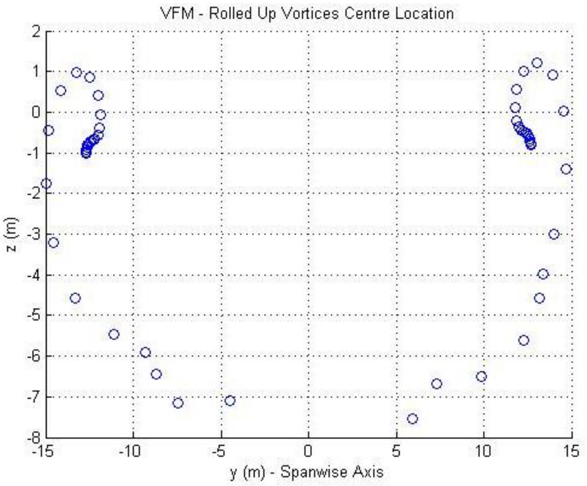VFM - Rolled Up Vortices Centre Location z (m) 2 1 0 -1 -2 -3 -4 -5 -6 -7 -8 -15 -10 -5 0 5 10 15 y (m) - Spanwise Axis
0.25g	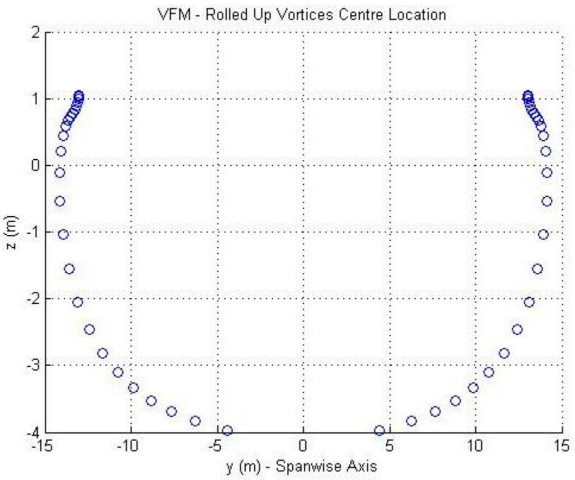VFM - Rolled Up Vortices Centre Location z (m) 2 1 0 -1 -2 -3 -4 -15 -10 -5 0 5 10 15 y (m) - Spanwise Axis	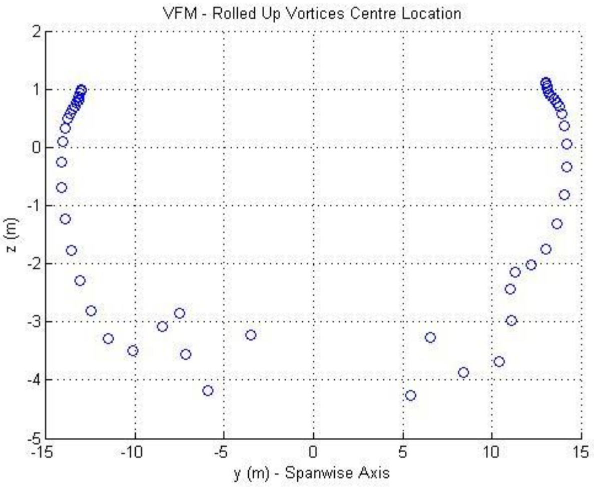VFM - Rolled Up Vortices Centre Location z (m) 2 1 0 -1 -2 -3 -4 -5 -15 -10 -5 0 5 10 15 y (m) - Spanwise Axis

Appendix E

E.1 EBE Faculty: Assessment of Ethics in Research Projects Form

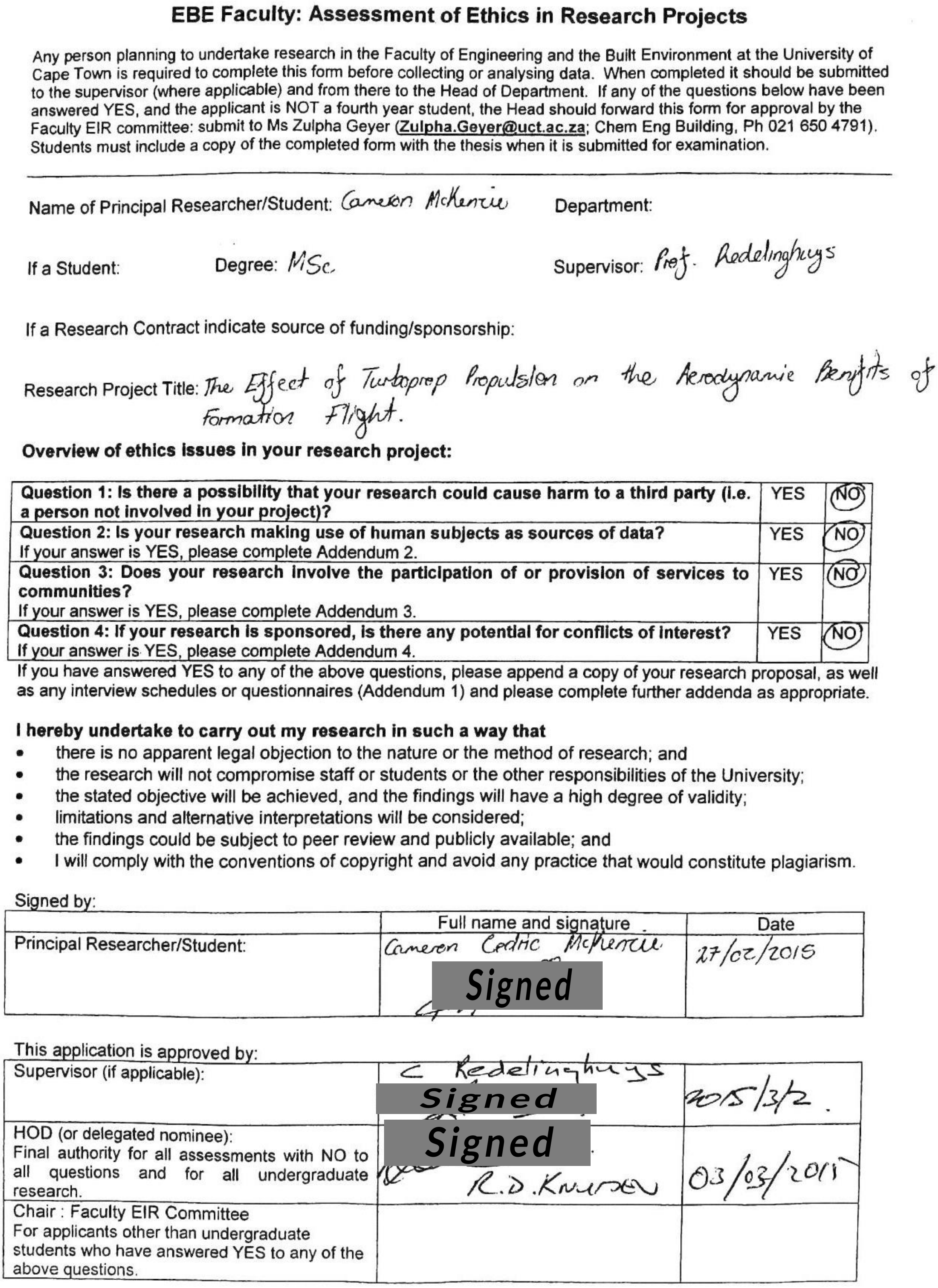

EBE Faculty: Assessment of Ethics in Research Projects

Any person planning to undertake research in the Faculty of Engineering and the Built Environment at the University of Cape Town is required to complete this form before collecting or analysing data. When completed it should be submitted to the supervisor (where applicable) and from there to the Head of Department. If any of the questions below have been answered YES, and the applicant is NOT a fourth year student, the Head should forward this form for approval by the Faculty EIR committee: submit to Ms Zulpha Geyer (Zulpha.Geyer@uct.ac.za; Chem Eng Building, Ph 021 650 4791). Students must include a copy of the completed form with the thesis when it is submitted for examination.

Name of Principal Researcher/Student: Cameron McKenzie Department:

If a Student: Degree: MSc Supervisor: Prof. Redelinghuys

If a Research Contract indicate source of funding/sponsorship:

Research Project Title: The Effect of Turboprop Propulsion on the Aerodynamic Benefits of Formation Flight.

Overview of ethics issues in your research project:

Question 1: Is there a possibility that your research could cause harm to a third party (i.e. a person not involved in your project)?	YES	[✓ NO]
Question 2: Is your research making use of human subjects as sources of data? If your answer is YES, please complete Addendum 2.	YES	[✓ NO]
Question 3: Does your research involve the participation of or provision of services to communities? If your answer is YES, please complete Addendum 3.	YES	[✓ NO]
Question 4: If your research is sponsored, is there any potential for conflicts of interest? If your answer is YES, please complete Addendum 4.	YES	[✓ NO]

If you have answered YES to any of the above questions, please append a copy of your research proposal, as well as any interview schedules or questionnaires (Addendum 1) and please complete further addenda as appropriate.

I hereby undertake to carry out my research in such a way that

- there is no apparent legal objection to the nature or the method of research; and
- the research will not compromise staff or students or the other responsibilities of the University;
- the stated objective will be achieved, and the findings will have a high degree of validity;
- limitations and alternative interpretations will be considered;
- the findings could be subject to peer review and publicly available; and
- I will comply with the conventions of copyright and avoid any practice that would constitute plagiarism.

Signed by:

	Full name and signature	Date
Principal Researcher/Student:	Cameron Cedric McKenzie [redacted]	27/02/2015

This application is approved by:

Supervisor (if applicable):	C Redelinghuys [redacted]	2015/3/2.
HOD (or delegated nominee): Final authority for all assessments with NO to all questions and for all undergraduate research.	[redacted] R.D. Knutsen	03/03/2015
Chair : Faculty EIR Committee For applicants other than undergraduate students who have answered YES to any of the above questions.		